



Leibniz-Institut
für Festkörper- und
Werkstoffforschung
Dresden

Annual Report 2016

Contents

3 Flashback to 2016

7 Facts & Figures

Research Area 1: **Functional Quantum Materials**

- 9 Spin-orbit coupling in iron-based superconductors revealed by ARPES
- 13 Elucidating exotic ground states of correlated materials by electron spectroscopy
- 17 Defect engineering reduces the hysteresis of magnetocaloric Heusler alloys
- 21 Reproducibility in density functional theory calculations of solids and the Full-Potential Local-Orbital code
- 25 Electron-lattice interactions strongly renormalize the charge transfer energy in the spin-chain cuprate Li_2CuO_2

Research Area 2: **Function through Size**

- 29 Structural, dynamic and electronic properties of $\text{Ge}_2\text{Sb}_2\text{Te}_5$ phase-change alloy in liquid state
- 33 Hybrid material microtubes for optoplasmonics and sensing
- 37 Weyl semimetals
- 41 A novel processing route for integrated micro thermoelectric coolers

Research Area 3: **Quantum Effects at the Nanoscale**

- 45 The role of the superconducting layer morphology in the superconducting spin valve effect
- 49 Charge transfer, band-like transport, and magnetic ions at F_{16}CoPc /rubrene interfaces
- 53 Valence-state reflectometry of complex oxide heterointerfaces
- 57 Quantum effects at the nanoscale
- 61 Spin-orbit coupling in tubular photonic microcavities
- 65 Josephson Currents Induced by the Witten Effect
- 68 Emergent magnetic ground state in iridium oxides with strong spin-orbit coupling
- 73 Selective synthesis of endohedral metallofullerenes with methane

Research Area 4: **Towards Products**

- 77 Surface Acoustic Waves: concepts, materials and applications
- 80 Superconducting magnetic bearings in high-speed ring spinning machines
- 83 Entirely flexible on-site conditioned magnetic sensorics

Appendix

- 87 Publications and invited talks
- 116 Patents
- 118 Graduation of young researchers
- 120 Calls and awards
- 121 Scientific conferences
- 122 Guests and scholarships
- 125 Guest stays of IFW members at other institutes
- 126 Board of Trustees, Scientific Advisory Board
- 128 Organization chart of the IFW Dresden



Flashback to 2016

Dear Reader of this Report,

At the Leibniz Institute for Solid State and Materials Research Dresden, 2016 was again a very productive and successful year. Our scientific output has been on the same high level as in the previous years. The appendix to this report contains the record of our publications, invited talks, patent applications, completed graduations and guest stays. The main part presents outstanding scientific results for each Research Area of our research program:

- Research Area 1: Functional quantum materials
- Research Area 2: Function through size
- Research Area 3: Quantum effects at the nanoscale
- Research Area 4: Towards products

The range of materials that we investigate is broad but well-defined. It contains Quantum Materials, a highly topical class of materials in condensed matter physics, as well as Functional Materials, representing an important part of modern materials engineering. In addition, in the last years, Nanoscale Materials became a strong focus of present-day materials science and a crucial material class for cutting-edge developments in electrical engineering. These three classes, Quantum Materials, Functional Materials and Nanoscale Materials, provide the three materials-oriented pillars of our scientific work. The research area “Towards Products” binds together materials science and scientific engineering that is at the borderline to prototypes and products. Establishing, fostering and promoting the contact to industry partners is the main aspect within this activity. While being distinctly multidisciplinary, there is a clear common thread to all our activities: all researchers at the IFW Dresden investigate yet unexplored properties of novel materials with the aim to establish new functionalities and applications.

In July 2016, Burkard Hillebrands took over the position of the Scientific Director, and the two-years interim period of Manfred Hennecke being the Scientific Director ended. During the first months in office, the new Scientific Director launched a mission-and-



vision process with special emphasis on the further development of the IFW's research program. A program meeting with all responsible scientists of IFW is scheduled for spring 2017. Together with the IFW's Administrative Director, Doreen Kirmse, he defined several priority fields of action like the promotion of young academics, development of resources and personnel, improved integration into federal, regional and local environments, internationalization as well as public relations and marketing. We are waiting for a successor for the director position of the Institute for Complex Materials, who will be appointed by a joint committee between IFW and Technische Universität Dresden. We are looking forward to the presentation of invited candidates in spring 2017 and hope for a fast and appropriate procedure to fill the vacant position.

A further important management issue in 2016 was the election of Doreen Kirmse as one of the four Vice Presidents of the Leibniz Association. This is a great opportunity for the IFW – as one of the large Leibniz Institutes – both to take more responsibility and to obtain more visibility within the Leibniz Association.

In 2016, three IFW scientists have been appointed as professors at universities: Fei Ding at University of Hannover (Germany), Qingming Deng at Huaiyin Normal University (China) and Laura Corredor-Bohórquez at the University Rio Grande do Norte (Brazil).

The training of students and young scientists remains a very important concern of our work. PhD and diploma students are involved in nearly all scientific projects and in the resulting publications. Altogether, 29 PhD theses have been successfully completed in 2016, nine of them with the best grade possible – summa cum laude. The IFW acknowledges these outstanding achievements of young scientist by awarding the Tschirnhaus-Medal.

As a Leibniz Institute, the IFW is financed by the federal government and the German federal states in equal parts. However, a considerable extension of capability is the amount of third-party project funding which is also an important index of quality. The level of third-party funding in 2016 amounts to 9.6 Mio. Euro – a level at the forefront within the Leibniz Association. Most of this project funding was acquired in a highly

Dr. Doreen Kirmse says farewell to Prof. Dr. Manfred Hennecke as Scientific Director, June 30, 2016

Handing-over ceremony of the Scientific Director, 4 October 2016

Parting members of the Scientific Advisory Board have been honored with the IFW Leibniz-Medal: Prof. Dr. P. Fauchet, Prof. Dr. E. Umbach, Prof. Dr. X. Obradors and Prof. Dr. A. L. Greer.



competitive mode from the DFG and the European Commission. In particular, a substantial participation in the Collaborative Research Centre 1143 on “Correlated magnetism: From frustration to topology” at the Technische Universität Dresden shows our competitive capability. Among the large number of other third-party funded projects are two DFG Priority Programs that are coordinated by scientists from the IFW, as well as seven DFG Priority Programs and three DFG Research Groups where scientists from the IFW participate. As in the previous years the IFW has been very successful in initiating and participating in EU-funded projects. After having been awarded two ERC Starting Grants in 2012, one ERC Advanced Grant in 2013 and two ERC Consolidator Grants in 2015, again IFW researchers received highly prestigious funding in 2016 with two more ERC Starting Grants. Dr. Axel Lubk received an ERC Starting Grant for his proposal entitled “Nanoscale materials: revealing electromagnetic and deformation fields, chemical composition and quantum states at atomic resolution - ATOM”. Prof. Dr. Fei Ding received an ERC Starting Grant for his research on “Elementary quantum dot networks enabled by on-chip nano-optomechanical systems - QD-NOMS”.

Essentially publicly funded, it is our mission to make our research results public. We have published more than 400 letters, papers and reports in scientific journals and conference proceedings. 189 invited talks were presented by our scientists at conferences, workshops, seminars and other occasions around the world. In 2016, we were granted 18 patents, and applications for 12 more patents have been made. Apart from these scientific communications the IFW continued its large efforts to make scientific work accessible for the general public and to inspire young people to study science or engineering. We took part in many joint actions of the Dresden network of universities and research institutions. From July 4th until October 3rd, 2016, we participated in the joint Science Exhibition at the Dresden Neumarkt Square where the partners of DRESDEN-concept jointly presented their research highlights. Another large event was the presentation of Saxon Leibniz-Institutes during the celebration of the German Unification Day from October 1st to 3rd, 2016 in Dresden. In front of the unique backdrop of the Frauenkirche thousands of visitors were visiting the exhibition tents eager to obtain an impression of Saxony’s research landscape. A much closer look to our research, especially in the fields of magnetism and superconductivity, was offered to the participants

Demonstrator of scanning tunneling microscopy
(photo: C. Hüller)

Award ceremony of Tschirnhaus Medals
for the best PhD theses, 7 March 2016



of the “Junior Doctor” action and the visitors of the “Dresden Long Night of Sciences”. Besides these big events we organize almost weekly lab-tours for various visitor groups, from school classes through official representatives to guests from foreign organizations. The youngest guests have been kindergarten groups during the three children’s days at IFW in September 2016.

A crucial part of the IFW’s identity is its vivid life including the cultivation of the scientific dialogue, family-friendly working conditions, intercultural diversity and the support of sportive and cultural activities. In 2016 we organized a series of workshops, colloquia and talks to foster the scientific dialogue and, along the way, allow for social and communication aspects of cooperation. Social events like the annual IFW Summer Day, the Christmas party and vernissages to our art exhibitions also contribute to a good working atmosphere among all IFW groups.

The positive development of the IFW is being fostered continuously by the engagement of colleagues and partners from universities, research institutes and industry, our Scientific Advisory Board and the Board of Trustees as well as the funding organizations.

We are now looking forward to 2017. It is an important milestone that we celebrate 25 years of IFW Dresden, which was founded on January 1, 1992.

We would like to thank all our partners and friends for their support and cooperation.

Dresden, February 2017

Prof. Dr. Burkard Hillebrands
Scientific Director

Dr. Doreen Kirmse
Administrative Director

Prof. Dr. Fei Ding received an ERC starting grant (photo: M. Hultsch)

Dr. Axel Lubk received an ERC starting grant (photo: M. Hultsch)

New apprentices starting their professional training at IFW in 2016



Facts & Figures

Organization

The Leibniz Institute for Solid State and Material Research Dresden (IFW) is one of currently 91 institutes of the Leibniz Association in Germany. It is a legally independent association, headed by the Scientific Director, Prof. Dr. Burkard Hillebrands, and the Administrative Director, Dr. Doreen Kirmse.

The scientific body of the IFW Dresden is structured into five institutes, the directors of which are simultaneously full professors at Dresden, and Chemnitz Universities of Technology:

- Institute for Solid State Research, Prof. Dr. Bernd Büchner
- Institute for Metallic Materials, Prof. Dr. Kornelius Nielsch
- Institute for Complex Materials, Dr. Thomas Gemming (temp.)
- Institute for Integrative Nanosciences, Prof. Dr. Oliver G. Schmidt
- Institute for Theoretical Solid State Physics, Prof. Dr. Jeroen van den Brink

Further divisions are the Research Technology Division and the Administrative Division.

Financing

The institutional funding of IFW is supplied by the Federal government and by the German states (Länder) in equal parts. In 2016, this funding was about 33.378 million euros in total.

In addition, the IFW receives project funding from external sources of about 9,6 million euros. Thereof, about 40,5% came from German Research Foundation (DFG), 29% from European Union programs, 11,1% from Federal Government projects, 12,1% from industry and 7,4% from other donors including the Free State of Saxony.



Personnel

On 31 December 2016, 483 staff members were employed at the IFW, including 94 doctorate students as well as 18 apprentices in seven different vocational trainings and two business students of a vocational academy.

Gender equality, as well as work life balance, are defined goals of the IFW Dresden. In 2016, the percentage of women in scientific positions was 25 % and the percentage of women in scientific leading positions was 21 %. The IFW is regularly audited for the certificate "audit berufundfamilie" (a strategic management tool for a better compatibility of family and career).

Number of publications and patents

In terms of publications, the qualitative and quantitative level remains high at the IFW. In 2016, IFW scientists have published more than 400 refereed journal articles, a considerable number of them in high impact journals. Furthermore, IFW members held 189 invited talks at conferences and colloquia.

By 31 December 2016, the IFW holds 113 patents in Germany and 80 international patents.

Christmas Lecture at IFW by
Prof. Dr. Jens Freudenberger

Get-together of students with automobile
and aerospace industry at IFW Dresden
(photo: C.-I. Mokry)

Micro-actuator for vaporization of fluids based
on Surface Acoustic Waves (SAW)

Research Area 1

Spin-orbit coupling in iron-based superconductors revealed by ARPES

S. Borisenko, D. Evtushinsky, A. Fedorov, Y. Kushnirenko, E. Haubold, Z. Liu, I. Morozov, R. Kappenberger, S. Wurmehl, B. Büchner, A. Yaresko¹, T. Kim², M. Hoesch², T. Wolf³, N. Zhigadlo⁴

Abstract: Spin-orbit coupling (SOC) is a fundamental interaction in solids that can induce a broad spectrum of unusual physical properties from topologically non-trivial insulating states to unconventional pairing in superconductors. In iron-based superconductors (IBS) its role has so far been considered insignificant with the models based on spin- or orbital fluctuations pairing being the most advanced in the field. Using high-resolution angle-resolved photoemission spectroscopy (ARPES) we have detected a significant splitting of the electronic states due to spin-orbit interaction with the energy scale exceeding that of nematic order in all main representatives of IBS. This splitting occurs in the immediate vicinity to the Fermi level and the involved electrons turn out to be the most sensitive to the superconductivity itself, implying the intimate relation between this fundamental interaction and mechanism of high-temperature superconductivity.

Detection of spin-orbit splitting in LiFeAs

A well known from the textbooks fact is that in the presence of spin-orbit coupling, the spin of electron quantized along any axis is no longer a good quantum number and the electronic states are better described by the total angular momentum. This canonical interaction may result in a lifting of the degeneracy of the electronic states and lead to the fascinating physical phenomena such as spin Hall effects, spin relaxation, topological insulation, occurrence of Dirac, Majorana and Weyl fermions, etc. No wonder that the systems with SOC are in the focus of intensive research in the field of spintronics – there is a unique opportunity to manipulate the spin without the aid of magnetic field. A special role has been played by SOC in the field of superconductors. In low-dimensional or noncentrosymmetric systems it can promote and stabilize superconductivity [1], allow ferromagnetism to coexist with superconductivity [2] or even rise T_c [3]. SOC could be a very important ingredient in describing the superconducting state in Sr_2RuO_4 , where it is larger than the superconducting gap [4]. In iron-based superconductors (IBS), where the low-energy electronic states are composed of different orbitals, SOC-induced spin anisotropy together with the orbital mixing may directly influence the orbital and spin angular momentum of the Cooper pairs, thus making the determination of the pairing symmetry non-trivial. However, until now SOC in IBS was considered insignificant.

We start with the example of LiFeAs, which is a special representative of iron-based family of superconductors [5]. This material is one of the most studied due to its stoichiometry and non-polar surfaces. Its electronic structure is believed to be well understood from numerous ARPES experiments and the parameterization of its electronic dispersions has been used to test the most developed theoretical approaches [6-8].

According to the band structure calculations the most convenient places to detect the spin-orbit splitting in LiFeAs is exactly in the center of the Brillouin Zone (BZ) and at the BZ-boundary where it crosses the electron-like pockets [9]. In Fig.1a we show the ARPES data taken along the high-symmetry direction in the BZ running through the Γ -point. From this intensity plot one is able to resolve three hole-like dispersions forming the corresponding Fermi surface pockets around Γ . Two of the dispersions have their maxima below the Fermi level and these are non-degenerate, i.e. the tops of these bands are located at slightly different binding energies. This is confirmed by panel b) of Fig. 1 where the energy-distribution curve taken at zero momentum is shown. There are two features separated by 9.5 meV and this distance is due to SOC.

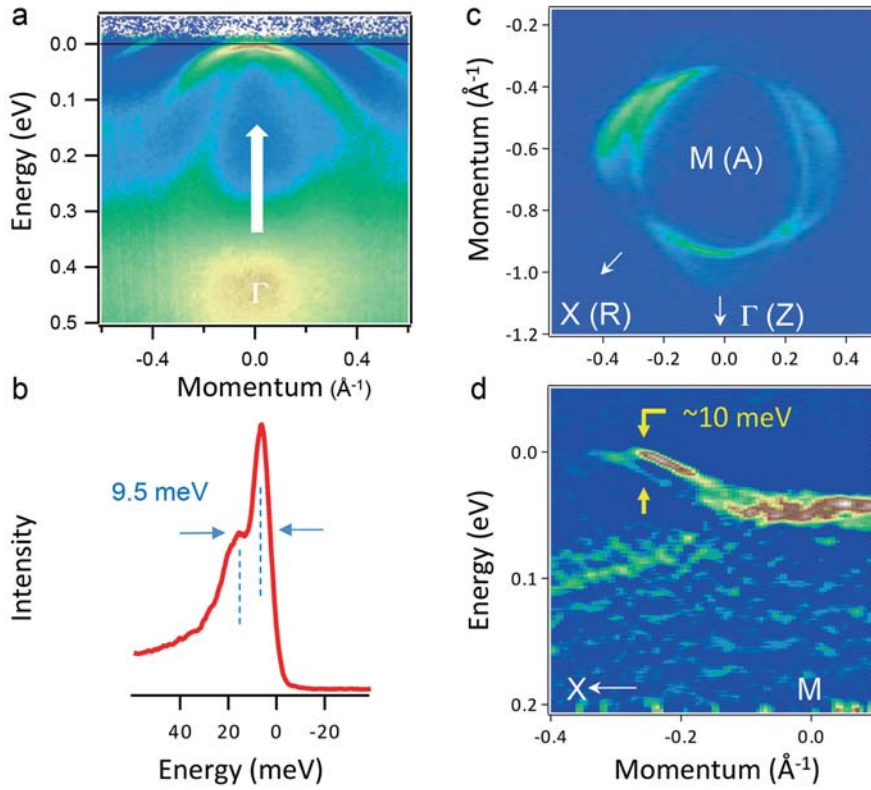


Fig. 1: (a) ARPES data along the high-symmetry direction in LiFeAs multiplied by the Fermi function. (b) Energy-distribution curve corresponding to zero momentum in panel (a). (c) High-precision Fermi surface map of electron pockets in LiFeAs. (d) Second derivative of ARPES intensity recorded along the MX-direction.

To measure the magnitude of the SOC on the electron pockets we have to switch to the other location in the k -space mentioned earlier. Since the SOC split dispersions cross the Fermi level in (k_x, k_y) plane, we can observe this splitting in the momentum space with high resolution. We have recorded the detailed Fermi surface map near the corner of the BZ especially for this purpose. Indeed, as follows from Fig. 1c, electron pockets are no longer degenerate along the MX-direction, contrary to what is expected from non-relativistic band structure. To quantify the effect in terms of energy, we plot the intensity as a function of momentum along MX and energy in panel d). The dispersions are again split by ~ 10 meV demonstrating the lifting of the degeneracy of electron pockets along the high symmetry directions and closely corresponding to the value determined in the center of the BZ. As predicted by the calculations, we have thus directly observed the SOC in LiFeAs.

Universality of spin-orbit coupling in iron-based superconductors family

The similar experiments on FeSe reveal the presence of SOC and support the dominant role of this interaction in comparison with the nematic splitting [10]. In Fig. 2a,b we show the data similar to those from Fig. 1a, but for FeSe and taken at two different excitation photon energies corresponding to Γ and Z-points of the BZ. In this case the separation of the tops of the bands is larger (~ 25 meV) and this is not only due to the larger SOC. FeSe is also known for hosting the electronic nematic transition and this order at low temperatures contributes to the lifting of the degeneracy at the center of the BZ. On the other hand, nematic order parameter results in the splitting of the bands exactly in the corners of the BZ and this fact allowed us to determine two energy scales (SOC and nematicity) independently. It turned out that in FeSe spin-orbit interaction is stronger [10].

The analogous data for other two main families of IBS are presented in other panels of Fig. 2. In the case of the optimally hole-doped 122 material ($T_c \sim 38$ K), there is no possibility to determine the SOC directly at the center of the BZ since tops of all hole-like bands are well above the Fermi level in accordance with lower electron concentration.

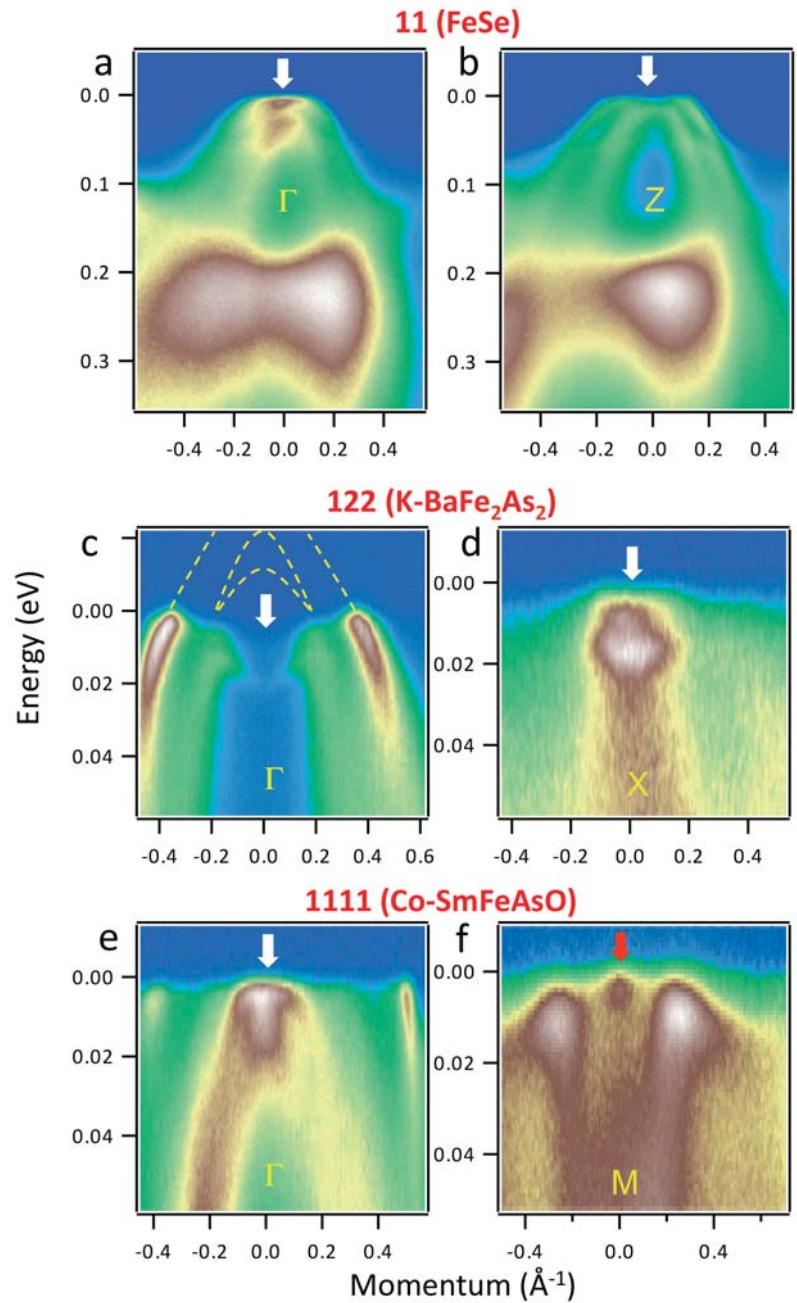


Fig. 2: (a) Photoemission intensity along the cut in the k-space running through the Γ -point in FeSe. (b) Same as (a), but for the cut running through Z-point. (c) Same as (a) for K-BaFe₂As₂. Dashed lines show the anticipated dispersions in the unoccupied part of the spectrum. (d) ARPES intensity plot for the cut, going through the corner of the BZ in K-BaFe₂As₂. (e) and (f) Same as (c) and (d) in the case of Co-SmFeAsO material. White arrows show the doublets while the red arrow shows a singlet.

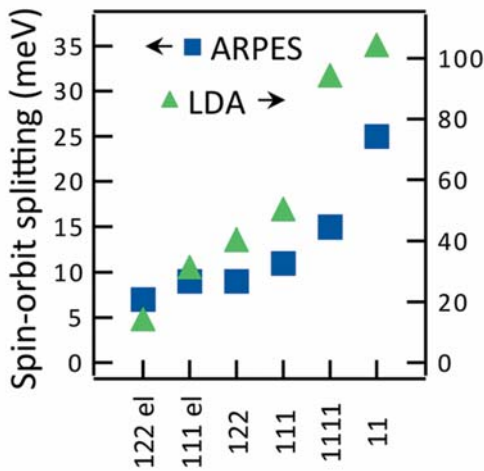
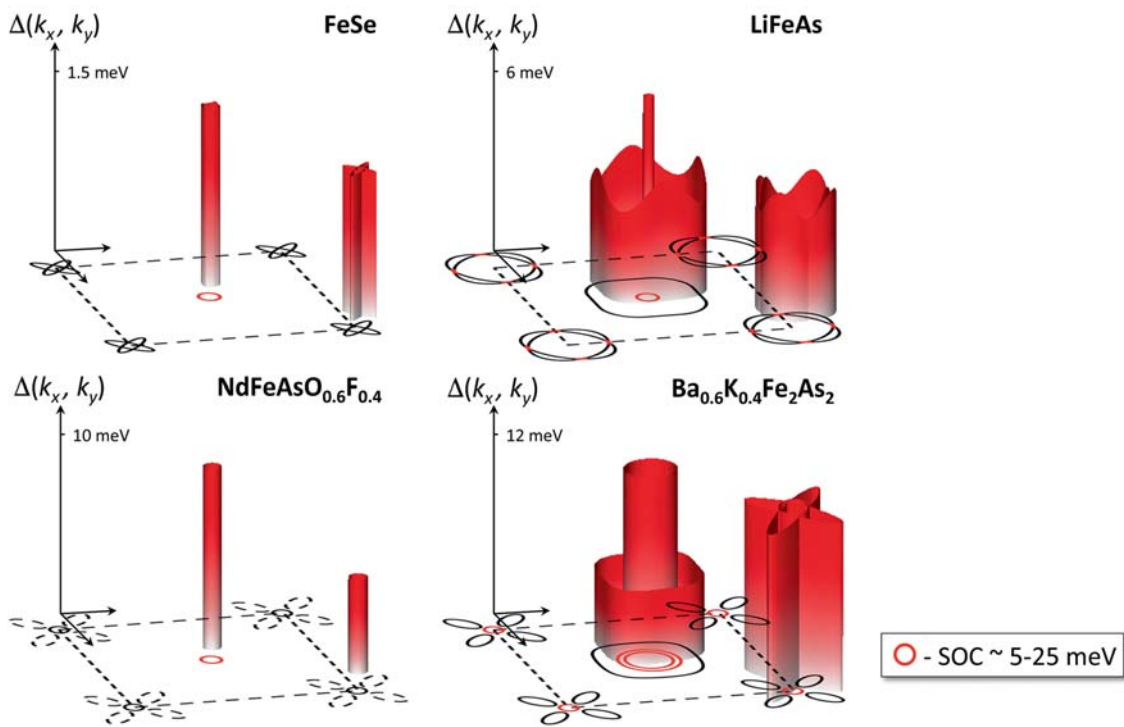


Fig. 3: Comparison of the experimental values for SOC obtained by reading the peak positions from the corresponding energy-distribution curves, with the theoretical values. 'el' means electron pocket.

We went around this limitation by the following procedure. Because of the sizeable super-conducting gap and proximity of the band's edges to EF, the top of the band is "reflected" from the Fermi level to the occupied side of the spectrum below critical temperature T_c (see Fig. 2c and Fig. 4h in Ref. 9). The SOC can be determined from the energy-distribution curve (not shown) going through the reflected tops. Another distinction of the 122 family from 11 and 111 materials is that the SOC does lift the degeneracy right at the corner of the BZ (now X-point, not M, since BZ is different) because of different crystal symmetry. This splitting is visible in Fig. 2d I. Finally, we detect the splitting also in the representative of 1111 family, the Co-SmFeAsO ($T_c \sim 16$ K). In accordance with the calculations, there is a doublet in Γ and a singlet in M-point (Fig. 2e,f). We summarized our observations in Fig. 3 where we plotted the experimentally determined values of SOC together with those predicted by the band structure calculations. There is a clear correlation between the two datasets, which speaks in favor of our interpretation of the observed splitting. We note, that experimental value for FeSe is slightly overestimated since the nematic order contributes to the splitting at the center of the BZ, but this contribution remains noticeably smaller than that of SOC.



Relation to the mechanism of high-temperature superconductivity

We expect that these findings are highly relevant for the superconductivity in IBS. Existing approaches strongly rely on the presence of shallow bands crossing the Fermi level with energy dispersion of the order of the pairing interaction. Another theoretical study demonstrates that the inclusion of SOC leads to further mixing of triplet pairing, as well as to an anisotropic energy gap on all Fermi surfaces in iron-based superconductors [11], the latter being observed experimentally [12]. In Fig. 4 we schematically show the Fermi surface contours and gap functions for the representatives of IBS families having the highest T_c . We mark in red those Fermi surfaces or their portions, which are formed by the spin-orbit split states. Remarkably, the largest superconducting gap in each material is supported by the SOC-induced Fermi surfaces. Moreover, in 11 and 122 IBS, where the SOC in the corner of the BZ is comparable to that in the centre, one sees correspondingly considerable superconducting gaps.

We have thus observed the decisive influence of the spin-orbit interaction on the low-energy electron dynamics of all representative iron-based superconductors, which is stronger than possible nematic effects. The size of SOC is comparable to the pairing gap and the Fermi energy, which may have profound implications on the mechanism of superconductivity in these materials.

Fig. 4: Sketches of the Fermi contours are shown in the horizontal plane. Fully red or partially red contours are the states at the Fermi level induced by the large (5–25 meV) spin-orbit splitting detected experimentally. Gap functions are given by the third axis and shown only for the centres and one of the corners of the BZ for simplicity. All gap functions are normalized to the maximum value indicated in each plot.

- [1] A. D. Caviglia et al., Phys. Rev. Lett. 104, 126803 (2010).
- [2] D. A. Dikin et al., Phys. Rev. Lett. 107, 056802 (2011).
- [3] H. Jeffrey Gardner et al., Nat. Phys. 7, 895–900 (2011).
- [4] M. W. Haverkort et al., Phys. Rev. Lett. 101, 026406 (2008).
- [5] S. V. Borisenko et al., Phys. Rev. Lett. 105(6), 067002 (2010).
- [6] Y. Wang et al., Phys. Rev. B 88(17), 174516 (2013).
- [7] F. Ahn et al., Phys. Rev. B 89(14), 144513 (2014).
- [8] T. Saito et al. Phys. Rev. B 90, 035104 (2014).
- [9] S. V. Borisenko et al. Nat. Phys. 12, 311 (2016).
- [10] A. Fedorov et al. Sci. Rep. 6, 36834 (2016).
- [11] V. Cvetkovic and O. Vafek, Phys. Rev. B 88, 134510 (2013)
- [12] S. V. Borisenko et al., Symmetry 4, 251–264 (2012).

Funding: DFG (B01912/2-2, B01912/3-1, BE1749/13 and WU595/3-1)

Cooperation: ¹MPI FKF Stuttgart, ²Diamond Light Source Ltd. UK, ³KIT,

⁴Univ. of Bern, Dept. of Chemistry and Biochemistry

Elucidating exotic ground states of correlated materials by electron spectroscopy

A. Koitzsch, C. Habenicht, N. Heming, H. Kandpal, M. Knupfer,
E. Müller, B. Büchner, J. van den Brink

Abstract: Understanding the properties of materials is at the core of condensed matter physics and often the basis for applications. The complex quantum materials, the subject of this research area, are especially challenging in this regard but frequently hold great promises for future technologies. Here we demonstrate how state-of-the-art spectroscopy combined with theoretical investigations help to elucidate important aspects of the ground state properties of two such materials, α -RuCl₃ and CeB₆. Our results serve as a starting point of systematic material modifications and concrete follow-up investigations and promote better understanding of a variety of compounds.

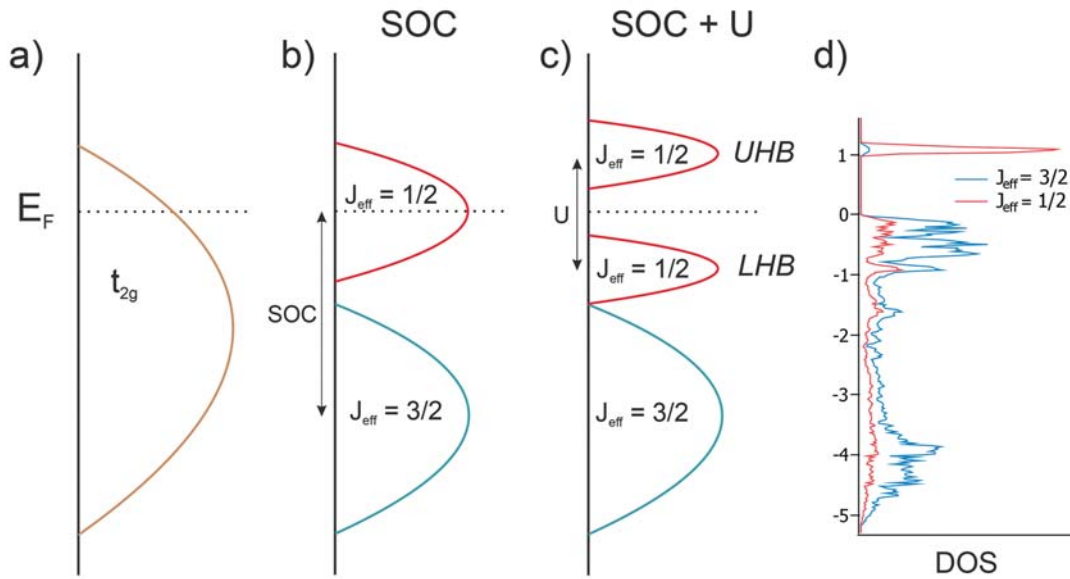
J_{eff} Description of the Honeycomb Mott Insulator α -RuCl₃

The search for novel electronic and magnetic ground states has ever been a driving force of condensed matter physics. The effects of strong spin-orbit coupling, possibly competing with other energy scales, have turned out to be especially fruitful in this respect in recent years. This is most prominently manifested by the advent of topological insulators [1]. More recently, the Kitaev model was established, which describes the bond-dependent spin interactions on a honeycomb spin $\frac{1}{2}$ lattice [2]. The Kitaev model attracts enormous attention because it is exactly solvable and its ground state is an exotic quantum spin liquid. However, unambiguous experimental evidence is lacking so far. The prime candidates for the realization of Kitaev physics have been the 5d⁵ iridates A₂IrO₃ (A = Na, Li) [3]. This thread of research relies on the realization of effective $J_{\text{eff}} = \frac{1}{2}$ pseudospins by the combined interaction of spin-orbit coupling and crystal field splitting. But the concept of $J_{\text{eff}} = \frac{1}{2}$ pseudospins is under debate for the iridates due to substantial lattice distortions lifting the t_{2g} degeneracy, which, strictly speaking, invalidates the J_{eff} description.

α -RuCl₃ appeared recently against this background as a 4d analogue to the iridates [4]. Ru is in a 3+ state and features a d⁵ electron count with a low spin state. Its spin-orbit coupling ($\lambda \approx 0.1$ eV) is strongly reduced as compared to the iridates, but so is its bandwidth W due to presumed correlation effects. Importantly, the local cubic symmetry is almost perfect in contrast to the iridates. Hence, the J_{eff} description might be still operable for α -RuCl₃. Another practical advantage is that it can be synthesized as large, easy-to-cleave single crystals, which offer the possibility of exfoliation. RuCl₃ has been known for a long time and is even of some importance as a chemical. Its electronic structure has been repeatedly investigated over the years by optical spectroscopy and photoemission. The picture of a Mott-insulating state was proposed where the Ru 4d bands are situated close to E_F but show little dispersion [5].

Here we elucidate the electronic structure of α -RuCl₃ by state of the art photoemission (PES), electron-energy-loss spectroscopy (EELS), density-functional-theory (DFT), and multiplet calculations. We achieve a consistent, quantitative picture of a spin-orbit assisted Mott insulator. The central question of this study, and decisive for the prospects of α -RuCl₃ as a possible carrier of Kitaev ground states, is whether or not the $J_{\text{eff}} = \frac{1}{2}$ description of the electronic structure is appropriate. Based on the comparison of the DFT calculations with results from angle-resolved photoemission spectroscopy (ARPES), we can answer this question affirmatively [6].

Fig. 1 shows schematically the J_{eff} description along with the outcome of the DFT calculations. Starting with a situation where only the crystal field splitting is considered (Fig. 1a), subsequently the spin-orbit coupling (Fig. 1b) and on-site correlations (Fig. 1c) are taken into account, leading, in an ideal case, to a splitting of the pure $J_{\text{eff}} = \frac{1}{2}$ band.



As seen in Fig. 1d, already the DFT results are more complex. This can be compared to experiment. Fig. 2 presents ARPES results compared to theory. The overall experimental bandstructure is reasonably well described by the DFT (Fig. 2a). We observe weakly dispersing, broad valence bands (Fig. 2b). The comparison is significantly better for the calculation, where the spin-orbit coupling is included, indicating its relevance for the ground state properties (Figs. 2c-e).

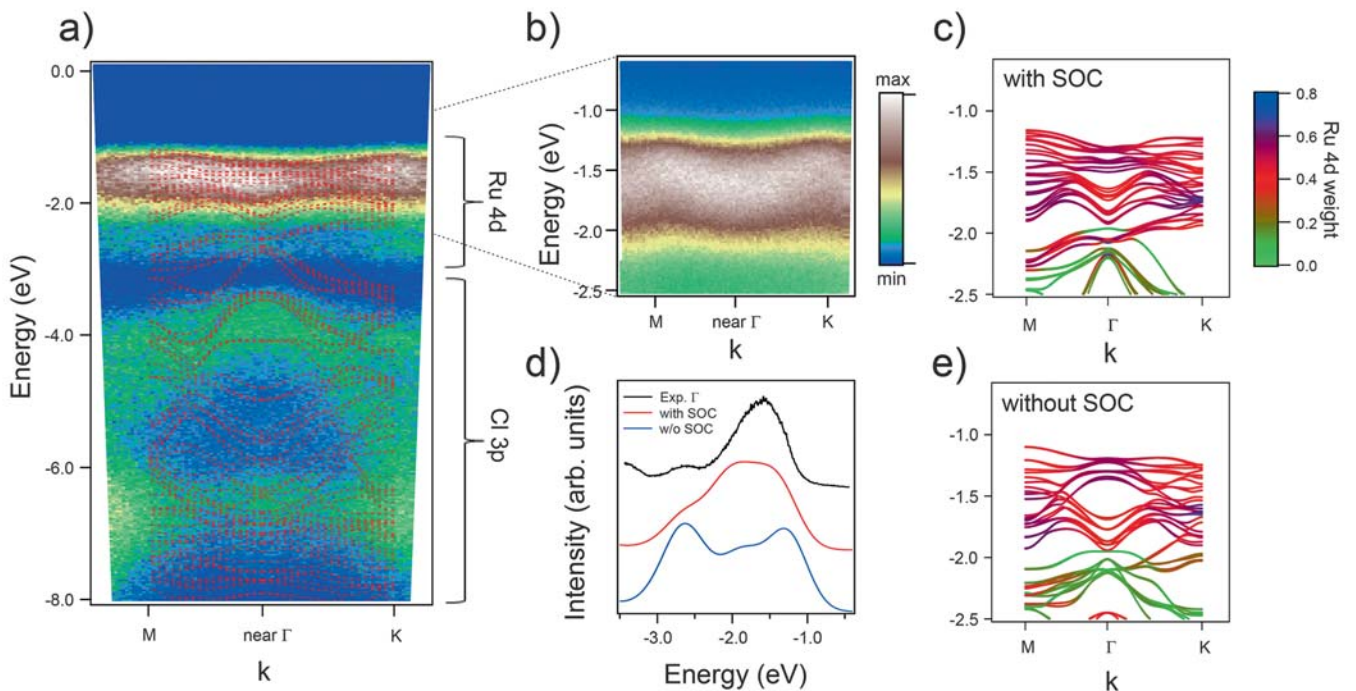
The above findings convey the picture of a Mott insulator whose low-energy structure is dictated by a mixture of the local cubic symmetry and spin-orbit coupling which might give rise to exotic magnetic ground states [7].

Nesting-driven multipolar order in CeB₆ from photoemission tomography

Some heavy fermion materials show so-called hidden-order phases which are invisible to many characterization techniques and whose microscopic origin remained controversial for decades. Among such hidden-order compounds CeB₆ is of model character due to its simple electronic configuration and crystal structure. CeB₆ is a heavy-fermion material showing a mass enhancement of the order of 100 [8], which is due to the hybridization of the localized f-electrons with the itinerant conduction electrons. Mag-

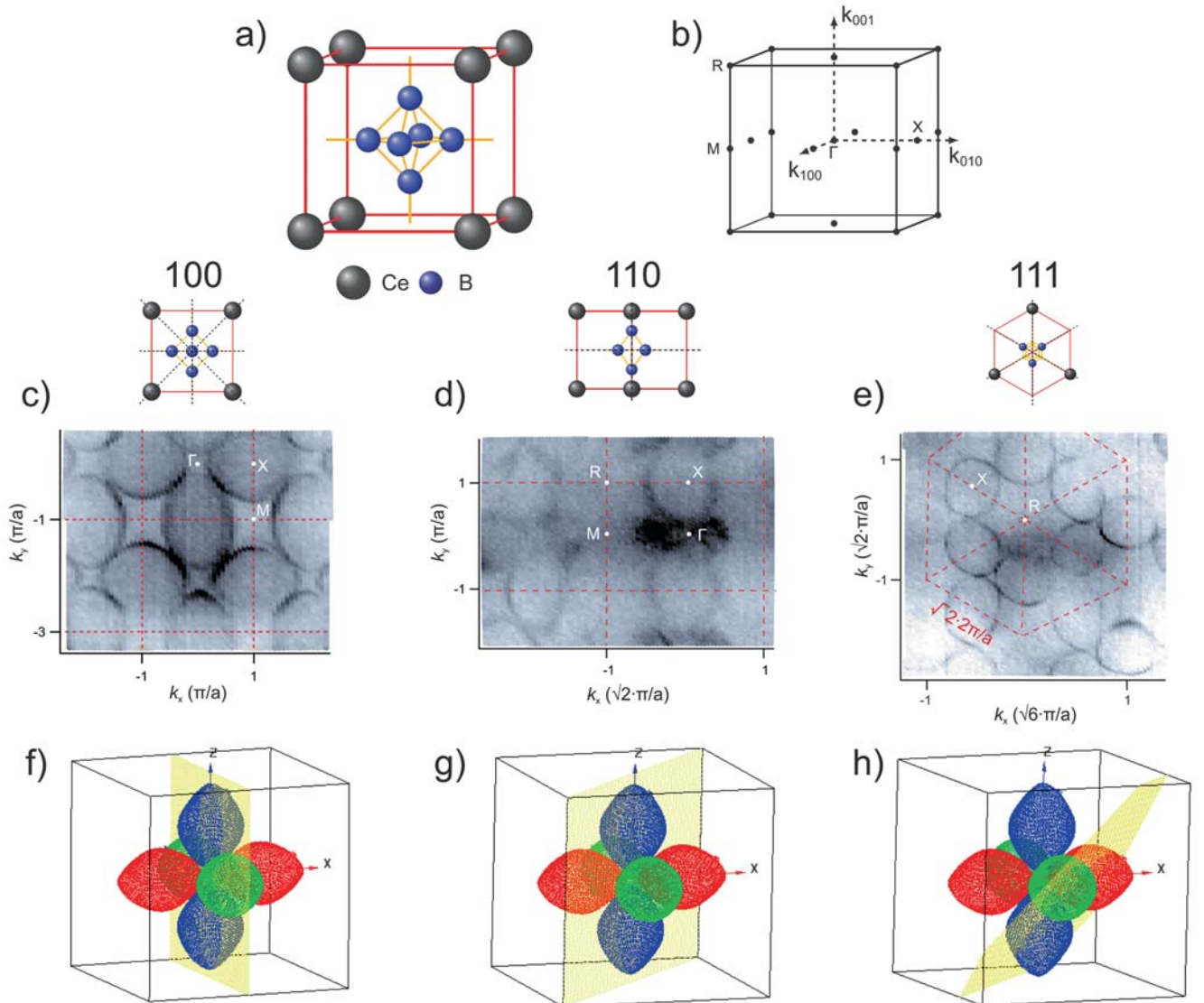
Fig. 1: (a)–(c) J_{eff} description of the d-level electronic structure. (a) Schematic density of states without interactions. (b) Under the presence of strong spin-orbit coupling. (c) With spin-orbit coupling and on-site correlation U . (d) Calculated density of states of α -RuCl₃ with spin-orbit coupling and on-site correlation.

Fig. 2: (a) Angle dependence of the valence band of α -RuCl₃. Red dotted lines are results of band structure calculations. **(b)** Expansion of the Ru 4d region. **(c)** Band structure with inclusion of the SOC. **(d)** Comparison of experimental and theoretical Γ -point spectra extracted from calculations with and without spin-orbit coupling (SOC). **(e)** Band structure without SOC.



netism of heavy fermion materials is determined by the competition of Kondo screening and the Ruderman–Kittel–Kasuya–Yosida (RKKY) interaction, the former quenching the local moments and favouring paramagnetic behaviour, the latter promoting magnetic order mediated by the conduction electrons. In CeB_6 the usual paramagnetic response is found before antiferromagnetic order with a double- \mathbf{Q} commensurate structure characterized by the propagation vectors $\mathbf{Q}_{\text{AFM1}} = (\pi/2, \pi/2, 0)$ and $\mathbf{Q}_{\text{AFM2}} = (\pi/2, \pi/2, \pi)$ sets in below $T_N = 2.3$ K. However, the phase diagram is more complex: the antiferromagnetism is preceded by a famous hidden order state at $T_Q = 3.2$ K, the so called antiferro-quadrupolar phase (AFQ), which has been explained by the ordering of quadrupole moments with $\mathbf{Q}_{\text{AFQ}} = (\pi, \pi, \pi)$ [9]. The latter has long been elusive to neutron diffraction experiments. Attempts were made to describe these observations by theories emphasizing the local character of the magnetic moments [10]. In an itinerant picture, on the other hand, the strength of the magnetic interactions is mediated by the conduction electrons and depends on the low-energy electronic structure. It can be expressed within linear response theory by the Lindhard function. The latter quantifies the propensity of a given electronic structure towards nesting instabilities of the Fermi surface and the subsequent formation of a new, in our case magnetically ordered, state. An interesting question in this context is whether or not the AFQ state also is directly linked to the electronic structure in a similar way. However, although CeB_6 has been studied for more than 50 years, the three-dimensional (3D) electronic structure of CeB_6 was not known so far neither from experiment nor from theory with sufficient accuracy to test this

Fig. 3: (a) Crystal structure of CeB_6 . (b) Brillouin zone with high symmetry points. (c–e) Fermi surfaces and representations of the different cleavage planes. (c) (100), taken with a photon energy of $h\nu = 700$ eV; (d) (110), $h\nu = 609$ eV; (e) (111), $h\nu = 700$ eV; measured at 12 K. (f–h) 3D representation of the measured Fermi surface and the measurement plane. The different colours of the ellipsoids are for clarity.



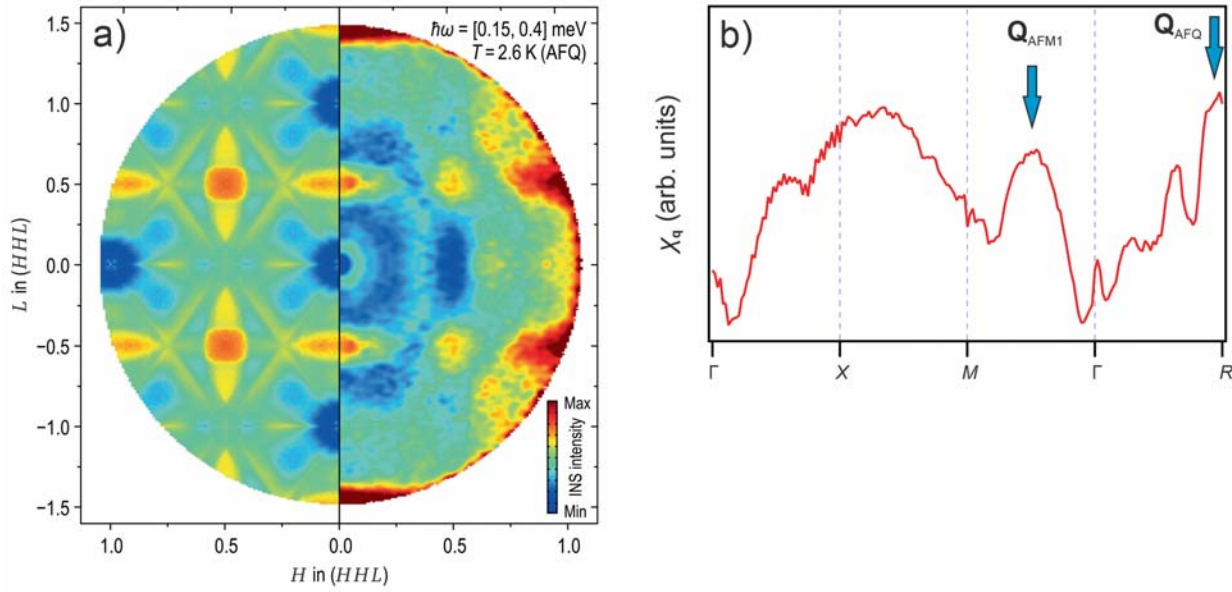


Fig. 4: (a) Two-dimensional representation of the Lindhard function in the (HHL) plane compared with the distribution of magnetic quasielastic scattering intensity measured by inelastic neutron scattering at $T = 2.6$ K in reciprocal lattice units. (b) Lindhard function extracted for certain high symmetry directions with the indication of peaks coinciding with the propagation vectors of low-temperature ordered phases.

hypothesis. This deficiency called for a detailed investigation of the band structure and the Fermi surface of CeB_6 . Here we implement a rigorous and innovative approach: We measured samples cleaved along all high-symmetry crystallographic planes (100), (110), (111). This probes different planes of \mathbf{k} -space, resembling a tomographic type of measurement that yields complete 3D information about the electronic structure in contrast to conventional angle-resolved photoemission spectroscopy (ARPES), in which one direction orthogonal to the surface is always inferior to two others. Fig. 3 presents the experimental results obtained in this way. Fig. 3a, b show schematically the crystal structure and the Brillouin zone of CeB_6 . Fig. 3c-e present the ARPES data for the three different cleavage planes, which clearly reflect the underlying crystal symmetry. Fig. 3f-h provide 3D representations of the measured \mathbf{k} -space cuts. Additionally, we conducted photon-energy dependent measurements in the soft X-ray regime spanning a wide k_z interval (not shown). We use the entire dataset to calculate the Lindhard function and compare it with neutron scattering data (see Fig. 4). From the consistency of both, we conclude that the magnetic excitations and the AFQ propagation vector in CeB_6 are dictated by the Fermi-surface geometry [11]. Hence, the hidden order is mediated by itinerant electrons.

Our findings will serve as a paradigm for the investigation of hidden-order phases in f-electron systems, but also generally for situations where the itinerant electrons drive orbital or spin order.

- [1] Z. Hasan, Rev. Mod. Phys. 82, 3045 (2010)
- [2] A. Kitaev, Ann. Phys. (Amsterdam) 321, 2 (2006)
- [3] J. Chaloupka, Phys. Rev. Lett. 105, 027204 (2010)
- [4] K.W. Plumb, Phys. Rev. B 90, 041112 (2014)
- [5] I. Pollini, Phys. Rev. B 53, 12769 (1996)
- [6] A. Koitzsch, Phys. Rev. Lett. 117, 126403 (2016)
- [7] R. Yadav, Scientific Reports, 37925 (2016)
- [8] T. Mueller, J. Magn. Magn. Mater. 7677, 35 (1988)
- [9] J. M. Effantin, J. Magn. Magn. Mater. 47, 145 (1985)
- [10] P. Thalmeier, J. Phys. Soc. Jpn. 67, 2363 (1998)
- [11] A. Koitzsch, Nature Communications 7, 10876 (2016)

Funding: Deutsche Forschungsgemeinschaft (KO 3831/3-1; SFB 1143)

Cooperation: TU Dresden; Frantsevich Institute Kiev, Ukraine; Paul Scherrer Institute, Villigen, Switzerland; Institut Laue-Langevin, Grenoble, France

Defect engineering reduces the hysteresis of magnetocaloric Heusler alloys

R. Niemann, A. Diestel, B. Schleicher, S. Schwabe, L. Schultz, K. Nielsch, S. Fähler

Magnetocaloric materials as promising solid-state refrigerants

A large fraction of the energy consumed worldwide is used for air conditioning and refrigeration in households, transportation and industry. Magnetocaloric materials are promising as alternative solid-state refrigerants for more sustainable and environmentally friendly cooling devices. The highest caloric effects occur in materials that exhibit first-order phase transitions that can be induced by external magnetic fields or mechanical stress [1, 2]. These transformations proceed by nucleation and growth of a low temperature phase with a different crystal structure and mostly different magnetic properties. The structural misfit between the phases leads to a hysteresis. All irreversible processes during the transformation are undesired since they heat up the material and reduce the efficiency of any cooling application. We study Ni-Mn-Ga, a shape memory alloy that exhibits a martensitic transformation and a large magnetocaloric effect. By nanoindentation into epitaxial films, we create well-defined defects that promote the formation of the low-temperature phase in their vicinity [3].

Hysteresis as challenge for materials with a first-order transformation

Hysteresis in first-order transitions is a consequence of the formation and movement of phase boundaries. This leads to energy barriers that have to be overcome to form a nucleus and grow the product phase. In order to reduce the energy barriers and thus the hysteresis in magnetocaloric applications, different approaches have been proposed which are either structure or microstructure related.

Approaches tackling the structure try to decrease the lattice misfit between both phases at the phase boundary. This can be achieved by tuning the chemical composition, but this commonly also changes other important intrinsic parameters like the transformation temperature or magnetization difference between the phases, which directly influence the magnetocaloric effect. Microstructural methods usually try to decrease the nucleation barrier. In general, these barriers are drastically reduced close to defects, where heterogeneous nucleation is possible. Consequently, the hysteresis can be effectively reduced by introducing defects, e.g., via ion irradiation or precipitations.

Nanoindentation reduces the nucleation barrier in a Ni-Mn-Ga film

A 1.5 μm thick epitaxial $\text{Ni}_{48}\text{Mn}_{33}\text{Ga}_{19}$ film was grown by sputter deposition onto a single crystalline MgO substrate. X-ray diffraction (not shown) revealed that the film undergoes a transformation from a cubic phase (austenite) to a monoclinic phase (martensite) when cooled below 400 K.

To create a permanent surface defect, nanoindentation was performed at room temperature in the martensitic state with a pyramidal Berkovich tip and a maximum force of 20 mN. The plastically deformed surface area close to the remanent indent was analyzed at room temperature by atomic force microscopy (Fig. 1). The tip has left a regular triangular indent with an edge length of about 1 μm and with a depth of about 170 nm. Its shape is not perfectly pyramidal; there is a kink in the left face of the indent. The large depth compared to the film thickness shows that the deformation near the indent was mostly plastic by movement of dislocations and not entirely pseudo-plastic by twin boundary movement. The latter is additionally hindered by the complex arrangement of twin boundaries in the martensite.

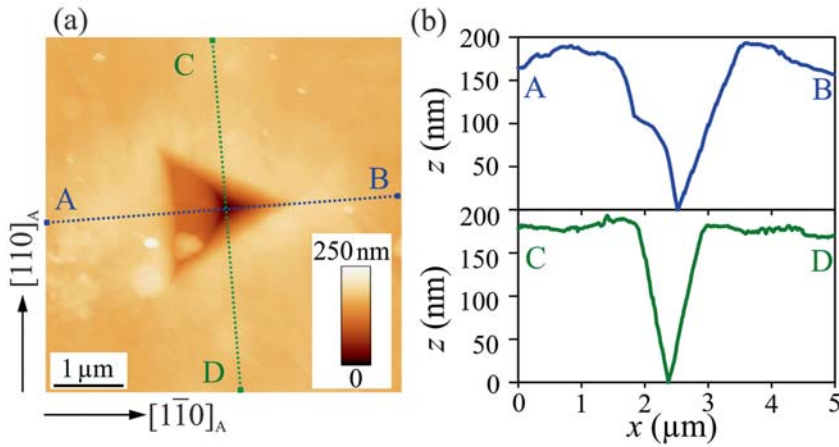


Fig. 1: (a) AFM images of the remanent indent in an epitaxial Ni-Mn-Ga film. Additional topography from the martensitic microstructure is visible. (b) Height z along the profiles A-B and C-D.

To determine how the indent influences the martensitic transformation on a local scale, a series of scanning electron micrographs was acquired during the martensitic transformation [3].

Fig. 2a shows the martensitic microstructure around the indent at 353 K. The microstructure consists of diagonal features (called “type X” martensite) and horizontal and vertical features (called “type Y” martensite). Above the transformation temperature at 423 K (Fig. 2b), the film is almost entirely in the austenitic state except for a few remanent type Y needles that are preserved very close to the indent. After cooling the sample to 408 K (Fig. 2c), these needles grow away from the indent and hence the phase fraction of martensite very close to the indent is increased. The rest of the observed sample remains in the austenitic phase. Upon further cooling to 404 K (Fig. 2d), the needles close to the indent grow further along $[110]_A$. Additionally, a martensitic needle along the $[010]$ direction forms directly at the indent (red arrow). Near the right edge of the image, a new

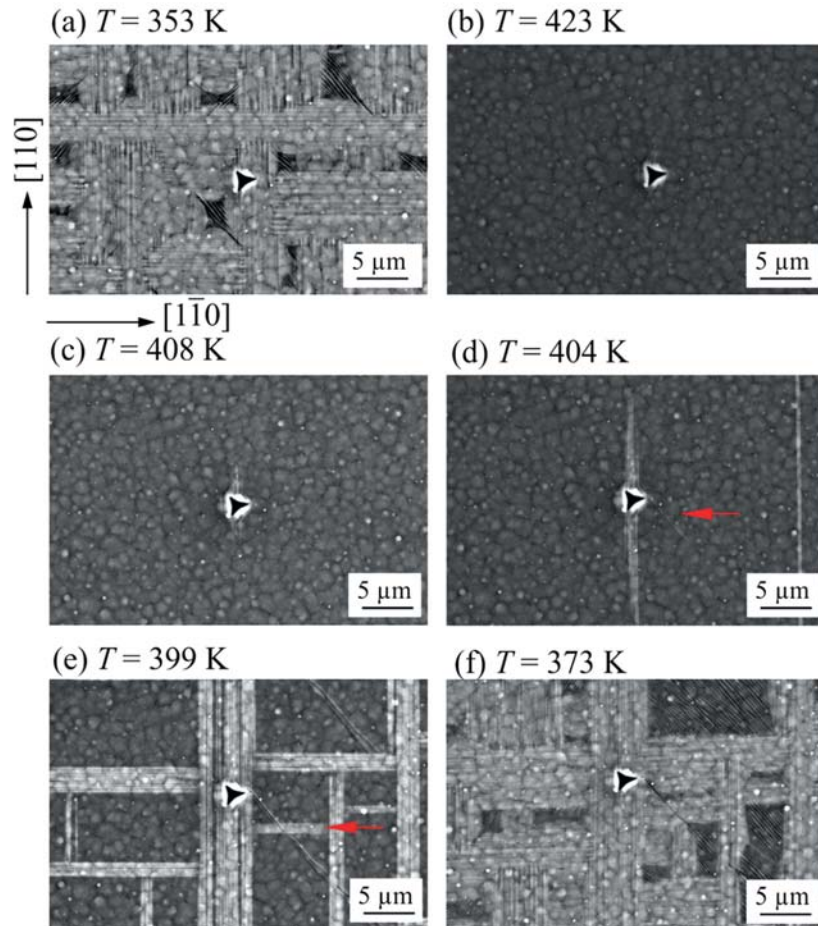
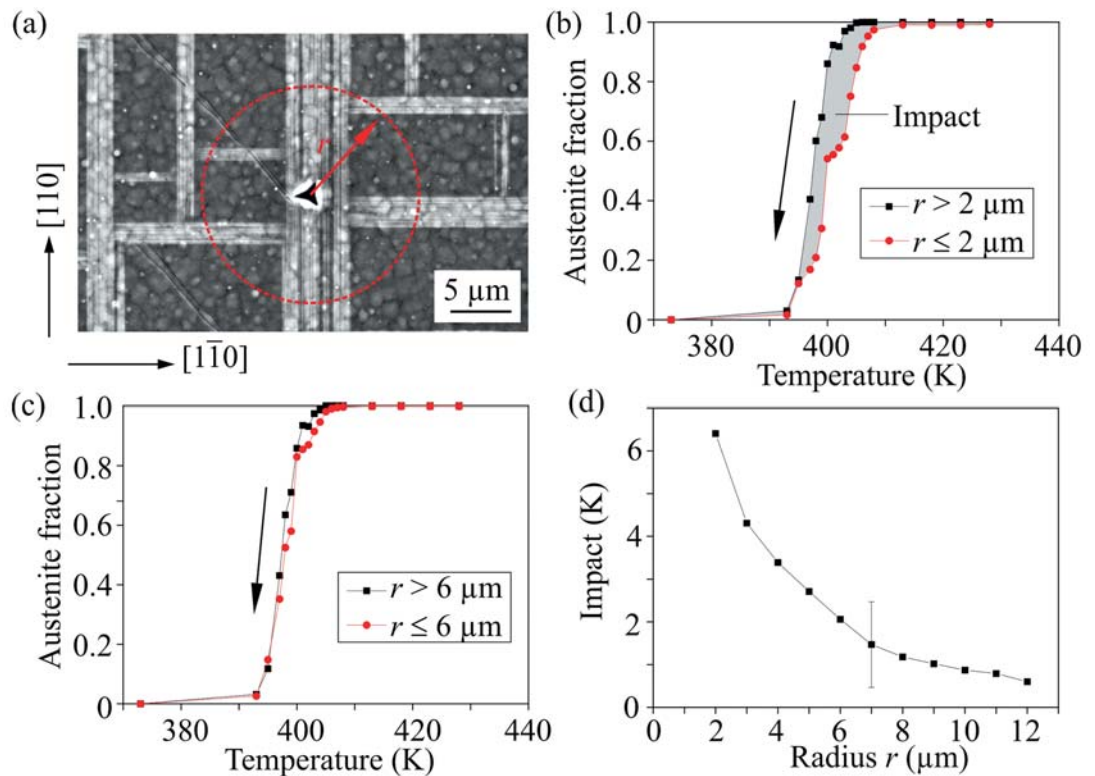


Fig. 2: SEM micrographs show the martensitic microstructure near the indent at different temperatures. (a) The microstructure after indentation. (b) After heating, the sample becomes austenitic. (c) and (d) Upon cooling, the martensitic transformation starts at the indent by formation of type Y martensite and a separate type X needle (red arrow). (e) The martensite grows further until (f) a final, different microstructure is reached.

group of type Y needles forms, which is not directly connected to the indent. It may have nucleated independently at another defect or due to some long-range elastic stray field of the indent. At 399 K (Fig. 2e), we observe an increased fraction of type Y martensite. The central group of needles near the indent has thickened and additional needles that are oriented along the $[\bar{1}\bar{1}0]_A$ direction have formed. Those cannot grow across existing martensite. Finally, at 373 K (Fig. 2f), almost the entire sample is in the martensitic state. The microstructure again consists only of type X and Y elements but the particular pattern is significantly different compared to the original martensitic microstructure from Fig. 2a. Only near the indent, the type and orientation of the martensite (type Y along $[110]$) were preserved. This illustrates that the transformation path is very sensitive to small variations in the boundary conditions.

To quantify the effect of the indent on the transformation, the series of electron micrographs was further evaluated: the phase fractions were determined by measuring the surface area covered by austenite and martensite, respectively (Fig. 3). By processing all images from the temperature series, this analysis yields an approximation of the phase fraction as a function of temperature. To identify the radius of influence of the indent, we defined a cut-off radius r . The quantitative evaluation of the phase fraction was then performed separately for the surface area lying within and outside the cut-off radius, respectively (Fig. 3a). The cut-off radius was varied between $1\text{ }\mu\text{m}$ and $12\text{ }\mu\text{m}$. These limits are given by the size of the indent and of the observed area, respectively. As a result of this evaluation, the temperature dependence of the austenite phase fraction is plotted exemplarily for $r = 2\text{ }\mu\text{m}$ in Fig. 3b. Inside the radius of $2\text{ }\mu\text{m}$, the phase fraction of austenite starts to decrease already at around 410 K while outside the radius, the austenite is stable until 400 K. This is obviously a consequence of the martensite growing first near the indent. During further cooling, the austenite phase fraction far from the indent remains larger than the austenite fraction inside the radius. In Fig. 3c, the phase fraction is plotted for a radius of $6\text{ }\mu\text{m}$. In this case, there is almost no difference between the transformation outside and inside the radius. Apart from little deviations near the beginning of the transformation, no significant difference can be observed. We quantify

Fig. 3: Quantification of the impact of an indent measured for decreasing temperature. **(a)** Microstructure near the remanent indent during the martensitic transformation. A critical radius around the indent is defined. The dependence of the fraction of austenite inside (red) and outside (black) a cut-off radius of **(b)** $2\text{ }\mu\text{m}$ and **(c)** $6\text{ }\mu\text{m}$ around the remanent indent is shown. The fraction was calculated by measuring the surface coverage of both phases. **(d)** The integral of the difference between the phase fraction inside and outside the radius is called impact (gray area in (b)) and is a measure for the influence of the indent for any given radius. Shown is the dependency of the impact on the radius. For radii smaller than $6\text{ }\mu\text{m}$, a significant influence is observed.



the “impact” of the indent by a single number obtained from an integration of the difference between the phase fraction inside and outside the radius. This area is highlighted in gray in Fig. 3b. The radius of influence around an indent is achieved by plotting the impact as a function of r (Fig. 3d). The impact monotonously decays with increasing radius, which is expected since the influence should vanish at large distances. From these measurements, we can conclude that one indent controls nucleation within a radius of about $6\text{ }\mu\text{m}$. This is significantly larger than the indent itself, illustrating that nanoindentation is an effective way to control nucleation. However, the affected radius is still in the order of the film thickness of $1.5\text{ }\mu\text{m}$, indicating that the influence radius is mostly limited by clamping of the film to the rigid substrate. The present work demonstrates that an indent can promote the martensitic transformation on a local scale. The well-defined experiment allows for a better understanding of the observation that martensite usually starts to grow, e.g., near scratches at the surface of a sample. The underlying mechanism is the increase of the temperature at which the transformation takes place. This is caused by the elastic stray field around a plastic deformation. This leads to a relative shift of the respective free energy curves of both phases and results in a stress induced martensite. Due to the local increase of the temperature at which the transformation takes place, this martensite will nucleate first.

Our observation is that one indent does not result in a switching of the entire sample but only predominantly affects the transformation in a radius of the order of less than $10\text{ }\mu\text{m}$, which suggests that the local change of transformation temperature is more important. In the film-shaped sample we used, the effect is limited to a small area around each indent. To influence the transformation on a macroscopic scale, the indents could be placed preferably in a hexagonal lattice and with a lattice constant in the order of several μm , which corresponds to a density in the order of $\approx 10^{10}\text{ m}^{-2}$. For a bulk process, we propose to add defects, e.g., by precipitation reactions or adding inert microparticles. As the transformation proceeds by nucleation and growth, one should optimize defect size and distribution not only with respect to their nucleation ability but also for a minimized pinning potential.

- [1] A. Diestel et al., JAP 118 (2015) 023908
- [2] B. Schleicher et al., JAP 118 (2015) 053906
- [3] R. Niemann et al., APL Mater. 4 (2016) 64101

Funding: DFG SPP 1599 www.ferroiccooling.de

Cooperation: Technische Universität Chemnitz; Texas A&M University, USA; University of Barcelona, Spain; Institute of Physics, Academy of Science of the Czech Republic

Reproducibility in density functional theory calculations of solids and the Full-Potential Local-Orbital code

K. Koepernik, U. Nitzsche, M. Richter

Abstract: Density functional theory (DFT) is a popular quantum mechanical method for both academic and commercial applications. It is increasingly used in an automated fashion to build large databases or to apply multi-scale techniques with limited human supervision. Therefore, the reproducibility of DFT results underlies the scientific credibility of a substantial fraction of current work in the natural and engineering sciences. Here, we introduce the variety of DFT solvers that partly provide specific capabilities but also share a large class of calculated properties. The latter can be used for benchmarking and for testing the reproducibility of the results obtained with completely independent implementations. Results of a recent comparison of equation-of-state data among 40 different DFT codes are presented. Finally, we summarize important features of the FPLO code being developed at IFW.

Introduction [1]

Each chapter of J. M. Ziman's famous textbook *Principles of the Theory of Solids* is headed by a citation. In particular, he introduces the chapter about *Electronic states* with R. Kipling's lines

There are nine and sixty ways of constructing tribal lays,
And-every-single-one-of-them-is-right.

Kipling's wisdom is a pray for tolerance of variety, and Ziman makes the point that even in aiming at a result of mathematical rigor there may be all the good reasons to justify a variety of ways to reach the goal. However, everybody who has been working in the field of electronic structure theory knows, that quantitative comparisons between different codes can be unsatisfactory on a physically relevant scale of accuracy.

This statement does not refer to the never ending discussion of the question, which particular flavor of density functional theory (DFT) would be the preferable approximation for a given system. What is meant is the purely numerical implementation of a well-defined task. Take several band structure codes and let all of them calculate the lattice constant of fcc thorium in local density approximation (LDA). You may get answers deviating from each other by a much larger amount than the scatter of related experimental data, see Fig. 1. Remember, we do not want to discuss the problem of so-called over-binding in LDA. This latter problem can only be tackled if we know what the numerically well defined LDA result is.

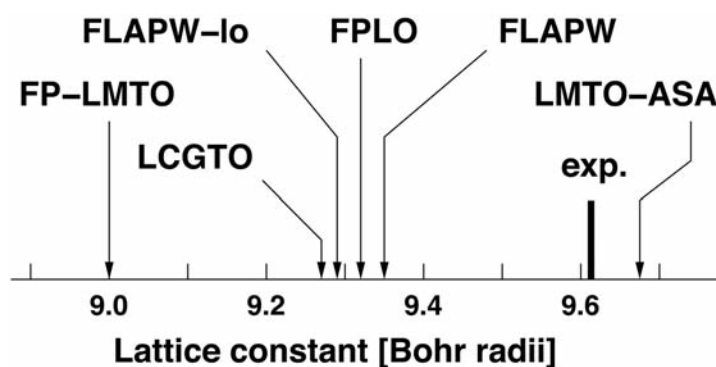


Fig. 1: (adapted from [1]) LDA lattice constant of fcc thorium obtained with the fully relativistic FPLO method in comparison with different published LDA results and with the experimental value. The thickness of the line denoted „exp.“ indicates the scatter of different experimental data.

At this point it is fair to state that tremendous advances in the numerical techniques have been achieved since John Slater's days. A large number of numerical methods to solve the Kohn-Sham equations, a set of nonlinear integro-differential equations summarizing DFT, has been implemented in past decades. Though these equations are included in every modern solid state theory textbook, their accurate solution requires a large arsenal of numerical methods. The related codes usually consist of several hundred-thousand lines. Depending on the number of add-ons and on the level of accuracy and sophistication, their development may take several 10 person-years.

DFT solvers can be categorized according to

(i) the level of accuracy in the construction of potential and charge density like atomic-sphere approximation (ASA) or the most accurate full-potential (FP) approach; (ii) the treatment of the atomic core states: pseudo-potential (PP) or all-electron (AE); (iii) the choice of the basis set for the Bloch states like augmented plane waves (APW), muffin-tin orbitals (MTO), plane waves (PW), or local orbitals (LO).

As a rule of thumb, a better accuracy of the numerical method consumes more computational resources. However, the level of sophistication in the numerical approaches and, in particular, in the choice of the basis states, can essentially influence the relation between accuracy and effort. Since there is less than no hope to get exact analytical solutions to a representative selection of significant problems, the only way to judge numerical accuracy is to compare output numbers of different approaches corresponding to exactly the same input numbers.

Is accuracy an issue at all? The answer is given in Fig. 1, showing the state-of-the-art of the year 2007. While the scatter of the experimental data amounts to about 0.1%, the difference between ASA and FP variants of the same method (LMT0) amounts to more than 7%. Even results obtained with different sophisticated FP methods scatter within about 3.5%. Only if this number can be reduced to less than 1% it is possible to judge the quality of approximations to DFT, like LDA or the generalized gradient approximation (GGA), with respect to the evaluation of lattice geometries and elastic properties.

Reproducibility test among 40 different DFT implementations [2]

The reproducibility of results is one of the fundamental principles of science. An observation can only be accepted by the scientific community if it can be confirmed by independent studies. This includes numerical studies – computer experiments – with independent algorithmic implementations of the same set of equations.

Initiated and coordinated by a DFT group at Ghent University, a pairwise comparison of a wide range of methods with respect to their calculated equations of state of 71 elemental crystals was performed. This effort required the combined expertise of a large group of DFT code developers and expert users, including the authoring IFW team.

Equation-of-state data were evaluated for four classes of DFT solver implementations, totaling 40 methods. Most codes are found to agree very well, with pairwise differences that are comparable to those between different high-precision experiments. Even in the case of PP approaches, which largely depend on the atomic potentials used, a similar precision can be obtained as when using an AE method. The remaining deviations are due to subtle effects, such as specific numerical implementations or the treatment of relativistic terms.

The conducted work [2] demonstrates that the numerical error of DFT implementations can be determined, even in the absence of an absolute reference code (which is not available by definition). Although this was not the case 10 years ago, most of the commonly used codes and methods are now found to produce essentially identical results, see Fig. 2. The established precision of DFT codes not only ensures the reproducibility of DFT predictions but also puts several past and future developments on a firmer footing.

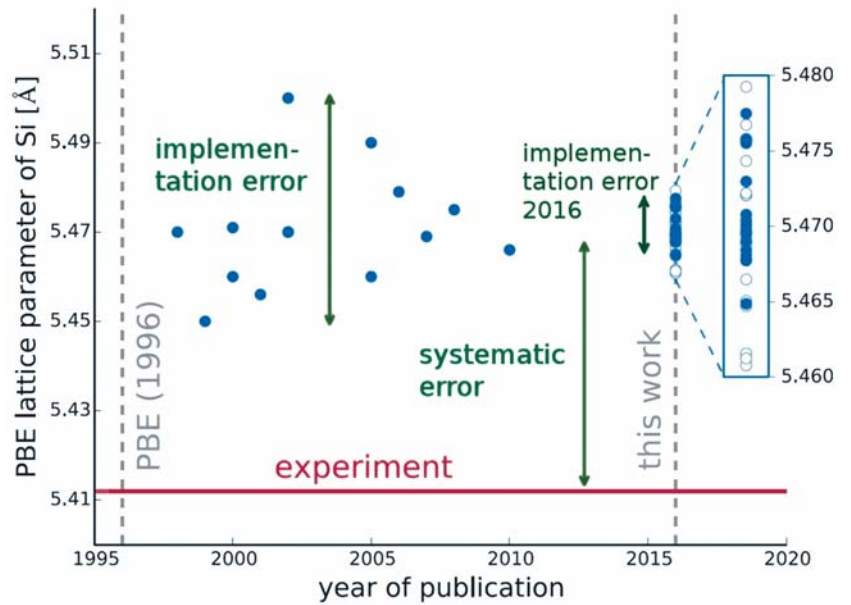


Fig. 2: (adapted from [2]) Historical evolution of the DFT equilibrium lattice parameter for silicon. All data points represent calculations within the DFT-PBE framework. Values from literature (data points before 2016) are compared with (i) predictions from the different codes used in the study [2] (2016 data points, magnified in the inset; open circles indicate data produced by older methods or calculations with lower numerical settings) and (ii) the experimental value, extrapolated to 0 K and corrected for zero-point effects (red line). The systematic error due to the approximation of the DFT functional and the implementation errors are illustrated.

Any newly developed methodology can now be tested against the benchmark and new DFT applications can be shown to have used a sufficiently precise method. Moreover, high-precision DFT calculations are essential for developing improvements to DFT methodology, such as new density functionals, which may further increase the predictive power of the simulations.

FPL0 code [3,4]

The FPL0 code has been developed at IFW Dresden for two decades [3]. It is one of the six AE codes that participated in the described reproducibility check [2]. FPL0 fulfills the criteria for a high-precision implementation but has the smallest number of basis functions and, thus, the least numerical effort among the AE methods. Our code comprises a number of important features like

- a user interface "XFPL0" for visualization of structures, Fermi surfaces, other data;
- a cluster version on the same footing as the periodic version;
- a full-relativistic 4-component Dirac-Kohn-Sham implementation;
- a numerical noise level below 10^{-6} eV/atom;
- full relativistic LSDA+U and GGA+U approaches in different versions;
- an orbital polarization correction (OPC) scheme;
- band structures with orbital weights ("fat bands");
- molecular-orbital projected DOS and band weights;
- calculation of optical spectra;
- band-unfolding for the interpretation of ARPES data;
- calculation of Z_2 -invariants for systems with inversion center;
- downscaling of the exchange field ("LSDA • x");
- real-space plots of Bloch wave functions and energy-resolved densities;
- maximally projected Wannier functions;
- a fixed spin moment method extended to full relativistic calculations.

The whole package contains several 10^5 lines source code in FORTRAN90 and C. It has been licenced for more than 200 groups worldwide with a total number of FPL0 publications amounting to about 1000. Regular tutorials do not only focus on code handling but also on the problem of reproducibility that requires publication of the complete parameter set used in the computation.

- [1] M. Richter et al., in: *Condensed Matter Physics in the Prime of the 21st Century*, 43rd Karpacz Winter School of Theoretical Physics, Ed. J. Jedrzejewski, World Scientific, Singapore 2008, pgs. 271-291.
- [2] K. Lejaeghere et al., *Science* 351, 1415 (2016).
- [3] K. Koepnik and H. Eschrig, *PRB* 59, 1743 (1999).
- [4] <http://www.fplo.de/>

Funding: EC (RTN contract NPRN-CT-2002-00295) „Ab-initio Computation of Electronic Properties of f-Electron Materials“; DFG (SPP 1145) „Orbital magnetism in molecules and solids“.

Cooperation: Center for Molecular Modeling, Ghent University.

Electron-lattice interactions strongly renormalize the charge transfer energy in the spin-chain cuprate Li_2CuO_2

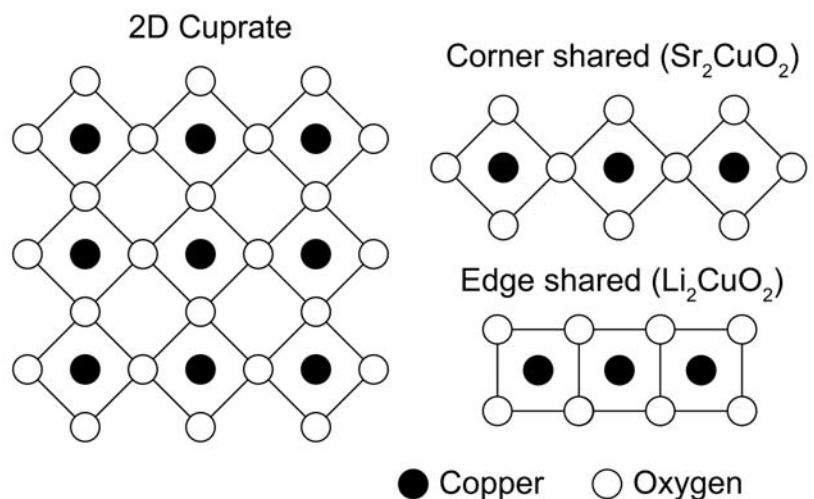
S. Johnston, S.-L. Drechsler, J. Geck, R. Kraus, B. Büchner, J. van den Brink

Abstract: Strongly correlated materials are governed by competition and cooperation among the spin, charge, orbital, and lattice degrees of freedom. The central challenge for the field is to unravel the action of each interaction in establishing novel phases of matter. Over the past decade, resonant inelastic x-ray scattering (RIXS) has emerged as a versatile experimental probe for this purpose. Recently, we have collaborated with experimentalists from the PAUL SCHERRER Institute in Switzerland to study several quasi-one-dimensional copper-oxides using this technique. In doing so, we have gained new insights into several fundamental problems including the nature of their quasi-particle states (the so-called ZHANG-RICE singlets and triplets) and the unexpected role of the electron-lattice interactions in determining their fundamental electronic properties.

Motivation – In strongly correlated materials, several of the charge, orbital, spin, and lattice degrees of freedom are often active and interacting with one another. These materials have rich phase diagrams with many competing orders, and often exhibit giant responses to small perturbations. These are characteristics of complex systems, where the realized phases can depend strongly on perturbing interactions and indirect factors. One of the primary challenges in this field is then to identify the relevant interactions in a material and unravel their respective roles in producing each new phase. This task is an incredibly challenging, however, as even weak interactions can have a large effect.

The two-dimensional copper oxides are perhaps the most well-known example of these principles, where a complicated mix of interactions gives rise to high-temperature (high- T_c) superconductivity and other phenomena; however, despite more than 30 years of research on these materials, the exact mechanisms underlying these phenomena are not understood. Motivated by this, we have been studying spin chain cuprates [1] such as Li_2CuO_2 [2-4], $\text{Ca}_2\text{Y}_2\text{Cu}_5\text{O}_{10}$ [5,6], and Sr_2CuO_2 [7], which are quasi-1D compounds formed from the same fundamental CuO_4 building blocks of the high- T_c cuprates (Fig. 1). Working in close collaboration with experimentalists from the PAUL SCHERRER Institute (Switzerland), we have studied these systems with resonant inelastic x-ray scattering to address critical questions about the physics underlying copper-oxide materials.

Fig. 1: Three of the many possible arrangements [1] of CuO_4 plaquettes to form cuprate materials. The two-dimensional arrangement is typical of the high- T_c superconducting cuprates. The quasi-one-dimensional edge- and corner-shared arrangements are typical of quantum spin chains studied by our team.



Resonant Inelastic X-ray Scattering – Resonant inelastic x-ray scattering (RIXS) is a powerful probe of correlated materials [8]. In a typical RIXS experiment, photons with energy ω_{in} and momentum κ_{in} are incident on a sample. Here, the phonon energy is tuned to one of the material's absorption edges, such that the photon stimulates a resonant dipole transition between an atomic core level and an empty state in the valence bands. After the core electron excitation, the resulting intermediate excited state propagates in time under the influence of the core hole's potential U_c , generating several excitations. This process continues until the core hole radiatively decays, emitting a photon with energy ω_{out} and momentum κ_{out} , and leaving the system in a final state with energy and crystal momentum $\mathbf{q} = (\kappa_{\text{out}} - \kappa_{\text{in}})$. The excitations generated in the intermediate state encode information about the elementary excitations of the solid. Thus, by examining the RIXS intensity, one obtains information about the excitation pathways of a material. Due to the resonant nature of this technique, it is extremely sensitive to charge, orbital, spin, and lattice excitations.

Dressing electronic interactions – The cuprates and other 3d transition metal oxides belong to a challenging class of correlated systems, which are the focus of modern solid-state physics. Primarily two fundamental energy scales determine their physical properties: the COULOMB onsite repulsion U_d and the charge transfer energy Δ . The former reflects the energy cost associated with charge excitations between the cation orbitals in the solid. The latter is the energy cost for creating $(d^{n-1}\bar{L})$ -type charge excitations, where a hole moves from the cation site to the ligand oxygen atoms (Fig. 2). In particular, the properties of their quasiparticles, including the ZHANG-RICE singlets and triplets, depend crucially on the ratio of these values for the so called charge transfer insulators [9], where $U_d > \Delta$. (This is in contrast to simple MOTT insulators dominated by U_d , where $U_d < \Delta$.)

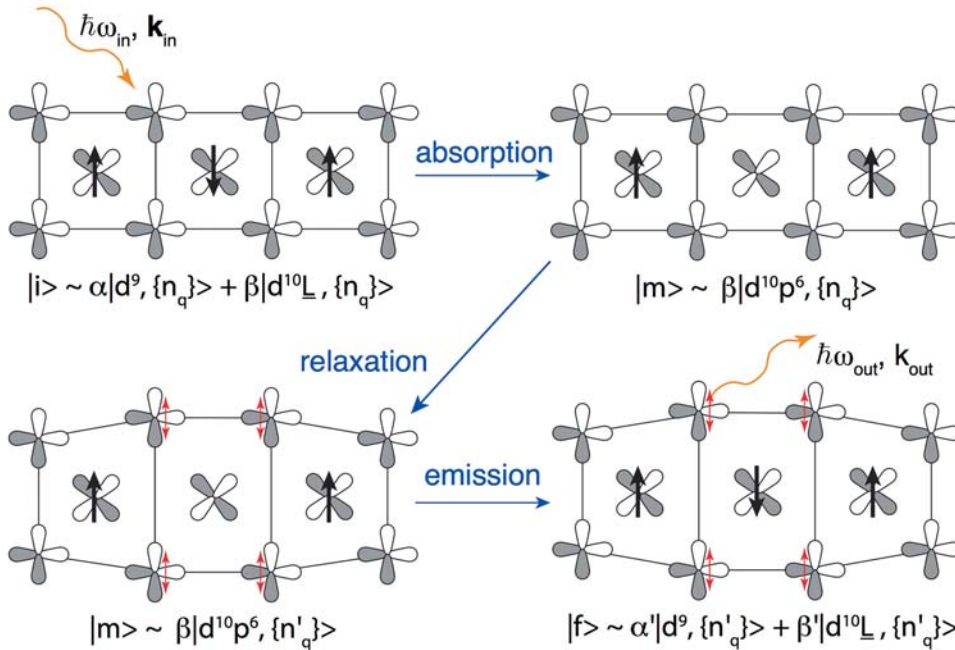


Fig. 2: A sketch of the RIXS process whereby the lattice built from edge-sharing CuO_4 chains is excited. The initial electronic state is predominantly of $|i\rangle_{\text{el}} \sim \alpha|d^9\rangle + \beta|d^{10}\bar{L}\rangle$ character, where \bar{L} denotes a hole delocalized on the ligand O sites, while the initial lattice state involves a coherent state of phonon quanta that describes the shifted equilibrium position of the O atoms. Thick black arrows: low-temperature ferromagnetic spin structure of the CuO_2 chains. After the $1s \rightarrow 2p$ transition, an intermediate state is formed, corresponding to an upper Hubbard band excitation where the number of holes on the Cu site has changed. The lattice relaxes in response to the change in the Cu density, until the $1s$ core hole is filled, leaving the system in an excited electronic and lattice configuration. Red arrows: direction of the O atom's motion.

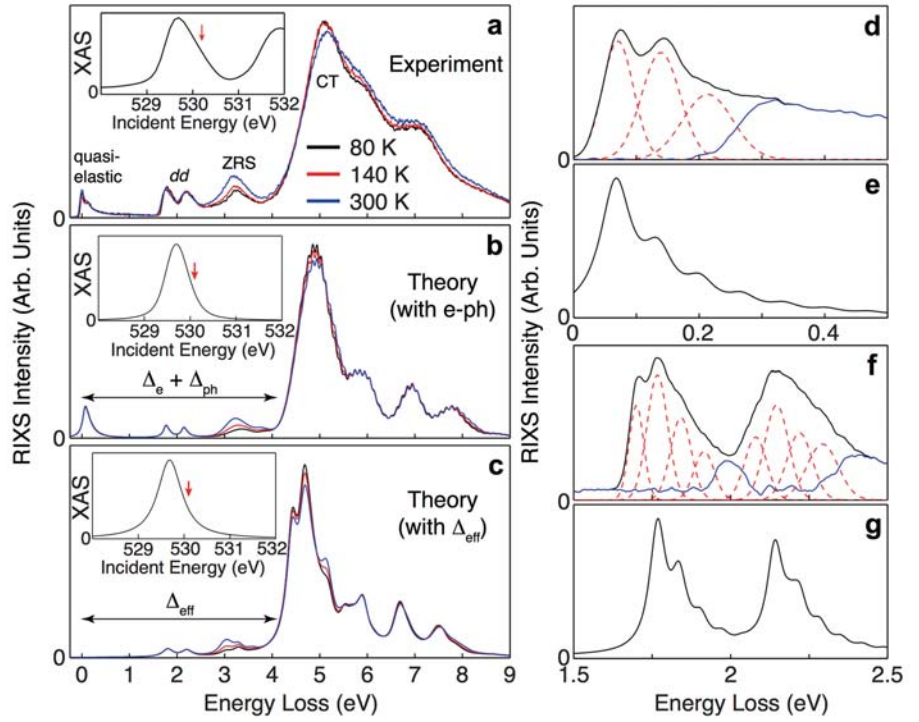


Fig. 3: XAS and RIXS spectra at the O K-edge. **a** The measured RIXS spectra, recorded at various temperatures, as indicated. The incident photon energy for these measurements was detuned slightly from the upper Hubbard band peak in the XAS, as shown in the inset. The red arrow indicates the incident phonon energy. **b** The calculated RIXS spectra obtained using a cluster model that includes coupling to the O-O bond-stretching mode. The calculated XAS spectrum is shown in the inset. For comparison, **c** shows the calculated spectra for a model without el-ph coupling but with an increased value of $\Delta = \epsilon_p - \epsilon_d = 4.6$ eV. The detailed measured RIXS spectra highlighting the harmonic phonon excitations in the quasi-elastic and dd-excitation energy loss range are shown in **d** and **f**, respectively. Red dashed lines: Gaussian fits to the data that highlight the individual phonon excitations. Blue line: the difference between the data and the red dashed lines. The corresponding RIXS calculations are shown in **e** and **g**, resp. In **d** the incident photon energy coincides with the peak in the XAS intensity. Note that the elastic line has been removed from the calculated RIXS spectra for clarity.

The value of the charge transfer energy has traditionally been thought to be determined by the chemistry of ions in the solid; however, in our recent work published in Nature Communications [2], we have shown that up to 50 % of the value of Δ in Li_2CuO_2 stems from the strong el-ph interaction in the materials (Figs. 2 & 3). In this case, the relevant phonon mode modulates the Cu-O bond in the direction perpendicular to the chain axis but within the plane of the CuO_4 plaquette, which also modifies the Cu-O-Cu bond angles. We have measured and theoretically analyzed XAS and RIXS data for Li_2CuO_2 adopting a six-band HUBBARD model with O 1s and planar 2p orbitals and the half-filled Cu 3 d_{xy} orbitals (see Fig. 1). In this process the incoming photon excites an oxygen 1s core electron is transferred to an unoccupied state, resulting in an additional electron in the valence band. In the intermediate state, the lattice responds this change in density by relaxing and creating a number of phonon excitations that appear as satellite features in the RIXS spectra (Figs. 2d-2g). Through detailed modeling of the data, we determined the strength of the interaction between the lattice and the electrons. Importantly, if the electron-lattice interaction is omitted in our analysis, the spectra imply an effective value $\Delta \sim 4.6$ eV; however, when the interaction with the lattice is properly accounted for, this value separates into a purely electronic contribution of $\Delta_{\text{el}} \sim 2.1$ eV, and a very substantial lattice contribution $\Delta_{\text{lat}} \sim 2.5$. These results show that the el-ph interaction plays a much larger role in low-dimensional cuprates than was previously thought.

Probing the fundamental quasiparticles – As originally proposed by ZHANG and RICE [10], a bound state formed by two holes on the same plaquette is a natural quasiparticle in hole-doped copper oxides. Called a ZHANG-RICE singlet (ZRS) in the case of opposite spins, this quasiparticle consists of a pair of holes, where one is localized on the Cu site and the other is delocalized on the surrounding four oxygens, that form a spin singlet. Recently, we investigated the electronic excitations of Li_2CuO_2 with RIXS and x-ray absorption spectroscopy performed at the O K edge [3,4] and identified distinct excitonic ZRS excitations associated with both intra- [3] and interchain [4] excitations. These observations allowed us to obtain new insights into the ways in which these fundamental excitations can be formed. For example, by exploiting temperature-dependent RIXS measurements, we were able to determine several important energies including the binding energy of the ZRS, which is directly relevant for models of the 1D and 2D cuprates. We also identified the corresponding Zhang-Rice triplet excitation in the RIXS spectra for the first time, revealing the rich nature of the elementary excitations in the cuprates.

- [1] Hk. Müller and U. Lehmann, *Z. Anorg. Allg. Chem.* **447**, 47 (1978).
- [2] S. Johnston, *et al.*, *Nature Commun.* **7**, 10653 (2016).
- [3] C. Monney *et al.*, *Phys. Rev. Lett.* **110**, 087403 (2013).
- [4] C. Monney *et al.*, *Phys. Rev. B* **94**, 165118 (2016).
- [5] W. S. Lee *et al.*, *Phys. Rev. Lett.* **110**, 265502 (2013).
- [6] R. O. Kuzian *et al.*, *Phys. Rev. Lett.* **109**, 117207 (2012).
- [7] J. Schalppa *et al.*, *Nature* **485**, 82 (2012).
- [8] L. J. P. Ament *et al.*, *Rev. Mod. Phys.* **83**, 705 (2011).
- [9] J. Zaanen, G. A. Sawatzky, and J. W. Allen, *Phys. Rev. Lett.* **55**, 418 (1985).
- [10] F. C. Zhang and T.M. Rice, *Phys. Rev. B* **37**, 3759 (1988).

Funding: Swiss National Foundation and DFG DACH Programme (SNSF Grants 2000211, 141325, PZP002 154867, and GE 1647/3-1), Sinenergia Mott physics beyond the Heisenberg model (MPBHM), EMMY NOETHER program (DFG GE1647/2-1)

Cooperation: University of Tennessee, Knoxville TN (USA); Paul-Scherrer Institute, Villigen (Switzerland); Institute of Physics, Zurich (Switzerland); National Synchrotron, Light sources II, Brookhaven National Lab. Upton, NY (USA); Institute of Physics of the Czech Acad. Sciences, Prague (Czech Republic); Max-Planck-Institute for Chemical Physics of Solids, Dresden (Germany)

Research Area 2

Structural, dynamic and electronic properties of $\text{Ge}_2\text{Sb}_2\text{Te}_5$ phase-change alloy in liquid state

I. Kaban, H. Weber

Abstract: Structural, dynamic and electronic properties of $\text{Ge}_2\text{Sb}_2\text{Te}_5$ phase-change alloy in the liquid state have been studied in the frame of a collaborative work [1] supported by the German Research Foundation (DFG). The structural models of liquid $\text{Ge}_2\text{Sb}_2\text{Te}_5$ were obtained by a combined approach including X-ray and neutron diffraction, reverse Monte-Carlo simulations and *ab-initio* molecular dynamics modeling based on the density functional theory. The electronic density of states and viscosity values extracted from the AIMD models are compatible with electrical resistivity and viscosity measurements.

Ge-Sb-Te alloys along the $\text{GeTe-Sb}_2\text{Te}_3$ pseudo-binary line exhibit a fast and reversible amorphous-to-crystalline transition and remarkable differences of the physical properties of the crystalline and the amorphous phases [2]. The optical reflectivity contrast is exploited in the optical data storage media such as CDs, DVDs and Blue-ray discs [3]. Recently, a high interest in the Ge-Sb-Te has arisen in view of their potential application in the non-volatile phase-change memory (PCM), utilizing the electrical resistivity difference between the amorphous and crystalline state [4]. It is expected that PCM will outperform existing, e.g. Flash memory, and emerging technologies [5].

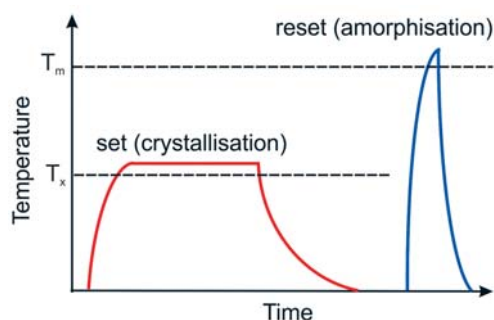


Fig. 1: Schematic of phase-change memory operation (T_x – crystallisation temperature, T_m – melting temperature).

Functioning of the PCM is based on a rapid switching of an active material from the amorphous to the crystalline state in a set-operation and from the crystalline to the amorphous state in a reset-operation, as shown schematically in Fig. 1. The transition is thermally activated by laser or electric current pulses. Thereby, the phase-change material passes either via the supercooled liquid state (crystallisation) or via the liquid state (amorphisation). The performance of the PCMs is to a large extent determined by the atomic structure and dynamics of the phase-change material. In particular, high fragility which describes the deviation of the viscosity from the Arrhenius-type behaviour is responsible for the stability of the amorphous phase at low temperature and the fast crystallisation at high temperature [5].

In the recent work [1], $\text{Ge}_2\text{Sb}_2\text{Te}_5$ phase-change alloy in the liquid state has been studied by a combined experimental and computational approach. For this, high-energy X-ray diffraction (XRD), neutron diffraction with Ge isotopic substitution (NDIS), viscosity and density measurements were performed. On the other hand, structural, electronic and kinetic properties of the liquid $\text{Ge}_2\text{Sb}_2\text{Te}_5$ were extracted from the models obtained by *ab-initio* molecular dynamics (AIMD) simulations based on the density functional theory (DFT).

High-energy XRD experiments were carried out at the German Electron Synchrotron DESY (Hamburg, Germany) and at the European Synchrotron Radiation Facility ESRF (Grenoble, France). Neutron diffraction measurements were performed at the ISIS pulsed neutron and muon source of the Rutherford Appleton Laboratory (Oxford, UK). The density was determined by a high-energy γ -ray attenuation method at the Department of Physics of the Niigata University (Niigata, Japan). The dynamic viscosity was measured with an oscillating-cup viscometer at the IFW Dresden.

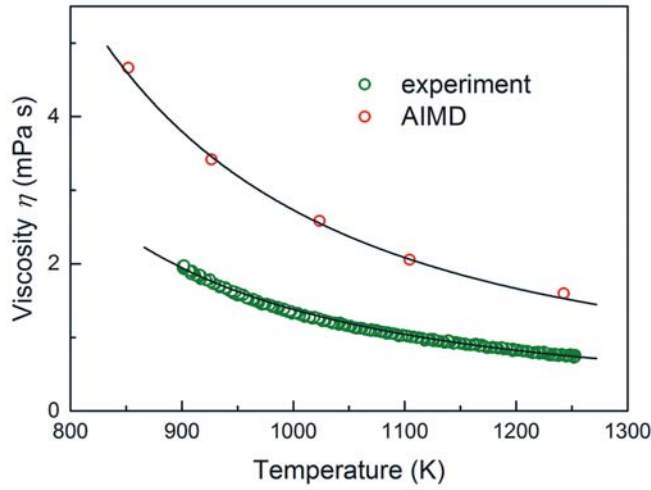


Fig. 2: Dynamic viscosity of liquid $\text{Ge}_2\text{Sb}_2\text{Te}_5$ alloy: experiment and AIMD calculation. The measurement was performed upon cooling at 1 K/min. The lines are the fits with the Arrhenius equation $\eta = \eta_0 \cdot \exp\left(\frac{E_a}{k_B T}\right)$.

The dynamic viscosity of liquid $\text{Ge}_2\text{Sb}_2\text{Te}_5$ alloy shows an Arrhenius-type behaviour in the liquid state (Fig. 2). The experimental values are well fitted by the function

$$\eta = \eta_0 \cdot \exp\left(\frac{E_a}{k_B T}\right)$$

with the activation energy for the viscous flow $E_a = 0.266$ eV and a constant $\eta_0 = 0.063$ mPa s; k_B is the Boltzmann constant, and T is the absolute temperature. The temperature dependence of the dynamic viscosity excellently correlates with the structural data. The X-ray diffraction structure factors $S(Q)$ of liquid $\text{Ge}_2\text{Sb}_2\text{Te}_5$ exhibit a continuous evolution upon cooling until crystallization (Fig. 3). The structural parameters such as the position and the height of the peaks change linearly with the temperature. A similar behavior follows from the temperature dependences for the total structure factors measured by neutron diffraction as well as from the corresponding total pair distribution functions (not shown).

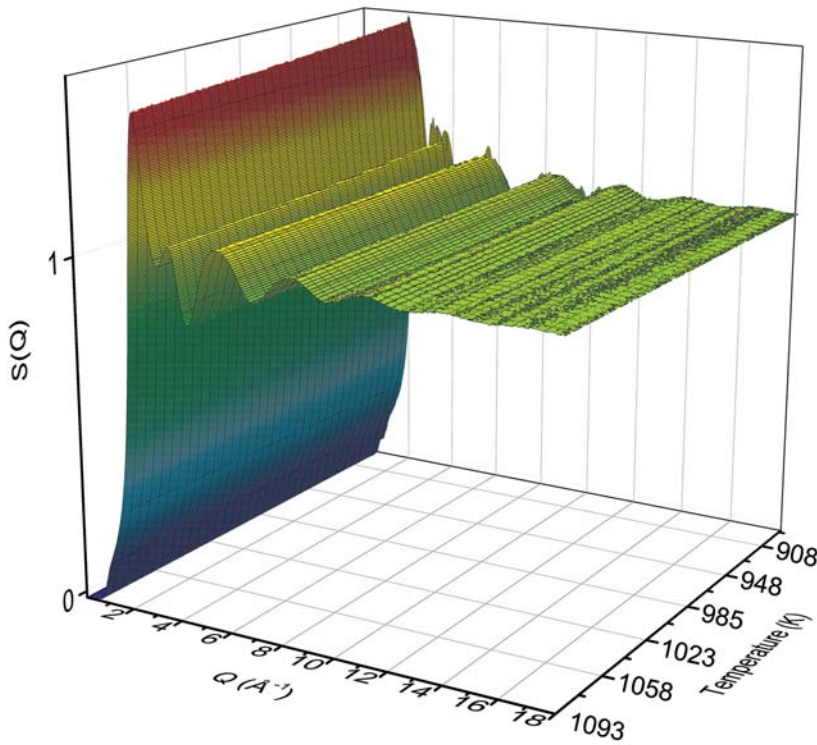


Fig. 3: XRD total structure factors of liquid $\text{Ge}_2\text{Sb}_2\text{Te}_5$ measured upon cooling at 5 K/min.

In order to describe the chemical and topological short-range order in a three-component liquid or amorphous alloy knowledge of the six partial pair distribution functions (PDF) is needed. This requires the same number of independent and sufficiently different diffraction measurements, which is not possible. To obtain the structural information, liquid $\text{Ge}_2\text{Sb}_2\text{Te}_5$ was modeled by DFT-based AIMD simulations in work [1]. Standard

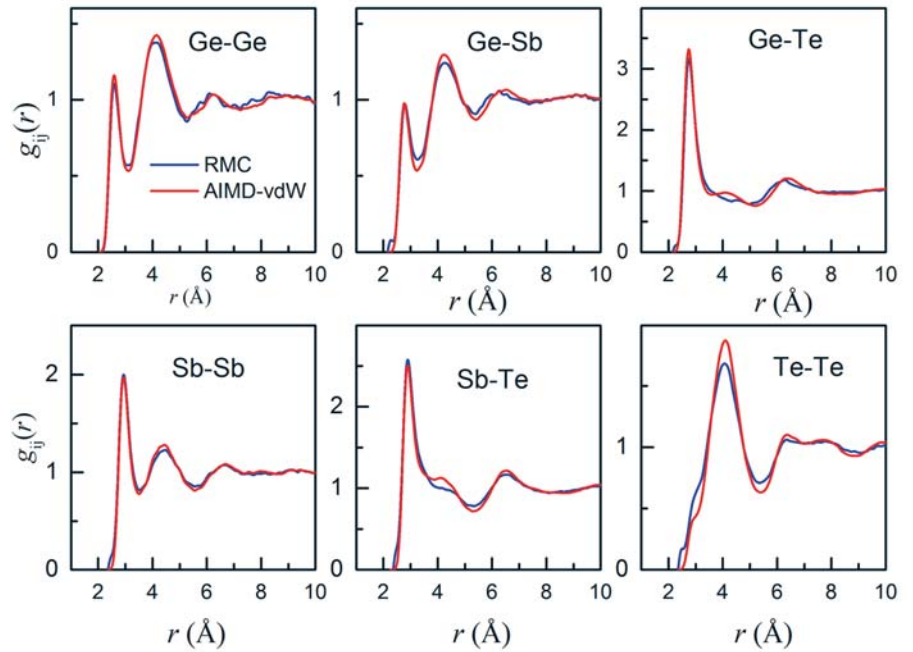


Fig. 4: Partial pair distribution functions $g_{ij}(r)$ for liquid $\text{Ge}_2\text{Sb}_2\text{Te}_5$ at 925 K: *red lines* – extracted from the AIMD model using vdW-DF2 functional; *blue lines* – RMC fits of the vdW-DF2 AIMD PDFs and experimental XRD and ND structure factors simulated simultaneously.

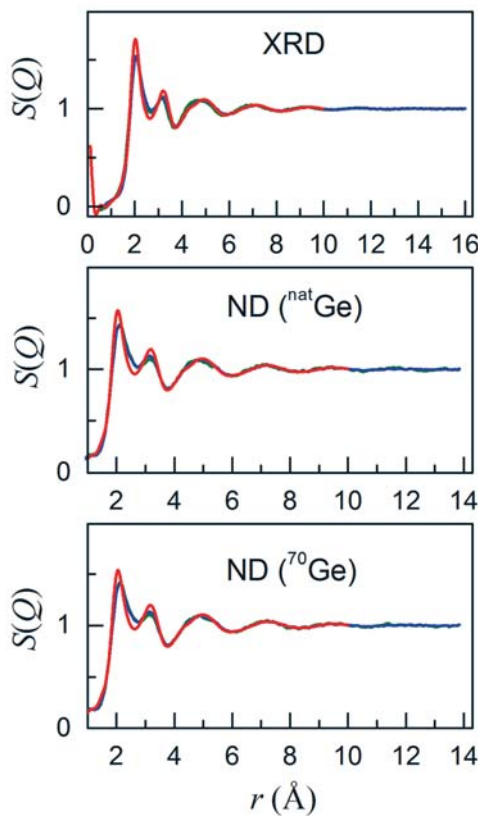


Fig. 5: XRD and ND structure factors $S(Q)$ for liquid $\text{Ge}_2\text{Sb}_2\text{Te}_5$ measured at 923 K (*olive*) compared to the structure factors obtained from vdW-DF2 AIMD simulations (*red*) and RMC simulations (*blue*).

generalized-gradient-approximation functional of Perdew, Burke and Ernzerhof (PBE) for the exchange-correlation energy and a van der Waals density functional which includes non-local correlations (vdW-DF2) were used to generate particle trajectories at different temperatures, from which the partial pair distribution functions were extracted.

To test the partial PDFs obtained by AIMD simulations, they were fitted simultaneously with the XRD and ND structure factors in the frame of the reverse Monte-Carlo (RMC) simulation technique [7]. It has been demonstrated in a number of works that RMC is a very effective tool for structure modelling of disordered systems by simultaneous fitting different experimental and theoretical datasets and constraints. The AIMD vdW-DF2 model showed a good agreement with the experimental data (Figs. 4 and 5). Therefore, the respective partial pair distribution functions were used for determination of the partial coordination numbers and bond lengths [1]. A significant number of Ge-Ge and Ge-Sb bonds was observed in liquid $\text{Ge}_2\text{Sb}_2\text{Te}_5$. These bonds were supposed to be responsible for the presence of tetrahedral structures in amorphous $\text{Ge}_2\text{Sb}_2\text{Te}_5$. Te-Te bonds were also found in the liquid state but their number decreases drastically upon quenching to the amorphous state.

The bond angle distributions (BADs) and the angular-limited three-body correlations (ALTBCs) were calculated from the AIMD trajectories. The BADs displayed a peak centred at 90° , being an indicative of predominant (defective) octahedral coordination. Upon increasing temperature, the height of the peak decreased and the probability of observing bond angles below 80° and above 110° became more significant. Analysis of the ALTBC distributions revealed alternating short and long bonds, indicative of Peierls distortion, which appeared to decrease with increasing temperature.

The electronic density of states (DOS) and the diffusion coefficient D for liquid $\text{Ge}_2\text{Sb}_2\text{Te}_5$ were extracted from the vdW-DF2 AIMD simulations. The density of states showed a pronounced pseudogap at the Fermi energy in the supercooled liquid state and at the melting temperature, which decreased at higher temperatures. This correlates with the negative temperature coefficient of the electrical resistivity of liquid $\text{Ge}_2\text{Sb}_2\text{Te}_5$.

The dynamic viscosity was obtained from the AIMD diffusion coefficient D using the Stokes-Einstein relation $\eta = \frac{k_B T}{6\pi R_{hyd} D}$, where R_{hyd} is the hydrodynamic radius. The calculated viscosity showed a very good qualitative agreement with the experimental data (Fig. 2). Fitting the theoretical values with the Arrhenius equation yielded the activation energy $E_a = 0.256$ eV and a constant $\eta_0 = 0.140$ mPas (compare to $E_a = 0.266$ eV and $\eta_0 = 0.063$ mPas from the fit of the experimental data). Somewhat larger theoretical viscosity might be explained by the approximations inherent in the employed exchange-correlation functional, by the finite size effects due to the periodic boundary conditions, or by the use of thermostats.

In summary, the structural, electronic and kinetic properties of $\text{Ge}_2\text{Sb}_2\text{Te}_5$ phase-change alloy in the liquid and weakly supercooled liquid state were obtained using state of the art experimental and theoretical techniques in work [1]. A good agreement of the experimental and theoretical structural characteristics as well as the physical properties suggest that the van der Waals density functional (vdW-DF2) used in the present AIMD simulations provides a good description of liquid $\text{Ge}_2\text{Sb}_2\text{Te}_5$.

- [1] M. Schumacher et al., Sci. Rep. 6 (2016) 27434.
- [2] Yamada et al., J. Appl. Phys. 69 (1991) 2849.
- [3] M. Wuttig & N. Yamada, Nat. Mater. 6 (2007) 824.
- [4] S. Raoux et al., MRS Bull. 39 (2014) 703.
- [5] J. S. Meena et al. Nanoscale Res. Lett. 9 (2014) 526.
- [6] J. Orava et al., Nat. Mater. 11 (2012) 279.
- [7] R.L. McGreevy & L. Pusztai, Mol. Simul. 1 (1988) 359.

Funding: DFG Grants: Ka 3209/6-1, Ma-5339/2-1

Cooperation: RWTH Aachen University, Aachen, Germany; Institute for Solid State Physics and Optics, Budapest, Hungary; Niigata University, Niigata, Japan

Hybrid material microtubes for optoplasmonics and sensing

Y. Yin, S. Li, E. S. Ghareh Naz, V. Engemaier, S. Böttner, S. Giudicatti,
S. Weiz, L. Ma, M. Medina-Sánchez, O. G. Schmidt

Abstract: Rolled-up nanotechnology has been used to develop opto-plasmonic micro-tubular cavities as well as high performance electrochemical biosensors. Such platforms have served in one side to comprehensively investigate the hybridization mechanism of photon-plasmon modes and for the selective coupling of localized surface plasmons and resonant light in three- dimensionally confined tubular microcavities; and on the other side, by integrating electrodes in the tubular cavities, to determine DNA concentration changes as well as to study DNA conductive and conformational changes due to the intrinsic electric field distribution within the tubular geometry.

Hybridization of photon-plasmon modes in opto-plasmonic microcavities

The coupling between photon and surface plasmons in opto-plasmonic microcavities results in hybrid photon-plasmon modes, which has attracted extensive interest from both fundamental and applied physics. In previous reports, the location of plasmon-type field of hybrid mode has been contradictorily reported to occur at either the inner or outer surface of metal layer coated on a microcavity. Recently, we comprehensively investigated the hybridization mechanism of photon-plasmon modes based on opto-plasmonic microtubular cavities [1]. We revealed that the occurrence and location of hybrid photon-plasmon mode is determined by the coupling strength. As shown in Fig. 1, three types of photon-plasmon modes are identified as weakly, moderately and strongly hybridized modes. An effective potential approach is used to illustrate the generation and transition of these kinds of hybrid modes based on the competition between light confinement in the cavity and the potential barrier induced by the metal layer.

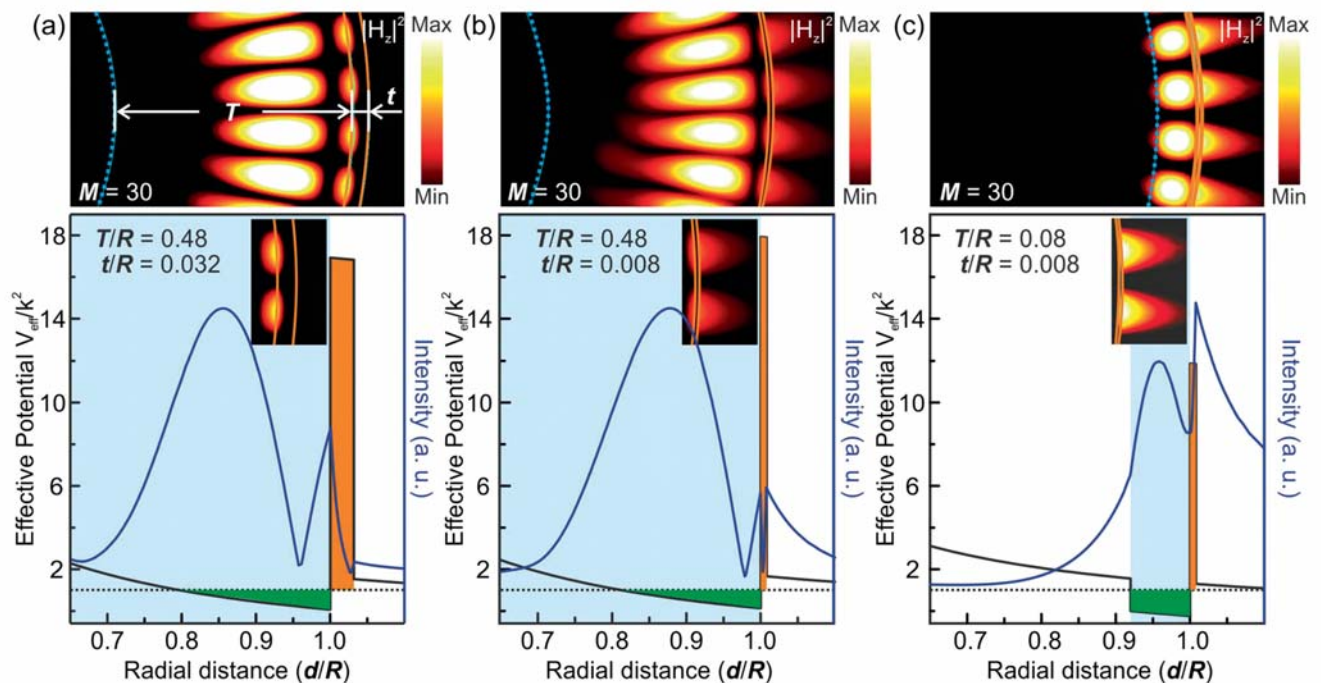


Fig. 1: Field distributions and effective potentials along the radial direction of (a) weakly, (b) moderately and (c) strongly hybridized photon-plasmon modes. The thicknesses of the cavity wall (T) and the metal coating layer (t) are set as $T/R = 0.48$ and $t/R = 0.032$, $T/R = 0.48$ and $t/R = 0.008$, $T/R = 0.08$ and $t/R = 0.008$, respectively.

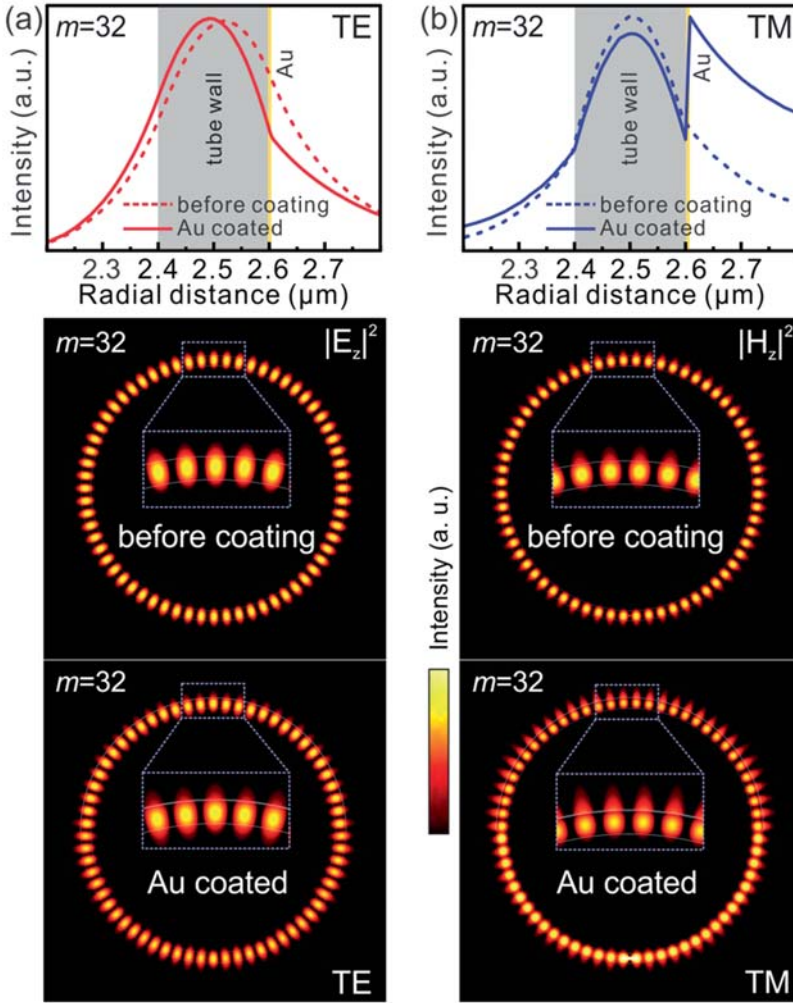


Fig. 2: Optical field distributions in the tube wall before and after the gold nanocap deposition. **(a)** The maximum of the electric field profile (TE mode) slightly shifts towards the center of the cavity after the gold coating, as shown in the top panel. The middle and bottom panels show the mode profiles before and after the gold coating, respectively. **(b)** Efficient coupling between the TM photonic mode and the surface plasmon supported by the gold nanocap results in an enhanced EM field at the gold surface, as shown in the top panel. The mode profile in the gold-coated section (bottom panel) clearly shows a strong hybrid mode compared to that before the gold coating (middle panel).

Among the three types of hybrid mode, strongly hybridized photon-plasmon modes are particularly interesting for enhanced light-matter interactions. We experimentally demonstrated strongly hybridized photon-plasmon modes thin-walled microtube cavities [2], as shown in Fig. 2. The generation of strongly hybridized modes is relevant to both fundamental and applied physics, paving the way for enhanced light-matter interactions in opto-plasmonic microcavities. These works provide a universal picture for understanding the basic physical mechanisms of photon-plasmon mode hybridization in metal-coated WGM microcavities, and is relevant for opto-plasmonic cavity designs.

Localized surface plasmons selectively coupled to resonant light in opto-plasmonic microcavities

Optical microcavities constitute an important platform for the study of light-matter interactions, where the size mismatch between the optical wavelength and any interacting nano-objects is bridged by cavity quantum electrodynamics or plasmonic nanostructures integrated within the cavities. In our recent work, for the first time a plasmonic nanogap was designed in microtubular cavities to demonstrate efficient coupling of localized surface plasmons (LSPs) and resonant light [3], as shown in Fig. 3. Moreover, selective coupling of LSPs and resonant modes were achieved, exhibiting spatial dependence of the plasmonic nanogap on the microcavities. This selective coupling between optical axial modes and localized surface plasmons is explained by a modified quasi-potential model based on perturbation theory. Our work reveals the interaction between surface plasmon resonances localized at the nanoscale and optical resonances confined in WGM microcavities at the microscale, thus establishing a unique platform for future investigations of light-matter interactions.

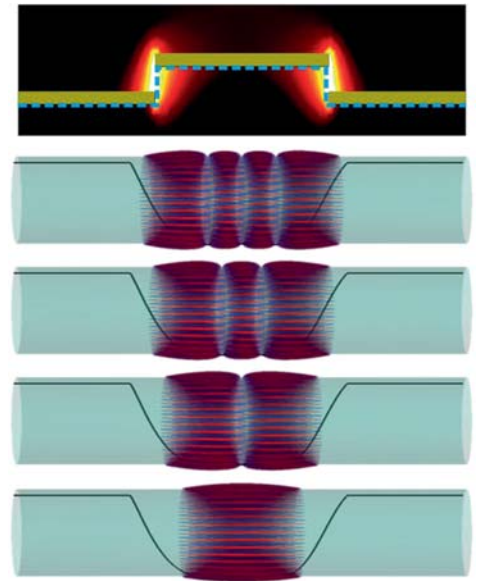


Fig. 3: Localized surface plasmons (LSPs) selectively coupled to different order of axial photonic modes in a rolled-up microtube cavity. The axial modes are confined within a lobe region on the tube while the LSPs are supported by vertical metal nanogap which is created at the lobe edge.

Ultrasensitive impedimetric DNA biosensor

An ultrasensitive DNA biosensor based on strain-engineered tubular electrodes was developed [4,5]. The inner electrode surface was modified with a specific DNA sequence of Avian Influenza Virus subtype H1N1 (Fig. 4a). Electrochemical impedance spectroscopy (EIS) in presence of $[\text{Fe}(\text{CN})_6]^{3-}$ redox probe was employed for the label-free detection of the complementary DNA, in a range of 20 aM–2 pM, obtaining the lowest limit of quantification reported so far for DNA sensors without amplification (20 aM) (Fig. 4b). The sensor showed four orders of magnitude sensitivity improvement compared to its planar counterpart. An opposite impedance response was also observed when the hybridization event occurred in the tubular electrode. The results suggest that there is an enhancement of electron hopping/tunneling along the DNA chains due to the enriched electric field inside the tube (Fig. 4c). Likewise, conformational changes of DNA might also contribute to this effect. In this geometry, the increase in the electric

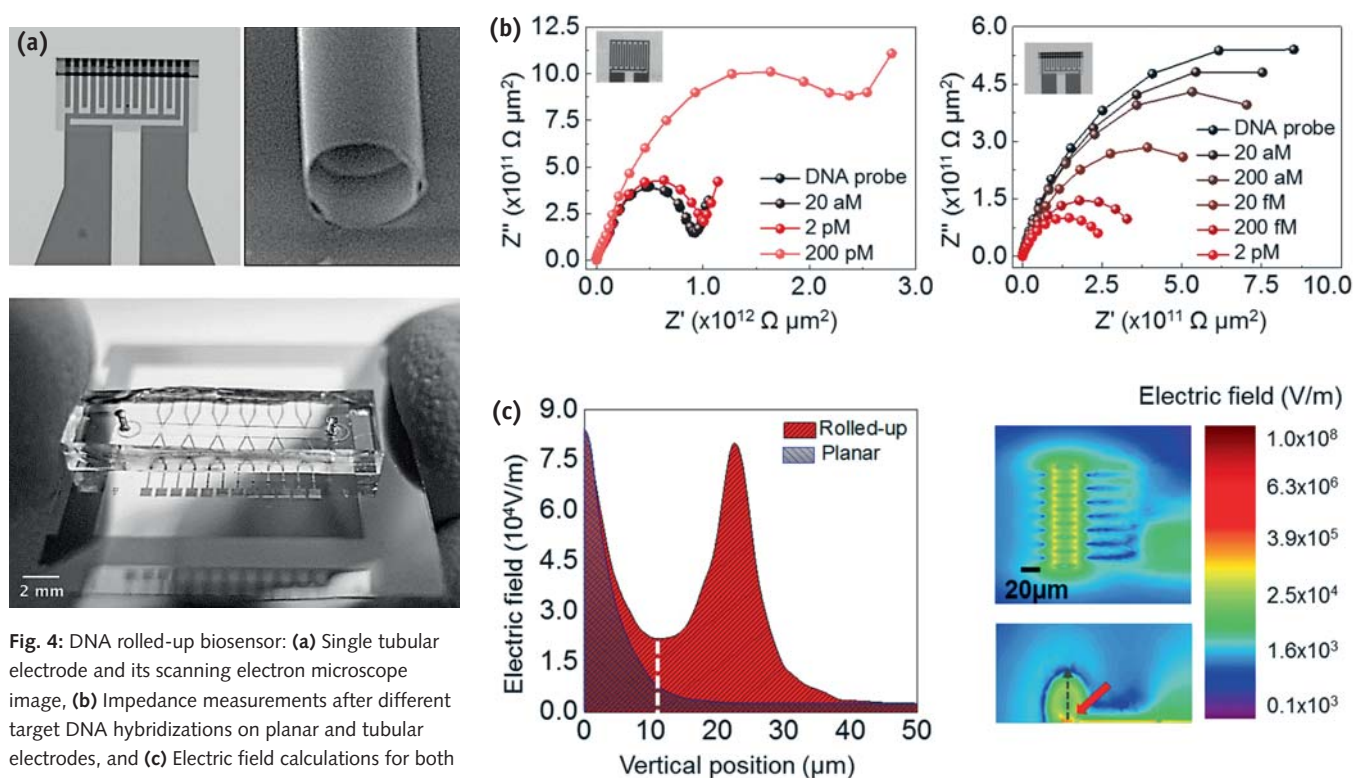


Fig. 4: DNA rolled-up biosensor: (a) Single tubular electrode and its scanning electron microscope image, (b) Impedance measurements after different target DNA hybridizations on planar and tubular electrodes, and (c) Electric field calculations for both planar and tubular electrodes.

field at distances corresponding to the typical depletion layer thickness of ferricyanide, favors ionic migration. Combined with the ability of the rolled-up electrodes to accumulate charge at its surface, this makes the charge transfer via conduction through double stranded DNA much more efficient than for the planar electrodes. In that latter case the variation in impedance would arise because of the building up of a dielectric barrier, which can be noticed only at higher DNA concentrations. In this way the opposite behavior of the impedance and the higher sensitivity of the rolled-up electrodes can be explained. Moreover, it has been shown that under strong enough electric fields (hundreds of volts per centimeter), single stranded DNA undergoes isotropic compression [6]. DNA conformational changes due to this difference in electric field compared to the planar ones would be enough to change the impedance response after the hybridization event. In the planar electrodes, the hybridization would produce an increase of the organic layer, therefore increasing the impedance. On the contrary, in the tubular electrodes, the hybridization would facilitate the expansion of the DNA strands, opening in this way channels for the electron transfer and decreasing impedance.

These highly integrated three-dimensional sensors provide a tool to study electrical properties of DNA under versatile experimental conditions and open a new avenue for novel biosensing applications (i.e. for protein, enzyme detection or monitoring of cell behavior under in-vivo like conditions). The nanomembrane engineering used in the fabrication process sets the current biosensor apart from others previously reported in three key aspects: no additional labels or materials are needed, a very simplified measurement setup is sufficient, and just microliter sample volumes are required, showing high integration level for point-of-care diagnostic platforms with minimum setup requirements.

- [1] Y. Yin et al., *Phys. Rev. Lett.* 116 (2016) 253904.
- [2] Y. Yin et al., *Phys. Rev. B* 92 (2015) 241403(R).
- [3] Y. Yin et al., *Phys. Rev. A* 94 (2016) 013832.
- [4] M. Medina-Sánchez et al., *Nano Lett.* 16 (2016), 4288.
- [5] M. Medina-Sánchez et al., 9th International Workshop on Impedance Spectroscopy (2016), Chemnitz-Germany. Best paper award.
- [6] A. Balducci et al., *Macromolecules*, 41, (2008), 5485.

Funding: Volkswagen Foundation (I/84072), DFG priority program FOR 1713, China Scholarship Council (No. 201206090008), DFG-Research Unit 1713 “Sensoric Micro and Nanosystem”

Cooperation: TU Chemnitz, TU Dresden (Chair Materials Science and Nanotechnology

Weyl semimetals

S. Bäßler¹, S. Borisenko, B. Büchner⁵, D.V. Efremov, A. Fedorov⁷, C. Felser², T. Förster^{5,11}, J. Gooth⁴, E. Haubold, C. Hess⁵, M. Hoesch⁸, R. Hühne, D. Kasinathan², S. Khim², T.K. Kim⁸, A. Kimura⁹, J. Klotz^{5,11}, K. Koepnick, Y. Kushnirenko, K. Nielsch, A. C. Niemann, T. Okuda¹⁰, H. Reith, B. Rellinghaus, M. Schmidt², P. Sergeius¹, C. Shekhar², M.I. Sturza, K. Sumida⁹, V. Süß², K. Taguchi⁹, J. van den Brink^{5,6}, C. Wiegand¹, J. Wosnitzer^{5,11}, S.-C. Wu², S. Wurmehl⁵, B. Yan^{2,3}, T. Yoshikawa⁹, R. Zierold¹

Abstract: While the physical concept of Weyl fermions was derived as one solution of the Dirac equation as early as in the late 1920s, the experimental realization of such fermions came only in 2015 as quasi-particles in Weyl semimetals. In this new topological matter, conduction and valence bands touch linearly near the Fermi level and the crossing points of these linear bands – so-called Weyl nodes – always appear in spatially separated pairs of opposite chirality. The IFW engaged in the scientific discussion about this newly realized, topological matter by theoretical modelling of new materials and magnetometry as well as magneto-transport experiments.

Theoretical Modelling – TaIrTe₄: A Ternary type-II Weyl semimetal

In metallic condensed matter systems, two different types of Weyl fermions can in principle emerge, with either a vanishing (type-I) or with a finite (type-II) density of states at the Weyl node energy. As of the date of this publication, only WTe₂ and MoTe₂ were predicted to be type-II Weyl semimetals.

Using density functional methods we identified TaIrTe₄ as a third member of this family of topological semimetals [1] – a finding which served us as a starting point for a broad investigation of TaIrTe₄ including ARPES [2] and quantum oscillation measurements [3]. TaIrTe₄ is structurally similar to the other two compounds although with a unit cell doubled in the *b*-direction. However, this analogy does not carry very far since the electronic structure differs in that it shows corrugated electron pockets (labelled 4 and 5 in Fig. 1) closer to the Γ -point and two sets of nested hole pockets (labelled 1 and 2 for larger *k_x*). The hole pockets each contain two Weyl points (WPs) of opposite chirality, resulting in the smallest possible total number of four Weyl points imposed by crystal symmetry. We calculated the Berry curvature to prove the topological nature of these WPs and to determine their chirality. It is interesting to note that the four WPs of TaIrTe₄ reside at similar positions as some of the WPs of the other two type-II Weyl semimetals. Since TaIrTe₄ contains the smallest possible number of WPs, one could speculate if their occurrence is a more generic feature of this class of compounds.

We also performed calculations of the surface spectral function for the surfaces of ideal semi-infinite slabs to demonstrate the existence of topological surface states (Fermi arcs) (Fig. 2). The attractive feature of TaIrTe₄ is that its Weyl points are well-separated within the Brillouin zone (BZ), resulting in Fermi arcs connecting pairs of Weyl nodes of opposite chirality in each hole pocket. The two symmetry inequivalent surfaces which are created by cleaving the compound at its natural cleavage plane carry different Fermi arcs connecting two Weyl points either in the first BZ (Fig. 2, upper row) or in the second BZ (Fig. 2, lower row). The first case with a (001)-surface is more promising, since here the Fermi arcs extend to about 1/3 of the surface Brillouin zone and are clearly removed from the bulk spectrum. This large momentum-space separation is very favourable for detecting the Fermi arcs spectroscopically and in transport experiments.

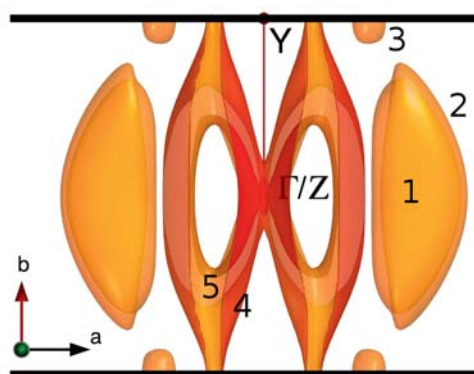
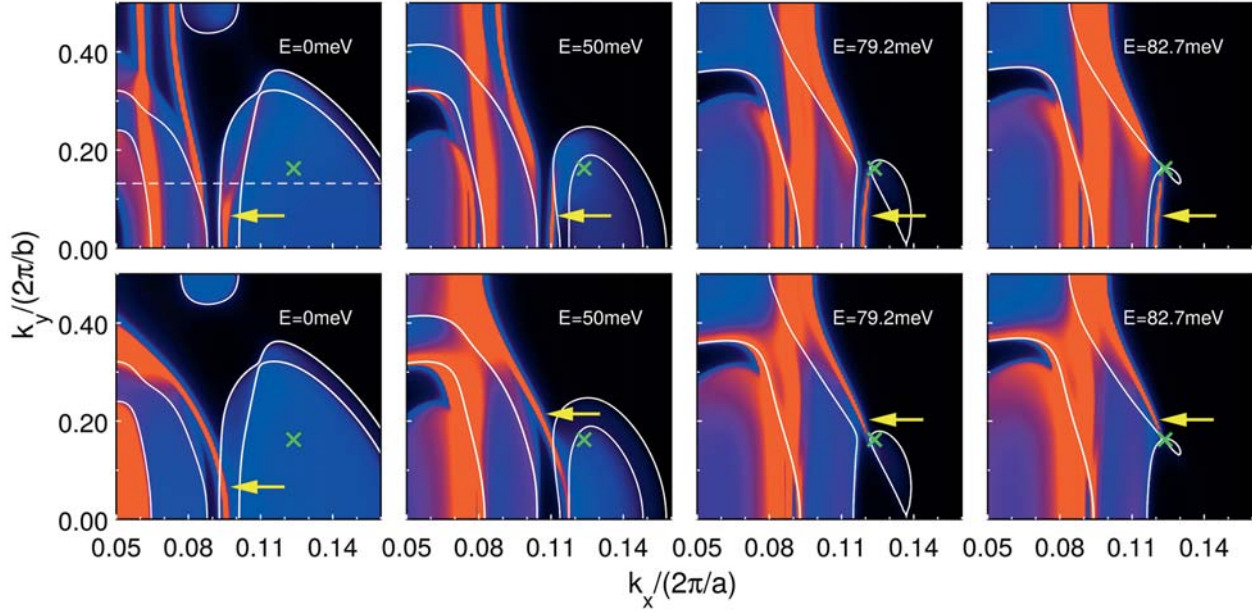


Fig. 1: The bulk Fermi surface of TaIrTe₄ viewed down the *c*-axis. The individual sheets are labelled 1 and 2 for the nested hole pockets, 3 for the small hole pocket and 4 and 5 for the electron pockets. Only the relevant portion of the BZ is shown in *a*-direction.



A possible complication for experimental observation of these topological surface states lies in the fact that at least in the calculations the Weyl points occur in the unoccupied bands at 82 meV above the Fermi level. Our calculations suggest that the Fermi arcs should be clearly detectable in an energy range from 50 – 82 meV. Doping and mass renormalization effects could bring them closer to the Fermi level.

Magnetometry experiments – Berry phase and band structure analysis of the Weyl semimetal NbP

NbP is a recently discovered Weyl semimetal and the lightest member of the inversion breaking TaAs compound family. It has a non-centrosymmetric crystal structure in a tetragonal lattice (space group I_41md) (Fig. 3) and shows many remarkable properties like extremely large magnetoresistance due to electron-hole resonance or Fermi arcs – a projection of the berry curvature onto the surfaces. In contrast to other Weyl semimetals, there is only weak spin orbit coupling in NbP because of the low atomic mass of Nb, which leads to the existence of additional parabolic bands apart from the Weyl bands.

To bring more insight to the band structure of NbP, we performed quantum oscillation measurements on a single crystalline NbP sample in a vibrating sample magnetometry (VSM) setup [4]. The magnetic moment as a function of the magnetic field shows a superposition of quantum oscillations of various frequencies due to the de-Haas-van Alphen (dHvA) effect (Fig. 4 a, b) – reflecting the multiple involved conduction channels in NbP. To obtain access to individual conduction bands and their properties, a Fourier transformation was conducted over the entire magnetic field range (Fig. 4 c, d). We were able to identify 4 oscillation frequencies in the k_x/k_y direction – $\beta = 0.8$ T, $\gamma = 2.5$ T, $\delta = 31.7$ T, $\varepsilon = 137.6$ T – and 2 oscillation frequencies in the k_z direction – $\eta = 6.6$ T, $\theta = 31.25$ T – of physical relevance.

To identify the nature of the conduction channels associated with these frequencies – parabolic band or linear Weyl band – several properties of the charge carriers have been evaluated. Firstly, a non-trivial Berry phase hints at a relativistic Weyl band, whereas the Berry phase gives the phase factor of an adiabatically driven, quantum mechanical system. Secondly, charge carriers on linear Weyl bands show a significantly lower effective mass as the conventional charge carrier on parabolic bands. Effective masses were calculated for each conduction channel individually by the temperature-dependent dHvA-oscillation amplitude damping. Thirdly, the Fermi surface and Fermi vectors were calculated for each conduction channel, while the oscillation cross section was approximated as a circle. Subsequently, the according energy values, carrier life time and the mobility have been derived.

Fig. 2: Surface spectral function of two possible terminations of an ideal semi-infinite slab; upper row: (001) and lower row: (00-1) surface. The individual panels show the results for different energies ranging from the bulk Fermi level (at the left) to the Weyl point energy 82.7 meV (at the right). The solid lines are $k_z = 0$ cuts of the bulk Fermi surface at the corresponding energies. Only a part of the upper right quadrant of the surface Brillouin zone is shown. The cross marks the position of the Weyl point and the arrow the Fermi arc. The small loop of the Fermi surface cut at the Weyl point energy and position in the right panels indicates the type-II nature of the Weyl point.

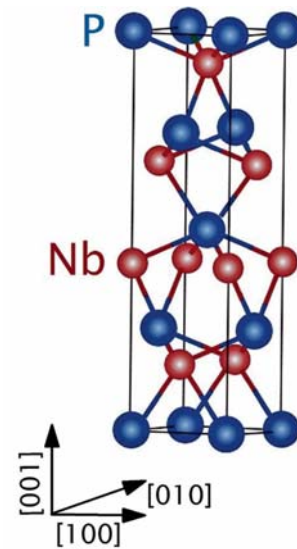


Fig. 3: The non-centrosymmetric crystal structure in a tetragonal lattice (space group I_41md) of NbP.

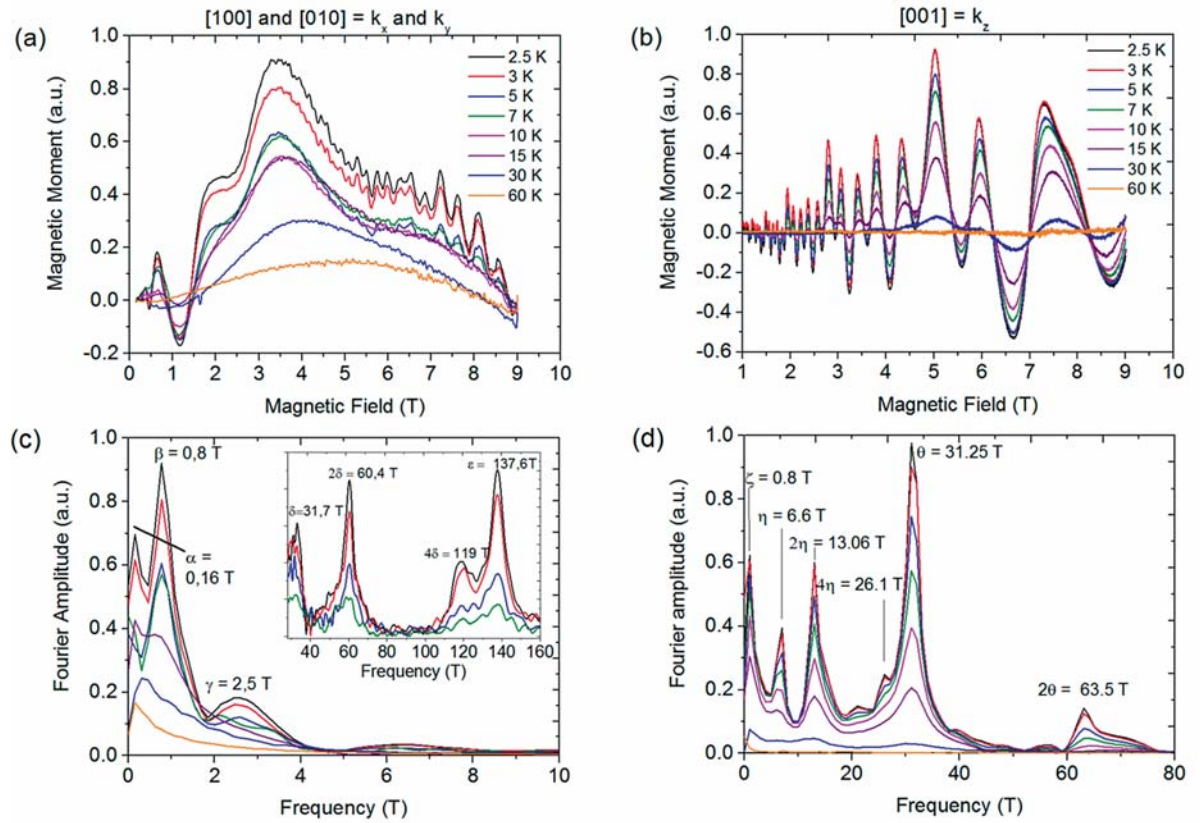


Fig. 4: (a,b) dHvA oscillations of the magnetic moment as a function of the magnetic field between 2.5 K and 60 K are shown. In the graphs, the raw data are shown with a subtracted linear background and several superpositions of different oscillation frequencies are visible. (c,d) The fast Fourier transforms of the measurement data as a function of the inverse magnetic field is displayed. Several oscillation peaks and their higher harmonics can be observed.

Taking all the criteria into account, we are able to identify the β -band as a carrier of Weyl fermions for the following reasons: It has a non-trivial Berry phase, the lowest effective mass of $0.048 m_0$, a high mobility ($25800 \text{ cm}^2/\text{Vs}$) and the Weyl node lies only 3.7 meV away from the Fermi level. This close distance between Fermi level and Weyl nodes is required for the Weyl fermions' activation.

Magneto-transport experiments – Chiral magnetoresistance in Ga-doped Weyl semimetal NbP

In Weyl semimetals, chirality is, in principle, a strictly conserved quantum number. However, in the case of parallel aligned electric and magnetic fields ($E \parallel B$), a breakdown of this chiral symmetry occurs (Fig. 5). The resulting, additional topological current leads to the observation of a negative magnetoresistance (NMR) in Weyl semimetals for $E \parallel B$. In intrinsic NbP the observation of such a chiral anomaly induced NMR has not been realized so far, because of the large distance of the Weyl points from the Fermi level (E_F).

Here, we choose the approach of material engineering via a Ga-etching, focused ion beam process to achieve a more favourable Fermi level position for the observation of chiral anomaly induced NMR in NbP [5]. In this process, a Ga-doped NbP micro-ribbon (Fig. 6a) of the dimension $50 \mu\text{m} \times 2.5 \mu\text{m} \times 0.5 \mu\text{m}$ was prepared. A SEM-EDX analysis showed a concentration of 53% Nb, 45% P and 2% Ga on the surface of the micro-ribbon (Fig. 6a). In transverse magneto-transport measurements at low temperatures, we observed Shubnikov-de-Haas (SdH) oscillations (Fig. 6b). Utilizing a Fourier transformation on the resistivity vs. inverse magnetic field data, we were able to identify six different SdH oscillation frequencies (Fig. 6c). Comparing these frequencies with ab initio simulations of the NbP band structure confirms a shift of E_F by +10 meV compared to the pristine, undoped NbP sample.

In longitudinal magneto-transport measurements, we observed NMR which we attribute to the chiral anomaly effect. The NMR is seen over the whole temperature range from 5 K to 300 K (Fig. 6d) with a slightly increasing effect size for increasing temperatures which

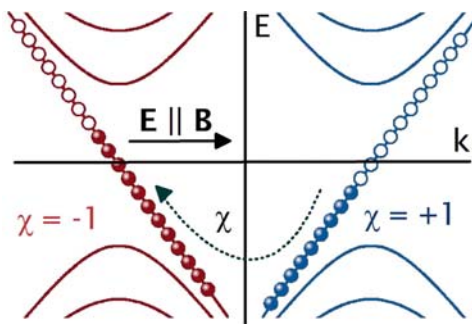


Fig. 5: Sketch of chiral anomaly in a Weyl semimetal: The energy spectrum of left- and right-handed chirality fermions (red and blue, respectively) in parallel applied electric and magnetic fields is shown. In the zeroth Landau level, left-handed particles and right-handed antiparticles have been produced, leading to an additional topological current.

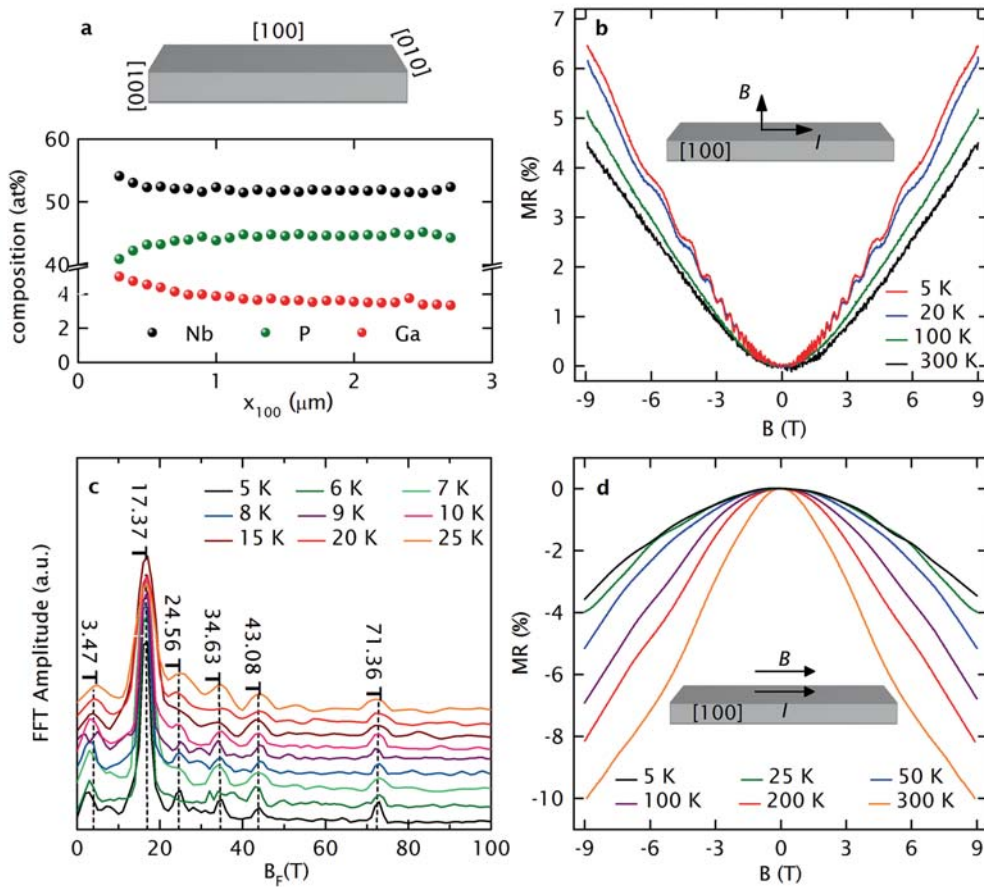


Fig. 6: (a) SEM-EDX data of the first 3 μm from the left sample edge along the $[100]$ direction of the NbP micro-ribbon reveals an average 53 % Nb, 45 % P and 2 % Ga composition. (b) The temperature-dependent, transverse MR reveals SdH oscillations below 75 K. (c) FFT spectra from 5 K to 25 K show six fundamental SdH frequencies at $F_1 = 3.47$ T, $F_2 = 17.37$ T, $F_3 = 24.56$ T, $F_4 = 34.63$ T, $F_5 = 43.08$ T and $F_6 = 71.36$ T. (d) NMR is observed in parallel magnetic and electric fields from 5 K to 300 K.

we attribute to the increasing ionization of Ga at elevated temperatures, pushing E_F even closer to the Weyl points. Furthermore, angle-dependent magnetoresistance measurements showed a $\cos^2(\varphi)$ -dependence of the resistivity with φ as the angle between electric and magnetic field, which further strengthens our assignment of the NMR for E||B to the chiral anomaly effect in Ga-doped NbP.

To further explore the chiral anomaly effect in Ga-doped NbP samples, we plan on detailed thermoelectric studies in the future.

- [1] K. Koepf *et al.*, Phys. Rev. B **93**, 201101R (2016)
- [2] E. Haubold *et al.*, arXiv: 1609.09549
(available at <https://arxiv.org/abs/1609.09549>)
- [3] S. Khim *et al.*, Phys. Rev. B **94**, 165145 (2016)
- [4] P. Sergelius *et al.*, Sci. Rep. **6**, 33859 (2016)
- [5] A. C. Niemann *et al.*, arXiv: 1610.01413
(available at <https://arxiv.org/abs/1610.01413>)

Funding: DFG-FOR 1346, DFG-SFB 1143, DFG-RSF-Project No. (NI 616/22-1), ERC Advanced Grant No. (291472), Harvard-MIT CUA,

Cooperation: ¹Universität Hamburg, Germany; ²MPI-CPFS Dresden, Germany; ³MPI-PKM, Germany; ⁴IBM Zürich, Switzerland; ⁵TU Dresden, Germany; ⁶Harvard University, USA; ⁷Universität zu Köln, Germany; ⁸Diamond Light Source, Harwell Campus, United Kingdom; ⁹Hiroshima University, Japan; ¹⁰HSRC, Hiroshima University, Japan; ¹¹HLD-EMFL, Germany

A novel processing route for integrated micro thermoelectric coolers

J. Garcia, D. A. L. Ramos, V. Linseis¹, M. Mohn, K. Nielsch,
N. Perez Rodriguez, H. Reith, G. Schierning, H. Schlöör

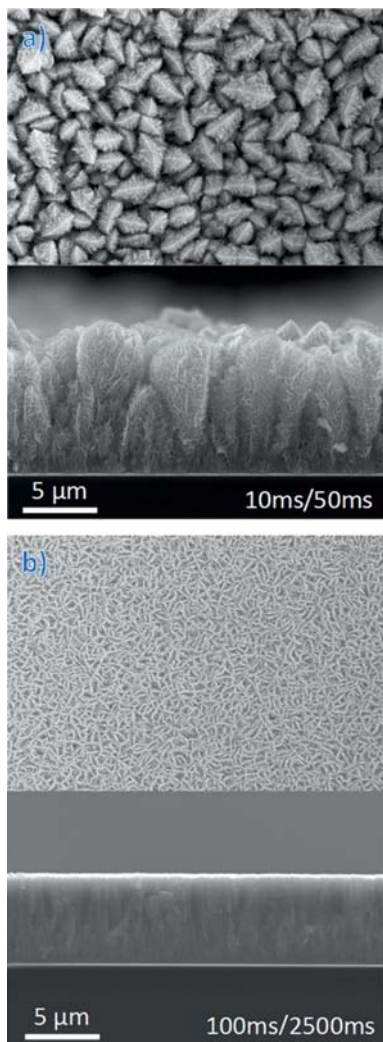


Fig. 1: SEM top-view and cross-sections of $(\text{Bi}_x\text{Sb}_{1-x})_2\text{Te}_3$ films deposited at a pulse time of **a)** ton/toff = 10 ms/50 ms and **b)** ton/toff = 100 ms/2500 ms deposited with surfactant.

Abstract: To enable further miniaturization and closer integration of photonic integrated circuits (PICs), driven by the continuously growing network traffic, local heat management on the chip component scale is required. A contribution to this local heat management is envisioned by integrated micro thermoelectric coolers. A cost-efficient and highly scalable synthesis method, that is compatible with existing IC processing techniques, is the electrochemical deposition. At the IFW we developed a new fabrication process for micro thermoelectric coolers using a laser lithographic process combined with electrochemical deposition of thermoelectric p- and n-type materials into pre-structured cavities [1]. By optimizing the pulsed electrochemical deposition of ternary n-type $\text{Bi}_2(\text{Te}_x\text{Se}_{1-x})_3$ and p-type $(\text{Bi}_x\text{Sb}_{1-x})_2\text{Te}_3$ materials, compact and smooth films with thermoelectric properties close to the bulk counterpart can be achieved. We investigated the influence of the deposition parameters on the film composition and crystal structure as well as the thermoelectric properties for thick films and confined structures.

Electrochemical deposition of $\text{Bi}_2(\text{Te}_x\text{Se}_{1-x})_3$ and $(\text{Bi}_x\text{Sb}_{1-x})_2\text{Te}_3$ thick films

Low resistance thermally oxidized silicon wafers coated with 5 nm of Ti and 100 nm of Pt are used as working electrodes for the electrochemical deposition of the BiTe-based materials. These substrates are placed in a three electrode electrochemical cell, with a Pt mesh as a counter electrode and a Ag/AgCl reference electrode. The bath chemistry of both, the n-type material, $\text{Bi}_2(\text{Te}_x\text{Se}_{1-x})_3$, and the p-type material, $(\text{Bi}_x\text{Sb}_{1-x})_2\text{Te}_3$, was optimized and additives were used to achieve more compact and even films [2].

The use of additives in precise amounts and the choice of pulsed deposition conditions allowed to greatly improve the compactness and evenness of the deposited $(\text{Bi}_{1-x}\text{Sb}_x)_2\text{Te}_3$ continuous films. Fig. 1 shows SEM images of as-deposited films. Electrodeposition with short pulse times results in dendritic and non-compact growth (Fig. 1a). Deposition with longer pulse times and surface-adsorbing additives results in levelled and compact layers (Fig. 1b).

The electrochemical deposition of these materials into confined structures revealed a different growth mechanism. Using previously optimized deposition conditions for continuous films the deposition in confined structured results in more dendritic deposits, together with an uncontrolled overgrowth along the edges of the cavities. In order to overcome this issue, the deposition potential as well as the pulse time was adjusted in combination with ultrasonic stirring of the electrolyte during deposition leading to compact and smooth deposits. For further improvement of the morphology and to reduce the roughness first experiments with heated substrates during deposition show promising results.

Thermoelectric characterization of films

The transport properties of thermoelectric films highly depend on the deposition parameters controlling the stoichiometry as well as the morphology of the films. The thermoelectric efficiency of a material is defined by the figure of merit $zT = \sigma S^2 T / \lambda$ therefore a good thermoelectric material should have a high Seebeck coefficient S as well as a high electrical σ and low thermal conductivity λ .

To optimize the deposition conditions the Seebeck coefficient is the most critical transport parameter as it highly depends on the stoichiometry. The Seebeck coefficient at room temperature of the deposits is measured using a potential Seebeck microprobe

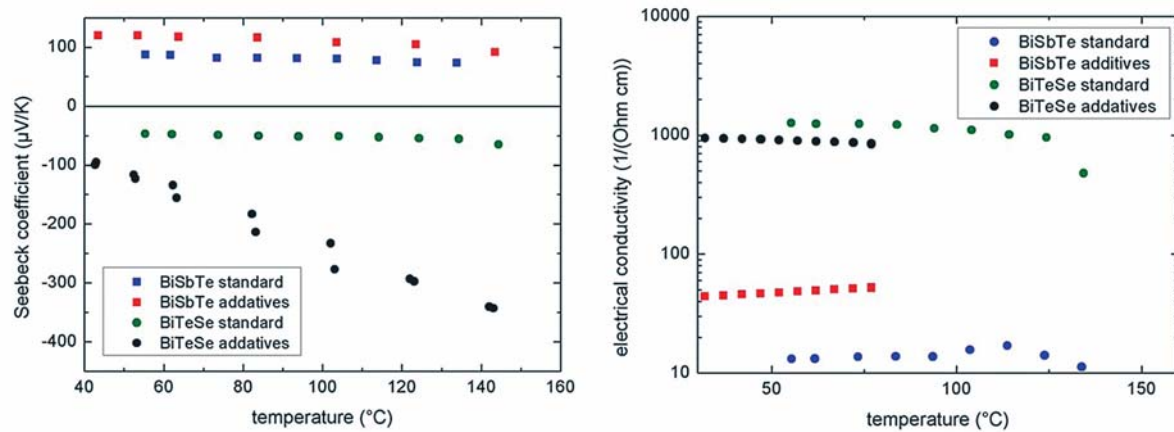


Fig. 2: Temperature dependent a) Seebeck coefficient and b) electrical conductivity of $\text{Bi}_2(\text{Te}_x\text{Se}_{1-x})_3$ and $(\text{Bi}_x\text{Sb}_{1-x})_2\text{Te}_3$ films deposited with and without additives.

system (PSM, Panco). For the temperature dependent characterization of the Seebeck coefficient and the electrical conductivity a commercial setup (LSR, Linseis) is used. In Fig. 2 the temperature dependent Seebeck coefficient and the electrical conductivity of p-type $(\text{Bi}_{1-x}\text{Sb}_x)_2\text{Te}_3$ and n-type $\text{Bi}_2(\text{Te}_x\text{Se}_{1-x})_3$ with and without additives are presented. The samples with additives show an improvement in the thermoelectric properties. The power factor ($\text{PF} = \sigma S^2$) of the n-type material with additives is as high as $1 \text{ mWm}^{-1}\text{K}^{-1}$ around RT and can be further improved by annealing.

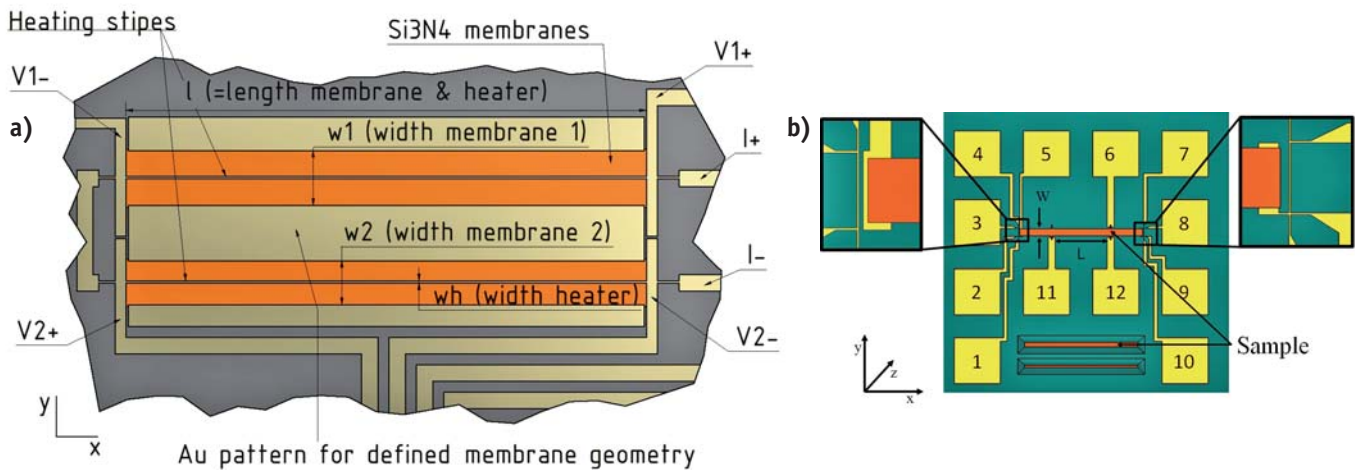


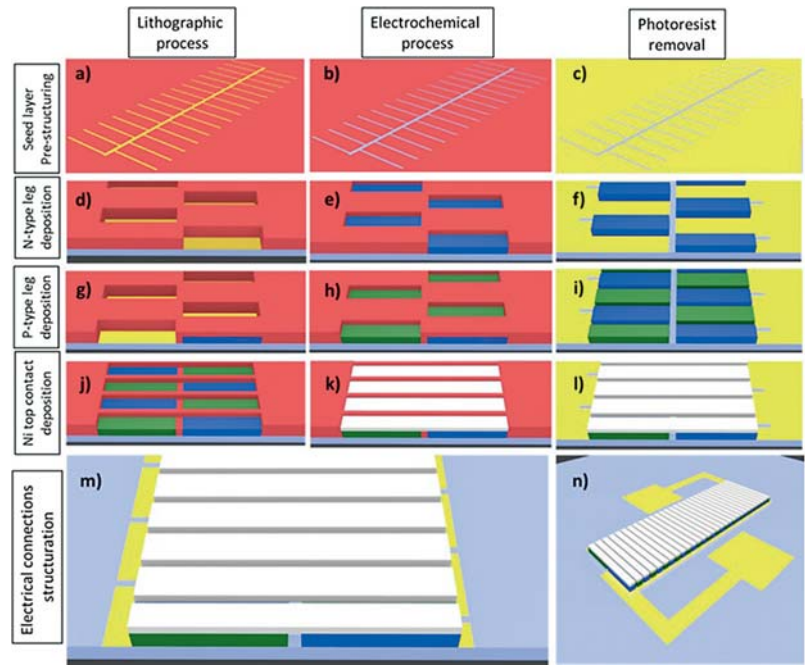
Fig. 3: a) Schematic back side view of the hot stripe setup on two Si_3N_4 membranes to measure the thermal conductivity; b) Front side of the measurement chip showing the Hallbar structure which is used for the electrical conductivity and the Seebeck measurement.

Recently we developed a chip-based platform to simultaneously measure the in-plane electrical and thermal conductivity as well as the Seebeck coefficient in collaboration with Linseis Messgeräte GmbH [3]. The chip is combining 2 measurement structures; (1) a hot stripe measurement setup on a suspended Si_3N_4 membrane (s. Fig. 3) for either steady state or transient thermal conductivity measurements and (2) a 4-point measurement setup (s. Fig. 3) for the determination of the electrical transport properties as well as the Seebeck coefficient. The measurement chip made it possible to measure the thermal conductivity of our deposits which is a challenge with common measurement techniques, like time domain thermal reflectance or laser flash due to the high roughness and the low thickness of the deposits, respectively. To determine the thermal conductivity of the deposits first the thermal conductivity seed layer had to be measured to be subtracted afterwards resulting in a thermal conductivity of the p- and n-type deposits of around $1 \text{ Wm}^{-1}\text{K}^{-1}$ at RT which is in good agreement with previous reported data for thick films [4].

Fabrication of micro thermoelectric coolers

The processing steps for the fabrication of Π -structured micro-thermoelectric devices were chosen to be compatible with complementary metal-oxide-semiconductor (CMOS) technology. Considering the integration of the micro-thermoelectric coolers, the

Fig. 4: **a), b)** and **c)** laser lithographic pre-structuring of photoresist (red) to pattern Cr/Au seed layer (yellow) via wet chemical etching followed by photoresist stripping; **d), e)** and **f)** represent the corresponding procedure for the electrodeposition of the $\text{Bi}_2(\text{Te}_x\text{Se}_{1-x})_3$ component of the leg-pair (blue) and **g), h)** and **i)** for the $(\text{Bi}_x\text{Sb}_{1-x})_2\text{Te}_3$ component (green); The template used for top contact fabrication is shown in **j)**, while the result after Au sputtering and Ni electrodeposition (white) is represented in **k)** before, and **l)** after photoresist removal. Final Cr/Au seed layer structuring is required to avoid electrical shortcut between consecutive leg-pairs **m)** and for the electrical contact pads **n)**.



different electronic or photonic components as transistors, gates or lasers to be encased by the thermoelectric device may represent irregularities on the substrate with respect to the topology up to the micrometre scale. For that reason a laser photolithographic approach using thick photoresists was chosen.

The process flow followed to fabricate the micro thermoelectric coolers is schematized in Fig. 4. As it is shown, the fabrication process consists of four major steps of mixed photo-patterning and wet chemical etching or electrochemical deposition, followed by a final structuring of the electrodes, defining the electrical contacts of the device. Figure 4a-c represent the pre-structuring of the Cr/Au seed layer to avoid an electrical shortcut between consecutive leg-pairs. The pre-structured substrate is used for spin-coating and cavities of $20 \times 140 \mu\text{m}^2$ are subsequently structured at specific positions as can be seen in Fig. 4d. These cavities are then used as template for the electrochemical deposition of the first component of the leg-pair, for instance the n-type $\text{Bi}_2(\text{Te}_x\text{Se}_{1-x})_3$ (Fig. 4e and f). The electrodeposition time is chosen to achieve $12 \mu\text{m}$ thick leg. This process is repeated, although now the cavities are structured in front of the previous structures as demonstrated in Fig. 4g. The n-type material is protected by the photoresist during the deposition of the $12 \mu\text{m}$ p-type $(\text{Bi}_x\text{Sb}_{1-x})_2\text{Te}_3$ to prevent cross-contaminations.

The last step of micro thermoelectric cooler fabrication comprises the deposition of the top contact. The photolithography process for this purpose is not trivial and requires two different exposures. The final structure of the photoresist is schematized in Fig. 4j. In this case, the photoresist that covers the previously deposited legs is completely exposed and developed in order to obtain a clean top surface of the legs for the top contact deposition process. However, the photoresist deposited between the leg-pairs, which will conform the II-structure, has to be levelled with the legs. For this reason, these areas have been exposed with the specific dose that within the 12 minutes of development the resulting thickness is $12 \mu\text{m}$. Moreover, as this gap is not conductive, a homogeneous Au seed layer has been sputtered before the top contact Ni electrodeposition process, Fig. 4k and 4l. The entire micro thermoelectric cooler is coated again with photoresist in order to etch away the remaining Au bottom seed layer which defines the electrical connection of consecutive leg pairs in series, as shown in Fig. 4m. This process can be used also to define the electrical connections with an external measurement equipment, Fig. 4n.

With the presented work flow, a first working leg pair could be fabricated arranged in the desired micro thermoelectric cooler structure which geometrical characteristics fits with the requirements for its application on a PIC. A tilted SEM image is shown in Fig. 5. As can be seen, high compactness of leg-pairs has been achieved. Furthermore, free standing Ni contacts between the legs are stable enough for a robust micro thermoelectric cooling device. Such top contacts are deposited on top of both n-type and p-type materials ensuring homogeneous contacts.

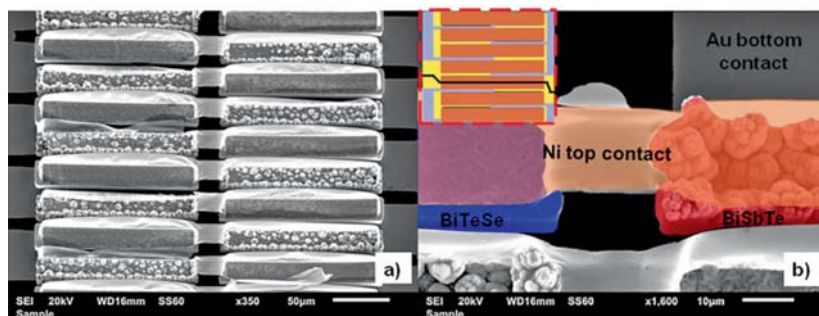


Fig. 5: a) SEM picture of several leg pairs from the micro-thermoelectric cooler; b) false color image of a leg-pair with highlighted Bi₂(Te_xSe_{1-x})₃ (blue), (Bi_xSb_{1-x})₂Te₃ (red) and Ni top contact (brown). The inset shows the electrical configuration for the characterization of a single leg pair (black line indicates the electrical path).

In order to electrically characterise a single leg-pair, the remaining Cr/Au seed layer has been patterned. The values of the total resistance measured in different leg-pairs has been found to be around 80 Ω. Taking into account the low resistance of the n- and p-type legs fabricated, the contribution of the contact resistance, which was studied using the Cox Strack method for different contact materials, has a strong impact on the total resistance. This effect is even more pronounced due to the high roughness that increases the total contact area, especially in the case of the (Bi_xSb_{1-x})₂Te₃ material.

[1] J. Garcia et al., JSS 6 (2017) N1

[2] Patent DE102016217419.3

[3] V. Linseis et al., JMR 31 (2016) 3196

[4] C. Schumacher et al., Adv. Energy Mater. 3 (2013) 95

¹Linseis Meßgeräte GmbH, Vielitzerstrasse 43, 95100 Selb, Germany

Funding: H2020 EU-Project TIPS (ID 644453), SAB Project GroTEGs

Cooperation: Tyndall National Institute (TNI, Ireland); Centre National de la Recherche Scientifique (CNRS, France); Lyon Institute of Nanotechnology (INL-CNRS, France); Institute of Light and Matter (ILM-CNRS, France); Materials Institute Jean Rouxel (IMN-CNRS, France); Communicraft (Ireland); Alcatel-Lucent Bell Labs (Ireland); Alcatel-Lucent Bell Labs (France); Alcatel Thales III-V Lab (France); Lionix BV (Netherlands); Stokes Laboratories (Ireland); University of Hamburg

Research Area 3

The role of the superconducting layer morphology in the superconducting spin valve effect

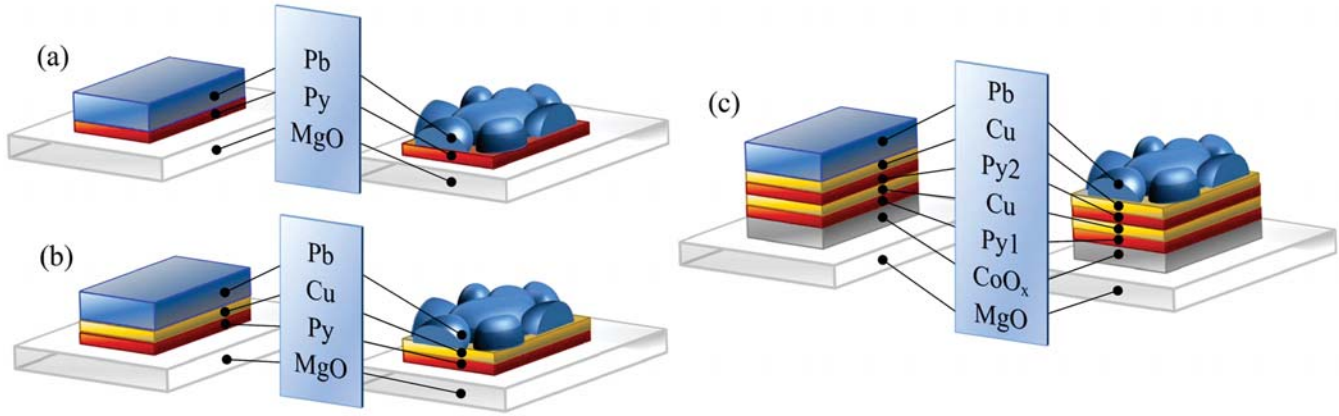
P. Leksin, A. Kamashev¹, J. Schumann, V. Kataev, J. Thomas,
T. Gemming, B. Büchner, I. Garifullin¹

Abstract: Superconducting spin valves based on the superconductor/ferromagnet (S/F) proximity effect are considered to be a key element in the emerging field of superconducting spintronics [1]. Considering this, we have studied the influence of the superconducting layer morphology on the proximity effect in the S/F based structures [2]. The investigation of two types of heterostructures, with a rough and with a smooth superconducting layer, respectively, was carried out using the transmission electron microscopy in combination with transport and magnetic characterization. The suppression of the critical temperature of the S layer turned out to be the same for both kinds of the structures. However, the magnitude of the conventional superconducting spin valve effect significantly increases, when the morphology of the S layer is changed from the type of overlapping islands to a smooth one. We attribute this drastic effect to a homogenization of the Green function of the superconducting condensate over the S/F interface in the S/F1/F2 valve with a smooth S layer surface.

The interplay between superconductivity and ferromagnetism in thin layered heterostructures gives rise to a number of new physical phenomena, such as the S/F/S π -phase Josephson effect, the so-called cryptoferromagnetic state, conventional (singlet) and unconventional (triplet) superconducting spin valve effects (SSVE), etc. (see, e.g., a recent review [1] and references therein). SSVE for a sequence of two metallic F layers and one S layer, S/F1/F2, was theoretically proposed in 1997 by Oh *et al.* [3]. The physical mechanism of SSVE relies on the idea to manipulate the phase and the amplitude of the superconducting wave function penetrating into the F1 layer and, hence, the superconducting critical temperature T_c , by changing the magnetic state of the F1/F2 part of the heterostructure. A similar theory for the F1/S/F2 multilayer was proposed in 1999 by Tagirov [4] and Buzdin *et al.* [5]. Later, a triplet spin valve effect was theoretically described for S/F1/F2 structures by Fominov *et al.* [6–8]. At present, there is a number of experimental works, confirming SSVE effect. In most of the cases the magnitude of the effect $\Delta T_c = T_c^{AP} - T_c^P$ turned out to be of the order of 10 – 40 mK, whereas the width of the superconducting transition was $\delta T_c \sim 100$ mK (see references in [1]). Therefore no full switching between the normal and the superconducting states could be achieved. Finally, for the case of the S/F1/F2 multilayer, the full switching due to SSVE was realized by means of a notable reduction of δT_c [9].

Up to now, the role of the microscopic structure of the superconducting layer in S/F and S/F1/F2 proximity effects has been given little attention from both, theoretical and experimental side. In our work [2] we experimentally demonstrate that an important reason for the small magnitude of SSVE in metallic S/F1/F2 heterostructures is the rough surface of the S layer composed of overlapped islands which can reduce ΔT_c down to zero. By improving the morphology of the S layer to the smooth one we were able to significantly enhance ΔT_c up to 100 mK. This highlights a key role of the quality of the S layer for the S/F proximity related SSVE in metallic heterostructures.

In order to investigate the influence of the S layer structure type on the S/F proximity effect we have prepared the following groups of samples: bilayer S/F structures [Fig. 1(a)] and S/F1/F2 based spin valve samples [Fig. 1(c)]. We have also prepared a trilayer sample S/AD/F [see Fig. 1(b)] to demonstrate the importance of the antidiffusion (AD)



layer introduced between the S and F layers for the improvement of the quality of the superconducting transitions without influencing the S/F proximity effect. Each of these groups had two types of the S layer: (i) S layer composed of overlapping islands which will be further called a rough S layer, and (ii) smooth S layer (Fig. 1).

For the implementation of the S/F1/F2 based spin valve we prepared samples with the layer sequence AF/F1/N/F2/AD/S deposited on the MgO(100) substrate [Fig. 1(c)]. Here, N is the nonmagnetic metallic layer between F1 and F2 layers that decouples magnetizations of the F layers. The antiferromagnetic (AF) layer pins the magnetization of the F1 layer, whereas the magnetization of the F2 layer remains free. The materials choice was the following: for F layers we used permalloy $\text{Py} = \text{Ni}_{0.81}\text{Fe}_{0.19}$, N and AD layers were made of Cu, Pb was used for the S layer, and CoO_x was used for the AF layer.

The deposition of layers was performed using an e-gun in ultra-high vacuum with pressure 10^{-9} mbar. To examine the layer stacks regarding the thickness of the layers as well as the interface roughness and the morphology of the Pb layer cross sections of the samples were investigated with a transmission electron microscope FEI TEM/STEM Tecnai F30 working at an acceleration voltage of 300 kV. All the details of the sample preparation and the microscopic measurements can be found in [2]. The interfaces between the single layers could clearly be seen in the TEM micrographs as well as in the STEM-HAADF images (Fig. 2). As can be seen in Figs. 2(b) and 2(c), in the MgO/Py/Pb structure prepared at $T_{\text{sub}} = 300$ K the Pb layer grows in a shape of overlapping islands with an island size of 0.2 - 1 μm ; in the case of MgO/Py/Cu/Pb structure prepared at $T_{\text{sub}} = 150$ K the TEM image of the cross-section reveals a smooth surface of the Pb layer [Fig. 2(e)].

Fig. 1: Schematic design of the samples: Bilayer (a), trilayer (b) and spin valve structures (c) with the rough (right side) and a smooth surface (left side) of the S film.

Fig. 2: Microscopic characterization of the samples with a rough (top row) and a smooth (bottom row) S layer deposited at the substrate temperatures of 300 K and 150 K, respectively. Micrographs of the surface of the Pb layer and TEM images of the cross-section obtained with HAADF detector at two magnifications are shown on panels (a), (b) and (c) for the Py(5)/Pb(70) structure with the rough Pb layer, and on panels (d), (e) and (f) for the Py(5)/Cu(2)/Pb(70) structure with the smooth Pb layer, respectively.

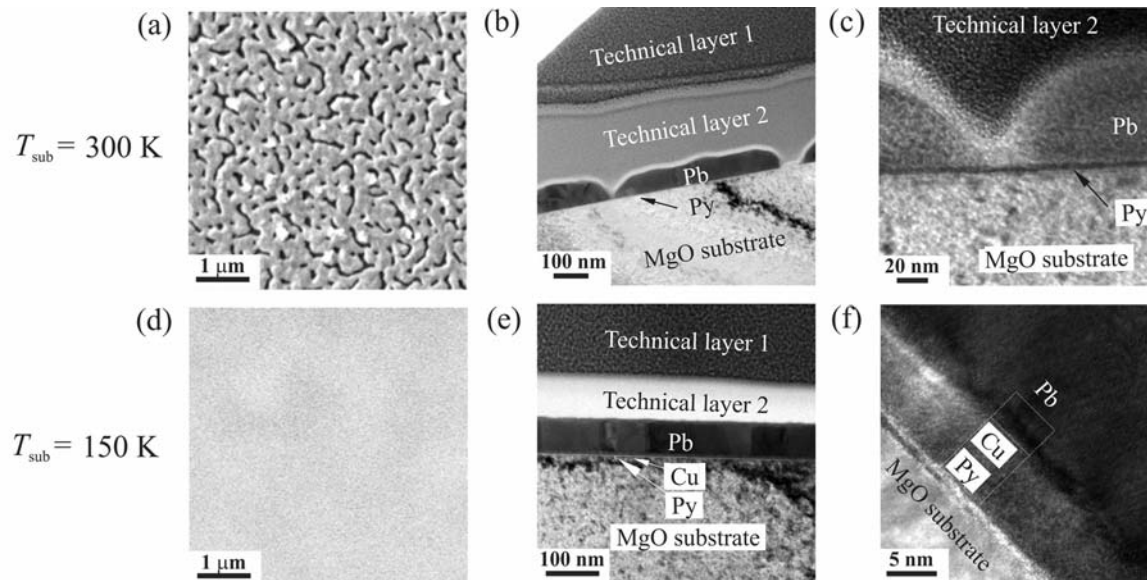
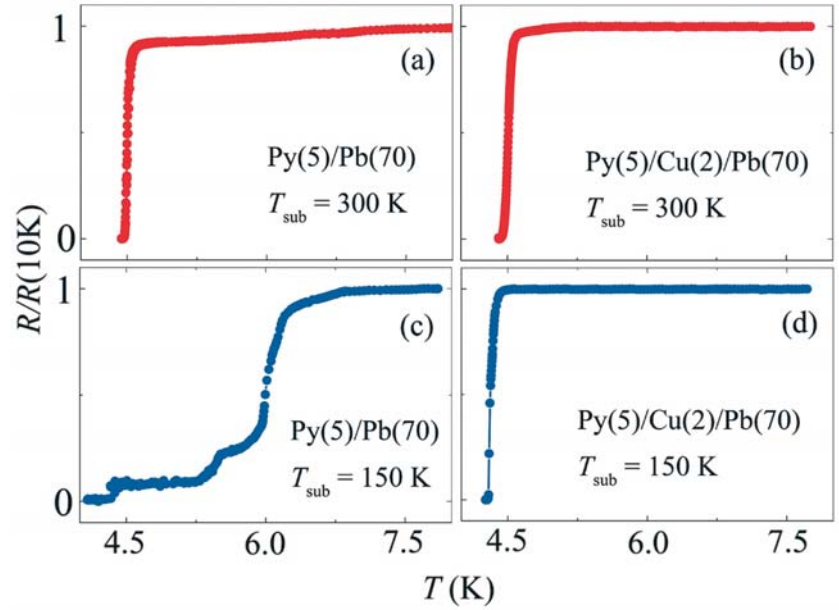


Fig. 3: Electrical transport characterization of the samples. Superconducting transitions curves for samples Py(5)/Pb(70) and Py(5)/Cu(2)/Pb(70) with the rough Pb layer ($T_{\text{sub}} = 300\text{ K}$) are shown in panels (a) and (b), the curves for the respective samples with the smooth Pb layers ($T_{\text{sub}} = 150\text{ K}$) are shown in panels (c) and (d).



The superconducting properties of the samples were studied using a 4-contact resistivity measurement. The details of the experiment can be found in [2]. We found that the residual resistivity ratio $RRR = \rho(300\text{ K})/\rho(10\text{ K})$ of the studied samples lies in the interval $10 < RRR < 17$ with no notable difference with regard to the S layer type. Fig. 3 shows characteristic superconducting transitions for the rough and smooth type Py/Pb and Py/Cu/Pb structures. Comparison of Figs. 3 (a) and (b) reveals that for samples prepared $T_{\text{sub}} = 300\text{ K}$ the Cu AD layer does not influence the superconducting properties. The transition is sharp in both cases with the same value of T_c . In contrast, the transition curve of the Py/Pb sample prepared at $T_{\text{sub}} = 150\text{ K}$ exhibits several steps indicating degraded superconducting properties [Fig. 3(c)]. Insertion of the Cu AD layer drastically improves the quality of the transition [Fig. 3(d)] making it even superior to those in Figs. 3 (a) and (b). This result is similar to our earlier findings [10].

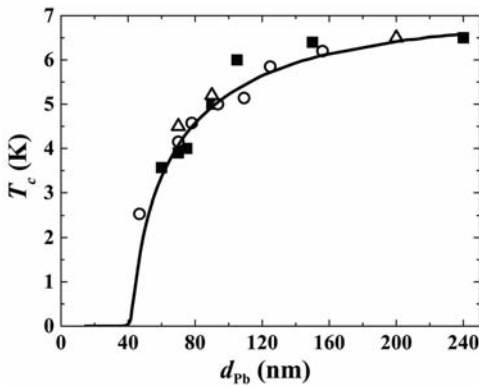


Fig. 4: Dependence of T_c on the thickness of the superconducting Pb layer d_{Pb} for Py/Pb and Py/Cu/Pb structures with a rough Pb layer (squares and opened triangles), and for Py/Cu/Pb structures with a smooth Pb layer (open circles). Solid line denotes the theory fit.

All structures were magnetically characterized using a 7 T VSM SQUID magnetometer from Quantum Design. First, the samples were cooled down from 300 K to 10 K in the presence of the in-plane magnetic field of +4 kOe. At 10 K the magnetic field was varied from +4 kOe to -4 kOe and then back to +4 kOe. In a strong positive field the magnetizations of F1 and F2 layers M_1 and M_2 are aligned parallel and the sample is fully magnetized. M_2 follows the sign change of the applied field and flips giving rise to a step of the $M(H)$ curve [insert in Fig. 5(a)]. Eventually M_1 is reversed in a field of -2.5 kOe, and the structure is fully magnetized in the opposite direction.

Fig. 4 depicts the dependence of T_c on the Pb layer thickness d_{Pb} for systems Py/Cu/Pb and Py/Pb with rough and smooth Pb layers. Interestingly, the measured samples show very similar $T_c(d_{\text{Pb}})$ dependence suggesting that the Cu antidiffusive layer does not affect the S/F proximity effect and that the morphology of the S structure does not influence the character of the suppression of T_c . We fit the experimental data with the theory by Fominov *et al.* [12] (see the details in [2]). For the spin valve samples we have chosen $d_{\text{Pb}} = 70\text{ nm}$ because it is large enough to provide measurable T_c , and yet it is close to the critical thickness $d_{\text{Pb}}^{\text{cr}} = 40\text{ nm}$, which is favorable for the observation of SSVE. We prepared the superconducting spin valve samples $\text{CoO}_x(3)/\text{Py}^1(3)/\text{Cu}(4)/\text{Py}^2(1)/\text{Cu}(2)/\text{Pb}(70)$ with a rough and a smooth Pb layer. The SQUID characterization (see Fig. 5(a) and the insert therein) did not reveal any difference in magnetic properties between these two systems. However, for the system with the rough S layer we found no shift of T_c when switching between the AP and P states, suggesting the absence of

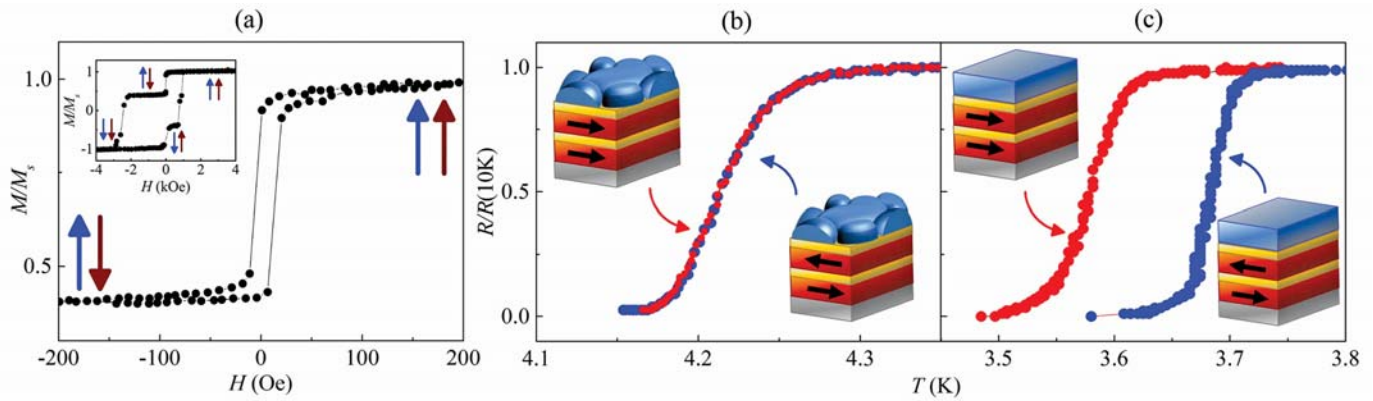


Fig. 5: Magnetic and superconducting properties of the spin valve samples with rough and smooth S layer. Minor magnetic hysteresis loop corresponding to the magnetization reversal of the free Py^2 layer (a), and the major hysteresis loop [insert in panel (a)] for the sample $\text{CoO}_x/\text{Py}^1(3)/\text{Cu}(4)/\text{Py}^2(1)/\text{Cu}(2)/\text{Pb}(70)$ with a smooth Pb layer. This magnetic behavior is also typical for the spin valve sample with a rough Pb layer. Superconducting transitions, measured for AP and P states for $\text{CoO}_x/\text{Py}^1(3)/\text{Cu}(4)/\text{Py}^2(1)/\text{Cu}(2)/\text{Pb}(70)$ with a rough (b) and a smooth Pb layer (c). Arrows depict mutual orientation of the magnetizations of the Py^1 and Py^2 layers.

SSVE, $\Delta T_c = 0$ [Fig. 5(b)]. In contrast, for the spin valve system with the smooth S layer the ΔT_c amounts to 100 mK [Fig. 5(c)]. The results in Figs. 5 (b) and (c) clearly demonstrate a drastic influence of the morphology of the S layer on SSVE. We argue that the most possible reason is that the in-plane inhomogeneity of the S layers "converts" into the inhomogeneity of the superconducting pair Green function in the F layer causing the suppression of SSVE, whereas the dependence of T_c on the thickness of the S layer remains unaffected by its surface morphology. (for more details see [2]) The magnitude of SSVE ΔT_c can be turned down to zero by increasing the roughness of the S surface and boosted up to $\Delta T_c = 100$ mK by flattening the S layer. This finding provides new insights into the sensitivity of the microscopic mechanism of SSVE to the real morphology of the superconducting spin valves and can be important for the implementation of SSVE in superconducting spin electronic devices.

- [1] J. Linder et al., *Nature Physics* (2015), 11, 307–315.
- [2] P. V. Leksin et al., *Nano Res.* (2016), 9, 1005–1011.
- [3] S. Oh; et al., *Appl. Phys. Lett.* (1997), 71, 2376–2378..
- [4] L. R. Tagirov et al., *Phys. Rev. Lett.* (1999), 83, 2058–2061.
- [5] A. I. Buzdin, et al., *Europhys. Lett.* (1999), 48, 686 –691.
- [6] Ya. V. Fominov et al., *Pis'ma Zh. Eksp. Teor. Fiz.* (2010), 91, 329-333 [JETP Lett. (2010), 91, 308-313].
- [7] R. G. Deminov, et al., *J. Magn. Magn. Mater.* (2015), 16-17, 373.
- [8] R. G. Deminov et al., *Solid State Phenom.* (2015), 233-234, 745-249.
- [9] P. V. Leksin et al., *Appl. Phys. Lett.* (2010), 97, 102505.
- [10] P. V. Leksin et al., *Pis'ma Zh. Eksp. Teor. Fiz.* (2013), 97, 549-553 [JETP Lett. (2013), 97, 478-482].
- [11] P. V. Leksin et al., *Phys. Rev. B* (2015), 91, 214508.
- [12] Ya. V. Fominov et al., *Phys. Rev. B* (2002), 66, 014507.

Funding: Deutsche Forschungsgemeinschaft through Grant LE 3270/1-1.
Russian Foundation for Basic Research through Grant number 14-02-00350-a
Program of the Russian Academy of Sciences.

Cooperation: ¹Zavoisky Physical-Technical Institute, Kazan Scientific Center of Russian Academy of Sciences, 420029 Kazan, Russia

Charge transfer, band-like transport, and magnetic ions at F₁₆CoPc/rubrene interfaces

Y. Krupskaya, F. Rückerl, M. Knupfer, A. F. Morpurgo¹

Abstract: Organic semiconductors offer great flexibility to control electronic states of interfacial electronic systems. Here we present a first step in realizing organic charge transfer interfaces that combine both electrical conductivity and magnetism. We have performed a detailed investigation of the F₁₆CoPc/rubrene interface by means of charge transport measurements, Hall effect, scanning Kelvin probe microscopy and photoemission spectroscopy. We found that the amount of charge transfer across the F₁₆CoPc/rubrene interface is high enough to cause significantly enhanced electrical conductivity and the band-like transport in rubrene crystals at the interface. Moreover, photoemission studies have shown that the charge transfer at the F₁₆CoPc/rubrene interface involves electronic orbitals of the magnetic Co ions in the phthalocyanine molecules. Thus, F₁₆CoPc/rubrene is the first organic interface where the charge transfer responsible for the interfacial conductivity fully involves the metal Co core of the phthalocyanine molecules.

Charge transport at the interface

F₁₆CoPc/rubrene interface devices were formed on a polydimethylsiloxane (PDMS) substrate. First a rubrene single crystal (grown by physical vapor transport) was laminated on PDMS and then a 70 nm F₁₆CoPc film was evaporated (under high vacuum conditions) on top of the crystal. In order to maintain its quality, the rubrene crystal was kept at room temperature throughout the deposition of the evaporated film. As a result, the morphology of the F₁₆CoPc film was expected to be far from ideal, as indeed indicated by atomic force microscopy (AFM) measurements showing F₁₆CoPc films with rather rough surfaces, consisting of small grains with irregular orientation. Electrical contacts to the interface were realized manually using conducting carbon paste, following a strategy adopted earlier to perform transport measurements on different organic single crystal interfaces [1]. An optical microscope image of one of the devices investigated is shown in Fig. 1a.

Charge transport at F₁₆CoPc/rubrene interfaces was measured in vacuum using a multi-terminal device configuration by means of an Agilent Technology E5270B parameter analyzer. The I-V curve of an F₁₆CoPc/rubrene interface (Fig. 1b) exhibits linear charac-

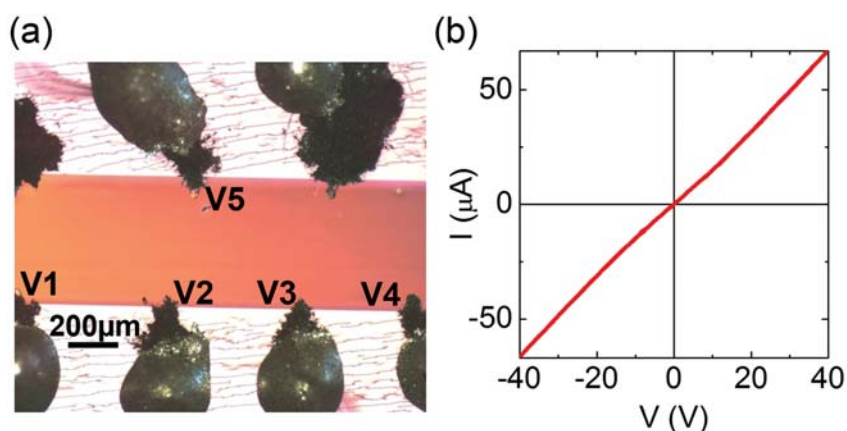


Fig. 1: (a) Optical microscope image of an F₁₆CoPc/rubrene interface device. The rubrene single crystal is covered by a 70 nm F₁₆CoPc film and contacted with conducting carbon paste. Contacts V1/V4 were used to source and drain current, contacts V2/V3 to measure the voltage and perform four-terminal resistance measurements, and contacts V2/V5 for Hall voltage measurements. (b) Room temperature I-V curve for the F₁₆CoPc/rubrene device measured in a four-terminal configuration.

teristics and indicates that the measured conductance is many orders of magnitude larger than the conductance of the individual materials forming the interface. Specifically, the room temperature resistivity for all measured devices was found to be in the range of 260–350 k Ω /square. Moreover, the results of temperature dependent transport measurements (Fig. 2a) show a decrease in resistivity upon cooling, indicating that transport at F₁₆CoPc/rubrene interfaces exhibit clear signatures of the intrinsic band-like regime, down to $T \sim 130$ K.

Hall effect measurements performed on the same devices (Fig. 2b) show that charge transport in the F₁₆CoPc/rubrene interface is dominated by holes in rubrene crystals, as it may have been expected, since the charge carrier mobility in organic films is generally significantly lower than in crystals. Indeed, in our F₁₆CoPc/rubrene interfaces the electrons in F₁₆CoPc can be considered as fully localized and their contribution to transport ignored. This is confirmed by spectroscopic data discussed below. From the measured Hall resistance and longitudinal resistivity we extract the values of the interfacial hole density ($n = 1.6 \cdot 10^{13} \text{ cm}^{-2}$) and mobility ($\mu = 1.2 \text{ cm}^2 \text{ V}^{-1} \text{ s}^{-1}$) for our F₁₆CoPc/rubrene interfaces. With the exception of TTF-TCNQ [1], the interfacial hole density in F₁₆CoPc/rubrene is the highest among all studied organic charge transfer interfaces [1–6].

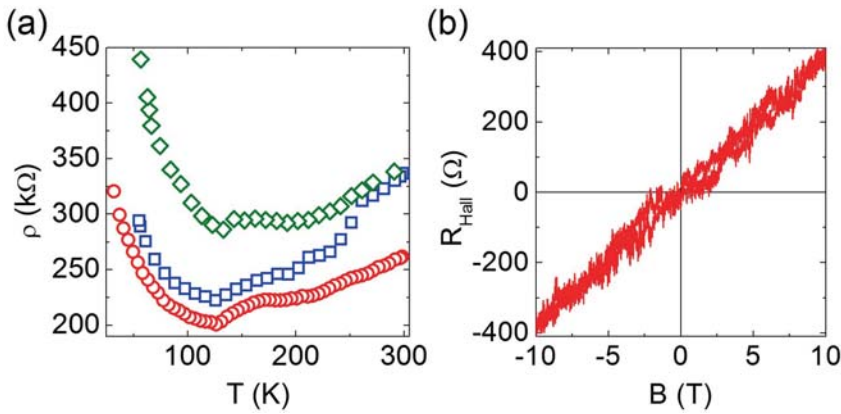


Fig. 2: (a) Temperature dependence of the resistivity of three different, nominally identical, F₁₆CoPc/rubrene devices. (b) Hall resistance vs. applied magnetic field measured at room temperature.

To gain a better microscopic understanding of the energetics of F₁₆CoPc/rubrene interfaces, we have performed scanning Kelvin probe microscopy (SKPM) [7] experiments. Here we have measured the contact potential difference between rubrene and F₁₆CoPc, which corresponds to the difference ΔE_F between the chemical potentials in the two materials. The measurements were performed on samples consisting of a 70 nm F₁₆CoPc film evaporated onto a SiO₂ substrate, onto which a rubrene crystal was subsequently laminated. Measuring the difference in contact potential by scanning across the F₁₆CoPc/rubrene interface is particularly effective, because it enables the contact potential to be measured directly independently of the work function of the tip. A representative SKPM image and a line-scan contact potential measurement are shown in Figs. 3a and 3b, respectively. The difference in the chemical potentials of the F₁₆CoPc film and the rubrene crystal, ΔE_F , can be extracted directly from the data and is found to be approximately 290 meV (Fig. 3b). This value is larger than the one obtained for F₄-TCNQ/rubrene, $\Delta E_F \sim 250$ meV, the largest in the F_x-TCNQ/rubrene family of interfaces [6]. Since a larger value of ΔE_F is normally conducive to a larger charge transfer, the outcome of SKPM experiments support the conclusions obtained from the transport measurements, namely that the charge transfer at the F₁₆CoPc/rubrene interface is larger than the charge transfer at any of interface of the F_x-TCNQ/rubrene family [6].

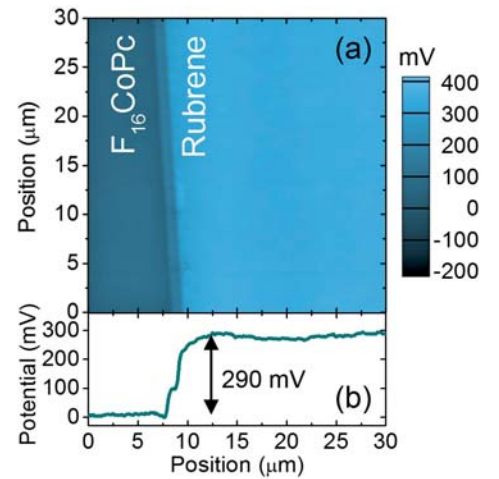
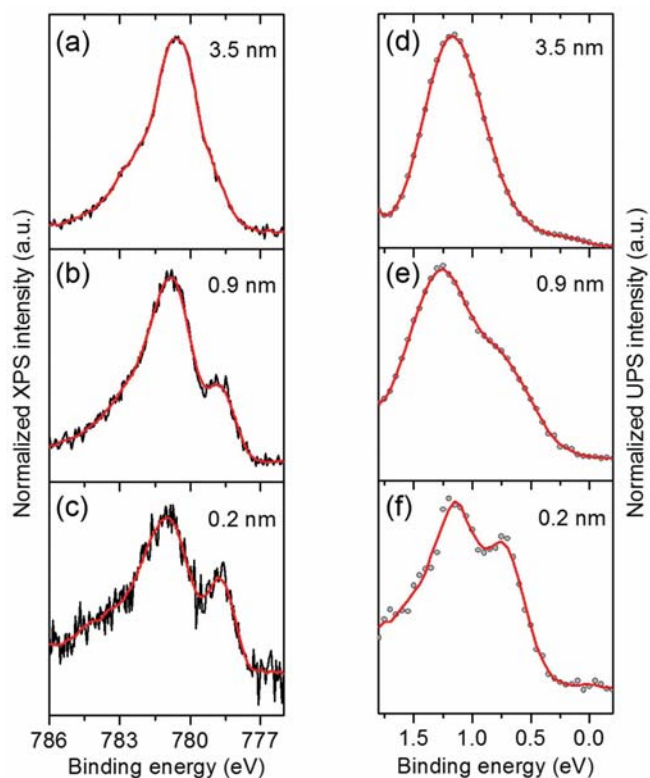


Fig. 3: Scanning Kelvin probe microscopy measurements on an F₁₆CoPc/rubrene heterostructure. The results exhibit a clear step in both the topography (not shown) and in the contact potential (a) as the tip is moved from the surface of F₁₆CoPc film (left side of the images) to rubrene crystal (right side of the images). (b) Line-cut extracted from the SKPM image (a); the step corresponds to the difference in contact potential measured on the F₁₆CoPc and the rubrene.

Fig. 4: **Left:** Photoemission core level (XPS) spectra at the Co $2p_{3/2}$ core level of a $F_{16}CoPc$ /rubrene film heterostructure with different $F_{16}CoPc$ film thickness: 3.5 nm **(a)**, 0.9 nm **(b)** and 0.2 nm **(c)**. An additional feature related to the interfacial states appears in the spectrum of the thinner $F_{16}CoPc$ film. **Right:** Valence band photoemission (UPS) spectra of the valence region of $F_{16}CoPc$ with different film thickness: 3.5 nm **(d)**, 0.9 nm **(e)** and 0.2 nm **(f)**. The contribution of a pure rubrene film was subtracted from the spectra. The second peak in the spectrum of the thinner $F_{16}CoPc$ film corresponds to the $3d_{z^2}$ orbital of the phthalocyanines Co center that is empty in the normal state and gets filled due to the charge transfer from rubrene molecules.



Photoemission spectroscopy

The electronic states of $F_{16}CoPc$ /rubrene interfaces have been probed by photoemission (PES) spectroscopy in the valence as well as the core level region. Since straightforward photoemission spectroscopy on bulk rubrene crystals are prevented by charging effects [8], measurements were performed on $F_{16}CoPc$ /rubrene thin film interfaces. These interfaces were prepared using a gold (100) single crystal as a substrate, onto which a 5 nm rubrene film was deposited, followed by an $F_{16}CoPc$ film. Samples with different nominal thickness of the $F_{16}CoPc$ film ranging from 0.1 nm to 3.5 nm were investigated in order to identify particular changes that represent the interface region.

Fig. 4 summarizes the results of the photoemission studies of $F_{16}CoPc$ /rubrene interfaces with different thicknesses of the $F_{16}CoPc$ layer. Panels a-c of Fig. 4 depict the Co $3p_{3/2}$ core level emission spectra for three selected layer thicknesses. The spectrum obtained for the thick $F_{16}CoPc$ layer of 3.5 nm (Fig. 4a) consists of a single, slightly asymmetric line which represents the two valent Co(II) in the center of $F_{16}CoPc$; the width and the shape of the spectral feature is determined by the Co $2p_{3/2}$ multiplet [9]. In the case of thinner $F_{16}CoPc$ layers we observe changes in the Co $2p_{3/2}$ spectrum (Fig. 4b). Here, a second spectral feature appears at lower binding energies, which corresponds to the $F_{16}CoPc$ molecules at the interface to rubrene. With further reducing the thickness of the $F_{16}CoPc$ film (i.e. increasing the contribution of the interfacial $F_{16}CoPc$ molecules to the measured signal) we see a clear increase of the relative intensity of the second feature (Fig. 4c). These observations are in good agreement with a number of studies where the interaction of Co-phthalocyanines with metal substrates has been reported [10–12]. The second feature in the spectrum arises due to a strong interaction at the interface that leads to a charge transfer and a consequent change in the valence of the Cobalt ion in $F_{16}CoPc$ to Co(I) [10, 11, 13]. Thus, our results demonstrate that at the $F_{16}CoPc$ /rubrene interface the Co center of the $F_{16}CoPc$ is reduced due to a charge transfer from the rubrene molecules.

Photoemission spectra of the valence region of $F_{16}\text{CoPc}$ for three different layer thicknesses are presented in panels d-f of Fig. 4. The data are fully consistent with the results obtained from the core level presented above. For a thick $F_{16}\text{CoPc}$ layer (Fig. 4d) the spectrum consists of an emission line at about 1.2 eV binding energy arising from the highest occupied molecular orbital (HOMO) of $F_{16}\text{CoPc}$ [11]. However for thinner layers, where the relative contribution to the signal from interfacial molecules is higher (Figs. 4e and 4f), an additional feature appears at lower binding energy (about 0.75 eV). This feature can be associated to the $3d_{z^2}$ orbital of the phthalocyanines Co center [14] that gets filled due to the charge transfer from rubrene molecules and becomes therefore visible in PES.

Finally, the photoemission spectroscopy investigations complement our transport studies as they clearly indicate a charge transfer at the $F_{16}\text{CoPc}$ /rubrene interface concomitant with a hole doping of rubrene. Moreover, the measurements allow us to conclude that the charge transfer, which causes enhanced electrical conductivity in $F_{16}\text{CoPc}$ /rubrene, fully involves the metal Co core of the phthalocyanine molecules making this system to be the first conducting organic interface in which charge transfer involves magnetic ions.

- [1] H. Alves et al., *Nature Mat.* 7 (2008) 574.
- [2] M. Nakano et al., *Appl. Phys. Lett.* 96 (2010) 232102.
- [3] I. Gutiérrez Lezama et al., *Nature Mater.* 11 (2012) 788.
- [4] H. Alves et al., *Nature Commun.* 4 (2013) 1842.
- [5] Y. Takahashi et al., *Chem. Mater.* 26 (2014) 993.
- [6] Y. Krupskaya et al., *Adv. Funct. Mater.* 26, (2016) 2334.
- [7] D. J. Ellison et al., *J. Am. Chem. Soc.* 133 (2011) 13802.
- [8] L. J. Brillson, *Surfaces and Interfaces of Electronic Materials*, Wiley, Germany, 2010.
- [9] T. Kroll et al., *J. Chem. Phys.* 137 (2012) 054306.
- [10] F. Petraki et al., *J. Phys. Chem. C* 114 (2010) 17638.
- [11] S. Lindner et al., *Appl. Phys. A* 105 (2011) 921.
- [12] M. Schmid et al., *Surf. Sci.* 606 (2012) 945.
- [13] Z. Li et al., *Acc. Chem. Res.* 43 (2010) 954.
- [14] S. Lindner et al., *J. Chem. Phys.* 138 (2013) 024707.

Funding: DFG Research Fellowships: KR 4364/1-1 and KR 4364/2-1,
DFG Forschergruppe: FOR 1154 (KN 393/14)

Cooperation: ¹Department of Quantum Matter Physics (DQMP), University of Geneva

Valence-state reflectometry of complex oxide heterointerfaces

J. E. Hamann-Borrero, S. Macke^{1,2}, W. S. Choi^{3,4}, R. Sutarto⁵, F. He⁵, A. Radi¹, I. Elfimov¹, R. J. Green¹, M. W. Haverkort⁶, V. B. Zabolotnyy⁷, H. N. Lee³, G. A. Sawatzky¹, V. Hinkov⁷

Abstract: Development in the atomic layer by layer synthesis of transition metal oxide materials and the possibility to put dissimilar materials face-to-face at an interface has provided a vast playground for exciting emergent physics [1]. Prominent examples are the formation of a 2D electron gas at the $\text{LaAlO}_3/\text{SrTiO}_3$ interface [2] and the observation of superconductivity at interfaces of non-superconducting copper oxides [3], among others [4,5]. The nature of these new phenomena has been addressed to be closely related to reconstruction of the charge, spin and orbital states that takes place as a consequence of the local symmetry breaking at the interface. Notwithstanding, since these interfaces are normally buried deep below the samples surface, the study of their electronic and structural properties is an experimental challenge. In this regard, resonant x-ray reflectivity (RXR) provides a unique experimental tool to study such effects. It is non-destructive, interface sensitive and, since the experiment is performed at energies close to absorption edges, it yields depth resolved element specific spectroscopic information [6,7]. Using an element and valence specific description of RXR we obtain the electronic density profile of the different Co species along the polar (001) direction of a LaCoO_3 film on NdGaO_3 . Our analysis reveals a pronounced valence state reconstruction from Co^{3+} in the bulk to Co^{2+} at the surface, with an areal density close to 0.5 Co^{2+} ions per unit cell. An identical film capped with polar (001) LaAlO_3 maintains the Co^{3+} valence over its entire thickness. We interpret this as evidence for electronic reconstruction in the uncapped film, involving the transfer of 0.5 e^- per unit cell to its polar surface.

Heterostructures comprising transition-metal oxides (TMOs) exhibit a particularly rich variety of physical phenomena, which largely emerges due to the interplay between their structural, electronic and magnetic degrees of freedom, tuned by heteroepitaxial exposure and strain [4]. A prominent example is the formation of a two-dimensional electron gas at the (001) interface between the two band insulators SrTiO_3 (STO) and LaAlO_3 (LAO) [6]. Various ideas have been put forward to explain this [2,8], many of them related to the fact that ionic and heteropolar films of certain orientations consist of charged planes: this would lead to a sizable potential along the film normal (polar catastrophe), unless its polar interfaces carry opposite compensating charge. This charge can be provided by various reconstruction mechanisms [2,8], including structural distortion effects and interface stoichiometry changes. A different possibility is electronic reconstruction, the pure transfer of charge between the opposite polar interfaces [2]. In the particular LAO/STO case, such electronic reconstruction would entail the transfer of 0.5 e^- per two-dimensional unit cell (u.c.) from the LAO surface to the interface, hence leading to a Ti valence reduction and to the observed two-dimensional electron gas in the intrinsically non-polar STO. Experimentally, however, the reported LAO/STO interfacial electron concentrations vary widely and often deviate by orders of magnitude from values consistent with electronic reconstruction [9,10]. Therefore, the origin of the two-dimensional electron gas in LAO/STO remains highly debated, and microscopic evidence is required, which supports the whole concept of electronic reconstruction in polar TMO films in general.

We have found such evidence on a LaCoO_3 (LCO) film grown on NdGaO_3 (NGO), using a novel approach to resonant X-ray reflectivity (RXR). RXR is a non-destructive, element- and interface-specific technique, that directly probes the valence band electrons of the transition metal and their profile across the interface. In this new approach we have used

distinct optical constants for the different valence states of Co, as obtained from X-ray absorption spectroscopy (XAS). And used them to model their electronic density profiles by fitting experimental data.

From the fits of the resonant reflectivity data (Fig. 1) we were able to extract the element and valence depth concentration profiles of all the ionic species of the heterostructure (Fig. 2). The profiles reveal that the uncapped LCO//NGO sample exhibit a narrow Co^{2+} accumulation localized at the film surface with a full width at half maximum of 8.6 \AA ($\sim 2 \text{ u.c.}$), concomitant with a decline in Co^{3+} concentration (Fig. 2a). Importantly, the total amount of Co^{2+} , if it was confined to one monolayer, would correspond to an areal density of 0.55 ± 0.15 ions per u.c., close to half coverage. This, and the fact that we achieve our fits using Co^{2+} and Co^{3+} spectra typical for bulk cobaltates, strongly indicate that both samples maintain their crystallinity up to the LCO surface, and are not subject to chemical decomposition. By depositing a protective LAO (polar) layer on top of the LCO film, we were able to switch off the polar/non-Polar (P/NP) character of the vacuum/LCO interface in a controlled way: this moves the P/NP interface to the LAO surface, hence keeping the LCO electronic properties intact (i.e., Co^{3+}) throughout the film thickness (Fig. 2b).

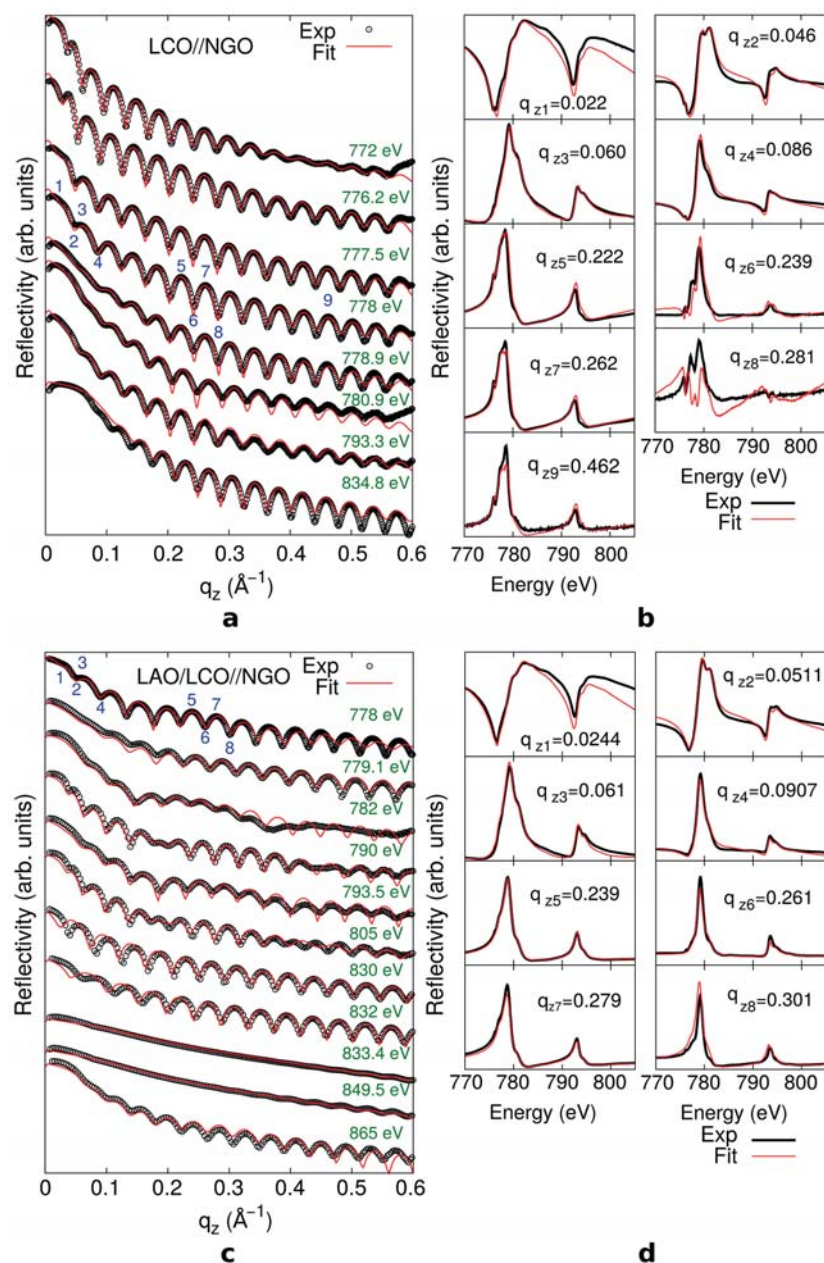


Fig. 1: RXR data and fits. Data measured in the constant-energy and constant- q_z modes (black symbols) are shown, along with the best obtained fits (red lines), based on the profiles shown in Fig. 2. (a) Constant-energy scans for the uncapped sample. (b) Constant- q_z scans for the uncapped sample. (c) Constant-energy scans for the capped sample. (d) Constant- q_z scans for the capped sample. The constant-energy data are shown on a logarithmic scale, the constant- q_z on a linear scale. For clarity, the scans have been shifted along the y axis with respect to each other in (a and c). The constant- q_z scans in (b and d) were measured at the q_{zi} positions marked with blue numbers i in (a and c).

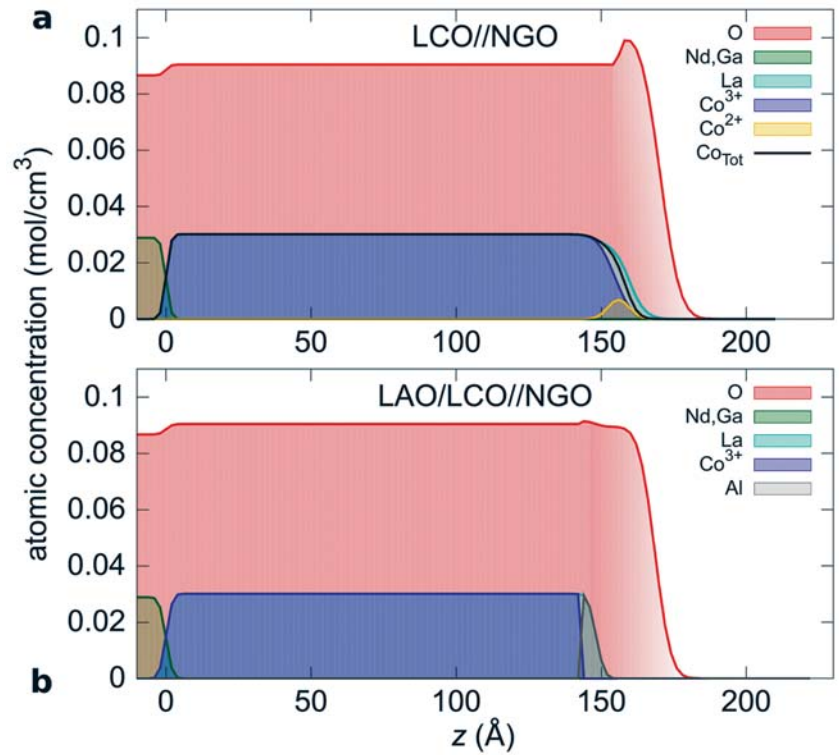


Fig. 2: Element and valence depth concentration profiles. **(a)** Profiles of the uncapped sample. **(b)** Profiles of the capped sample. The region at the surface of the samples marked in lighter red is likely to contain further light elements such as carbon, in addition to oxygen.

The reconstruction scenario applied to the LCO surface resulting from our analysis is outlined in Fig. 3a. Beginning from the surface, the atomic layer sequence is $\text{LaO}/\text{CoO}_2/\text{LaO}/\text{CoO}_2/\dots$, which nominally corresponds to a charge concentration sequence of $+e/-e/+e/-e/\dots$ per u.c. over the sample thickness, including the entire substrate. The compensation of the associated internal potential occurs resulting in effective charges of $-e/2$ and $e/2$ per u.c. at the LCO film surface and backside of the substrate.

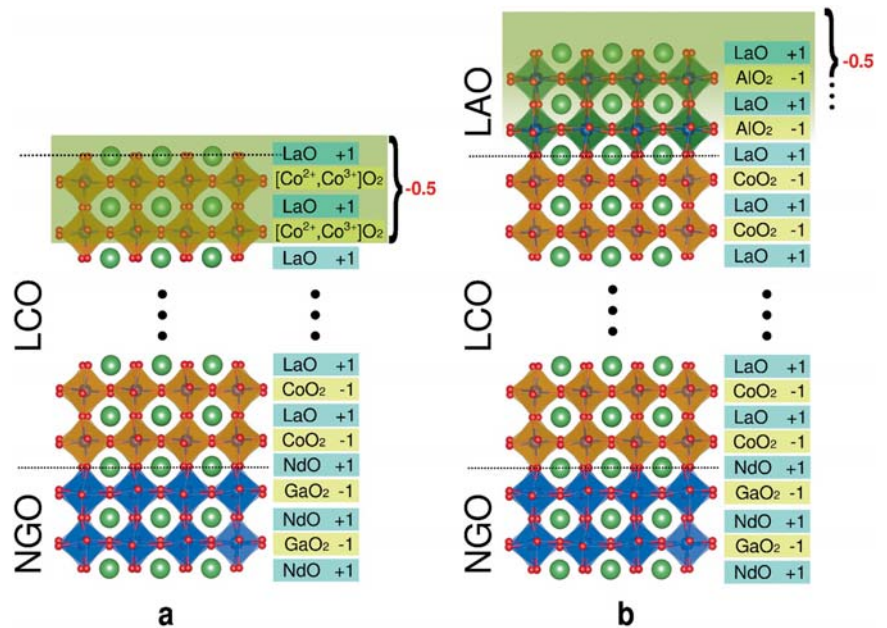


Fig. 3: Crystal structures and schematic charge and valence profiles for both samples. **(a)** Uncapped sample with the electronically reconstructed surface following from our analysis. **(b)** Sample capped with LAO. The reconstruction of the LAO surface is not known and beyond the scope of this work. A charge of $-0.5e$ proximate to the surface follows from the reconstruction.

Regarding the reconstruction mechanism, La and O have a rather stable single valence and do not exhibit bands near the chemical potential, whereas LDA+U calculations, have established that the first electron affinity state is within a Co d-band [11]. Therefore, it is energetically favorable to leave the potential uncompensated over the topmost half u.c. and accommodate the compensating charge in the buried CoO_2 layer, leading to the reconstructed surface configuration $\text{LaO} (+1)/\text{CoO}_2 (-1.5)$. This changes the Co valence to 2.5+, which is spectroscopically observed as a superposition of Co^{3+} and Co^{2+} in the XAS spectra (not shown). This electronic reconstruction scenario involving the subsurface layer is very different from the scenarios discussed for LAO/STO and related materials. Moreover, the close proximity of the observed Co^{2+} concentration to 0.5 per u.c. and the fact that it is energetically favorable to change the Co valence in a purely electronic way [11] leaves electronic reconstruction as the explanation by far most consistent with our data.

In summary, we have demonstrated that RXR is an excellent tool to study reconstruction phenomena in heterostructures comprising complex materials. We have shown direct microscopic evidence for electronic reconstruction on the polar (001) surface of LaCoO_3 . Our results indicate that LCO films are dominated by Co^{3+} and that Co^{2+} is limited to the surface: this sets stringent boundary conditions for the interpretation of ferromagnetism in LCO thin films [12] and powders [13]. It suggests that Co^{3+} spin-state transitions in the bulk drive the ferromagnetism and excludes schemes involving the presence of Co^{4+} at the surface [13].

- [1] J. Chakhalian, et al. *Nat. Mater.*, **11**, 92, (2012)
- [2] A. Ohtomo, H.Y. Hwang, *Nature* **427**, 423 (2004)
- [3] A. Gozar, et al. *Nature*, **455**, 782 (2008)
- [4] H.Y. Hwang, et al. *Nat. Mater.*, **11**, 103 (2012)
- [5] P. Zubko, et al. *Annu. Rev. Cond. Mat. Phys.*, **2**, 141 (2011)
- [6] M. Zwiebler, et al. *New J. Phys.*, **17**, 083046, (2015)
- [7] S. Macke, et al. *Adv. Mater.*, **26**, 6554, (2014)
- [8] Z. Q. Liu, et al. *Phys. Rev. X* **3**, 021010 (2013)
- [9] G. Herranz, et al. *Phys. Rev. Lett.* **98**, 216803 (2007).
- [10] M. Basletic, et al. *Nat. Mater.* **7**, 621 (2008).
- [11] R. Kurian, et al. *J. Phys.: Condens. Matter* **24**, 452201 (2012).
- [12] C. Pinta, et al. *Phys. Rev. B* **78**, 174402 (2008).
- [13] J.-Q. Yan, et al. *Phys. Rev. B* **70**, 014402 (2004).

Funding: German Research Foundation DFG (HA6470/1-2); German Research Foundation DFG (SFB 1170 ‘ToCoTronics’-project C04-); Canadian organisations NSERC, CFI and CRC; National Research Foundation of Korea (NRF-2014R1A2A2A01006478); The Canadian Light Source is funded by the Canada Foundation for Innovation, the Natural Sciences and Engineering Research Council of Canada, the National Research Council Canada, the Canadian Institutes of Health Research, the Government of Saskatchewan, Western, Economic Diversification Canada and the University of Saskatchewan; U.S. Department of Energy, Office of Science, Basic Energy Sciences, Materials Sciences and Engineering Division

Cooperation: ¹University of British Columbia, Vancouver, BC, Canada; ²Max Planck Institute for Solid State Research, Stuttgart, Germany; ³Oak Ridge National Laboratory, Oak Ridge, TN, USA; ⁴Sungkyunkwan University, Suwon, Korea; ⁵Canadian Light Source, Saskatoon, SK, Canada; ⁶Max-Planck Institute for Chemical Physics of Solids, Dresden, Germany; ⁷University of Würzburg, Germany

Quantum effects at the nanoscale

Y. Chen, J. Zhang, M. Zopf, R. Keil, B. Hoefer, Y. Zhang, K. Jung, F. Ding, O. G. Schmidt

Abstract: Many of the quantum information applications rely on indistinguishable sources of polarization entangled photons. Semiconductor quantum dots are among the leading candidates for a deterministic entangled photon source, however, due to their random growth nature, it is impossible to find different quantum dots emitting entangled photons with identical wavelengths. The wavelength tunability has therefore become a fundamental requirement for a number of envisioned applications. With a novel anisotropic strain engineering technique based on PMN-PT/silicon micro-electromechanical-system, we can recover the quantum dot electronic symmetry at different exciton emission wavelengths. Our device facilitates the scalable integration of indistinguishable entangled photon sources on-chip, and therefore removes a major stumbling block to the quantum-dot-based solid-state quantum information platforms.

Wavelength-tunable entangled photons from silicon-integrated III-V quantum dots

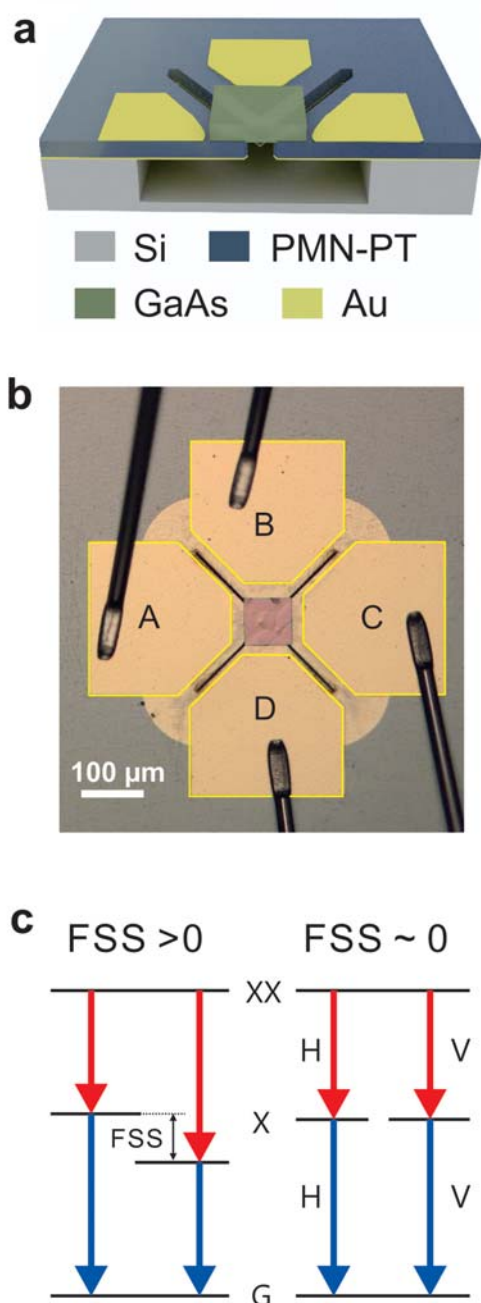
A topical challenge in quantum information processing (QIP) is the generation and manipulation of polarization entangled photon pairs [1, 2]. Spontaneous parametric-down-conversion (SPDC) and four-wave-mixing (FWM) have served as the main workhorses for these purposes in the past decade, and the implementation of a fully integrated quantum optoelectronic device is within reach by marrying these sources with chip-scale silicon photonics [3-5]. However the generated photons are characterized by Poissonian statistics, i.e. one usually does not know when an entangled photon pair is emitted. This fundamentally limits their applications in complex quantum protocols, e.g. an event-ready test of Bell's inequality and high efficiency entanglement purifications, where deterministic operations are much favoured.

We demonstrate wavelength-tunable entangled photon sources based on III-V QDs integrated on a silicon chip [6]. It has been predicted that the FSS of QDs can be effectively eliminated by uniaxial stresses when the strain axis is closely aligned along the [110] or [1-10] direction. With the application of a pair of orthogonal uniaxial stresses, it might be possible to eliminate the FSS with the emission wavelength on demand. To this end, we design and fabricate a device consisting of QD-embedded nanomembranes suspended on a four-legged thin-film PMN-PT ($[\text{Pb}(\text{Mg}_{1/3}\text{Nb}_{2/3})\text{O}_3]_{0.72}[\text{PbTiO}_3]_{0.28}$) actuator integrated on a silicon substrate. With the combined uniaxial stresses along two orthogonal directions, we are able to keep the FSS strictly below 1 μeV while shifting the exciton wavelength/energy by more than 3000 times of the QD radiative linewidth. High fidelity entangled photon emission is demonstrated when the FSS is tuned to below 1 μeV . Therefore wavelength-tunable entangled photons are generated on chip with a single device footprint of a few hundred microns.

We use the industrial transfer printing and die bonding techniques to realize the novel integration of III-V, PMN-PT and Si. A 15 μm PMN-PT thin film bonded on a silicon substrate is employed here to realize novel micro-electromechanical system (MEMS) devices with sophisticated functionalities on chip (Fig. 1). Arrays of QD-containing GaAs nanomembranes, each $80 \times 80 \mu\text{m}^2$ in size, were then transferred onto the PMN-PT MEMS with four actuation legs (Figs. 1a, b). The crystal axes [1-10] and [110] of the GaAs nanomembrane were carefully aligned along the designed stress axes of the actuators.

Fig. 1: Wavelength-tunable polarization entangled photon sources integrated on silicon.

(a) MEMS devices for anisotropic strain engineering of III-V QD based quantum light sources. (b) Micrograph showing the zoom-in of a completed device. Electrical contacts are made on the four legs A-D. The center region is a bonded QD-containing nanomembrane. (c) Illustration of the fine structure splitting (FSS) in a QD.



The uniaxial strain tuning behaviour of FSS is determined by the QD principal axis with respect to the uniaxial stress direction. For a QD whose principal axis is closely aligned with the stress direction, the FSS can be effectively eliminated. An example of the FSS tuning behaviour for such an aligned QD is given in Fig. 2a. The uniaxial stress tuning is done by sweeping the voltage V_{AC} from 0 V to 100 V on one pair of legs, while fixing the voltage V_{BD} at 0 V on the other pair of legs. With increasing V_{AC} the FSS first decreases monotonically to a minimum value and then increases. At V_{AC} of about 73 V the FSS is completely eliminated. The phase θ , which indicates the angle (see inset of Fig. 2a) between the exciton polarization and the [1-10] crystallographic direction of GaAs, undergoes a sharp phase change of 90 degrees.

Two dimensional scanning on the two pairs of legs, by sweeping both V_{BD} and V_{AC} is then performed. In Fig. 2b we show the results in a three dimensional plot. The astonishing result is that, with this four-legged device providing orthogonal uniaxial stresses, multiple zero FSS points with different exciton wavelength λ_x (energy E_x) can be achieved. At different V_{BD} , the electronic symmetry of quantum dot can be always recovered by sweeping V_{AC} and the FSS is erased. The dashed line on the bottom plane of the plot indicates the combinations of (V_{AC}, V_{BD}) at which the FSS reaches its minimum. A linear relationship is found for the ratio of voltage changes $\Delta V_{AC}/\Delta V_{BD}$. In terms of the applied stresses (X, Y), indeed, an effective two-level model for the FSS of QDs with exciton polarization closely aligned to principal stress axes predicts a zero FSS with a linear relationship $\Delta X/\Delta Y$ and confirms this experimental finding.

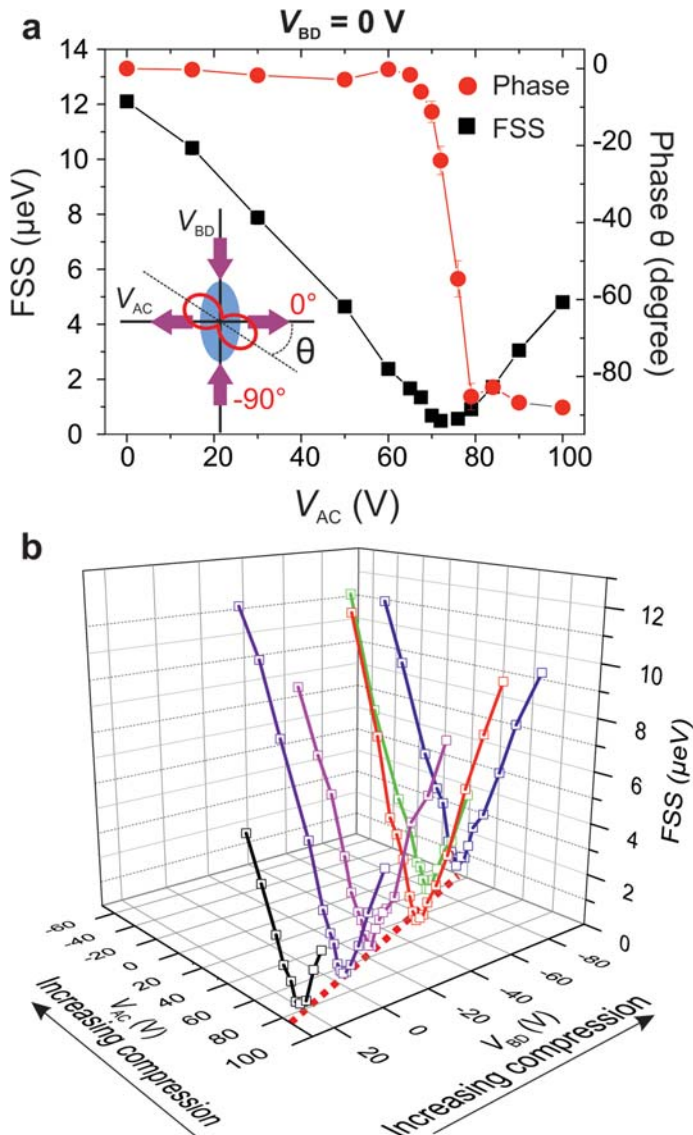


Fig. 2: Anisotropic strain engineering of a QD under orthogonal uniaxial stresses. **(a)** FSS and phase θ are plotted as a function of the voltage V_{AC} at a fixed voltage V_{BD} of 0 V. The inset in (a) gives the definition of θ . **(b)** The changes in FSS when both V_{BD} and V_{AC} are scanned. The dashed line on the bottom plane indicates a linear shift of the voltage combination (V_{AC}, V_{BD}) at which FSS reaches the minimum values.

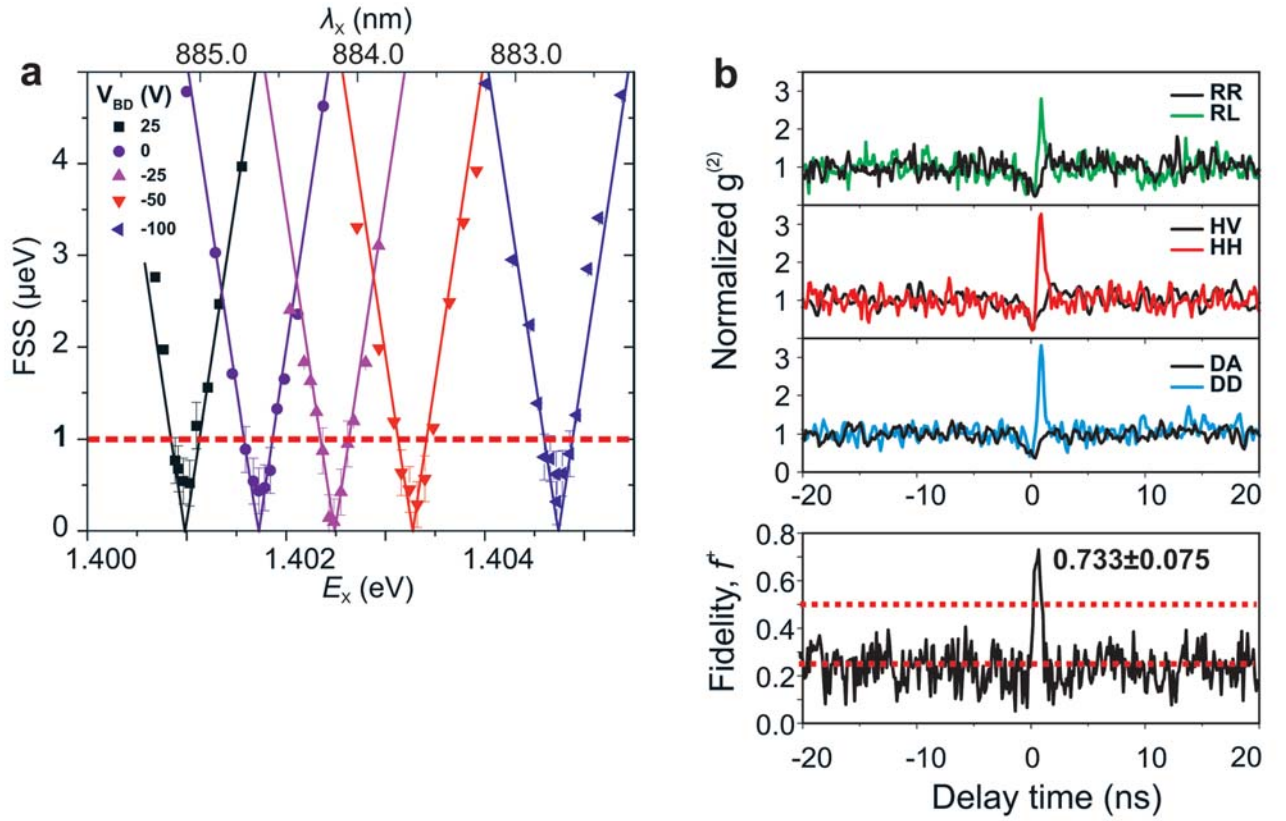


Fig. 3: Independent tunability of exciton wavelength and FSS. **(a)** FSS is plotted as a function of the exciton wavelength λ_x (energy E_x), at different values of V_{BD} . The solid lines are theoretical fits. **(b)** Polarization correlation spectroscopy are performed on the biexciton and exciton photons, when the QD FSS is tuned to zero.

We have performed the polarization cross-correlation spectroscopy on a brighter QD embedded inside another device on the same chip. The FSS is tuned to around zero ($0.21 \pm 0.20 \mu\text{eV}$) to demonstrate the polarization entanglement, and the data are presented in Fig. 3b. A key criterion for entanglement is the presence of a correlation independent of the chosen polarization basis, i.e. $|\psi^+\rangle = 1/\sqrt{2}(|H_{xx}H_x\rangle + |V_{xx}V_x\rangle) = 1/\sqrt{2}(|D_{xx}D_x\rangle + |A_{xx}A_x\rangle) = 1/\sqrt{2}(|R_{xx}L_x\rangle + |L_{xx}R_x\rangle)$, with D, A, R, L denoting the diagonal, anti-diagonal, right-hand circular and left-hand circular polarizations. Clear photon bunching, with a normalized second order correlation function $g^2(\tau) > 3$, can be observed for the co-polarized HH and DD photons, whereas in the circular basis the bunching occurs for the cross-polarized RL photons. The entanglement fidelity f^+ to the maximally entangled Bell state can be determined from the measurements in Fig. 3b, see Methods. The peak near the zero time delay yields a fidelity f^+ of 0.733 ± 0.075 without any background subtraction, which exceeds the threshold of 0.5 for a classically correlated state by more than 3 standard deviations. The above results are in line with previous experimental and theoretical works, and verify that highly entangled photons can be generated with our device with large wavelength tunability.

In summary, we have experimentally realized wavelength-tunable entangled photon sources on a III-V/Si chip, which represents an important step towards scalable entangled photon sources based on III-V QDs. The reported device will play an important role not only in building a solid-state quantum network based on entanglement swapping and quantum memories, but also in building advanced quantum photonic circuits for on-chip QIP applications. The MEMS based device features the advantages of sophisticated anisotropic stress control on chip. We envision that it will inspire many other topics in quantum and nano-technologies, and an interesting perspective is to replace the nanomembranes with the emerging two-dimensional materials and to study the strain-dependent photonic and electronic properties.

- [1] J. Pan et al., Rev. Mod. Phys. 84 (2012) 777.
- [2] P. Kwiat et al., Phys. Rev. A 60 (1999) 773.
- [3] J. O'Brien et al., Nature Photon. 3 (2009) 687.
- [4] A. Politi et al., Science 320 (2008) 646.
- [5] J. Silverstone et al., Nature Photon. 8 (2014) 104.
- [6] Y. Chen et al., Nature Commun. 7 (2016) 10387.

Funding: BMBF: Q.Com-H (16KIS0106), European Union Seventh Framework Programme 209 (FP7/2007-2013) under Grant, Agreement No. 601126 210 (HANAS)

Spin-orbit coupling in tubular photonic microcavities

L. B. Ma, S. L. Li, V. M. Fomin, M. Hentschel¹, J. B. Götze², Y. Yin,
E. Saei Ghareh Naz, V. Engemaier, O. G. Schmidt

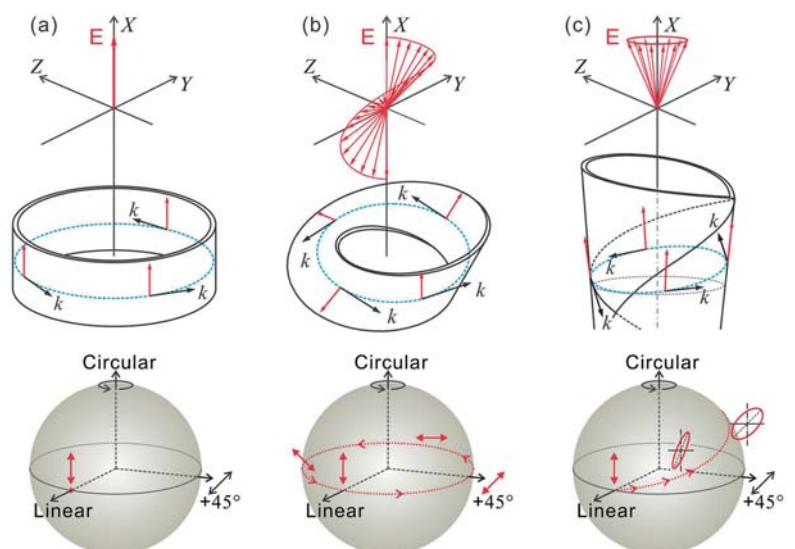
Abstract: In a non-trivial evolution in parameter space, light can acquire a geometric phase which plays an important role in a variety of physical contexts. However, in previous reports the evolution occurred exclusively on the macro-scale, which prevents the application in on-chip integrated photonics. Moreover, the concept of optical Berry phases has been generalized in the context of non-Abelian and non-cyclic evolution. Despite substantial efforts in theory, the experimental realization of non-Abelian evolution of light, in particular with non-cyclic Berry phase, has received little experimental verification. Here, we enable optical spin-orbit coupling in asymmetric microcavities and experimentally observe non-cyclic optical geometric phases acquired in non-Abelian evolutions. This work is interesting from both a fundamental and experimental point of view, and implies promising applications which would rely on manipulating photons in on-chip integrable quantum devices.

Spin-orbit coupling enabled in microtubular cavities

In optics, the spin-orbit coupling leads to the occurrence of geometric phase (also known as Berry phase) [1-4] which plays an important role in a surprisingly large number of physical contexts. The geometric phase of light depends only on the topology of the physical system evolution in parameter space, and thus is independent of the device material and photon energy. Photons propagating along a helically wound fiber represented the first physical system exploited to verify the existence of the Berry's geometric phase [4]. In optical microcavities (see Fig. 1(a)), which confine light to small volumes by resonant circulation along a closed trajectory, the optical spin-orbit interaction is irrelevant due to the trivial evolution of light, which results in ordinary discrete eigenmodes in optical WGM resonators.

However, optical spin-orbit coupling can be induced in specially designed cavity structure such as a Möbius strip. In the optical resonant circulation, the transverse electric field twists around during the propagation in the strip (see Fig. 1(b)). In this way, an effective orbital angular momentum (OAM), similar to that of an optical vortex [5], is generated for the spin-orbit coupling. The spin-orbit coupling leads to the occurrence of a geometric phase π . This extra phase leads to a half-integer number of waves for constructive interferences along a closed-loop trajectory, which has been revealed in classical Möbius-ring resonators [6]. Similar to the previously reported helical waveguides, this behavior represents an Abelian evolution.

Fig. 1: Optical spin-orbit coupling in WGM microcavities (top panel) and the corresponding polarization evolution on the Poincaré sphere (bottom panel). (a) In-plane polarized light does not provide orbital angular momentum in a symmetric ring resonator due to the unchanged electric field (**E**) vector with respect to the wave vector **k**, which results in a stationary point on the Poincaré sphere. (b) In a Möbius-ring resonator, the twisted electric field **E** along the Möbius strip causes a varying orbital angular momentum for spin-orbit coupling, which results in a cyclic evolution on the Poincaré sphere. (c) An effective orbital angular momentum along *X* is generated due to the rotation of the major axis of the electric field **E** regulated by the cone-shaped tube wall of an anisotropic medium, allowing for an interaction with the spin angular momentum, which results in a non-cyclic evolution on the Poincaré sphere. The variations of the major polarization axis of the field **E** (red arrows) are shown with respect to the laboratory coordinate frame (*XYZ*). The blue dashed lines represent light trajectories, while the red dotted lines represent the polarization evolution trace on Poincaré sphere.



Recently, we experimentally realized spin-orbit coupling of light in an on-chip cone-shaped microtube resonator. When resonant light propagates in the thin-walled microtube, the electric field vector rotates around the tube axis due to the cone-shape of the microtube (see Fig. 1(c)). This rotation generates an effective OAM along the tube axis [5]. In the cone-shaped tubes the resonant trajectory slightly tilts out of plane to reduce the optical path according to Fermat's principle. It is this tilted trajectory that causes the SAM to be not orthogonal to the OAM and which, in turn, enables the coupling between spin and orbital degree of freedom. In addition, the resonant light experiences an anisotropic refractive index in the asymmetric tube. Theoretical investigation has predicted that spin-orbit interacting light in a weakly anisotropic medium can experience a non-Abelian evolution [7], that is, an evolution for which there are no normal modes leading to a continuous transfer between any chosen basis states.

Occurrence of optical Berry phase and mode conversion in non-Abelian evolution

It is well known that the resonant light in WGM microcavities is either transverse magnetic (TM) or transverse electric (TE) linearly polarized [8]. For symmetric microtubes, the measured electric field of the light is linearly polarized and oriented parallel to the tube axis for the TM modes. However, in cone-shaped microtube cavities the resonant light is no longer linearly polarized. Figure 2 shows the intensity maps for the linearly (Lp) and elliptically polarized (Ep) modes as a function of the orientation angle (0 to 360°), which were respectively measured from a symmetric and an asymmetric tube. In the intensity map measured from the symmetric tube, the polarization state is clearly shown to be linearly polarized along the tube axis. In the asymmetric tube case, the varying but unbroken polarization trace is characteristic for elliptical polarization. Moreover, the major axis of the ellipse, or in other words the polarization orientation, is found to tilt away from the tube axis. The polar plots in Fig. 2(c) clearly reveal the eccentricity and the tilt angle ($\phi \sim 44.5^\circ$) of one of the measured polarization states after evolution in the asymmetric microtube cavity. These unusual phenomena go beyond the conventional knowledge of optical WGM resonances in microcavities and can be attributed to the occurrence of a geometric phase in a non-Abelian evolution of light [9].

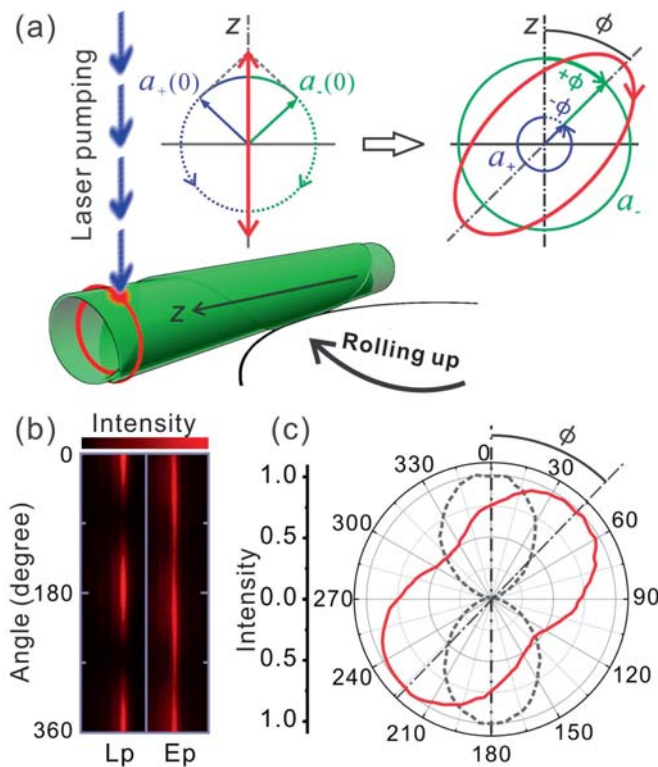


Fig. 2: Elliptical polarization state of light in a cone-shaped microtube cavity. **(a)** In a rolled-up asymmetric microtube being pumped by a laser beam (532 nm), the linearly polarized light evolves into elliptically polarized one with the major axis tilted out of (with an angle ϕ) the tube axis. **(b)** Resonant mode intensity maps of a linear polarization (Lp) state measured from a symmetric tube where spin-orbit interaction is absent and an elliptical polarization (Ep) state measured in the presence of spin-orbit coupling of light in an asymmetric tube. In the corresponding polar diagrams shown in **(c)** the linear polarization (dashed line) is oriented parallel to tube axis while the elliptical polarization exhibits a tilt angle ϕ with respect to the tube axis.

In the asymmetric microtube cavity, the initial state of the resonant light is linearly polarized. A linear polarization state is comprised of the right and left circular polarization components with the same probability amplitude, as schematically shown in Fig. 2(a). Due to the spin-orbit coupling, the right and left circular components acquire a geometric phase ϕ with opposite signs. In addition to the occurrence of geometric phase ϕ , mode conversion happened between the right and left circular polarization bases due to the spin-orbit coupling in non-Abelian evolution, as predicted in theory [7]. As shown in Fig. 2(a), the conversion of amplitudes between the two circular components leads to a change from a linear to an elliptical polarization, while the geometric phase causes the orientation of the major axis of the polarization to tilt by an angle (equal to ϕ) with respect to the initial orientation. Since the final output state differs from the initial one, the evolution generates a non-cyclic geometric phase. Here we show that the non-cyclic geometric phase can be readily measured by simply recording the tilt angle of the light polarization ellipse. The change of the circular bases is evidence for the lack of independent modes, which is a consequence of the intricate non-Abelian evolution.

In order to depict the evolution trace, a series of final polarization states were measured from different asymmetric tubes, in which the resonant light experiences different extents of the polarization evolution. It is found that a larger eccentricity is accompanied by a larger tilt angle (ϕ) due to their co-evolution in the asymmetric microcavities. This kind of the evolution trace can be well reproduced by previously reported theory, indicating a good agreement between the theoretical model and measurements. In addition, we have performed polarization measurements for different mode frequencies in the same tube cavity and found that the tilt angle as well as the eccentricity is independent of the wavelength. This is a clear evidence that the effect is of purely geometric, rather than dynamical origin.

In contrast to previous reports on optical spin-orbit coupling, where the right and left handed circular polarization bases are often spatially separated, here we do not observe such a spatial separation of the spin components, but rather an amplitude conversion between basis vectors during the evolution. This process is systematically shown in Fig. 3 by comparing the variation of the squared moduli of the coefficients accompanied by the tilt angle ϕ . Based on the measured results, the respective squared amplitudes for the right and left circular components are extracted. The two squared vector amplitudes vary in an opposite way and therefore result in the vector splitting of the spinning photons in a Hilbert space. The evolution traces of the two vector amplitudes can be well fitted by previously reported theoretical model, as shown in Fig. 3.

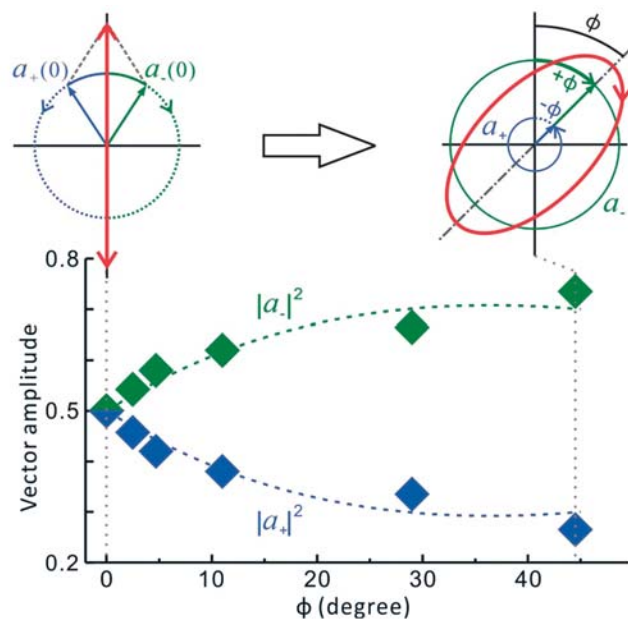


Fig. 3: Change in the magnitude of the polarization components. Measured vector amplitudes of the right (a_+) and left (a_-) components with the concurrent geometric phase ϕ . The evolution traces agree well with the theoretical model in Eq. (7) (dashed curves). Top panel shows **(left)** a linear polarization comprised of in-phase rotating right and left circular polarization components, and **(right)** geometric phase $+\phi$ (shown with bold green arc) acquired for a_- and $-\phi$ (shown with dotted blue arc) acquired for a_+ .

Our work shows that the non-cyclic geometric phase acquired in a non-Abelian evolution can be readily demonstrated in a compact optical microtube cavity. The cone-like asymmetric optical microcavities establish an ideal platform to realize spin-orbit coupling for the examination of non-trivial topological effects in the context of a non-Abelian evolution. Geometric phase and amplitude variations of components in the circular polarization basis reveal essential physical processes in a non-Abelian evolution, which is of interest for both fundamental and applied physics.

- [1] M. V. Berry, Proc. R. Soc. London Ser. A 392 (1984) 45.
- [2] M. V. Berry, Nature 326 (1987) 277.
- [3] K. Y. Bliokh et al., Nat. Photon. 2 (2008) 748.
- [4] A. Tomita et al., Phys. Rev. Lett. 57 (1986) 937.
- [5] L. Marrucci et al., Phys. Rev. Lett. 96 (2006) 163905.
- [6] D. J. Ballon et al., Phys. Rev. Lett. 101 (2008) 247701.
- [7] K. Y. Bliokh et al., Phys. Rev. A 75 (2007) 053821.
- [8] V. A. Bolaños Quiñones et al., Opt. Lett. 34 (2009) 2345.
- [9] L. B. Ma et al., Nat. Commun. 7 (2016) 10983.

Funding: Volkswagen Foundation (I/84072), U.S. Air Force Office of Scientific Research MURI program (Grant FA9550-09-1-0550), DFG priority program FOR 1713, China Scholarship Council (No. 2008617109 and 201206090008), National Science Foundation of China (Grant No. 11104343), Alexander von Humboldt Foundation

Cooperation: ¹TU Ilmenau, ²Max Planck Institute for the Physics of Complex Systems TU Chemnitz

Josephson Currents Induced by the Witten Effect

F. S. Nogueira and J. van den Brink

Abstract: We have predicted a new type of topological Josephson effect involving type II superconductors and three-dimensional topological insulators as tunnel junctions. We have demonstrated that vortex lines induce a variant of the Witten effect that is the consequence of the axion electromagnetic response of the topological insulator: at the interface of the junction each flux quantum becomes fractionally charged, acquiring an electrical charge of $e/4$. As a consequence, an external magnetic field applied perpendicular to the junction induces an AC Josephson effect in absence of any external voltage. We derived a number of further experimental consequences and proposed potential setups where these quantized, flux induced, Witten effects may be observed.

Fundamentally, the Josephson effect refers to coherent tunneling of Cooper pairs between two superconductors (SCs), governed by the basic equations [1],

$$I_J(\Delta\phi) = I_c \sin\Delta\phi, \quad \delta_t \Delta\phi = \frac{2eV}{\hbar} \quad (1)$$

where $\Delta\phi$ is the phase difference of the superconducting order parameters across the junction and V is an external voltage. When $V=0$ we have the DC Josephson effect, while for $V \neq 0$ the Josephson current oscillates with time, leading to the AC Josephson effect.

Another fundamental Josephson effect follows by setting $V=0$ and applying an external magnetic field parallel to the junction,

$$I = I_c \frac{\phi_0}{\pi\phi} \sin\left(\frac{\pi\phi}{\phi_0}\right) \sin\left(\Delta\phi + \frac{\pi\phi}{\phi_0}\right)$$

where ϕ is the total magnetic flux through the junction and $\phi_0 = hc/(2e)$ is the elementary flux quantum.

The standard Josephson effect described by the above equations typically features an insulating tunnel junction. In the past ten years there has been growing interest on tunnel junctions consisting of a topological insulator (TI) [2]. In this case a topological Josephson effect where a coherent tunneling of charge e quasi-particles is predicted to occur. This charge e object is composed by two Majorana fermions [3], one residing at the boundary of the left SC and the other one at the right SC, thus corresponding to a topologically protected bound state. The coherent tunneling of a charge e rather than $2e$ implies a Josephson current having 4π rather than the usual 2π one [2,3]. This fractional Josephson effect is believed to offer a promising avenue towards achieving topologically protected quantum computation, where the braiding of Majorana modes is used as a means to manipulate Qbits [3].

Recently we have demonstrated that due to the axion electromagnetic response of three-dimensional TIs [4] another topological Josephson effect is possible if a magnetic field is applied *perpendicular* to the junction, and the SCs involved are type II ones [5]. This is easily seen by noticing that the quantum Hall response on a TI surface implies that at interface between a type II SC and a TI (assumed to be located at $z=0$) the charge and current densities are quite generally given by,

$$\rho(\mathbf{r}, z) = \frac{\sigma_H}{c} \mathbf{B}(\mathbf{r}, z=0) \cdot \hat{\mathbf{z}} \delta(z), \quad \mathbf{j} = \sigma_H (\mathbf{E} \times \hat{\mathbf{z}})$$

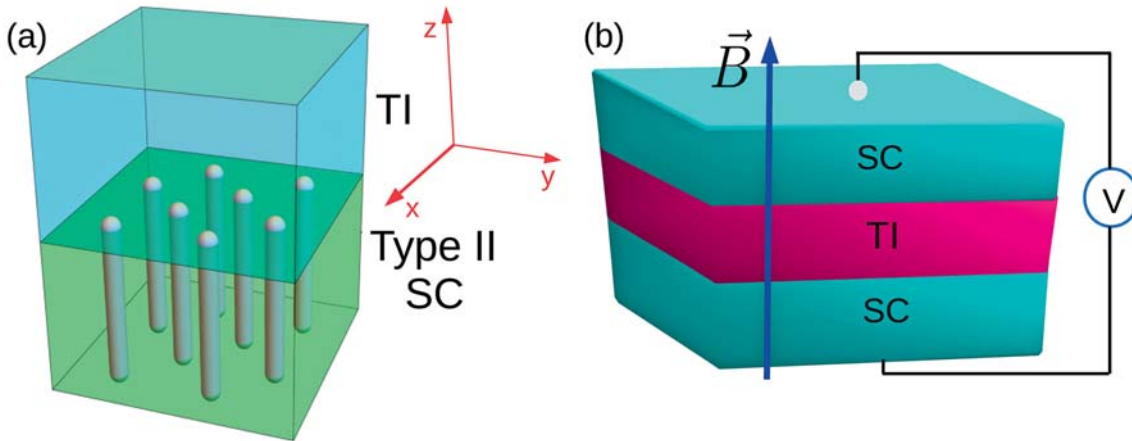
where $\sigma_H = e^2/(2h)$ is the Hall conductivity, which is known to be half-quantized for the surface of a three-dimensional TI [4]. As we have demonstrated in Ref. [5], it is now a

simple consequence of the expression for ρ that for a magnetic field of a single vortex line,

$$Q = \int d^3r \rho(\mathbf{r}, z) = \frac{\sigma_H}{c} \hat{z} \cdot \int d^2r \mathbf{B}(\mathbf{r}, z=0) = \frac{e}{4} \left(\frac{\phi}{\phi_0} \right) = \frac{ne}{4}$$

since for a single flux line $\phi = n\phi_0$ (n is an integer). The above simple result shows that a single vortex carries a fractional charge $e/4$ at the interface between a type II SC and a TI. This charge fractionalization due to vortices corresponds to a mechanism known as Witten effect [6]. In its original formulation, the Witten effect follows from an electric charge acquired by a 't Hooft-Polyakov magnetic monopole in the presence of an axion term, which in electrodynamics takes the form of a magnetoelectric term $\sim \mathbf{E} \cdot \mathbf{B}$ in the Lagrangian. In Ref. [5] we have shown that the Witten effect also works if vortex lines are used. Essentially the deep meaning behind our formulation of the Witten effect in a solid state system stems from a dual picture where vortex lines can be viewed as world-lines of magnetic monopoles. We have discussed this duality in detail in another recent publication [8].

Since a (vertical) tunnel junction SC-TI-SC made of a three-dimensional TI contains two interfaces, the charged vortices on each interface carry opposite charges, generating in this way a capacitance energy; a schematic representation of a possible experimental setup is shown in Fig. 1. The induced voltage is given by $V_{\text{ind}} = N_v e / (4C)$ [5], where C is the capacitance of the junction and N_v is the number of vortices. In view of Eq. (1) this implies an AC Josephson effect induced by the Witten effect having a frequency $\omega_W = N_v e^2 / (2\hbar C)$. Thus, due to the Witten effect, an AC Josephson effect can be induced in an SC-TI-SC junction in absence of an external voltage by simply applying a magnetic field perpendicular to the junction. By considering further quantum effects



via the path integral representation of the junction, it is possible to show that at least for small junctions the number of vortices must be quantized according to $N_v = 8m$, where m is a positive integer. Physically this means that a minimum charge of $2e$ must be attained in order to charge the junction, since each vortex carries a minimum fractional charge of $e/4$. Furthermore, if in addition an oscillating gate voltage is applied to the junction, Shapiro steps are doubly quantized according to,

$$V_{nm} = \frac{n\hbar\omega_1}{2e} - \frac{2me}{C}$$

in which case the usual Shapiro step result is obtained for $m = 0$. The above equation leads to a charge lattice, $Q_{nm} = CV_{nm}$, reminiscent of the Schwinger result [9] generalizing the Dirac quantization to dyons, namely, dipoles involving an electric and a magnetic charge.

Fig. 1: (a) Schematic view of a junction between a strong TI (e.g. Bi₂Se₃, Bi₂Te₃ or strained HgTe) and a type II SC (e.g. Nb, V, or a high T_c cuprate). The magnetic flux from the vortex lines at the interface induces a charge fractionalization due to the Witten effect. (b) Schematics of possible experimental setup to measure Josephson-Witten effect. The Witten effect acts on the vortex lines rather than on magnetic monopoles, thus creating a potential difference across the junctions.

An experimental realization of the above Josephson-Witten effect would have many important consequences. First, it would imply that vortices are fractionally charged in SC-TI-SC junctions, which at the same time would yield an indirect measurement of the half-quantized Hall conductivity, currently a practically impossible task to achieve in standard transport experiments. Second, this would provide evidence for the topological magnetoelectric effect in three-dimensional TIs [4]. Third, since vortices carry a minimal charge $e/4$, this would also provide direct evidence for anyon excitations.

- [1] M. Tinkham, *Introduction to Superconductivity*, 2nd Edition (Dover Publications, New York, 2004).
- [2] L. Fu and C. L. Kane, Phys. Rev. Lett. 100 (2008) 096407; Phys. Rev. B 79 (2009) 161408(R).
- [3] J. Alicea, Rep. Prog. Phys. 75 (2012) 076501.
- [4] X.-L. Qi, T. L. Hughes, and S.-C. Zhang, Phys. Rev. B 78 (2008) 195424.
- [5] F. S. Nogueira, Z. Nussinov, and J. van den Brink, Phys. Rev. Lett. 117 (2016) 167002.
- [6] E. Witten, Phys. Lett. B 86 (1979) 283.
- [7] G. 't Hooft, Nucl. Phys. B 79 (1974) 276; A.M. Polyakov, Zh. Eksp. Teor. Fiz. Pis'ma. Red. 20 (1974) 430 (1974) [JETP Lett. 20 (1974) 194].
- [8] F. S. Nogueira, Z. Nussinov, and J. van den Brink, Phys. Rev. D 94 (2016) 085003.
- [9] J. Schwinger, Science 165 (1969) 757.

Funding: SFB 1143, NSF grant no. CMMT 1411229 (Zohar Nussinov), MIT-Harvard Center for Ultracold Atoms

Cooperation: Zohar Nussinov, Physics Department, Washington University

Emergent magnetic ground state in iridium oxides with strong spin-orbit coupling

E. Plotnikova, S. Nishimoto, V. Katukuri, V. Yushankhai, H. Stoll, U. Roessler, M. Daghofer, I. Rousochatzakis, K. Wohlfeld, L. Hozoi, J. van den Brink

Abstract: The discovery that spin-orbit coupling (SOC) can induce topologically protected conducting states on the edge of the insulating materials has in recent years revived interest in SOC materials. The interplay of electron-electron interaction and SOC has also received enhanced attention: On one hand, the combination was soon discovered as a promising route to alternative topologically nontrivial states, from topological Mott over fractional Chern insulators to a potential realization for Kitaev's celebrated spin-liquid phase with its anyonic excitations.

On the other hand, SOC and correlated square-lattice iridates are emerging as a sister-system to high- T_c cuprates. Thus, we considered an interplay of all three interactions – electron-electron interaction, SOC and electron-phonon coupling in a form of Jahn-Teller on a model system of square-lattice Sr_2IrO_4 . Moreover, honeycomb-lattice iridates have been identified as platforms for the much anticipated Kitaev's topological spin liquid: In this context, we studied Li_2IrO_3 , a honeycomb iridate with two crystallographically inequivalent sets of adjacent Ir sites.

Due to strong spin-orbit (SOC) coupling, in a low energy limit 5d compounds with one hole in the lowest manifold like Sr_2IrO_4 and Li_2IrO_3 can be described by a total angular momentum $j_{\text{eff}} = 1/2$.

Jahn-Teller effect in square-lattice Sr_2IrO_4 [1]

In a 3d systems with negligible SOC a single hole (or electron) has an orbital degree of freedom in addition to spin – as opposed to the single $j_{\text{eff}} = 1/2$ degree of freedom of the 5d hole. As a consequence, an analogous 3d system can not only feature orbital order in addition to magnetism, but the orbital and lattice degrees of freedom would be coupled via so called Jahn-Teller effect, i.e. a structure distortion that occurs to lift an orbital degeneracy [cf. Fig. 1(a)]. In contrast, in 5d compounds the quenching of the orbital degree of freedom by SOC removes the possibility of orbital order and would at first sight also appear to suppress Jahn-Teller effect and coupling to the lattice. However, while Jahn-Teller effect is indeed absent for the ground state consisting of $j_{\text{eff}} = 1/2$ pseudospins, see Fig. 1(b), we have shown that it leaves clear signatures in the dynamics of collective excitations into the $j_{\text{eff}} = 3/2$ sector (i.e. excitons), which can be created in resonant inelastic X-ray scattering (RIXS) and has been discussed in two recent theoretical and experimental studies [2, 3]. As seen in Fig. 1(c), the Jahn-Teller effect is here not quenched and can allow for a novel type of excitonic propagation.

We have derived an analytical microscopical model describing the motion of such an exciton coupled to the $j_{\text{eff}} = 1/2$ magnons and shown that the Jahn-Teller coupling provides an additional channel for delocalization whose signatures can be clearly distinguished from the pure superexchange scenario. Both Jahn-Teller effect and superexchange can allow the exciton to exchange place with a nearest-neighbor isospin without flipping said isospin. This creates 'faults' in the alternating order, see Fig. 3(a), and thus creates or annihilates magnons. Jahn-Teller effect however also allows for a so-called free channel of exciton propagation [see Fig. 3(b)], i.e. allows the exciton to propagate without creating 'faults' in the AFM background. The reason is that in superexchange, both the exciton and a said isospin conserve their 'spin', i.e. their j_z quantum number. In an alternating isospin order, where nearest neighbors are always of opposite j_z , this necessarily creates or removes 'defects', see Fig. 3(a), and thus magnons. The Jahn-Teller effect, in contrast, allows the exciton and the isospin to flip their quantum numbers while exchanging places and this allows for the nearest neighbor hopping of an exciton

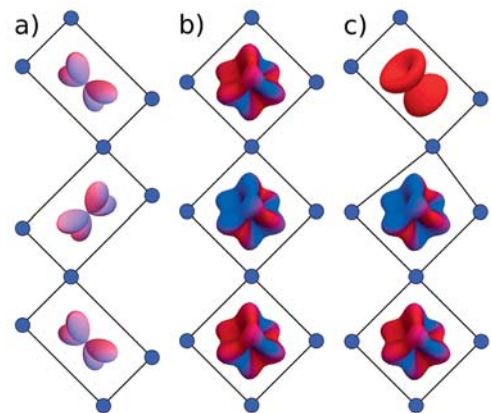


Fig.1: Cartoon picture showing the Jahn-Teller effect in systems *without* and *with* strong SOC: **(a)** Weak SOC – oxygen displacements following 'conventional' Jahn-Teller effect for the ground state with e.g. the d_{xz}/d_{yz} alternating orbital order. **(b)** Strong SOC – no oxygen displacements due to the quenched Jahn-Teller effect for the ground state with e.g. $|j = 1/2, j_z = 1/2\rangle |j = 1/2, j_z = -1/2\rangle$ alternating spin-orbital order (antiferromagnetic order of $j = 1/2$ isospins). **(c)** Strong SOC – oxygen displacements around the $|j = 3/2, j_z = -3/2\rangle$ exciton (which 'lives' in the antiferromagnetic $j = 1/2$ ground state) showing that such a system is Jahn-Teller active.

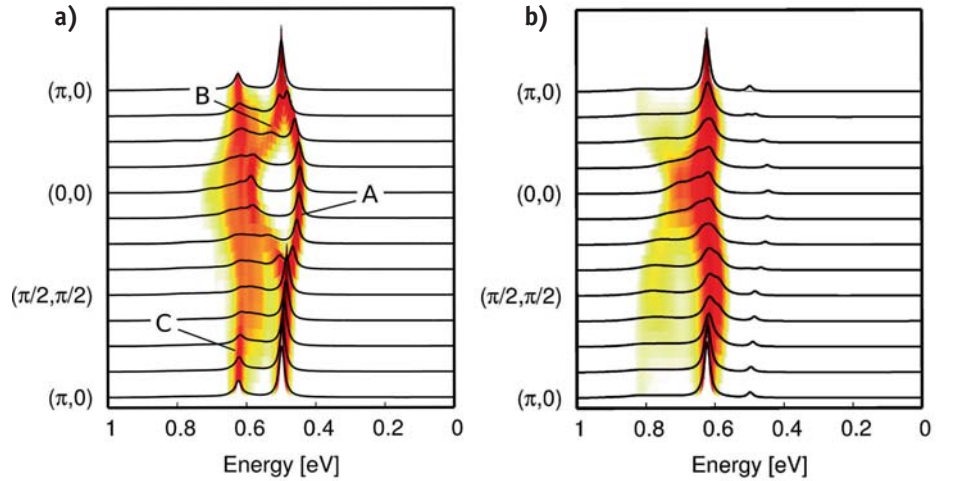


Fig. 2: Spin-orbit exciton with both superexchange and Jahn-Teller interaction calculated using the SCBA. Intensities are given for two RIXS geometries: **(a)** normal and **(b)** grazing incidence [3]. 'A', 'B', 'C' in panel (a) denote three main features of the spectrum. Superexchange parameters $J_2 = -0.33 J_1$, $J_3 = 0.25 J_1$, $W_1 = 0.5 J_1$ [3], and $W_2 = W_3 = 0$. Jahn-Teller interaction $V = 0.8 J_1$ and broadening $\delta = 0.05 J_1$. On-site energy of the exciton is $10 J_1 \approx 3/2 \lambda$ [3], crystal-field splitting between $|j_z| = 1/2$ and $|j_z| = 3/2$ states is $2.29 J_1$, and $J_1 = 0.06$ eV.

without creating magnons, i.e., a free excitonic dispersion. For a rigorous derivation of the model describing both types of exciton propagation we refer to [1].

The excitonic spectral functions are calculated taking into account 'matrix elements' depending on the angle of the incident beam [3], and shown in Fig. 2. The most striking difference to the pure superexchange scenario becomes visible in the so-called 'normal' RIXS geometry [cf. Fig. 2(a)]: a dispersive feature at around 0.4 eV (denoted as A in the figure) that has its minimal energy at $k = (0, 0)$ and disperses upward towards the zone boundary, where it merges with the B feature.

An unexplained feature with minimum at the Γ point was observed in normal-incidence RIXS experiments on Sr_2IrO_4 [3], albeit with a weaker intensity. It is worth noting that a similar peak was also seen in Na_2IrO_3 [4], where it does not merge with the higher-energy features, suggesting that the merging may be a detail specific to Sr_2IrO_4 . In contrast, the minimum at the Γ point is a robust and characteristic feature of Jahn-Teller-mediated propagation, because superexchange-driven peaks invariably have a *maximum* at the Γ point.

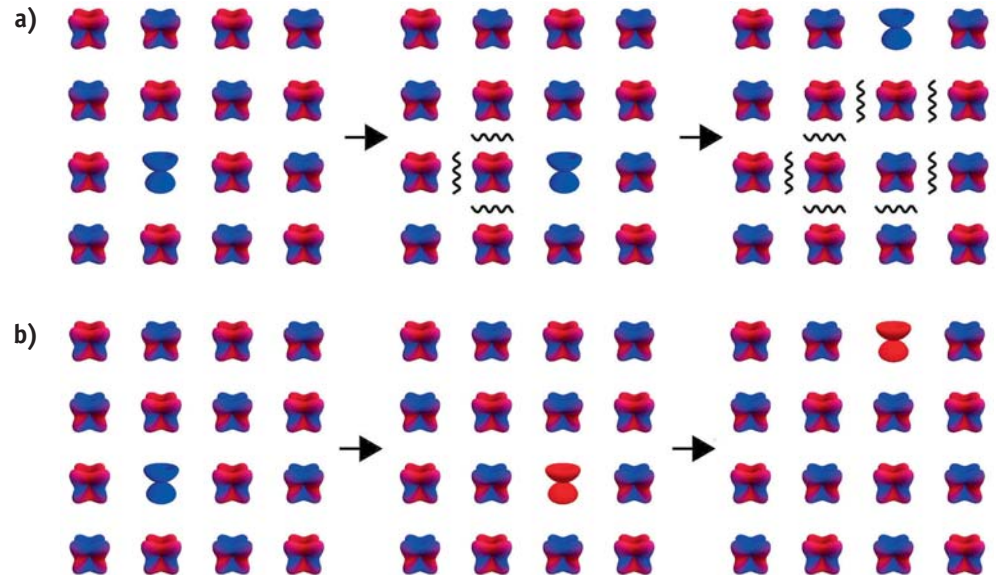


Fig. 3: Cartoon showing the two types of nearest neighbor hopping of a $j_{\text{eff}} = 3/2$ exciton in the antiferromagnetically ordered background: **(a)** Polaronic hopping (due to Jahn-Teller effect or superexchange): a $j_{\text{eff}} = 3/2$ exciton with the $j_z = -3/2$ quantum number (left panel) does not change its j_z quantum number during the hopping process to the nearest neighbor sites (middle/right panels) and thus the $j_e = 1/2$ magnons are created at each step of the excitonic hopping (wiggly lines on middle and right panels). **(b)** Free hopping (solely due to Jahn-Teller effect): a $j_{\text{eff}} = 3/2$ exciton with the $j_z = -3/2$ quantum number (left panel) hops to the nearest neighbor site and acquires $j_z = 3/2$ quantum number (middle panel). Note that in this case the $j_{\text{eff}} = 1/2$ magnons are not created in the system (middle/right panels).

Overall, we have found SOC to substantially affect the interplay of Jahn-Teller effect and superexchange. In 3d compounds with weak SOC and unquenched orbital degeneracy both act on the same microscopic degree of freedom (i.e. orbitals) and in general lead to similar signatures. In the strongly spin-orbit-coupled 5d case, however, Jahn-Teller effect (determined purely by the orbital) and superexchange (strongly affected by spin-orbit entanglement) address different microscopic degrees of freedom. Their interplay is thus far more intricate, as is coupling between ions with and without strong SOC.

Table 1: Effective exchange couplings (meV) in Li_2IrO_3 , obtained by *ab initio* wave-function quantum chemistry calculations. The values for each of the two distinct types of $[\text{Ir}_2\text{O}_{10}]$ units, B1 and B2/B3, are shown.

Effective couplings	b = B1	b = B2/B3
J_b	-19.2	0.8
K_b	-6.0	-11.6
$\Gamma_{x_b y_b}^b$	-1.1	4.2
$\Gamma_{z_b x_b}^b = -\Gamma_{y_b z_b}^b$	-4.8	2.0

Triplet dimer formation in honeycomb Li_2IrO_3 [5]

Employing *ab initio* wave-function quantum chemistry methods, we have estimated the signs and strengths of the nearest-neighbor (NN) exchange coupling parameters, namely, the Heisenberg J and Kitaev K couplings, for honeycomb iridate Li_2IrO_3 (Li213). The experimental data [6] indicate C_{2h} point-group symmetry for one set of NN IrO_6 octahedra, denoted as B1 in Fig. 4(a), and slight distortions of the Ir_2O_2 plaquettes that lower the symmetry to C_i for the other type of adjacent octahedra, labeled B2 and B3. The effective parameters were obtained as in Table 1. We have found that both J and K are ferromagnetic (FM) for the B1 links, in contrast to Na_2IrO_3 (Na213), where J is antiferromagnetic for all pairs of Ir NN's [7]. Insights into this difference between the Li and Na iridates are provided by the curves plotted in Fig. 5, displaying the dependence of the NN J on the amount of trigonal distortion for simplified structural models of both Li213 and Na213. The trigonal compression of the O octahedra translates into Ir-O-Ir bond angles larger than 90° . Interestingly, we can see that for 90° bond angle { the case for which most of the superexchange models are constructed – both J and K are very small, ≤ 1 meV.

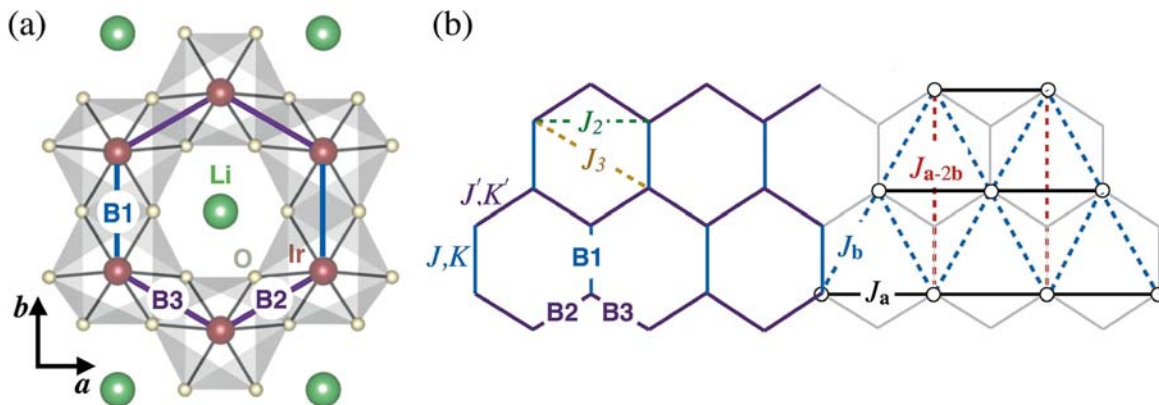


Fig. 4: (a) Honeycomb layer in Li_2IrO_3 . The two distinct sets of NN links [6] are labeled as B1 (along the crystallographic b axis) and B2/B3. The large FM interaction $J = -19.2$ meV on B1 bonds stabilizes rigid $T = 1$ triplets that frame an effective triangular lattice. (b) Representative exchange couplings for B1 (J, K), B2/B3 (J', K'), second neighbor (J_2) and third neighbor (J_3) paths on the original hexagonal grid are shown. J_δ ($\delta \in \{a, b, a-2b\}$) are isotropic exchange interactions on the effective triangular net.

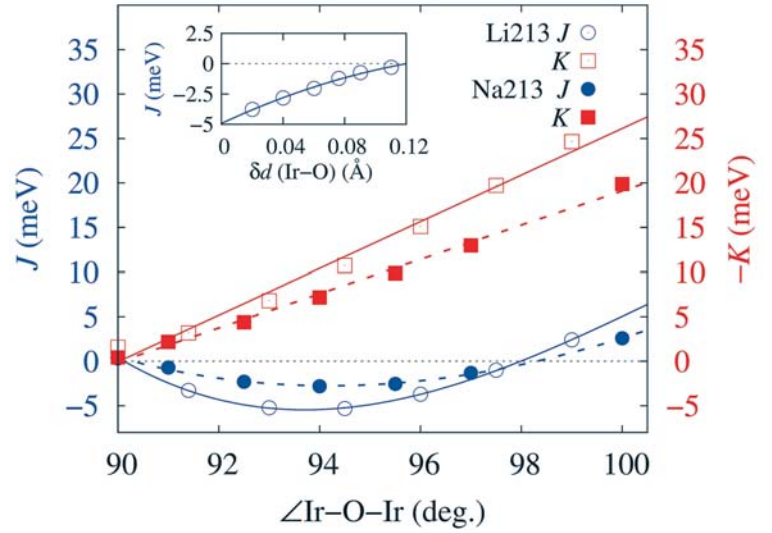
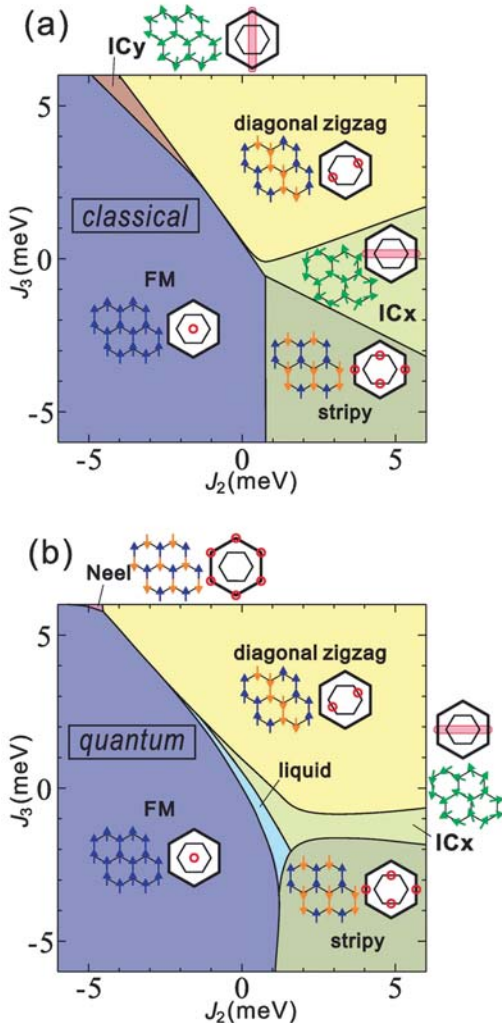


Fig. 5: Variation of the Heisenberg and Kitaev exchange couplings with the Ir-O-Ir angle in idealized honeycomb structural models. Results of spin-orbit MRCI calculations are shown, for NN Ir-Ir links in both Li213 (continuous lines) and Na213 (dashed). For each system, the NN Ir-Ir distances are set to the average value in the experimental crystal structure [6] and the Ir-O bond lengths are all the same. Consequently, $J = J'$ and $K = K'$. The variation of the Ir-O-Ir angles is the result of gradual trigonal compression. Note that $|J|, |K| \leq 1$ meV at 90° . Inset: dependence of the NN J in Li213 when the bridging O's are gradually shifted in opposite senses parallel to the Ir-Ir axis.



Having established the dominant NN couplings we now turn to the magnetic phase diagram of Li213 including the effect of second and third neighbor Heisenberg interactions J_2 and J_3 . The latter are known to be sizable and to significantly influence certain properties. However, since correlated quantum chemistry calculations for these longer-range interaction terms are computationally much too demanding, we have investigated their effect by computations for extended effective Hamiltonians that use the *ab initio* NN magnetic interactions listed in Table 1 and adjustable isotropic J_2 , J_3 exchange couplings. With strong FM exchange on the B1 bonds, a natural description of the system consists in replacing all B1 pairs of Ir 1/2 pseudospins by rigid triplet degrees of freedom. This mapping leads to an effective model of spin $T = 1$ entities on a triangular lattice [see Fig. 4(b)]. Since $T = 1$, the classical limit is expected to yield a rather accurate overall description of the phase diagram. As shown in Fig. 6(a), there exist five different regions for $|J_{2,3}| \leq 6$ meV, three with commensurate (FM, diagonal zigzag and stripy) and two with incommensurate (IC) Q (we call them ICx and ICy, with $Q = (q; 0)$ and $(0; q)$, respectively).

To establish the effect of quantum fluctuations and further test the triplet-dimer picture, we have additionally carried out exact diagonalization calculations on 24-site clusters for the original honeycomb spin-1/2 model including the effect of J_2 and J_3 . The resulting phase diagram is given in Fig. 6(b). For each phase, the real-space spin configuration and the reciprocal-space Bragg peak positions are shown. In the absence of J_2 and J_3 , the system is in a spin-liquid phase characterized by a structureless static spin structure factor $S(Q)$ that is adiabatically connected to the Kitaev liquid phase for $-K \gg J$. By switching on J_2 and J_3 , we recover most of the classical phases of the effective

Fig. 6: Phase diagram of Li213 in the J_2 - J_3 plane with the NN couplings listed in Table 1, along with schematic spin configurations and Bragg peak positions (red circles) for each phase. (a) Classical phase diagram of the effective spin $T = 1$ model on the triangular lattice. The actual ground-state configurations in the incommensurate regions ICx and ICy can be much richer than the standard coplanar helix states owing to anisotropy. (b) Quantum mechanical phase diagram for the original spin-1/2 model.

spin-1 model, including the ICx phase, albeit with a smaller stability region due to finite-size effects. We have also found an AF Néel state region, which is now shifted to larger J_3 's as compared to Na213 [7], due to the large negative J on B1 bonds. Except for the Néel and the spin-liquid phase, all other phases feature rigid triplets on the B1 bonds. This means that the effective triplet picture is quite robust.

Our result for rigid triplet degrees of freedom finds support in recent fits of the magnetic susceptibility data, which yield effective moments of $2.22 \mu_B$ for Li213 [8], much larger than the value of $1.74 \mu_B$ expected for an isotropic $\frac{1}{2}$ spin system. Turning finally to the nature of the actual magnetic ground state of Li213, we first note that the longer-range couplings J_2 and J_3 are expected to be both AF and to feature values not larger than 5–6 meV [9] in honeycomb iridates, which suggests that Li213 orders either with a diagonal-zigzag or ICx pattern. Recent magnetic susceptibility and specific heat measurements show indeed that the ground state is very different from zigzag in Li213 [10] while inelastic neutron scattering data [11] indicate clear signatures of incommensurate Bragg peaks. These experimental findings may be consistent with the ICx spin configuration.

- [1] E. Plotnikova et al., Phys. Rev. Lett. 116, 106401 (2016).
- [2] J. Kim et al., Phys. Rev. Lett. 108, 177003 (2012).
- [3] J. Kim et al., Nat. Commun. 5, 4453 (2014).
- [4] H. Gretarsson et al., Phys. Rev. Lett. 110, 076402 (2013).
- [5] S. Nishimoto et al., Nat. Commun. 7, 10273 (2016).
- [6] M. J. O'Malley et al., J. Solid State Chem. 181, 1803 (2008).
- [7] V. M. Katukuri et al., New J. Phys. 16, 013056 (2014).
- [8] H. Lei et al., Phys. Rev. B 89, 020409 (2014).
- [9] S. K. Choi et al., Phys. Rev. Lett. 108, 127204 (2012).
- [10] G. Cao et al., Phys. Rev. B 88, 220414 (2013).
- [11] S. C. Williams et al., Phys. Rev. B 93, 195158 (2016).

Funding: National Science Foundation under Grant No. NSF PHY11-25915; Deutsche Forschungsgemeinschaft (HO-4427, SFB 1143, and Emmy-Noether program); DOE-BES Division of Materials Sciences and Engineering (DMSE) under Contract No. DE-AC02-76SF00515 (Stanford/SIMES); Polish National Science Center (NCN) under Project No. 2012/04/A/ST3/00331

Cooperation: TU Dresden, University of Stuttgart, Stanford University and SLAC National Accelerator Laboratory, Joint Institute for Nuclear Research, MPIPKS, Univ. of Warsaw

Selective synthesis of endohedral metallofullerenes with methane

K. Junghans, M. Rosenkranz, Q. Deng, A. L. Svitova, C. Schlesier, N. A. Samoylova, C.-H. Chen, A. A. Popov

Abstract: Arc-discharge synthesis of endohedral metallofullerenes is accompanied by formation of larger amounts of undesired compounds, such as empty fullerenes, which dramatically complicate the separation of target metallofullerenes. Development of the conditions for selective synthesis are highly demanded. We describe how the use of methane as a reactive gas dramatically increases the selectivity in the synthesis of the various types of clusterfullerenes.

Selective synthesis of titanium-carbide clusterfullerenes $M_2TiC@C_{80}$ with lanthanides

Encapsulation of metal ions and clusters inside the carbon cage stabilizes the endohedral species and opens the way to materials with unusual electronic and magnetic properties [1]. However, the moderate yield of the arc-discharge synthesis and complicated multi-step chromatographic separation required to obtain endohedral metallofullerenes (EMFs) in pure molecular form remain serious obstacles on the way to the broader application of EMFs. In a conventional EMFs synthesis, empty fullerenes are formed with much higher relative yield and usually comprise more than 95% of the fullerenes formed. It is therefore desirable to develop more selective approaches for the synthesis of EMFs. The first selective method for the synthesis of EMFs was developed in IFW Dresden for nitride clusterfullerenes with composition $M_3N@C_{2n}$ ($M = Sc, Y$, lanthanides; $2n = 68 - 96$) [2]. Addition of NH_3 gas to the arc-discharge reactor atmosphere dramatically reduced the yield of empty fullerenes, but did not affect formation of nitride clusterfullerenes, which could be then obtained with high degree of selectivity. Similar effect could be achieved when solid nitrogen-containing organic molecules were used instead of NH_3 gas. Although very efficient for the synthesis of nitride clusterfullerenes, this method is not suitable when other types of clusterfullerenes (with endohedral carbon, sulfur etc.) is targeted in the synthesis. In developing synthetic routes for EMFs during the last years, we have found that methane CH_4 is an efficient selectivity booster for several types of clusterfullerenes, which will be reviewed in this Highlight.

Recently, in an attempt to obtain Ti-based nitride clusterfullerenes with Lu using NH_3 as a reactive gas or melamine as a solid organic nitrogen source, we have discovered a new type of clusterfullerene, $Lu_2TiC@C_{80}$, which has endohedral μ_3 -carbide ion and a double $Ti=C$ bond [3]. The molecule is an isostructural analogue of the $Lu_2ScN@C_{80}$, in which the $Sc-N$ fragment is replaced by the isoelectronic $Ti=C$ fragment. In the $Lu/Ti/NH_3$ or $Lu/Ti/melamine$ systems, $Lu_2TiC@C_{80}$ is only a minor by-product, whereas the main EMF products are $Lu_3N@C_{2n}$ nitride clusterfullerenes. However, the use of methane instead of NH_3 showed that in the $Lu/Ti/CH_4$ system $Lu_2TiC@C_{80}$ is formed as the main fullerene product. The possibility to use this approach for selective synthesis of Ti-carbide clusterfullerenes was then verified for the whole lanthanide row (Y, Ce, Nd, Gd, Dy, Er, and Lu) [4]. Figure 1 shows that under optimized conditions, Ti-carbide clusterfullerenes are the most abundant EMF products for Lu, Dy, Er, Y, and Gd. $M_2TiC@C_{80}$ -I (Roman number denotes the isomer) is the major or the only component of the fraction eluting near 36 min (highlighted in Fig. 1a). Thus, pure $M_2TiC@C_{80}$ -I molecules were obtained from the EMF extract in a single HPLC separation step (Fig. 1b). The ionic radius of the lanthanide ion (R^{3+}) plays a crucial role in the absolute yield of EMFs. Lu ($R^{3+} = 0.86 \text{ \AA}$), Er (0.90 \AA), and Dy (0.91 \AA) afford similar amounts of $M_2TiC@C_{80}$ -I per synthesis, the yields of $Gd_2TiC@C_{80}$ -I (0.94 \AA) and $Nd_2TiC@C_{80}$ -I (0.98 \AA) are roughly 6 and 20 times lower than that of $Dy_2TiC@C_{80}$ -I, respectively, whereas $Ce_2TiC@C_{80}$ (1.01 \AA) is not produced at all.

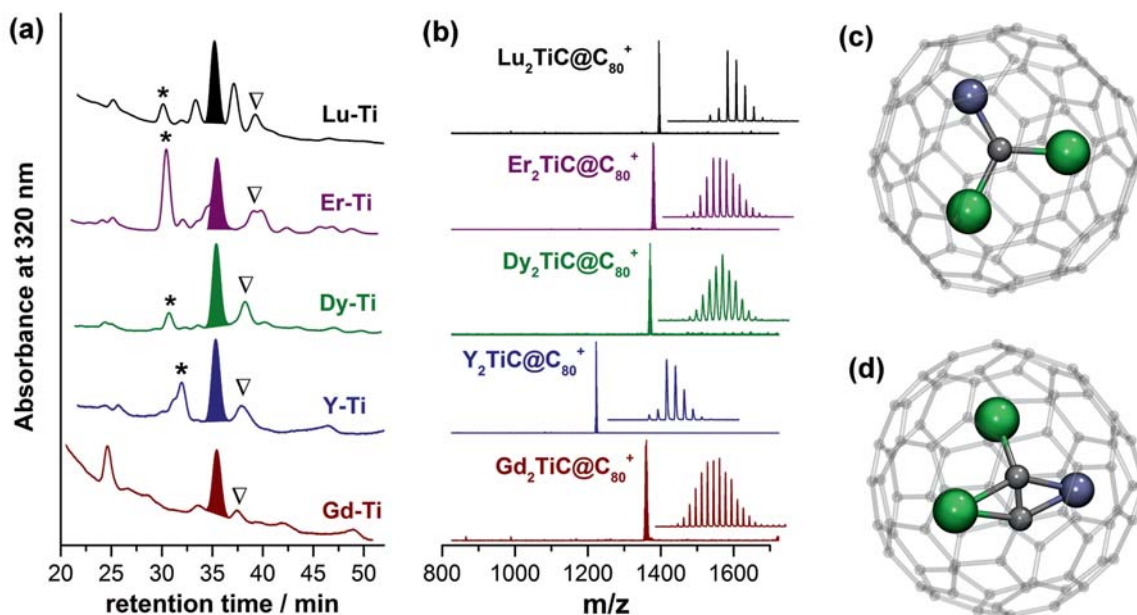


Fig. 1: (a) HPLC chromatograms of raw extracts obtained in metal/Ti/CH₄ arc-discharge syntheses; filled peaks highlight M₂TiC@C₈₀, whereas triangles denote the fractions containing M₂TiC₂@C₈₀. (b) positive ion MALDI mass spectra of isolated M₂TiC@C₈₀ compounds, insets show isotopic distributions. (c) molecular structure of M₂TiC@C₈₀; (d) molecular structure of M₂TiC₂@C₈₀. In (c) and (d), lanthanides atoms are green, Ti is cyan, endohedral carbons are grey.

The role of CH₄ in this type of synthesis is similar to that of NH₃ [2] in the synthesis of nitride clusterfullerenes: reactive gas increases selectivity of the process by suppressing the formation of empty fullerenes and making the EMFs with desired central atom(s) the main products. Increase of the selectivity of the synthesis by CH₄ reactive gas facilitated detection of other M-Ti carbide clusterfullerenes, which was not possible in the first report on Lu₂TiC@C₈₀-I [3]. Mass-spectrometry studies proved formation of M₂TiC@C_{2n} with larger cages (C₈₂, C₈₄). More importantly, we identified a new type of M-Ti-carbide clusterfullerene with one more carbon atom in the structure, M₂TiC₂@C₈₀ (Fig. 1d). Isolation of Dy₂TiC@C₈₀ and Dy₂TiC₂@C₈₀ allows us to study how the carbide cluster composition affect magnetic properties. Although both molecules are found to be single molecule magnets, the Dy₂TiC₂@C₈₀ exhibits a much narrower hysteresis compared to Dy₂TiC@C₈₀ showing that a substitution of a single carbide ion by acetylide unit in the endohedral cluster has a deteriorating effect on the SMM properties.

The role of methane in the synthesis of mixed-metal Sc-Ti clusterfullerenes

As Sc usually gives higher yields of EMFs in comparison to lanthanides, a series of arc-discharge syntheses with Sc, Ti, and CH₄ (Fig. 2) was performed to obtain a complete overview on the influence of individual metals and methane on the synthesis [5]. The results are summarized in Fig. 3. When methane was used as a reactive gas in the arc-discharge synthesis without metals, no empty cage fullerenes are formed. In the Sc/CH₄ system, the main fullerene products are carbide clusterfullerenes, including Sc₄C₂@C₈₀ (the most abundant EMF), Sc₃C₂@C₈₀, isomers of Sc₂C₂@C₈₂ and family Sc₂C_{2n} (2n = 74, 76, 82, 86, 90, etc.), as well as Sc₃CH@C₈₀. Besides, we have also detected formation of exotic carbides clusterfullerenes with odd number of carbon atoms and tetrahedral Sc₄ cluster, Sc₄C@C₈₀ and Sc₄C₃@C₈₀ [6].

Surprisingly, completely different behavior is observed in the Ti/CH₄ system. Instead of producing Ti-carbide EMFs, we found that Ti has a suppressing influence of CH₄ during the synthesis. As a result, the Ti/CH₄ system produced only empty cage fullerenes, but with a considerably different size and isomeric distribution [5]. Formation of Ti-EMFs in



Fig. 2: Schematic description of the EMF synthesis in the Sc/Ti/CH₄ system: metal atoms are packed into graphite rods and evaporated in the arc-discharge in the He atmosphere with addition of methane. From the cover page of Chem. Eur. J. Ref. [5].

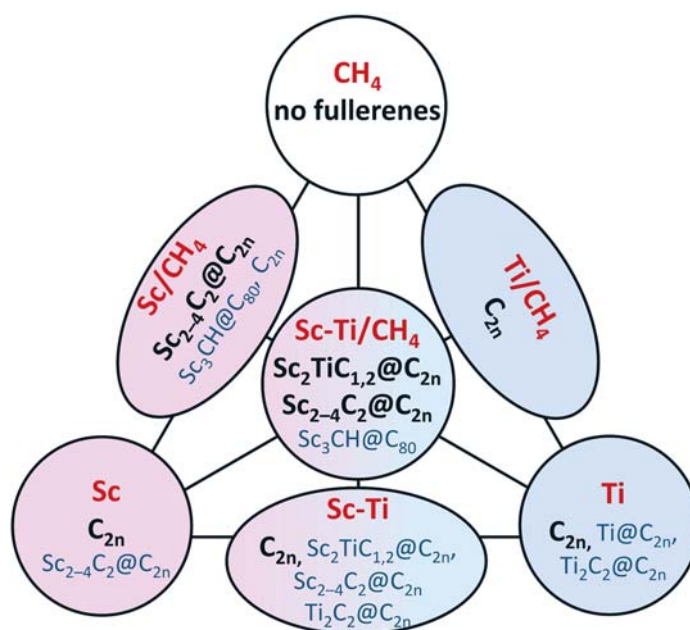


Fig. 3: Overview of the EMF syntheses in the Sc/Ti/CH₄ system and resulting fullerenes (the amount of graphite and helium gas is constant for all syntheses). Initial conditions (metals and reactive gas) are printed in red, main fullerene products in black, minor fullerene products in blue.

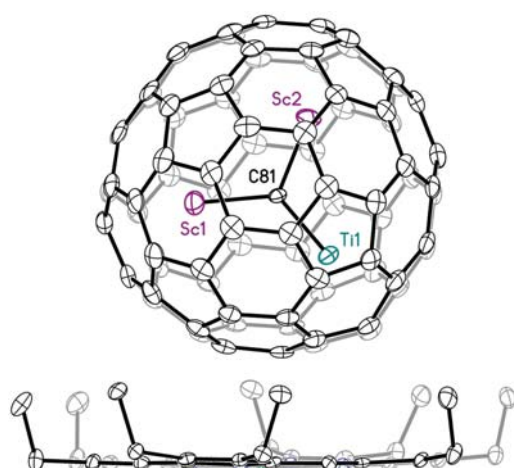


Fig. 4: View for the structure of Sc₂TiC@I_h(7)-C₈₀ Ni(OEP) toluene with hydrogen and solvent atoms omitted for clarity; only the predominant Sc and Ti positions (occupancy 0.87) are shown. Displacement parameters are shown at the 50% probability level. Selected bond lengths: Ti1–C81, 1.917(4) Å; Sc1–C81, 2.102(4) Å; Sc2–C81, 2.104(4) Å.

the Ti/CH₄ system could not be detected even by mass spectrometry. The mixed-metal Sc-Ti/CH₄ system methane efficiently suppresses empty cage fullerene formation. One of the major differences between the Sc/CH₄ and Sc-Ti/CH₄ systems is the decrease in yield of Sc₄C₂@C₈₀ in the presence of Ti. Sc₄C₂@C₈₀ is the main EMF formed in the Sc/CH₄ synthesis, but it is a minor component in the Sc-Ti/CH₄ system. Another major difference involves the formation of a series of mixed-metal Sc₂TiC_x clusterfullerenes with both even and odd numbers of carbon atoms. The most abundant EMF product in the Sc-Ti/CH₄ system is Sc₂TiC@C₈₀ (two isomers with *I_h* and *D_{5h}* cage symmetry) followed by Sc₂TiC₂@C₈₀ (also two isomers) and small amounts of Sc₂TiC@C₆₈ and Sc₂TiC@C₇₈. Elucidation of the molecular structure of two isomers of Sc₂TiC₈₁ and Sc₂TiC₈₂ was accomplished by ¹³C NMR spectroscopy. Sc₂TiC₈₁-I has a characteristic two-line spectrum, which unambiguously points to the freely rotating Sc₂TiC cluster encapsulated within the *I_h*(7)-C₈₀ cage. A similar spectrum with slightly different chemical shifts was observed for Sc₂TiC₈₂, which suggests that the compound can be formulated as Sc₂TiC₂@*I_h*(7)-C₈₀. The ¹³C NMR spectrum of Sc₂TiC₈₁-II has six lines, characteristic of the *D_{5h}*(6)-C₈₀ cage, which indicates that the compound is Sc₂TiC@*D_{5h}*(6)-C₈₀. Crystals suitable for X-ray diffraction were grown by cocrystallization of Sc₂TiC@*I_h*(7)-C₈₀ with Ni(OEP); OEP is the dianion of octaethylporphyrin. The crystals of Sc₂TiC@*I_h*(7)-C₈₀ • Ni(OEP) • 2(C₇H₈) are isostructural to crystals of Lu₂TiC@*I_h*(7)-C₈₀ • Ni(OEP) • 2(C₇H₈) [3]. The asymmetric unit contains one endohedral fullerene, one porphyrin, and two molecules of toluene. The endohedral fullerene consists of a nearly planar Sc₂TiC unit inside an *I_h*-C₈₀ cage, with the central C81 atom adopting a μ₃ configuration (Fig. 4).

Selective ¹³C enrichment of the central carbon atom in Sc₃CH@C₈₀

Optimized conditions of the EMF synthesis with methane allowed the synthesis of Sc₃CH@C₈₀ in amounts sufficient for its detailed structural and spectroscopic characterization [7]. Furthermore, Sc₃CH@C₈₀ offers a unique possibility to study the role of methane in the carbide clusterfullerene formation using ¹³C-rich reagents. The isotopic distribution of the central carbon atom can be determined by ¹H NMR from the relative intensity of the ¹³C satellites, whereas the net isotopic distribution in the whole molecule (obviously dominated by that of the carbon cage) can be deduced from the mass-spectra. To clarify how methane affects the EMF formation, we synthesized

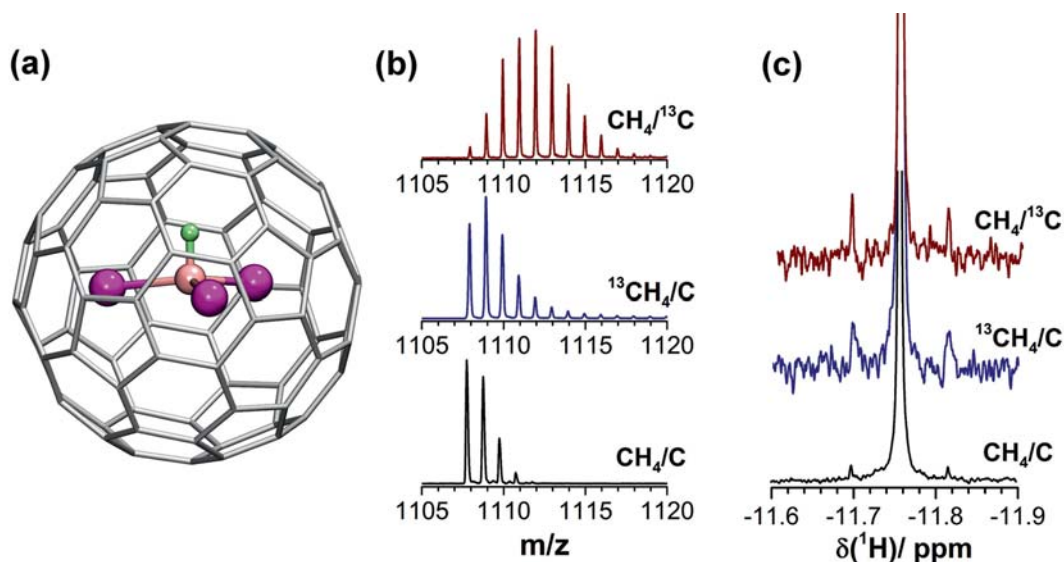


Fig. 5: (a) Molecular structure of $\text{Sc}_3\text{CH@C}_{80}$; (a) Mass-spectra of $\text{Sc}_3\text{CH@C}_{80}$ samples with different ^{13}C content obtained in $\text{CH}_4/^{13}\text{C}$, $^{13}\text{CH}_4/\text{C}$, and CH_4/C syntheses; (b) ^1H NMR spectra for the same samples, normalized to the intensity of the main singlet; satellites at 11.70 and 11.82 ppm are due to ^1H - ^{13}C coupling, and their intensity is proportional to the ^{13}C content for the central carbon atom.

^{13}C -enriched $\text{Sc}_3\text{CH@C}_{80}$ by applying either (i) $^{13}\text{CH}_4$ or (ii) ^{13}C powder (mixed with graphite powder with natural ^{13}C abundance). NMR and mass-spectrometry showed that the use of ^{13}C powder leads to the equal ^{13}C distribution in the carbon cage and the central carbon atom (Fig. 5). However, the use of $^{13}\text{CH}_4$ in the synthesis of $\text{Sc}_3\text{CH@C}_{80}$ results in selective enrichment of the central carbon atom with ^{13}C . This result proves that CH_4 is not just a source of hydrogen, but plays an active role during the clusterfullerene formation.

Our recent studies showed that carbide clusterfullerenes are not the only EMFs whose synthesis becomes more selective in the presence of CH_4 . Sulfide clusterfullerenes can also benefit from the use of methane as a reactive gas. The use of Dy_2S_3 as a simultaneous source of metal and sulfur and addition of CH_4 to the reactor atmosphere allowed us to synthesize $\text{Dy}_2\text{S@C}_{2n}$ EMFs with high degree of selectivity. Thus, the systematic study of the role of methane as a reactive gas in the synthesis of EMFs showed that is dramatically increases the selectivity of the synthesis.

- [1] A. A. Popov, et al. *Chem. Rev.* **2013**, 113, 5989.
- [2] L. Dunsch, et al. *J. Phys. Chem. Solids* **2004**, 65, 309.
- [3] A. L. Svitova, et al. *Nat. Commun.* **2014**, 5, 3568.
- [4] K. Junghans, et al. *Angew. Chem. Int. Ed.* **2015**, 54, 13411.
- [5] K. Junghans, et al. *Chem. Eur. J.* **2016**, 22, 13098.
- [6] Q. Deng, et al. *Theor. Chem. Acc.* **2015**, 134, 10.
- [7] K. Junghans, et al. *Chem. Commun.* **2016**, 52, 6561.

Funding: ERC Consolidator Grant: GraM3 (ERC-2015-CoG-648295); Deutsche Forschungsgemeinschaft (PO 1602/1-2, DU225/31-1)

Cooperation: TU Dresden; U. of California, Davis; U. Zurich

Research Area 4

Surface Acoustic Waves: concepts, materials and applications

S. Biryukov, E. Brachmann, A. Darinskii¹, T. Gemming, S. Menzel, G. Rane, W. Ren, H. Schmidt, M. Seifert, A. Sotnikov, M. Spindler, M. Weihnacht², R. Weser, A. Winkler

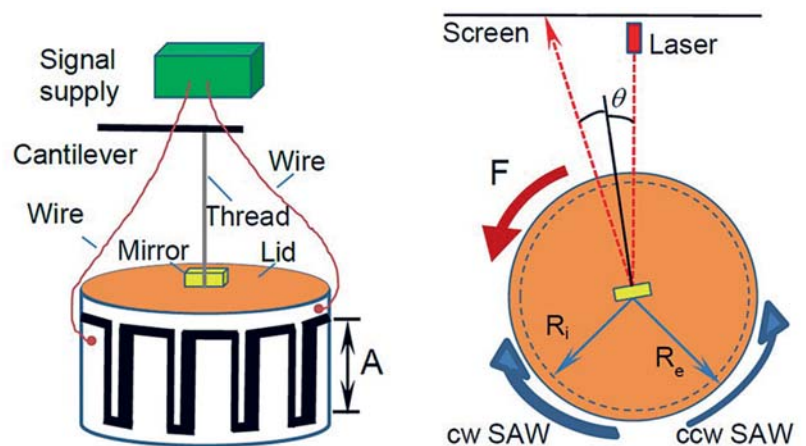
Abstract: In order to intensify application-oriented research on surface acoustic waves (SAW) the interdisciplinary expertise was extended concerning acoustic wave excitation and propagation effects, acoustofluidic interaction phenomena, dynamic behavior of polar dielectrics, advanced substrate and electrode materials and, finally, concepts for new applications. Important topics are SAW-based actuators, e.g. deployed for microfluidic lab-on-chip systems or efficient SAW-driven atomizers, as well as SAW-based wireless sensors for harsh environments. Here, the choice of appropriate material systems is the key to provide reliable operation under extreme conditions like very low or high temperatures. Besides precise characterization of promising piezoelectric crystals in a wide temperature range, extensive investigations have been devoted to novel electrode metallization systems to gain a comprehensive understanding for increasing temperature and RF power capability. In the following three special topics out of the research spectrum spanning from fundamentals to applications are introduced.

Surface acoustic wave momentum based rotation effect

Surface acoustic waves (SAW) have a momentum that can be deployed for interesting applications like novel rotary actuators. In this sense the idea of a new kind of stator-free motor was developed and the underlying rotation effect has been demonstrated experimentally [1]. The basic setup for this comprises a cylindrical tube made of piezoelectric $\text{Pb}(\text{Zr,Ti})\text{O}_3$ ceramics which is radially poled, i.e. perpendicular to the surface of the tube. To excite surface acoustic waves a periodic interdigital transducer was created on the external surface by means of a silver thin film. This transducer is a unidirectional transducer (UDT) designed for SAW excitation mainly into one direction. The UDT contains 10 periods, each of a length of 13.8 mm, covering the whole circumference of the tube. Transducer aperture is 20 mm and tube thickness 2 mm. For this dimensions the UDT provides SAW excitation with a maximum acoustic unidirectionality at a frequency of 273 kHz.

In order to realize a rotation effect, the tube was suspended to a cantilever by means of a thin thread (Fig. 1). Two thin wires connected the UDT with the signal supply realized by a signal generator cascaded with a power amplifier. Due to the elasticity of the thread and the wires the whole mechanical structure acted as a torsion pendulum. All movements of this pendulum have been visualized and monitored by a laser beam reflected from the mirror fixed to the top lid of the structure.

Fig. 1: Schematic experimental setup: UDT electrode pattern depicted in white (left). Clockwise (cw) and counterclockwise (ccw) propagating SAW of different amplitudes depicted by arrows of different thicknesses (right); A: UDT aperture; F: resultant rotation force; R_i and R_e : internal and external tube radius, resp.



Once the electrical signal was switched on, inside the UDT surface waves were excited with amplitudes proportional to the signal voltage. Due to the acoustic unidirectivity of the transducer there were two SAWs propagating into opposite directions along the surface round the tube with different amplitudes. The tube reacted on this with an oscillatory rotation, i.e. it rotated counterclockwise from the initial point by a certain rotation angle, then stopped and moved back to the initial point and so on. Cause of this rotation is the distributed rotation force F acting on the tube around the whole circumference. This force arises as a recoil of the excitation of two counter-propagating SAW with different amplitudes and momentums [1]. The value of this force as well as the maximum rotational angle depend on the signal level fed to the unidirectional transducer. From the experimental data a square-law dependence of the arising force F versus signal voltage U could be deduced which is also valid for the tube driven in the opposite direction after arranging the tube upside down (Fig. 2). According to this, the rotation effect is not proportional to the amplitude difference of the counter-propagating waves, but rather proportional to the difference of their square moduli.

Simulation of acoustic pressure produced by SAW in microfluidic channels

When propagating through a microchannel filled with fluids, the surface acoustic wave can pump the fluids or mix them or can manipulate fluid-borne microparticles. These relatively slowly time varying, or even time-independent, processes occur due to the non-linearity being inherent in the fluid dynamics. The initial step in estimating microfluidic phenomena is to compute the high-frequency (HF) acoustic pressure changing in the fluid with the SAW frequency. The correctness of determining the HF pressure via a linear boundary-value problem underlies the correctness of subsequent computations. Using the finite element method the HF pressure inside a microchannel was determined following two different approaches and the results were compared [2]. The first approach was solving the full scattering problem for the SAW propagating on the surface of a piezoelectric substrate and incident on the microchannel fabricated inside a polymer container. The HF pressure was computed self-consistently in parallel with the acoustic field in all parts of the structure. The computational domain was truncated by the so-called perfectly matched layer. An alternative way is to solve a simplified boundary-value. One of the widespread approximations is to compute only the acoustic field in the channel. The SAW displacement on the channel – substrate interface is fixed and the impedance boundary condition on the other three borders of the channel is used. This simplified model assumes that the fixed SAW displacement is as if the SAW propagated along the interface between two half-spaces occupied by the fluid and the substrate material. The example studied in our work showed that the difference between the results can be significant, ranging from several ten percent up to several times at different points inside the channel (Fig. 3). Therefore, believing that solving the full scattering problem yields more accurate results, it is reasonable to recommend its implementation despite an attractive simplicity of the approximate boundary-value problem.

High temperature stable W-Mo thin films for interdigital transducers

In order to study their phase formation behavior and electrical resistivity as a function of deposition parameters [3–5] as well as to develop a dedicated structuring process [6], Tungsten and Molybdenum layers and multilayers thereof have been investigated. The films were deposited by magnetron sputtering on thermally oxidized (100)Si as a reference substrate. Deposition at high substrate temperature (e.g. 400 °C) leads to the formation of the desired α -W phase that has a relatively low electrical resistivity (bulk $5.49 \mu\Omega\text{cm}$) compared with the β -W (bulk $150\text{--}350 \mu\Omega\text{cm}$). Within all the investigated films the bilayer as well as multilayers of W and Mo (upper layer) have the most significant improved electrical performance compared with the pure W or pure Mo films. Especially, the bilayer stack consisting of 95 nm Mo and 5 nm W shows a minimum in

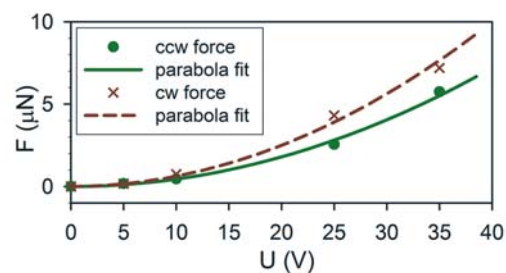


Fig. 2: Resultant rotation force F as a function of driving ac voltage amplitude U . The case related to ccw force F is shown in Fig. 1. The cw force corresponds to analog measurements for the tube upside down.

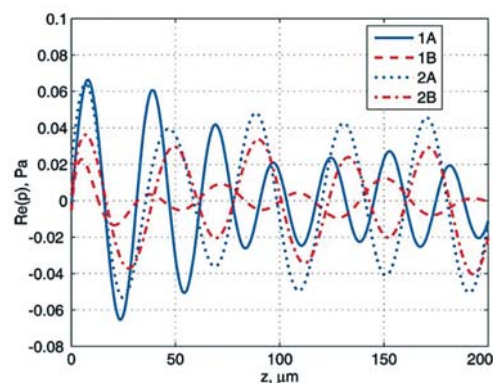


Fig. 3: Calculated acoustic pressure $\text{Re}(p)$ at vertical channel edges vs. distance z from the substrate. The channel height is 200 μm . Curves 1A, 1B: left-hand edge, curves 2A, 2B: right-hand edge. Curves 1A, 2A: full scattering problem, curves 1B, 2B: "approximate" boundary-value problem (preset SAW displacements and impedance boundary condition).

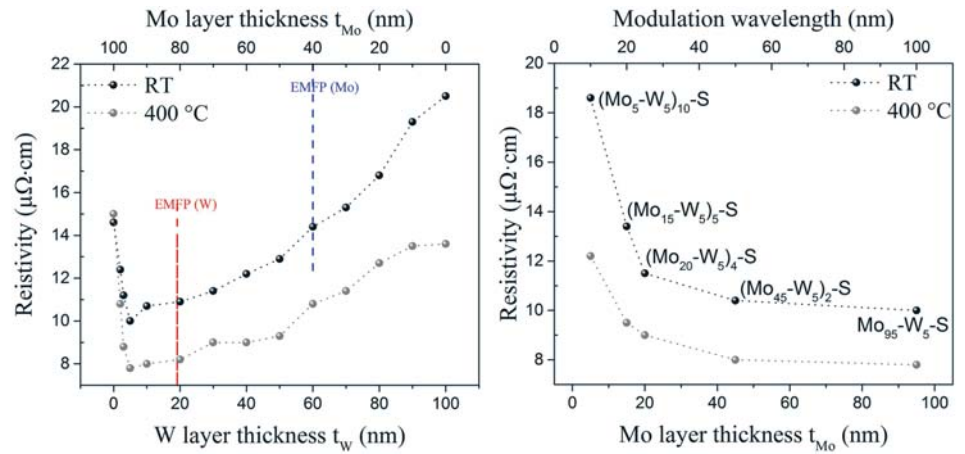


Fig. 4: Electrical resistivity of bilayers (**left**) and multilayers (**right**) of W-Mo deposited at room temperature or 400 °C onto 1 μm SiO₂/(100)Si substrate.

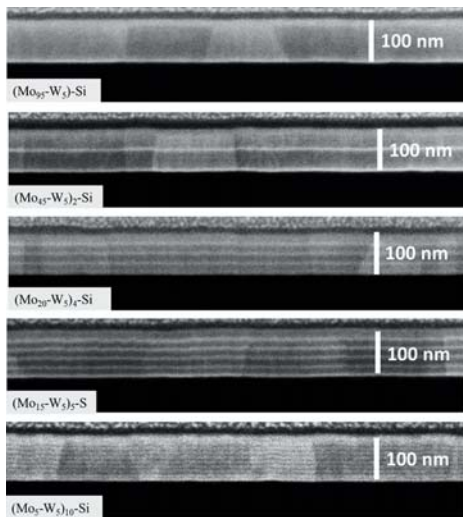


Fig. 5: FIB cross-section views of a series of multilayers deposited onto 1 μm SiO₂/(100)Si substrate with 5 nm W layer each (Foot numbers next to chemical symbols denote the individual layer thickness, while foot number outside the brackets denote the number of bilayers within the stack. The total film thickness was kept constant at 100 nm).

resistivity due to an “epitaxial-like” growth that results in a large grain microstructure with a low grain boundary volume (Fig. 4, 5). Here, the size effect and thus an increase of the resistivity by down-scaling the individual layer thickness is not observed although the 5 nm thickness of the W layer is below the EMFP of W (bulk 19.1 nm, from Choi, D. et al., Physical Review B, 2012, 86 (4)). Several effects were proved to attribute to that: i) The W and Mo layers grow epitaxially at coherent interfaces forming a columnar “super microstructure” when the W layer thickness is reduced to 5 nm. In this case the W layer acts as a template for the Mo layer growth on it avoiding the formation of tiny grains like observed for pure Mo films. ii) Because of a minimal re-sputtering effect the surface roughness does not significantly increase. The higher resistivity for other bi-layer films when W-layer thickness $t_w > 5$ nm partly relates to an increased re-sputtering effect. iii) Damage by the re-sputtering on W is much lower while depositing the Mo layer on top. Here, the Mo layer acts as a protection layer to retain the grain structure of the subjacent W layer. iv) Attributed to the higher amount of defects created by the re-sputtering process, W-rich multilayer stacks have in general a higher resistivity. v) A higher volume fraction of interfaces (including grain boundary volume) resulted in higher residual stress in polycrystalline films. Thus, to become thermodynamically favorable, a higher amount of misfit dislocations will be introduced to release the internal stress which further leads to an increase of resistivity.

- [1] S. Biryukov et al., Appl. Phys. Lett. 108 (2016) 134103.
- [2] A.N. Darinskii et al., Lab Chip 16 (2016) 2701.
- [3] G.K. Rane et al., Mat. Sci. Eng. B 202 (2015) 31.
- [4] G.K. Rane et al., Materials 9 (2016) 2, 101/1.
- [5] W. Ren, Thesis, IFW Dresden/TU Dresden (2016).
- [6] M. Spindler et al., Thin Solid Films 612 (2016) 322.

Funding: BMBF InnoProfile-Transfer (03IPT619A MiMi; 03IPT610Y HoBelAB)
Deutsche Forschungsgemeinschaft (SCHM 2365/12-1, SO 1085/2-1, WI 4140/2-1)
Creavac, SAW Components Dresden, Vectron International

Cooperation: TU Dresden; TU Clausthal, Goslar; Ioffe Physical Technical Institute RAS, St. Petersburg, Russia; ¹Institute of Crystallography RAS, Moscow, Russia; BTU Cottbus; Fraunhofer IPMS/CNT
Industry: BelektronikG; Creavac; ²InnoXacs; MLE Dresden; Prolatec;
SAW Components Dresden; Sensortechnik Meinsberg; Vectron International

Superconducting magnetic bearings in high-speed ring spinning machines

A. Abdkader¹, A. Berger, D. Berger, C. Cherif¹, T. Espenhahn, G. Fuchs, M. Hossain¹, R. Hühne, K. Nielsch, L. Schultz, M. Sparing

Abstract: The unique properties of superconducting magnetic bearings (SMB) – passive load bearing and contact-less motion – have been intensely studied in recent years e.g. for motors, flywheel energy storage systems and other high-speed rotating machines. In the framework of a joint DFG project with the Institute of Textile Machinery and High Performance Material Technology (ITM) at the TU Dresden we investigated the replacement of the conventional ring traveler twist element in ring spinning machines with a superconducting magnetic bearing. The goal of this project is to reduce the limiting process factors in the industrial production of short staple yarn by ring spinning, which are mainly frictional wear and heat in the twist element, with a new concept of the twist element based on SMB.

Development of a superconducting magnetic bearing twist element

Superconducting magnetic bearings (SMB) enable the levitation of a permanent magnet (PM) in an inherently stable position over a cooled superconductor (SC). No additional positioning system is necessary, but a material depending cryogenic temperature of the superconductor has to be guaranteed for their operation. These passive bearings are being investigated for applications of stationary levitation and contact free motion in all space dimensions. Linear superconducting magnetic bearings are used in the levitating transport systems like the Supratrans2 test facility [1]. In energy storage applications SMBs could prove advantage compared to the conventional system [2].

In our project, a rotating superconducting magnetic bearing is incorporated in a ring spinning machine as a replacement of the traditional, friction afflicted ring-traveler twist element [3, 4]. In general, the ring-spinning technology is the most widely used spinning method for short staple yarn production due to the high quality of the yarn and the flexibility of the process. The continuous ring spinning process converts a loose fiber roving to yarn by drawing, twisting, and winding up on a bobbin. The ring traveler system thereby induces twist in the processed material by guiding it around the spindle. In the twist element the yarn is guided through a c-shaped clip, the traveler, which is dragged along a ring surrounding the spindle. The traveler is slightly slower than the spindle, enabling the winding of the yarn onto the bobbin. The rotational speed and hence the productivity of the process is limited by the friction heat between ring and traveler. This heat damages the twist element which causes wear and also can lead to melting of synthetic yarns at high rotational speed. Therefore, the maximum rotational speed achievable in industrial yarn production with a conventional twist element is 25.000 rpm or less, depending on the raw material of the fibers.

To improve the behavior, a SMB twist element was developed und incorporated in a ring spinning tester as shown in Fig. 1. The schematic components of such a bearing are shown in Fig. 2. It consists of a fixed superconducting $\text{YBa}_2\text{Cu}_3\text{O}_{7-x}$ (YBCO) ring prepared from bulk segments, which is cooled down to 77 K. Levitating above is a rotating permanent magnetic ring with a fixed eyelet as yarn guide. The YBCO ring is cooled by a continuous flow cryostat using liquid nitrogen (LN_2) [5]. The special design cools down the superconductor by solid state conduction and hence allows the free positioning of the YBCO ring in the vacuum chamber. This is important to assure a small initial cooling distance (field cooling height) between PM ring and SC ring of 5 mm and hence good bearing properties like bearing force and stiffness. The SMB twist element significantly reduces the productivity limiting friction heat in the spinning process of short staple yarn and thus the process speed might be increased from commonly 25.000 rpm up to 50.000 rpm.

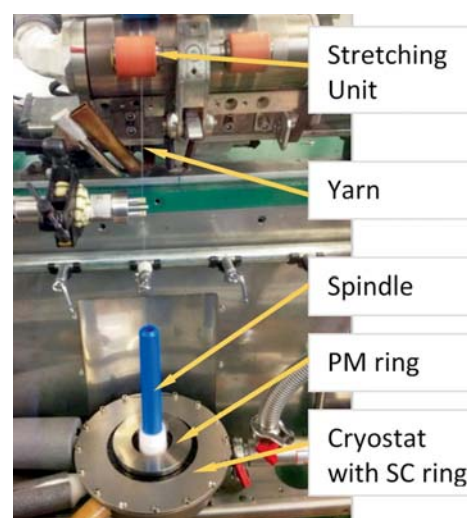


Fig. 1: SMB twist element in the ring spinning tester

Polyester yarn spun with the SMB twist element has similar properties to conventional yarn. Furthermore, the yarn surface of the SMB-yarn is more even and less hairy due to the reduced friction and heat in the SMB twist element.

Characterization of the SMB

During the project, we started to investigate the static and dynamic behavior of the SMB both experimentally and theoretically, e.g. forces, displacements and precession, with respect to the ring spinning process [6, 7]. The SMB as twist element in the ring spinning machine is mathematically described as a spring-mass-damper system, which is excited by an external force, i.e. the yarn force (Fig. 2). The yarn force acts at the eccentric contact point between yarn and magnet, i.e. the eyelet at the inner bore of the steel shell around the PM ring. The yarn force $F_Y(\omega)$ (components F_G^z , F_Y^z , F_Y^r) leads to a displacement of the ring in radial and axial direction and to an additional tilt (angle α) with respect to the position of the YBCO ring. They are counteracted by the restoring forces of the bearing F_B^z in axial and F_B^r in radial direction.

The bearing stiffness $k_i = dF_i/dx_i$ (index i being the displacement direction) causes forced oscillations in radial and axial directions. There is no restoring force in circumferential direction for this round SMB geometry, thus F_Y^ϕ acts as driving force for the free rotation of the PM ring. The rotation of the PM ring is superimposed by the above mentioned forced oscillations having an amplitude $A(\omega)$ and a decay constant δ . While the stationary stiffness k_i of SMBs is easily accessible by force vs. displacement measurements, the determination of the decay constant and the dynamic stiffness is more complex, which makes a correct prediction of maximum amplitude during operation difficult. Therefore, a measurement setup was developed to determine the damped oscillations of the bearing. As a result, the decay constant δ of the SMB was found to depend strongly not only on the field cooling distance but also on the initial radial displacement Δr . Since damping in SMB is caused by the depinning of flux lines during oscillation, the linear increase of δ with Δr can be attributed to an increase of the average number of pinning centers within the displacement distance.

The dependence of the decay constant δ on the initial displacement has consequences for the rotation frequency dependent amplitude of the oscillation $A(\omega)$ during the rotation of the PM ring. Fig. 3 shows the calculated amplitude of the oscillations in lateral, tilt and axial direction during rotation [6]. The obtained damped resonance frequency, where the amplitude of the oscillation $A(\omega)$ is maximal, remains below 1.500 rpm for all modes. These small rotational speeds are not relevant for the actual spinning process,

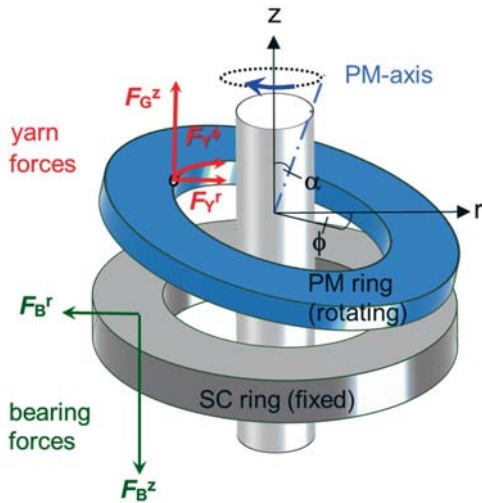


Fig. 2: Configuration of the SMB twist element with acting forces

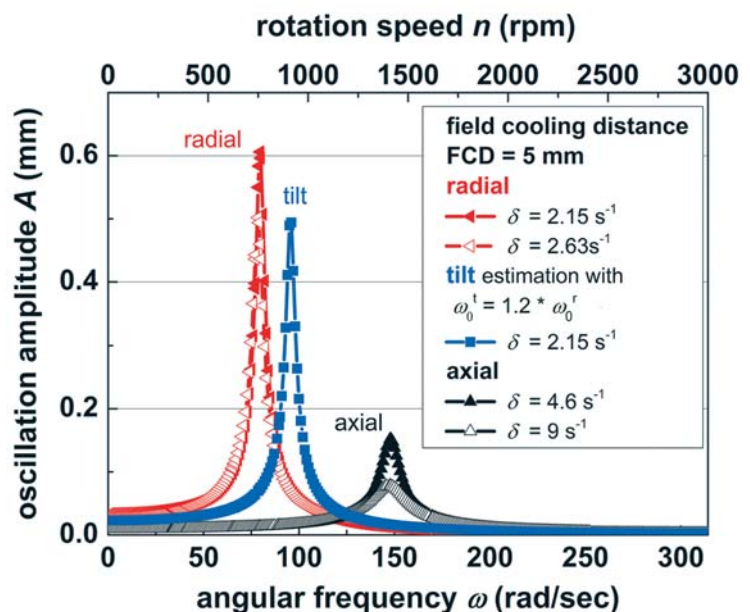


Fig. 3: Oscillation amplitude $A(\omega)$ of the PM ring for different decay constants δ [6]

which takes place between 5.000 and 25.0000 rpm. However, during the acceleration and deceleration of the process, these frequencies occur and the respective oscillation amplitudes have to be considered for the setup and operation of the SMB system in the ring-spinning machine.

To measure the real yarn force induced tilt and displacement of the PM ring during spinning, an array of optical positioning sensors is used, developed in cooperation with the IFW research technology department (Fig. 4). Additionally, the tilt of the PM due to the yarn forces in combination with high rotational speed leads to a hysteretic heat input in the superconductor. At high rotational speed, this hysteresis loss becomes an important factor on the bearing reliability. The resulting heat was estimated to be 13.4 W at 25.000 rpm for the maximum tilt in the resonance case during rotation [5]. This is significantly higher than the heat input due to convection, radiation and conduction, which is in the range of ~ 2.3 W. However, the real amount of displacement and hysteretic loss, which is important for the cooling efforts, has to be measured. Therefore, a calorimetric test facility was set up recently to measure the hysteretic losses on the SMB in dependence of the tilt angle and the rotation speed [8].

Future developments

The current SMB system was developed and tested for a maximum speed of 25.000 rpm. A new cryostat will be built and tested in the second project period, which started recently. The major aim of the new development is to operate the ring spinning process with a speed of up to 50.000 rpm. To realize this velocity, a new cryostat will operate at lower temperatures using a reduced pressure above the liquid nitrogen bath in order to increase the levitation force and bearing stability compared to the current first ring spinning tester. Additionally, the rotating permanent magnetic ring has to be reinforced by a shrunk-on steel shell in order to withstand the large tangential tensile stresses developing at speeds of 50.000 rpm.

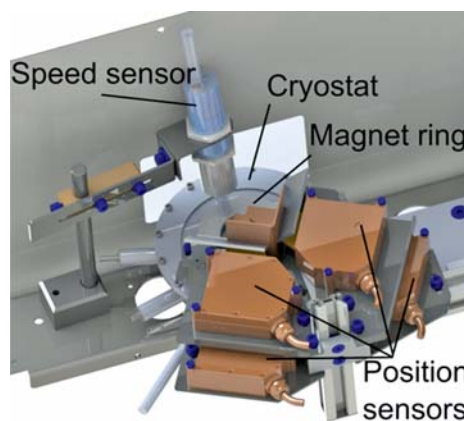


Fig. 4: Measurement setup for the characterization of the dynamic SMB properties

- [1] L. Kühn et al., *Elektrische Bahnen* **110** (2012) 461.
- [2] F. N. Werfel et al., *Supercond. Sci. Technol.* **25** (2012) 014007.
- [3] M. Hossain et al., *Textile Res. J.* **84** (2014) 871.
- [4] M. Sparing et al., *IEEE Trans. Appl. Supercond.* **25** (2015) 3600504.
- [5] A. Berger et al., *IEEE Trans. Appl. Supercond.* **26** (2016) 3601105.
- [6] M. Sparing et al., *IEEE Trans. Appl. Supercond.* **26** (2016) 3600804.
- [7] M. Hossain et al., *Textile Res. J.* (2016) in press
(DOI: <https://doi.org/10.1177/0040517516641363>).
- [8] A. Berger et al., *Proc. ISMB15* (2016) in press.

Funding: Deutsche Forschungsgemeinschaft (SCHU1118/12-1)

Cooperation: ¹TU Dresden, Evico GmbH, TUDATEX

Entirely flexible on-site conditioned magnetic sensorics

D. Karnaushenko, N. Münzenrieder^{1,2}, D. D. Karnaushenko,
M. Melzer, D. Makarov³, G. Tröster¹, O. G. Schmidt

Abstract: The establishment of shapeable magnetoelectronics was pioneered at the IFW Dresden and demonstrated magnetic sensorics with unique mechanical properties. Up to now, these developments were almost exclusively focused on individual magnetic sensing elements, only. In order to expand this technology to a wider field of applications that require more complex shapeable magnetosensitive systems and allow for the design of market ready prototypes, research efforts have been made to combine the magnetoresistive elements with signal conditioning circuitry on the same shapeable platform. Hence, the first entirely flexible integrated magnetic field sensor system was realized consisting of a magnetosensitive bridge, on-site conditioned using high-performance IGZO-based readout electronics. The system outperforms commercial fully integrated rigid magnetic sensors by at least one order of magnitude, whereas all components remain fully functional when bend to a radius of 5 mm.

Flexible electronics [1] naturally conform to static or dynamic complex shaped surfaces offering intimate yet durable contact with biological as well as synthetic tissue. The inherent feature of this new formulation of electronics of being soft and compliant enables a plethora of new applications, especially in medicine and consumer electronics, with a variety of flexible devices already available.

Up to now, the data acquired using *entirely flexible* and even *imperceptible* [2] sensorics, are mostly transmitted using wires to external conventional electronics for post-processing, *e.g.* signal amplification or multiplexing. This measurement scheme, however, possesses strong disadvantages in terms of the signal-to-noise ratio (SNR), applicability and reliability and narrows the bandwidth of the device. The signals are amplified together with the noise, which can be either picked up by the long wires or produced by the electronic circuit itself. To enhance the responsiveness and sensitivity of an acquisition system, the output of a sensory system should be amplified directly at the sensor location. This so called *frontend signal conditioning* is a standard approach in conventional rigid microelectronics, but is not yet established for flexible electronics.

In this work, we demonstrate a fully integrated yet entirely flexible magnetosensory system [3], which can be fabricated over large areas (Fig. 1). The complete device (Fig. 2a,b) is integrated on a single 50 μm thick polyimide foil and consists of a differential giant magnetoresistive (GMR) sensing element arranged in a Wheatstone bridge configuration (red frames and Fig. 2c), an NMOS operational amplifier with differential high impedance input and single ended output (green frames), built from 16 Indium-Gallium-Zinc-Oxide (IGZO) bottom-gate inverted thin-film transistors (TFTs) [4] and a high current output amplifier TFT (blue frames) operated as class A power amplifier with an open drain output to provide maximum adaptability to different loads. The GMR bridge consists of two reference non-magnetic Cu-based resistors and two magnetoresistive elements (Fig. 2c) implemented by giant magnetoresistive Co/Cu multilayer stacks coupled in the first antiferromagnetic maximum [5]. The saturation field of the GMR elements is tuned to be ≈ 4 kOe to ensure linear response in a broad field range from 20 Oe to about 1.8 kOe (Fig. 2f) as required *e.g.* for proximity sensing. The differential and power amplifier readout circuitry reveals a remarkable amplification of 48.6 dB and a unity gain frequency of about 200 kHz. Furthermore, the analogue differential signalling promotes an efficient rejection of common mode noises leading to an extremely low noise floor of -124 dBm Hz^{-1} . The GMR Wheatstone bridge, whose differential output is connected to the operational amplifier, allows processing of small signals in the microvolts range and efficiently rejects common mode noise.



Fig. 1: One specimen of the flexible high-performance magnetosensory system on 50 μm polyimide foil.

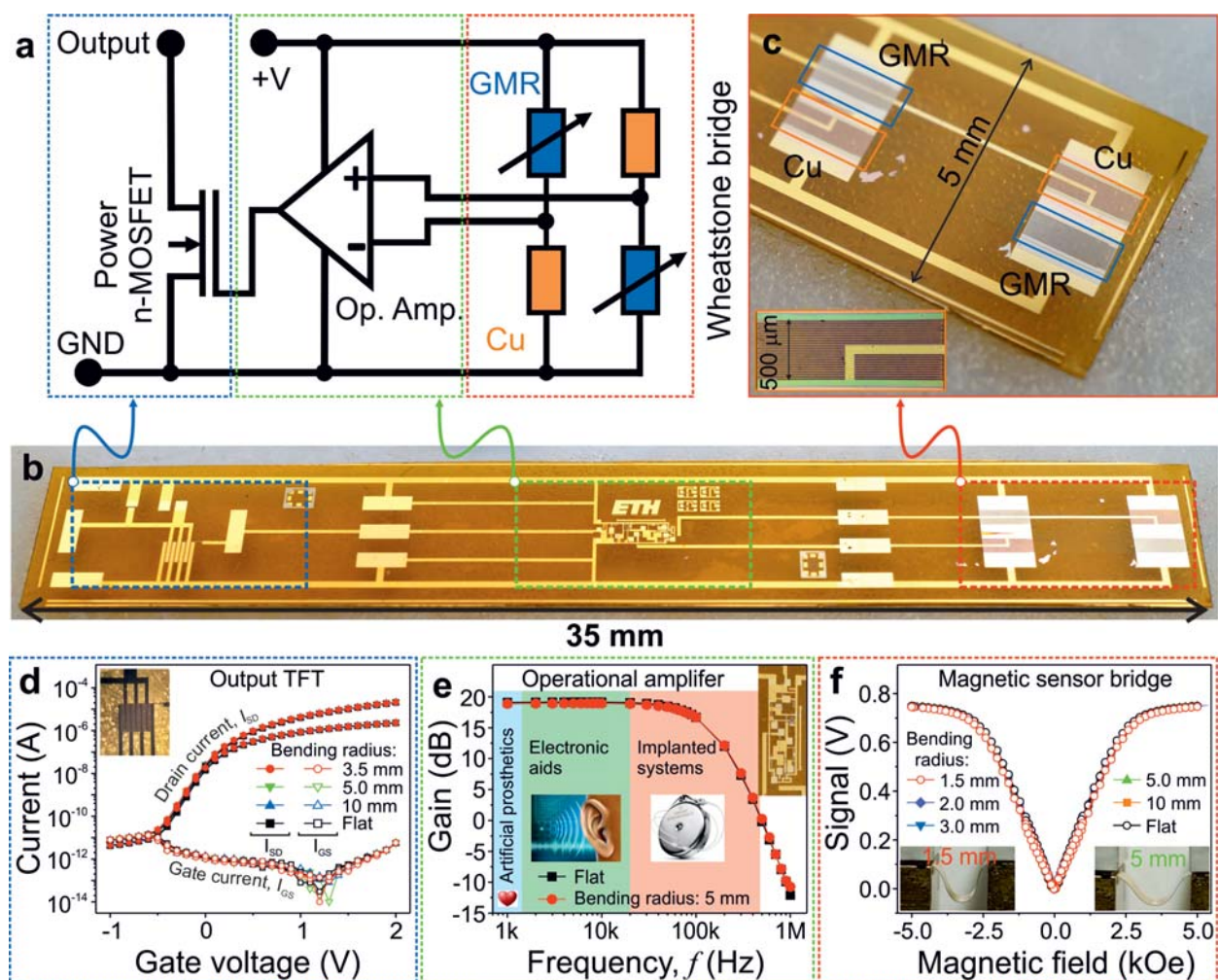


Fig. 2: The complete device (a,b) consists of an operational amplifier made of 16 IGZO based TFTs, an output power amplifier TFT and GMR multilayer meander elements arranged in a Wheatstone bridge configuration (c). (d) Transfer characteristics of the IGZO power transistor measured in the linear ($V_{DS} = 0.1$ V) and saturation ($V_{DS} = 5$ V) regime while flat and bent to different radii. (e) Bode plot of the operational amplifier (without power TFT) in planar and bent state and application examples operating at frequencies within its bandwidth. (f) Response function vs. applied magnetic field of the magnetic sensor bridge (without readout circuitry) measured at different bending radii. The insets show the sensory system mounted to the bending test stage at two different deformation states.

The presented work demonstrates for the first time, that IGZO semiconductor devices enable the realization of entirely flexible low-noise electronics, suitable for sensor readout circuits. IGZO-based electronics [4] has been chosen for its high-performance and low power operation. In particular a carrier mobility beyond $10 \text{ cm}^2/\text{Vs}$ and extreme bending radii down to the micrometer range [6] rendering IGZO an attractive alternative to organic semiconductor-based devices. The used IGZO TFTs also ensures a very high input impedance of $>10 \text{ G}\Omega$. The on-site amplification of the bridge output within the flexible sensor system results in a high responsiveness of $25 \text{ V V}^{-1} \text{ kOe}^{-1}$. This corresponds to a 270 times enhancement of the signal amplitude, which is the highest gain of flexible amplifiers reported so far. With these parameters, the *mechanically flexible magnetosensory system* outperforms even its rigid commercially available counterparts [3]. Operating at only 3 V supply, the open drain output enables the use of high and low impedance loads, and can reach a full scale amplitude with an output current of up to 3 mA (Fig. 2a) suggesting the possibility to directly drive external power demanding devices such as a relay or light emitting diodes (LEDs). Besides its high current driving capability, the device consumes less than 250 μW at 1.7 V and 450 μW at 3 V (internal with 1 M Ω

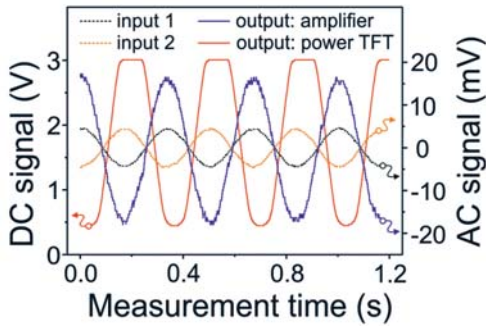


Fig. 3: Intermediate response of the operational amplifier (blue) and overall output of the readout electronics (red) on an externally applied differential sinus input signal, that mimics the output of the sensor bridge. The data reveals a total open loop gain of 48.6 dB, whereas the supply voltage was 3 V and the oscilloscope (1 M Ω) was used as a load element.

load), rendering the circuit the most power efficient entirely flexible fully integrated sensory system reported so far [3]. This remarkable energy efficiency potentially allows the system to be powered using renewable green energy sources, *e.g.* flexible energy harvesters and storage elements.

The entire sensory system shows remarkable compliance versus severe bending deformation. Upon flexure, the output power amplifier TFT remains fully operational down to a bending radius of 3.5 mm and exhibits only small DC parameter changes (Fig. 2d). The operational amplifier circuit is also tested under bending to a radius of 5 mm revealing a voltage gain of 18.9 dB, a unity gain frequency of 508 kHz and unchanged common mode rejection (Fig. 2e). The GMR characteristics of the sensor bridge, remain unchanged even when the system is bent down to a radius of 1.5 mm (Fig. 2f).

To assess the electrical performance of the flexible two-stage amplifier, the input of the operational amplifier is subjected to a differential 3 Hz sinusoidal signal with a peak-to-peak amplitude of 10 mV (Fig. 3). Here, the circuit input is biased to a DC offset of 1.5 V, in order to operate within the allowed common mode input range and to imitate the output signal of the GMR bridge, whereas the high current TFT is biased to 15 μ A using an external source. By monitoring the intermediate output signal of the operational amplifier and the overall output of the readout electronics a output signal amplitude of 40 mV and 2.7 V is measured, respectively.

Our high-performance flexible magnetosensory system represents a key step towards entirely flexible electronics, capable of sensing and processing signals without the need of rigid elements. The device bandwidth is appropriate to cover a broad range of sensor applications and we envision that the integrated GMR bridge can be used to trigger external devices or provide feedback signals paving the way towards the realization of entirely flexible magnetic gadgets and switches. These are highly relevant in medicine for applications where mechanical flexibility, light-weight and energy efficiency of the electronic components are of major relevance, *e.g.* heart pacemaker, brain implants, hearing aids, capsule endoscopes, mechanical prosthetics, health threat alarming devices or automatic delivery systems. In this respect, thin flexible fully integrated switches that are triggered by a small permanent magnet or an external magnetic field could reduce size and power consumption of the final wearable devices or smart implants. Furthermore, these components are needed for interactive consumer electronics in the spirit of the Internet of Things (IoT) concept. Especially, devices operating at frequencies below 100 kHz require low noise switches and sensory feedback (Fig. 2e).

The publication of this entirely flexible on-site conditioned magnetic sensorics system also includes significant demonstrator experiments, such as *flexible magnetic switch or linear proximity sensor operation* to highlight its versatile operation potential [3]. A supporting video showing the signal sequence of the operational amplifier and the entire system with simultaneously switching a commercial semiconductor LED by means of an external permanent magnet is available via the provided *QR-link*. The entire setup in this experiment is powered using 3 V external supply and consumes only 550 μ W including the LED.

The flexible monolithic integration of magnetic sensorics with TFT based electronics not only bears the great potential for signal amplification, but also allows for multiplexing, in order to operate and address large sensor arrays on a flexible sheet (*e.g.* in an active matrix), or to combine a variety of functional components to complex smart systems on a prototype level. As demonstrated for GMR sensors in the IFW Dresden [7], also the IGZO based electronics exploited here, has been proven for imperceptible forms electronics [6], suggesting their combination on such a platform, as well. Both aspects are subject of current efforts in this research topic. Although the TFT amplifying circuit in this work was designed and fabricated at the ETH Zürich, we are currently establishing IGZO fabrication capabilities in our venues, as well, to be able to extend this promising route of innovation for the future challenges in the FlexMag development center.

- [1] Y.G. Sun et al., Adv. Mater. 19 (2007) 1897.
- [2] M. Kaltenbrunner et al., Nature 499 (2013) 458.
- [3] N. Münzenrieder et al., Adv. Electron. Mater. 2 (2016) 1600188.
- [4] K. Nomura et al., Nature 432 (2004) 488.
- [5] S.S.P. Parkin et al., Appl. Phys. Lett. 58 (1991) 2710.
- [6] G.A. Salvatore et al., Nat. Commun. 5 (2014) 2982.
- [7] M. Melzer et al. Nat. Commun. 6 (2015) 6080.

Funding: This work is financed in part via the European Research Council within the European Union's Seventh Framework Programme (FP7/2007-2013) / ERC grant agreement no. 306277 and European Commission within the European Union's seventh framework program FLEXIBILITY / grant number 287568.

Cooperations: ¹Electronics Laboratory, ETH Zürich, Gloriastrasse 35, 8092 Zürich, Switzerland; ²Sensor Technology Research Center, University of Sussex, Falmer, Brighton, BN1 9QT, United Kingdom; ³Intelligente Werkstoffe und Funktionselemente, Helmholtz-Zentrum Dresden-Rossendorf, Bautzner Landstraße 400, 01328 Dresden



Supporting Video

Publications and invited talks 2016

Journal Papers

- 1) F. Klein, U. Treske, A. Koitzsch, D.R. Cavicchia, C. Thoenissen, R. Froemter, T. Roch, T. Muehl, *Nanoscale scanning electron microscopy based graphitization in tetrahedral amorphous carbon thin films*, Carbon 107 (2016), S. 536-541.
- 2) S. Abdi, S. Oswald, P.F. Gostin, A. Helth, J. Sort, M.D. Baro, M. Calin, L. Schultz, J. Eckert, A. Gebert, *Designing new biocompatible glass-forming $Ti_{75-x}Zr_{10}Nb_xSi_{15}$ ($x = 0, 15$) alloys: corrosion, passivity, and apatite formation*, Journal of Biomedical Materials Research Part B: Applied Biomaterials 104 (2016) Nr. 1, S. 27-38.
- 3) H. Bih, I. Saadoune, L. Bih, M. Mansori, H. Toufik, H. Fuess, H. Ehrenberg, *Synthesis, Rietveld refinements, Infrared and Raman spectroscopy studies of the sodium diphosphate $NaCr_yFe_{1-y}P_2O_7$ ($0 \leq y \leq 1$)*, Journal of Molecular Structure 1103 (2016), S. 103-109.
- 4) A. Raduta, M. Nicoara, C. Locovei, J. Eckert, M. Stoica, *Ti-based bulk glassy composites obtained by replacement of Ni with Ga*, Intermetallics 69 (2016), S. 28-34.
- 5) P. Ma, Y. Jia, K.G. Prashanth, S. Scudino, Z. Yu, J. Eckert, *Microstructure and phase formation in Al-20Si-5Fe-3Cu-1Mg synthesized by selective laser melting*, Journal of Alloys and Compounds 657 (2016), S. 430-435.
- 6) S. Khoramkhorshid, M. Alizadeh, A.H. Taghvaei, S. Scudino, *Microstructure and mechanical properties of Al-based metal matrix composites reinforced with $Al_{84}Gd_6Ni_7Co_3$ glassy particles produced by accumulative roll bonding*, Materials and Design 90 (2016), S. 137-144.
- 7) J. Balach, T. Jaumann, M. Klose, S. Oswald, J. Eckert, L. Giebeler, *Improved cycling stability of lithium-sulfur batteries using a polypropylene-supported nitrogen-doped mesoporous carbon hybrid separator as polysulfide adsorbent*, Journal of Power Sources 303 (2016), S. 317-324.
- 8) J. Sander, J. Hufenbach, L. Giebeler, H. Wendrock, U. Kuehn, J. Eckert, *Microstructure and properties of FeCrMoVC tool steel produced by selective laser melting*, Materials and Design 89 (2016), S. 335-341.
- 9) E. Brachmann, S. Menzel, S. Oswald, A. Winkler, *Material-related effects during ion beam treatment by an end-Hall ion source*, Vacuum 124 (2016), S. 65-71.
- 10) P. Jovari, P. Lucas, Z. Yang, B. Bureau, I. Kaban, B. Beuneu, C. Pantalei, J. Bednarcik, *On the structure of Ge-As-Te-Cu glasses*, Journal of Non-Crystalline Solids 433 (2016), S. 1-5.
- 11) F. Silze, G. Wiehl, I. Kaban, H. Wendrock, T. Gemming, U. Kuehn, J. Eckert, S. Pauly, *Wetting behaviour of Cu-Ga alloys on 304L steel*, Materials and Design 91 (2016), S. 11-18.
- 12) N. Mattern, Y. Yokoyama, A. Mizuno, J.H. Han, O. Fabrichnaya, M. Richter, S. Kohara, *Experimental and thermodynamic assessment of the La-Ti and La-Zr systems*, Calphad 52 (2016), S. 8-20.
- 13) A. Kauffmann, D. Geissler, J. Freudenberger, *Thermal stability of electrical and mechanical properties of cryo-drawn Cu and CuZr wires*, Materials Science and Engineering A 651 (2016), S. 567-573.
- 14) I. Kaban, R. Nowak, G. Bruzda, L. Xi, N. Sobczak, J. Eckert, L. Giebeler, *Wettability and work of adhesion of liquid sulfur on carbon materials for electrical energy storage applications*, Carbon 98 (2016), S. 702-707.
- 15) H. Vinzelberg, J. Schumann, *CrSi(O,N)-based cermet-like material for high-ohmic thin film resistor applications*, Physica Status Solidi A 213 (2016) Nr. 4, S. 1016-1024.
- 16) X. Lu, W. Si, X. Sun, B. Liu, L. Zhang, C. Yan, O.G. Schmidt, *Pd-functionalized MnO_x - GeO_y nanomembranes as highly efficient cathode materials for $Li-O_2$ batteries*, Nano Energy 19 (2016), S. 428-436.
- 17) J. Pang, A. Bachmatiuk, I. Ibrahim, L. Fu, D. Placha, G.S. Martynkova, B. Trzebicka, T. Gemming, J. Eckert, M.H. Ruemmeli, *CVD growth of 1D and 2D sp^2 carbon nanomaterials*, Journal of Materials Science 51 (2016) Nr. 2, S. 640-667.
- 18) H. Richert, H. Schmidt, S. Lindner, M. Lindner, B. Wenzel, R. Holzhey, R. Schaefer, *Dynamic Magneto-Optical Imaging of Domains in Grain-Oriented Electrical Steel*, Steel Research International 87 (2016) Nr. 2, S. 232-240.
- 19) O. Kataeva, M. Khrizanforov, Y. Budnikova, D. Islamov, T. Burganov, A. Vandyukov, K. Lyssenko, B. Mahns, M. Nohr, S. Hampel, M. Knupfer, *Crystal Growth, Dynamic and Charge Transfer Properties of New Coronene Charge Transfer Complexes*, Crystal Growth and Design 16 (2016) Nr. 1, S. 331-338.
- 20) L. Xi, I. Kaban, R. Nowak, G. Bruzda, N. Sobczak, J. Eckert, *Interfacial interactions between liquid Ti-Al alloys and TiB₂ ceramic*, Journal of Materials Science 51 (2016) Nr. 4, S. 1779-1787.
- 21) D.Y. Wu, K.K. Song, P. Gargarella, C.D. Cao, R. Li, I. Kaban, J. Eckert, *Glass-forming ability, thermal stability of B2 CuZr phase, and crystallization kinetics for rapidly solidified Cu-Zr-Zn alloys*, Journal of Alloys and Compounds 664 (2016), S. 99-108.

- 22) M. Seifert, G.K. Rane, S.B. Menzel, T. Gemming, *TEM studies on the changes of the composition in LGS and CTGS substrates covered with a RuAl metallization and on the phase formation within the RuAl film after heat treatment at 600 and 800 °C*, Journal of Alloys and Compounds 664 (2016), S. 510-517.
- 23) K.G. Prashanth, S. Scudino, A.K. Chaubey, L. Loeber, P. Wang, H. Attar, F.P. Schimansky, F. Pyczak, J. Eckert, *Processing of Al-12Si-TNM composites by selective laser melting and evaluation of compressive and wear properties*, Journal of Materials Research 31 (2016) Nr. 01, S. 55-65.
- 24) M. Medina-Sanchez, L. Schwarz, A.K. Meyer, F. Hebenstreit, O.G. Schmidt, *Cellular Cargo Delivery: Toward Assisted Fertilization by Sperm-Carrying Micromotors*, Nano Letters 16 (2016) Nr. 1, S. 555-561.
- 25) T. Jaumann, J. Balach, M. Klose, S. Oswald, J. Eckert, L. Giebeler, *Role of 1,3-Dioxolane and LiNO₃ Addition on the Long Term Stability of Nanostructured Silicon/Carbon Anodes for Rechargeable Lithium Batteries*, Journal of The Electrochemical Society 163 (2016) Nr. 3, S. A557-A564.
- 26) A. Stepanov, A. Mustafina, S. Soloveva, S. Kleshnina, I. Antipin, I. Rizvanov, I. Nizameev, R.G. Mendes, M.H. Ruemmeli, L. Giebeler, R. Amirov, A. Konovalov, *Amphiphiles with polyethyleneoxide-polyethylenecarbonate chains for hydrophilic coating of iron oxide cores, loading by Gd(III) ions and tuning R₂/R₁ ratio*, Reactive and Functional Polymers 99 (2016), S. 107-133.
- 27) D. Söpu, C. Soyarslan, B. Sarac, S. Bargmann, M. Stoica, J. Eckert, *Structure-property relationships in nanoporous metallic glasses*, Acta Materialia 106 (2016), S. 199-207.
- 28) R. Ummethala, D. Wenger, S.F. Tedde, C. Taeschner, A. Leonhardt, B. Buechner, J. Eckert, *Effect of substrate material on the growth and field emission characteristics of large-area carbon nanotube forests*, Journal of Applied Physics 119 (2016) Nr. 4, S. 44302/1-8.
- 29) A. Charnukha, K.W. Post, S. Thirupathaiah, D. Proepper, S. Wurmehl, M. Roslova, I. Morozov, B. Buechner, A.N. Yaresko, A.V. Boris, S.V. Borisenko, D.N. Basov, *Weak-coupling superconductivity in a strongly correlated iron pnictide*, Scientific Reports 6 (2016), S. 18620/1-7.
- 30) J. Acker, S. Buecker, V. Hoffmann, *Impact of the chemical form of different fluorine sources on the formation of AlF molecules in a C₂H₂/N₂O flame*, Journal of Analytical Atomic Spectrometry 31 (2016) Nr. 4, S. 902-911.
- 31) M. Herklotz, J. Weiss, E. Ahrens, M. Yavuz, L. Mereacre, N. Kiziltas-Yavuz, C. Draeger, H. Ehrenberg, J. Eckert, F. Fauth, L. Giebeler, M. Knapp, *A novel high-throughput setup for in situ powder diffraction on coin cell batteries*, Journal of Applied Crystallography 49 (2016) Nr. 1, S. 340-345.
- 32) U.B. Arnalds, J. Chico, H. Stopfel, V. Kapaklis, O. Baerenhold, M.A. Verschuuren, U. Wolff, V. Neu, A. Bergman, B. Hjoervarsson, *A new look on the two-dimensional Ising model: thermal artificial spins*, New Journal of Physics 18 (2016), S. 23008/1-8.
- 33) R. Streubel, F. Kronast, C.F. Reiche, T. Muehl, A.U.B. Wolter, O.G. Schmidt, D. Makarov, *Vortex circulation and polarity patterns in closely packed cap arrays*, Applied Physics Letters 108 (2016) Nr. 4, S. 42407/1-4.
- 34) S. Kumar Srivastava, M. Medina-Sanchez, B. Koch, O.G. Schmidt, *Medibots: Dual-Action Biogenic Microdaggers for Single-Cell Surgery and Drug Release*, Advanced Materials 28 (2016) Nr. 5, S. 832-837.
- 35) Y. Chen, J. Zhang, M. Zopf, K. Jung, Y. Zhang, R. Keil, F. Ding, O.G. Schmidt, *Wavelength-tunable entangled photons from silicon-integrated III-V quantum dots*, Nature Communications 7 (2016), S. 10387/1-7.
- 36) U. Stoeck, J. Balach, M. Klose, D. Wadewitz, E. Ahrens, J. Eckert, L. Giebeler, *Reconfiguration of lithium sulphur batteries: „Enhancement of Li-S cell performance by employing a highly porous conductive separator coating“*, Journal of Power Sources 309 (2016), S. 76-81.
- 37) J. Romberg, J. Freudenberger, H. Bauder, G. Plattner, H. Krug, F. Hollaender, J. Scharnweber, A. Eschke, U. Kuehn, H. Klauss, C.-G. Oertel, W. Skrotzki, J. Eckert, L. Schultz, *Ti/Al Multi-Layered Sheets: Accumulative Roll Bonding (Part A)*, Metals 6 (2016) Nr. 2, S. 30/1-14.
- 38) J. Romberg, J. Freudenberger, H. Watanabe, J. Scharnweber, A. Eschke, U. Kuehn, H. Klauss, C.-G. Oertel, W. Skrotzki, J. Eckert, L. Schultz, *Ti/Al Multi-Layered Sheets: Differential Speed Rolling (Part B)*, Metals 6 (2016) Nr. 2, S. 31/1-15.
- 39) J. Fink, *Influence of Lifshitz transitions and correlation effects on the scattering rates of the charge carriers in iron-based superconductors*, epl 113 (2016) Nr. 2, S. 27002/1-6.
- 40) K.E. Metlushka, D.N. Sadkova, L.N. Shaimardanova, K.A. Nikitina, K.A. Ivshin, D.R. Islamov, O.N. Kataeva, A.V. Alfonsov, V.E. Kataev, A.D. Voloshina, L.N. Punegova, V.A. Alfonsov, *First coordination polymers on the bases of chiral thiophosphorylated thioureas*, Inorganic Chemistry Communications 66 (2016), S. 11-14.
- 41) A. Stepanov, A. Mustafina, R.G. Mendes, M.H. Ruemmeli, T. Gemming, E. Popova, I. Nizameev, M. Kadirov, *Impact of heating mode in synthesis of monodisperse iron-oxide nanoparticles via oleate decomposition*, Journal of the Iranian Chemical Society 13 (2016) Nr. 2, S. 299-305.

- 42) D. Pohl, C. Damm, D. Pohl, L. Schultz, H. Schloerb, *TEM investigations on the local microstructure of electrodeposited galfenol nanowires*, Nanotechnology 27 (2016) Nr. 3, S. 35705/1-9.
- 43) H. Turnow, H. Wendrock, S. Menzel, T. Gemming, J. Eckert, *Structure and properties of sputter deposited crystalline and amorphous Cu-Ti films*, Thin Solid Films 598 (2016), S. 184-188.
- 44) H.Y. Jung, M. Stoica, S. Yi, D.H. Kim, J. Eckert, *Preparation of cast-iron-based nanocrystalline alloy with Cu and Nb addition*, Intermetallics 69 (2016), S. 54-61.
- 45) J.-K. Lee, S.-Y. Kim, R.T. Ott, J.-Y. Kim, J. Eckert, M.-H. Lee, *Effect of reinforcement phase on the mechanical property of tungsten nanocomposite synthesized by spark plasma sintering*, International Journal of Refractory Metals and Hard Materials 54 (2016), S. 14-18.
- 46) K. Witte, W. Bodnar, T. Mix, N. Schell, G. Fulda, T.G. Woodcock, A. Burkel, *A detailed study on the transition from the blocked to the superparamagnetic state of reduction-precipitated iron oxide nanoparticles*, Journal of Magnetism and Magnetic Materials 403 (2016), S. 103-113.
- 47) L. Zhang, S. Pauly, M.Q. Tang, J. Eckert, H.F. Zhang, *Two-phase quasi-equilibrium in β -type Ti-based bulk metallic glass composites*, Scientific Reports 6 (2016), S. 19235/1-10.
- 48) N. Forouzanmehr, M. Nili-Ahmadabadi, M.S. Khoshkhoo, *On the microstructure and mechanical properties of severely cold shape rolled Cu*, Materials Science and Engineering A 650 (2016), S. 264-272.
- 49) S. Demura, M. Tanaka, A. Yamashita, S.J. Denholme, H. Okazaki, M. Fujioka, T. Yamaguchi, H. Takeya, K. Iida, B. Holzapfel, H. Sakata, Y. Takano, *Electrochemical Deposition of FeSe on RABiTS Tapes*, Journal of the Physical Society of Japan 85 (2016) Nr. 1, S. 15001/1-2.
- 50) S. Kumar Srivastava, M. Guix, O.G. Schmidt, *Wastewater Mediated Activation of Micromotors for Efficient Water Cleaning*, Nano Letters 16 (2016) Nr. 1, S. 817-821.
- 51) S. Rex, F.S. Nogueira, A. Sudboe, *Nonlocal topological magnetoelectric effect by Coulomb interaction at a topological insulator-ferromagnet interface*, Physical Review B 93 (2016), S. 14404/1-6.
- 52) G.K. Rane, M. Seifert, S. Menzel, T. Gemming, J. Eckert, *Tungsten as a Chemically-Stable Electrode Material on Ga-Containing Piezoelectric Substrates Languisite and Catangasite for High-Temperature SAW Devices*, Materials 9 (2016) Nr. 2, S. 101/1-9.
- 53) A. Chirkova, K.P. Skokov, L. Schultz, N.V. Baranov, O. Gutfleisch, T.G. Woodcock, *Giant adiabatic temperature change in FeRh alloys evidenced by direct measurements under cyclic conditions*, Acta Materialia 106 (2016), S. 15-21.
- 54) D.I. Gorbunov, M.S. Henriques, A.V. Andreev, Y. Skourski, M. Richter, L. Havela, J. Wosnitza, *First-order magnetization process as a tool of magnetic-anisotropy determination: Application to the uranium-based intermetallic $U_3Cu_4Ge_4$* , Physical Review B 93 (2016) Nr. 6, S. 64417/1-7.
- 55) B. Rasche, A. Isaeva, M. Ruck, K. Koepf, M. Richter, J. van den Brink, *Correlation between topological band character and chemical bonding in a $Bi_{14}Rh_{31}I_9$ -based family of insulators*, Scientific Reports 6 (2016), S. 20645/1-7.
- 56) K. Duschek, D. Pohl, S. Faehler, K. Nielsch, K. Leistner, *Research Update: Magnetoionic control of magnetization and anisotropy in layered oxide/metal heterostructures*, APL Materials 4 (2016) Nr. 3, S. 32301/1-10.
- 57) X. Wang, Y. Chen, O.G. Schmidt, C. Yan, *Engineered nanomembranes for smart energy storage devices*, Chemical Society Reviews 45 (2016) Nr. 5, S. 1308-1330.
- 58) Z. Weiss, E.B.M. Steers, S. Mushtaq, V. Hoffmann, J.C. Pickering, *The use of radiative transition rates to study the changes in the excitation of Cu ions in a Ne glow discharge caused by small additions of H_2 , O_2 and N_2* , Spectrochimica Acta Part B: Atomic Spectroscopy 118 (2016), S. 81-89.
- 59) S. Mushtaq, E.B.M. Steers, G. Churchill, D. Barnhart, V. Hoffmann, J.C. Pickering, K. Putyera, *Does asymmetric charge transfer play an important role as an ionization mode in low power-low pressure glow discharge mass spectrometry?*, Spectrochimica Acta Part B: Atomic Spectroscopy 118 (2016), S. 56-61.
- 60) I.G. Gonzalez-Martinez, T. Gemming, R. Mendes, A. Bachmatiuk, V. Bezugly, J. Kunstmann, J. Eckert, G. Cuniberti, M.H. Ruemmel, *In-situ Quasi-Instantaneous e-beam Driven Catalyst-Free Formation Of Crystalline Aluminum Borate Nanowires*, Scientific Reports 6 (2016), S. 22524/1-9.
- 61) M. Guix, A.K. Meyer, B. Koch, O.G. Schmidt, *Carbonate-based Janus micromotors moving in ultra-light acidic environment generated by HeLa cells in situ*, Scientific Reports 6 (2016), S. 21701/1-7.
- 62) R. Niemann, S. Hahn, A. Diestel, A. Backen, L. Schultz, K. Nielsch, M.F.-X. Wagner, S. Faehler, *Reducing the nucleation barrier in magnetocaloric Heusler alloys by nanoindentation*, APL Materials 4 (2016) Nr. 6, S. 64101/1-7.
- 63) D.-N. Cho, J. van den Brink, H. Fehske, K.W. Becker, S. Sykora, *Unconventional superconductivity and interaction induced Fermi surface reconstruction in the two-dimensional Edwards model*, Scientific Reports 6 (2016), S. 22548/1-6.

- 64) R.O. Rezaev, E.A. Levchenko, V.M. Fomin, *Branching of the vortex nucleation period in superconductor Nb microtubes due to an inhomogeneous transport current*, Superconductor Science and Technology 29 (2016) Nr. 4, S. 45014/1-7.
- 65) A. Surrey, C. Bonatto Minella, N. Fechner, M. Antonietti, H.-J. Grafe, L. Schultz, B. Rellinghaus, *Improved hydrogen storage properties of LiBH₄ via nanoconfinement in micro- and mesoporous aerogel-like carbon*, International Journal of Hydrogen Energy 41 (2016) Nr. 12, S. 5540-5548.
- 66) M.R. da Silva, P. Gargarella, T. Gustmann, W.J. Botta Filho, C.S. Kiminami, J. Eckert, S. Pauly, C. Bolfarini, *Laser surface remelting of a Cu-Al-Ni-Mn shape memory alloy*, Materials Science and Engineering A 661 (2016), S. 61-67.
- 67) C.-Y. Yin, M.-F. Ng, B.-M. Goh, M. Saunders, N. Hill, Z.-T. Jiang, J. Balach, M. El-Harbawi, *Probing the interactions of phenol with oxygenated functional groups on curved fullerene-like sheets in activated carbon*, Physical Chemistry Chemical Physics 18 (2016) Nr. 5, S. 3700-3705.
- 68) L.B. Ma, S.L. Li, V.M. Fomin, M. Hentschel, J.B. Goette, Y. Yin, M.R. Jorgensen, O.G. Schmidt, *Spin-orbit coupling of light in asymmetric microcavities*, Nature Communications 7 (2016), S. 10983/1-6.
- 69) L. Fu, Y. Sun, N. Wu, R.G. Mendes, L. Chen, Z. Xu, T. Zhang, M.H. Ruemmeli, B. Rellinghaus, D. Pohl, L. Zhuang, L. Fu, *Direct Growth of MoS₂/h-BN Heterostructures via a Sulfide-Resistant Alloy*, ACS Nano 10 (2016) Nr. 2, S. 2063-2070.
- 70) S. Wicht, S.H. Wee, O. Hellwig, V. Mehta, S. Jain, D. Weller, B. Rellinghaus, *Atomic resolution strain analysis in highly textured FePt thin films*, Journal of Applied Physics 119 (2016) Nr. 11, S. 115301/1-8.
- 71) O.V. Pylypovskiy, D.D. Sheka, V.P. Kravchuk, K.V. Yershov, D. Makarov, Y. Gaididei, *Rashba Torque Driven Domain Wall Motion in Magnetic Helices*, Scientific Reports 6 (2016), S. 23316/1-11.
- 72) H. Shakur Shahabi, S. Scudino, I. Kaban, M. Stoica, B. Escher, S. Menzel, G.B.M. Vaughan, U. Kuehn, J. Eckert, *Mapping of residual strains around a shear band in bulk metallic glass by nanobeam X-ray diffraction*, Acta Materialia 111 (2016), S. 187-193.
- 73) I. Pethes, V. Nazabal, R. Chahal, B. Bureau, I. Kaban, S. Belin, P. Jovari, *Local motifs in GeS₂-Ga₂S₃ glasses*, Journal of Alloys and Compounds 673 (2016), S. 149-157.
- 74) J. Rogers, Y. Huang, O.G. Schmidt, D.H. Gracias, *Origami MEMS and NEMS*, MRS Bulletin 41 (2016) Nr. 2, S. 123-129.
- 75) M. Bendova, C.C. Bof Bufon, V.M. Fomin, S. Gorantla, M.H. Ruemmeli, O.G. Schmidt, *Electrical Properties of Hybrid Nanomembrane/Nanoparticle Heterojunctions: The Role of Inhomogeneous Arrays*, The Journal of Physical Chemistry C 120 (2016) Nr. 12, S. 6891-6899.
- 76) M.-I. Richard, A. Malachias, M. Stoffel, T. Merdzhanova, O.G. Schmidt, G. Renaud, T.H. Metzger, T.U. Schuelli, *Temperature evolution of defects and atomic ordering in Si_{1-x}Ge_x islands on Si(001)*, Journal of Applied Physics 119 (2016) Nr. 8, S. 085704/1-10.
- 77) D. Stephan, J. Bhattacharyya, Y.-H. Huo, O.G. Schmidt, A. Rastelli, M. Helm, H. Schneider, *Inter-sublevel dynamics in single InAs/GaAs quantum dots induced by strong terahertz excitation*, Applied Physics Letters 108 (2016) Nr. 8, S. 82107/1-4.
- 78) A. Bogusz, O.S. Choudhary, I. Skorupa, D. Buerger, A. Lawrenz, Y. Lei, H. Zeng, B. Abendroth, H. Stoecker, O.G. Schmidt, H. Schmidt, *Photocapacitive light sensor based on metal-YSMnO₃-insulator-semiconductor structures*, Applied Physics Letters 108 (2016) Nr. 5, S. 052103/1-5.
- 79) X. Lu, L. Zhang, X. Sun, W. Si, C. Yan, O.G. Schmidt, *Bifunctional Au-Pd decorated MnO_x nanomembranes as cathode materials for Li-O₂ batteries*, Journal of Materials Chemistry A 4 (2016) Nr. 11, S. 4155-4160.
- 80) J. Zhang, Y. Huo, F. Ding, O.G. Schmidt, *Energy-tunable single-photon light-emitting diode by strain fields*, Applied Physics B 122 (2016) Nr. 1, S. 1-7.
- 81) T. You, L.P. Selvaraj, H. Zeng, W. Luo, N. Du, D. Buerger, I. Skorupa, S. Prucnal, A. Lawrenz, T. Mikolajick, O.G. Schmidt, H. Schmidt, *An Energy-Efficient, BiFeO₃-Coated Capacitive Switch with Integrated Memory and Demodulation Functions*, Advanced Electronic Materials 2 (2016) Nr. 3, S. 1500352/1-9.
- 82) P. Chen, T. Etzelstorfer, F. Hackl, N.A. Katcho, H.-T. Chang, L. Nausner, S.-W. Lee, T. Fromherz, J. Stangl, O.G. Schmidt, N. Mingo, A. Rastelli, *Evolution of thermal, structural, and optical properties of SiGe superlattices upon thermal treatment*, Physica Status Solidi A 213 (2016) Nr. 3, S. 533-540.
- 83) G. Li, D. Grimm, V. Engemaier, S. Loesch, K. Manga, V.K. Bandari, F. Zhu, O.G. Schmidt, *Hybrid semiconductor/metal nanomembrane superlattices for thermoelectric application*, Physica Status Solidi A 213 (2016) Nr. 3, S. 620-625.
- 84) A. Koitzsch, N. Heming, M. Knupfer, B. Buechner, P.Y. Portnichenko, A.V. Dukhnenko, N.Y. Shitsevalova, V.B. Filipov, L.L. Lev, V.N. Strocov, J. Ollivier, D.S. Inosov, *Nesting-driven multipolar order in CeB₆ from photoemission tomography*, Nature Communications 7 (2016), S. 10876/1-7.
- 85) S. Johnston, C. Monney, V. Bisogni, K.-J. Zhou, R. Kraus, G. Behr, V.N. Strocov, J. Malek, S.-L. Drechsler, J. Geck, T. Schmitt, J. van den Brink, *Electron-lattice interactions strongly renormalize the charge-transfer energy in the spin-chain cuprate Li₂CuO₂*, Nature Communications 7 (2016), S. 10563/1-7.

- 86) A. Winkler, A. Kirchner, P. Bergelt, R. Huehne, S. Menzel, *Thin film deposition based on microacoustic sol atomization (MASA)*, Journal of Sol-Gel Science and Technology 78 (2016) Nr. 1, S. 26–33.
- 87) L. Opherden, M. Sieger, P. Pahlke, R. Huehne, L. Schultz, A. Meledin, G. Van Tendeloo, R. Nast, B. Holzapfel, M. Bianchetti, J.L. MacManus-Driscoll, J. Haenisch, *Large pinning forces and matching effects in $\text{YBa}_2\text{Cu}_3\text{O}_{7-\delta}$ thin films with $\text{Ba}_2\text{Y}(\text{Nb}/\text{Ta})\text{O}_6$ nano-precipitates*, Scientific Reports 6 (2016), S. 21188/1–10.
- 88) B.H. Stafford, M. Sieger, O. Troshyn, R. Huehne, J. Haenisch, M. Bauer, B. Holzapfel, L. Schultz, *Pinning Centers in ISD-MgO Coated Conductors via EB-PVD*, IEEE Transactions on Applied Superconductivity 26 (2016) Nr. 3, S. 6601105/1–5.
- 89) M. Sparing, A. Berger, F. Wall, V. Lux, S. Hameister, D. Berger, M. Hossain, A. Abdkader, G. Fuchs, C. Cherif, L. Schultz, *Dynamics of Rotating Superconducting Magnetic Bearings in Ring Spinning*, IEEE Transactions on Applied Superconductivity 26 (2016) Nr. 3, S. 3600804/1–4.
- 90) A. Berger, M. Hossain, M. Sparing, D. Berger, G. Fuchs, A. Abdkader, C. Cherif, L. Schultz, *Cryogenic System for the Integration of a Ring-Shaped SMB in a Ring-Spinning Tester*, IEEE Transactions on Applied Superconductivity 26 (2016) Nr. 3, S. 3601105/1–5.
- 91) S. Nishimoto, V.M. Katukuri, V. Yushankhai, H. Stoll, U.K. Roessler, L. Hozoi, I. Rousochatzakis, J. van den Brink, *Strongly frustrated triangular spin lattice emerging from triplet dimer formation in honeycomb Li_2IrO_3* , Nature Communications 7 (2016), S. 10273/1–7.
- 92) I. Razdolski, D. Makarov, O.G. Schmidt, A. Kirilyuk, T. Rasing, V.V. Temnov, *Nonlinear Surface Magnetoplasmonics in Kretschmann Multilayers*, ACS Photonics 3 (2016) Nr. 2, S. 179–183.
- 93) X.L. Bian, G. Wang, H.C. Chen, L. Yan, J.G. Wang, Q. Wang, P.F. Hu, J.L. Ren, K.C. Chan, N. Zheng, A. Teresiak, Y.L. Gao, Q.J. Zhai, J. Eckert, J. Beadsworth, K.A. Dahmen, P.K. Liaw, *Manipulation of free volumes in a metallic glass through Xe-ion irradiation*, Acta Materialia 106 (2016), S. 66–77.
- 94) J. Zhang, X. Liu, G. Neri, N. Pinna, *Nanostructured Materials for Room-Temperature Gas Sensors*, Advanced Materials 28 (2016) Nr. 5, S. 795–831.
- 95) L.H. Karlsson, J. Birch, A. Mockute, A.S. Ingason, H.Q. Ta, M.H. Rummeli, J. Rosen, P.O.A. Persson, *Residue reduction and intersurface interaction on single graphene sheets*, Carbon 100 (2016), S. 345–350.
- 96) J. Zeisig, J. Hufenbach, H. Wendrock, T. Gemming, J. Eckert, U. Kuehn, *A study of the micro- and nanoscale deformation behavior of individual austenitic dendrites in a FeCrMoVC cast alloy using micro- and nanoindentation experiments*, Applied Physics Letters 108 (2016) Nr. 14, S. 143103/1–5.
- 97) K. Lejaeghere, G. Bihlmayer, T. Bjorkman, P. Blaha, S. Bluegel, V. Blum, D. Caliste, I.E. Castelli, S.J. Clark, A. Dal Corso, S. de Gironcoli, T. Deutsch, J.K. Dewhurst, I. Di Marco, C. Draxl, M. Dulak, O. Eriksson, J.A. Flores-Livas, K.F. Garrity, L. Genovese, P. Giannozzi, M. Giantomassi, S. Goedecker, X. Gonze, O. Granaes, E.K.U. Gross, A. Gulans, F. Gygi, D.R. Hamann, J.P. Hasnig, N.A.W. Holzwarth, D. Iusan, D.B. Jochym, F. Jollet, D. Jones, G. Kresse, K. Koepernik, E. Kuecuekbenli, Y.O. Kvashnin, I.L.M. Locht, S. Lubeck, M. Marsman, N. Marzari, U. Nitzsche, L. Nordstroem, T. Ozaki, L. Paulatto, C.J. Pickard, W. Poelmans, M.I.J. Probert, K. Refson, M. Richter, G.-M. Rignanese, S. Saha, M. Scheffler, M. Schlipf, K. Schwarz, S. Sharma, F. Tavazza, P. Thunstroem, A. Tkatchenko, M. Torrent, D. Vanderbilt, M.J. van Setten, V. van Speybroeck, J.M. Wills, J.R. Yates, G.-X. Zhang, S. Cottenier, *Reproducibility in density functional theory calculations of solids*, Science 351 (2016) Nr. 6280, S. 123–262.
- 98) C. Pauly, B. Rasche, K. Koepernik, M. Richter, S. Borisenko, M. Liebmann, M. Ruck, J. van den Brink, M. Morgenstern, *Electronic Structure of the Dark Surface of the Weak Topological Insulator $\text{Bi}_{14}\text{Rh}_3\text{I}_9$* , ACS Nano 10 (2016) Nr. 4, S. 3995–4003.
- 99) R. Schmidt, V. Hoffmann, A. Helth, P.F. Gostin, M. Calin, J. Eckert, A. Gebert, *Electrochemical deposition of hydroxyapatite on beta-Ti-40Nb*, Surface and Coatings Technology 294 (2016), S. 186–193.
- 100) Y. Zhang, T. Kaempfe, G. Bai, M. Mietschke, F. Yuan, M. Zopf, S. Abel, L.M. Eng, R. Huehne, J. Fompeyrine, F. Ding, O.G. Schmidt, *Upconversion photoluminescence of epitaxial $\text{Yb}^{3+}/\text{Er}^{3+}$ codoped ferroelectric $\text{Pb}(\text{Zr,Ti})\text{O}_3$ films on silicon substrates*, Thin Solid Films 607 (2016), S. 32–35.
- 101) A.R. Jalil, H. Chang, V.K. Bandari, P. Robaschik, J. Zhang, P.F. Siles, G. Li, D. Buerger, D. Grimm, X. Liu, G. Salvan, D.R.T. Zahn, F. Zhu, H. Wang, D. Yan, O.G. Schmidt, *Fully Integrated Organic Nanocrystal Diode as High Performance Room Temperature NO_2 Sensor*, Advanced Materials 28 (2016) Nr. 15, S. 2971–2977.
- 102) M.S. Arshad, M.P. Proenca, S. Trafela, V. Neu, U. Wolff, S. Stienen, M. Vazquez, S. Kobe, K.Z. Rozman, *The role of the crystal orientation (c-axis) on switching field distribution and the magnetic domain configuration in electrodeposited hcp Co-Pt nanowires*, Journal of Physics D: Applied Physics 49 (2016) Nr. 18, S. 185006/1–13.
- 103) T. Gustmann, A. Neves, U. Kuehn, P. Gargarella, C.S. Kiminami, C. Bolfarini, J. Eckert, S. Pauly, *Influence of processing parameters on the fabrication of a Cu-Al-Ni-Mn shape-memory alloy by selective laser melting*, Additive Manufacturing 11 (2016), S. 23–31.

- 104) J. Sander, J. Hufenbach, U. Kuehn, *Verbesserung der mechanischen Eigenschaften durch Gefügefeinung bei geometrischer Gestaltungsfreiheit*, Konstruktion 4 (2016), S. 14-16.
- 105) C. Konczak, V. Haehnel, L. Schultz, H. Schloerb, *Adjusting the phase structure of electrodeposited Fe-Pd films*, Materials Chemistry and Physics 174 (2016), S. 150-155.
- 106) M. Nicoara, A. Raduta, R. Parthiban, C. Locovei, J. Eckert, M. Stoica, *Low Young's modulus Ti-based porous bulk glassy alloy without cytotoxic elements*, Acta Biomaterialia 36 (2016), S. 323-331.
- 107) M. Haft, M. Groenke, M. Gellesch, S. Wurmehl, B. Buechner, M. Mertig, S. Hampel, *Tailored nanoparticles and wires of Sn, Ge and Pb inside carbon nanotubes*, Carbon 101 (2016), S. 352-360.
- 108) A.A. Eliseev, N.I. Verbitskiy, A.A. Volykhov, A.V. Fedorov, O.Y. Vilkov, I.I. Verbitskiy, M.M. Brzhezinskaya, N.A. Kiselev, L.V. Yashina, *The impact of dimensionality and stoichiometry of CuBr on its coupling to sp^2 -carbon*, Carbon 99 (2016), S. 619-623.
- 109) K.C. Rippy, E.V. Bukovsky, T.T. Clikeman, Y.-S. Chen, G.-L. Hou, X.-B. Wang, A.A. Popov, O.V. Boltalina, S.H. Strauss, *Copper Causes Regiospecific Formation of C_4F_8 -Containing Six-Membered Rings and their Defluorination/Aromatization to C_4F_4 -Containing Rings in Triphenylene/ $1,4-C_4F_8I_2$ Reactions*, Chemistry - A European Journal 22 (2016) Nr. 3, S. 874-877.
- 110) B. Gadgil, P. Damlin, E. Dmitrieva, T. Aeaeritalo, C. Kvarnstrom, *Exploring amide linkage in a polyviologen derivative towards simultaneous voltammetric determination of Pb(II), Cu(II) and Hg(II) ions*, Electrochimica Acta 192 (2016), S. 482-488.
- 111) X. Tong, G. Wang, J. Yi, J.L. Ren, S. Pauly, Y.L. Gao, Q.J. Zhai, N. Mattern, K.A. Dahmen, P.K. Liaw, J. Eckert, *Shear avalanches in plastic deformation of a metallic glass composite*, International Journal of Plasticity 77 (2016), S. 141-155.
- 112) P. Gargarella, S. Pauly, M.S. Khoshkhoo, C.S. Kiminami, U. Kuehn, J. Eckert, *Improving the glass-forming ability and plasticity of a TiCu-based bulk metallic glass composite by minor additions of Si*, Journal of Alloys and Compounds 663 (2016), S. 531-539.
- 113) E.M. Paschalidou, F. Scaglione, A. Gebert, S. Oswald, P. Rizzi, L. Battezzati, *Partially and fully de-alloyed glassy ribbons based on Au: Application in methanol electro-oxidation studies*, Journal of Alloys and Compounds 667 (2016), S. 302-309.
- 114) K. Manna, S. Elizabeth, P.S.A. Kumar, *Anomalous re-entrant glassy magnetic phase in $LaMn_{0.5}Co_{0.5}O_3$ single crystals*, Journal of Applied Physics 119 (2016) Nr. 4, S. 43906/1-6.
- 115) S. Nayak, D.C. Joshi, M. Krautz, A. Waske, J. Eckert, S. Thota, *Reentrant spin-glass behavior and bipolar exchange-bias effect in 'Sn' substituted cobalt-orthotitanate*, Journal of Applied Physics 119 (2016) Nr. 4, S. 43901/1-12.
- 116) K.E. Hnida, S. Baessler, J. Mech, K. Szacilowski, R.P. Socha, M. Gajewska, K. Nielsch, M. Przybylski, G.D. Sulka, *Electrochemically deposited nanocrystalline InSb thin films and their electrical properties*, Journal of Materials Chemistry C 4 (2016) Nr. 6, S. 1345-1350.
- 117) M. Shaygan, K. Davami, B. Jin, T. Gemming, J.-S. Lee, M. Meyyappan, *Highly sensitive photodetectors using ZnTe/ZnO core/shell nanowire field effect transistors with a tunable core/shell ratio*, Journal of Materials Chemistry C 4 (2016) Nr. 10, S. 2040-2046.
- 118) F. Schmieder, M.E. Kinaci, J. Wartmann, J. Koenig, L. Buettner, J. Czarske, S. Burgmann, A. Heinzl, *Investigation of the flow field inside the manifold of a real operated fuel cell stack using optical measurements and Computational Fluid Mechanics*, Journal of Power Sources 304 (2016), S. 155-163.
- 119) Q. Deng, J. Zhao, *Triggering One-Dimensional Phase Transition with Defects at the Graphene Zigzag Edge*, Nano Letters 16 (2016) Nr. 2, S. 1244-1249.
- 120) Q. Deng, T. Heine, S. Irle, A.A. Popov, *Self-assembly of endohedral metallofullerenes: a decisive role of cooling gas and metal-carbon bonding*, Nanoscale 8 (2016) Nr. 6, S. 3796-3808.
- 121) P.Y. Portnichenko, J. Romhanyi, Y.A. Onykienko, A. Henschel, M. Schmidt, A.S. Cameron, M.A. Surmach, J.A. Lim, J.T. Park, A. Schneidewind, D.L. Abernathy, H. Rosner, J. van den Brink, D.S. Inosov, *Magnon spectrum of the helimagnetic insulator Cu_2OSeO_3* , Nature Communications 7 (2016), S. 10725/1-8.
- 122) T.H. Ly, D.J. Perello, J. Zhao, Q. Deng, H. Kim, G.H. Han, S.H. Chae, H.Y. Jeong, Y.H. Lee, *Misorientation-angle-dependent electrical transport across molybdenum disulfide grain boundaries*, Nature Communications 7 (2016), S. 10426/1-7.
- 123) R. Trotta, J. Martin-Sanchez, J.S. Wildmann, G. Piredda, M. Reindl, C. Schimpf, E. Zallo, S. Stroj, J. Edlinger, A. Rastelli, *Wavelength-tunable sources of entangled photons interfaced with atomic vapours*, Nature Communications 7 (2016), S. 10735/1-7.
- 124) T. Dey, A. Maljuk, D.V. Efremov, O. Kataeva, S. Gass, C.F.G. Blum, F. Steckel, D. Gruner, T. Ritschel, A.U.B. Wolter, J. Geck, C. Hess, K. Koepernik, J. van den Brink, S. Wurmehl, B. Buechner, *Ba_2YIrO_6 : A cubic double perovskite material with Ir^{5+} ions*, Physical Review B 93 (2016) Nr. 1, S. 14434/1-7.
- 125) J.W.F. Venderbos, M. Manzardo, D.V. Efremov, J. van den Brink, C. Ortix, *Engineering interaction-induced topological insulators in a (square root of) $3 \times$ (square root of) 3 substrate-induced honeycomb superlattice*, Physical Review B 93 (2016) Nr. 4, S. 45428/1-5.
- 126) L. Doering, C. Hengst, F. Otto, R. Schaefer, *Interacting tails of asymmetric domain walls: Theory and experiments*, Physical Review B 93 (2016) Nr. 2, S. 24414/1-10.

- 127) G.S. Tucker, J.S. White, J. Romhányi, D. Szaller, I. Kezsmarki, B. Roessli, U. Stuhr, A. Magrez, F. Groitl, P. Babkevich, P. Huang, I. Zivkovic, H.M. Ronnow, *Spin excitations in the skyrmion host Cu_2OSeO_3* , Physical Review B 93 (2016) Nr. 5, S. 54401/1-5.
- 128) B. Willenberg, M. Schaepers, A.U.B. Wolter, S.-L. Drechsler, M. Reehuis, J.-U. Hoffmann, B. Buechner, A.J. Studer, K.C. Rule, B. Ouladdiaf, S. Suellow, S. Nishimoto, *Complex Field-Induced States in Linarite $\text{PbCuSO}_4(\text{OH})_2$ with a Variety of High-Order Exotic Spin-Density Wave States*, Physical Review Letters 116 (2016) Nr. 4, S. 47202/1-5.
- 129) M. Madian, M. Klose, T. Jaumann, A. Gebert, S. Oswald, N. Ismail, A. Eychmueller, J. Eckert, L. Giebeler, *Anodically fabricated TiO_2 - SnO_2 nanotubes and their application in lithium ion batteries*, Journal of Materials Chemistry A 4 (2016) Nr. 15, S. 5542-5552.
- 130) E.M. Plotnikova, M. Daghofer, J. van den Brink, K. Wohlfeld, *Jahn-Teller Effect in Systems with Strong On-Site Spin-Orbit Coupling*, Physical Review Letters 116 (2016) Nr. 10, S. 106401/1-5.
- 131) A.P. Dioguardi, T. Kissikov, C.H. Lin, K.R. Shirer, M.M. Lawson, J.-H. Grafe, J.-H. Chu, I.R. Fisher, R.M. Fernandes, N.J. Curro, *NMR Evidence for Inhomogeneous Nematic Fluctuations in $\text{BaFe}_2(\text{As}_{1-x}\text{P}_x)_2$* , Physical Review Letters 116 (2016) Nr. 10, S. 107202/1-5.
- 132) S. Reja, J. van den Brink, S. Nishimoto, *Strongly Enhanced Superconductivity in Coupled t-J Segments*, Physical Review Letters 116 (2016) Nr. 6, S. 67002/1-5.
- 133) A.J. Achkar, M. Zwiebler, C. McMahon, F. He, R. Sutarto, I. Djianto, Z. Hao, M.J.P. Gingras, M. Huecker, G.D. Gu, A. Revcolevschi, H. Zhang, Y.-J. Kim, J. Geck, D.G. Hawthorn, *Nematicity in stripe-ordered cuprates probed via resonant x-ray scattering*, Science 351 (2016) Nr. 6273, S. 576-578.
- 134) Z. Yan, K. Song, Y. Hu, F. Dai, Z. Chu, J. Eckert, *Localized crystallization in shear bands of a metallic glass*, Scientific Reports 6 (2016), S. 19358/1-7.
- 135) I.H. Son, J.H. Park, S. Kwon, J.W. Choi, M.H. Ruemmeli, *Graphene Coating of Silicon Nanoparticles with CO_2 -Enhanced Chemical Vapor Deposition*, Small 12 (2016) Nr. 5, S. 658-667.
- 136) M. Guettler, A. Generalov, M.M. Otrokov, K. Kummer, K. Kliemt, A. Fedorov, A. Chikina, S. Danzenbaeher, S. Schulz, E.V. Chulkov, Y.M. Koroteev, N. Caroca-Canales, M. Shi, M. Radovic, C. Geibel, C. Laubschat, P. Dudin, T.K. Kim, M. Hoesch, C. Krellner, D.V. Vyalikh, *Robust and tunable itinerant ferromagnetism at the silicon surface of the antiferromagnet GdRh_2Si_2* , Scientific Reports 6 (2016), S. 24254/1-11.
- 137) M. Chernysheva, C. Mou, R. Arif, M. AlAraimi, M. Ruemmerli, S. Turitsyn, A. Rozhin, *High Power Q-Switched Thulium Doped Fibre Laser using Carbon Nanotube Polymer Composite Saturable Absorber*, Scientific Reports 6 (2016), S. 24220/1-10.
- 138) I. Rousochatzakis, U.K. Roessler, J. van den Brink, M. Daghofer, *Kitaev anisotropy induces mesoscopic Z2 vortex crystals in frustrated hexagonal antiferromagnets*, Physical Review B 93 (2016) Nr. 10, S. 104417/1-16.
- 139) S. Reja, J. van den Brink, S. Kumar, *Electronic route to stabilize nanoscale spin textures in itinerant frustrated magnets*, Physical Review B 93 (2016) Nr. 15, S. 155115/1-5.
- 140) G. Prando, R. Dally, W. Schottenhamel, Z. Guguchia, S.-H. Baek, R. Aeschlimann, A.U.B. Wolter, S.D. Wilson, B. Buechner, M.J. Graf, *Influence of hydrostatic pressure on the bulk magnetic properties of $\text{Eu}_2\text{Ir}_2\text{O}_7$* , Physical Review B 93 (2016) Nr. 10, S. 104422/1-8.
- 141) R. Lou, Y. Cai, Z. Liu, T. Qian, L. Zhao, Y. Li, K. Liu, Z. Han, D. Zhang, J. He, G. Chen, H. Ding, S. Wang, *Interplay between multiple charge-density waves and the relationship with superconductivity in Pd_xHoTe_3* , Physical Review B 93 (2016) Nr. 11, S. 115133/1-6.
- 142) P.V. Leksin, N.N. Garif'yanov, A.A. Kamashev, A.A. Validov, Y.V. Fominov, J. Schumann, V. Kataev, J. Thomas, B. Buechner, I.A. Garifullin, *Isolation of proximity-induced triplet pairing channel in a superconductor/ferromagnet spin valve*, Physical Review B 93 (2016) Nr. 10, S. 100502/1-5.
- 143) S. Bhattacharjee, S. Erfanifam, E.L. Green, M. Naumann, Z. Wang, S. Granovsky, M. Doerr, J. Wosnitza, A.A. Zvyagin, R. Moessner, A. Maljuk, S. Wurmehl, B. Buechner, S. Zherlitsyn, *Acoustic signatures of the phases and phase transitions in $\text{Yb}_2\text{Ti}_2\text{O}_7$* , Physical Review B 93 (2016) Nr. 14, S. 144412/1-8.
- 144) M.F.P. Wagner, F. Voelklein, H. Reith, C. Trautmann, M.E. Toimil-Molares, *Fabrication and thermoelectrical characterization of three-dimensional nanowire networks*, Physica Status Solidi A 213 (2016) Nr. 3, S. 610-619.
- 145) M. Cassinelli, A. Romanenko, H. Reith, F. Voelklein, W. Sigle, C. Trautmann, M.E. Toimil-Molares, *Low temperature annealing effects on the stability of Bi nanowires*, Physica Status Solidi A 213 (2016) Nr. 3, S. 603-609.
- 146) S.V. Borisenko, D.V. Evtushinsky, Z.-H. Liu, I. Morozov, R. Kappenberger, S. Wurmehl, B. Buechner, A.N. Yaresko, T.K. Kim, M. Hoesch, T. Wolf, N.D. Zhigadlo, *Direct observation of spin-orbit coupling in iron-based superconductors*, Nature Physics 12 (2016), S. 311-317.
- 147) D. Vehlouw, R. Schmidt, A. Gebert, M. Siebert, K.S. Lips, M. Mueller, *Polyelectrolyte Complex Based Interfacial Drug Delivery System with Controlled Loading and Improved Release Performance for Bone Therapeutics*, Nanomaterials 6 (2016) Nr. 3, S. 53/1-21.

- 148) G. Cirillo, U.G. Spizzirri, M. Curcio, S. Hampel, O. Vittorio, D. Restuccia, N. Picci, F. Iemma, *Carbon Nanohybrids as Electro-Responsive Drug Delivery Systems*, Mini-Reviews in Medicinal Chemistry 16 (2016) Nr. 8, S. 658-667.
- 149) P. Ramasamy, M. Stoica, A.H. Taghvaei, K.G. Prashanth, R. Kumar, J. Eckert, *Kinetic analysis of the non-isothermal crystallization process, magnetic and mechanical properties of FeCoBSiNb and FeCoBSiNbCu bulk metallic glasses*, Journal of Applied Physics 119 (2016) Nr. 7, S. 73908/1-9.
- 150) P. Sergelius, J.G. Fernandez, S. Martens, M. Zocher, T. Boehnert, V.V. Martinez, V.M. de la Prida, D. Goerlitz, K. Nielsch, *Statistical magnetometry on isolated NiCo nanowires and nanowire arrays: a comparative study*, Journal of Physics D 49 (2016) Nr. 14, S. 145005/1-7.
- 151) A. Sypien, M. Stoica, T. Czeppe, *Properties of the $Ti_{40}Zr_{10}Cu_{36}Pd_{14}$ BMG Modified by Sn and Nb Additions*, Journal of Materials Engineering and Performance 25 (2016) Nr. 3, S. 800-808.
- 152) D. Makarov, M. Melzer, D. Karnaushenko, O.G. Schmidt, *Shapeable magnetoelectronics*, Applied Physics Reviews 3 (2016) Nr. 1, S. 11101/1-24.
- 153) S.V. Biryukov, A. Sotnikov, H. Schmidt, *Piezoelectric tube rotation effect owing to surface acoustic wave excitation*, Applied Physics Letters 108 (2016) Nr. 13, S. 134103/1-3.
- 154) Q. Zhang, S. Tan, R.G. Mendes, Z. Sun, Y. Chen, X. Kong, Y. Xue, M.H. Ruemmel, X. Wu, S. Chen, L. Fu, *Extremely Weak van der Waals Coupling in Vertical ReS_2 Nanowalls for High-Current-Density Lithium-Ion Batteries*, Advanced Materials 28 (2016) Nr. 13, S. 2616-2623.
- 155) P.F. Siles, T. Hahn, G. Salvan, M. Knupfer, F. Zhu, D.R.T. Zahn, O.G. Schmidt, *Tunable charge transfer properties in metal-phthalocyanine heterojunctions*, Nanoscale 8 (2016) Nr. 16, S. 8607-8617.
- 156) R. Fuge, M. Liebscher, C. Schroefl, S. Oswald, A. Leonhardt, B. Buechner, V. Mechtcherine, *Fragmentation characteristics of undoped and nitrogen-doped multiwalled carbon nanotubes in aqueous dispersion in dependence on the ultrasonication parameters*, Diamond and Related Materials 66 (2016), S. 126-134.
- 157) M. Goettlicher, M. Rohnke, A. Kunz, J. Thomas, R.A. Henning, T. Leichtweiss, T. Gemming, J. Janek, *Anodization of titanium in radio frequency oxygen discharge - Microstructure, kinetics & transport mechanism*, Solid State Ionics 290 (2016), S. 130-139.
- 158) H. Schwab, F. Palm, U. Kuehn, J. Eckert, *Microstructure and mechanical properties of the near-beta titanium alloy Ti-5553 processed by selective laser melting*, Materials and Design 105 (2016), S. 75-80.
- 159) S. Abdi, M. Boenisch, S. Oswald, M.S. Khoshkhoo, W. Gruner, M. Lorenzetti, U. Wolff, M. Calin, J. Eckert, A. Gebert, *Thermal oxidation behavior of glass-forming Ti-Zr-(Nb)-Si alloys*, Journal of Materials Research 31 (2016) Nr. 9, S. 1264-1274.
- 160) A.K. Chaubey, S. Scudino, N.K. Mukhopadhyay, J. Eckert, *Processing, microstructure and mechanical properties of Al-based metal matrix composites reinforced with mechanically alloyed particles*, Journal of Materials Research 31 (2016) Nr. 9, S. 1229-1236.
- 161) P. Pahlke, M. Lao, M. Eisterer, A. Meledin, G. Van Tendeloo, J. Haenisch, M. Sieger, A. Usoskin, J. Stroemer, B. Holzapfel, L. Schultz, R. Huehne, *Reduced J_c Anisotropy and Enhanced In-Field Performance of Thick $BaHfO_3$ -Doped $YBa_2Cu_3O_{7-\delta}$ Films on ABAD-YSZ Templates*, IEEE Transactions on Applied Superconductivity 26 (2016) Nr. 3, S. 6603104/1-4.
- 162) M. Sieger, P. Pahlke, J. Haenisch, M. Sparing, M. Bianchetti, J. MacManus-Driscoll, M. Lao, M. Eisterer, A. Meledin, G. Van Tendeloo, R. Nast, L. Schultz, B. Holzapfel, R. Huehne, *$Ba_2Y(Nb/Ta)O_6$ -Doped YBCO Films on Biaxially Textured Ni-5at.% W Substrates*, IEEE Transactions on Applied Superconductivity 26 (2016) Nr. 3, S. 7500305/1-5.
- 163) P. Pahlke, M. Sieger, P. Chekhonin, W. Skrotzki, J. Haenisch, A. Usoskin, J. Stroemer, L. Schultz, R. Huehne, *Local Orientation Variations in YBCO Films on Technical Substrates - A Combined SEM and EBSD Study*, IEEE Transactions on Applied Superconductivity 26 (2016) Nr. 3, S. 7201505/1-5.
- 164) J. He, I. Kaban, N. Mattern, K. Song, B. Sun, J. Zhao, D.H. Kim, J. Eckert, A.L. Greer, *Local microstructure evolution at shear bands in metallic glasses with nanoscale phase separation*, Scientific Reports 6 (2016), S. 25832/1-8.
- 165) J. Orava, H. Weber, I. Kaban, A.L. Greer, *Viscosity of liquid Ag-In-Sb-Te: Evidence of a fragile-to-strong crossover*, Journal of Chemical Physics 144 (2016) Nr. 19, S. 194503/1-6.
- 166) A. Mohan, S. Singh, S. Partzsch, M. Zwiebler, J. Geck, S. Wurmehl, B. Buechner, C. Hess, *Single crystal growth of spin-ladder compound $La_8Cu_7O_{19}$ by the travelling-solvent floating zone method*, Journal of Crystal Growth 448 (2016), S. 21-28.
- 167) C. Salazar, J. Lach, F. Rueckert, D. Baumann, S. Schimmel, M. Knupfer, B. Kersting, B. Buechner, C. Hess, *STM Study of Au(111) Surface-Grafted Paramagnetic Macrocyclic Complexes $[Ni_2L(Hmba)]^+$ via Ambidentate Coligands*, Langmuir 32 (2016) Nr. 18, S. 4464-4471.
- 168) S. Khim, M. Gillig, R. Klingeler, S. Wurmehl, B. Buechner, C. Hess, *Unusual magnetotransport properties in a FeAs single crystal*, Physical Review B 93 (2016) Nr. 20, S. 205129/1-5.

- 169) Y. Krupskaya, F. Rueckerl, M. Knupfer, A.F. Morpurgo, *Charge Transfer, Band-Like Transport, and Magnetic Ions at $F_{16}CoPc/Rubrene$ Interfaces*, Advanced Materials Interfaces 3 (2016) Nr. 10, S. 1500863/1-5.
- 170) P. Marra, J. van den Brink, S. Sykora, *Theoretical approach to resonant inelastic x-ray scattering in iron-based superconductors at the energy scale of the superconducting gap*, Scientific Reports 6 (2016), S. 25386/1-10.
- 171) J. Zhang, T. Wang, D. Pohl, B. Rellinghaus, R. Dong, S. Liu, X. Zhuang, X. Feng, *Interface Engineering of MoS_2/Ni_3S_2 Heterostructures for Highly Enhanced Electrochemical Overall-Water-Splitting Activity*, Angewandte Chemie International Edition 55 (2016) Nr. 23, S. 6702-6707.
- 172) Y. Chen, I.E. Zadeh, K.D. Joens, A. Fognini, M.E. Reimer, J. Zhang, D. Dalacu, P.J. Poole, F. Ding, V. Zwiller, O.G. Schmidt, *Controlling the exciton energy of a nanowire quantum dot by strain fields*, Applied Physics Letters 108 (2016) Nr. 18, S. 182103/1-5.
- 173) A. Madani, V.A.B. Quinones, L.B. Ma, S.D. Miao, M.R. Jorgensen, O.G. Schmidt, *Overlapping double potential wells in a single optical microtube cavity with vernier-scale-like tuning effect*, Applied Physics Letters 108 (2016) Nr. 17, S. 171105/1-4.
- 174) A. Ulhaq, Q. Duan, E. Zallo, F. Ding, O.G. Schmidt, A.I. Tartakovskii, M.S. Skolnick, E.A. Chekhovich, *Vanishing electron g factor and long-lived nuclear spin polarization in weakly strained nanohole-filled GaAs/AlGaAs quantum dots*, Physical Review B 93 (2016) Nr. 16, S. 165306/1-12.
- 175) A. Madani, L. Ma, S. Miao, M.R. Jorgensen, O.G. Schmidt, *Luminescent nanoparticles embedded in TiO_2 microtube cavities for the activation of whispering-gallery-modes extending from the visible to the near infrared*, Nanoscale 8 (2016) Nr. 18, S. 9498-9503.
- 176) A.R. Akkineni, T. Ahlfeld, A. Funk, A. Waske, A. Lode, M. Gelinsky, *Highly Concentrated Alginate-Gellan Gum Composites for 3D Plotting of Complex Tissue Engineering Scaffolds*, Polymers 8 (2016) Nr. 5, S. 170/1-16.
- 177) A. Kirchner, A. Winkler, S.M. Menzel, B. Holzapfel, R. Huehne, *Surface Acoustic Waves - A New Thin-Film Deposition Approach for Coated Conductors*, IEEE Transactions on Applied Superconductivity 26 (2016) Nr. 3, S. 6602704/1-4.
- 178) M. Mietschke, S. Engelhardt, S. Faehler, C. Molin, S. Gebhardt, L. Schultz, R. Huehne, *Structural and ferroelectric properties of 0.9PMN-0.1PT thin films*, Ferroelectrics 499 (2016) Nr. 1, S. 57-63.
- 179) S. Scudino, K.B. Surreddi, G. Wang, G. Liu, *Effect of stress concentration on plastic deformation of $Zr_{41.2}Ti_{13.8}Cu_{12.5}Ni_{10}Be_{22.5}$ bulk metallic glass under compressive loading*, Materials Letters 179 (2016), S. 202-205.
- 180) A. Gebert, D. Eigel, P.F. Gostin, V. Hoffmann, M. Uhlemann, A. Helth, S. Pilz, R. Schmidt, M. Calin, M. Goettlicher, M. Rohnke, J. Janek, *Oxidation treatments of beta-type Ti-40Nb for biomedical use*, Surface and Coatings Technology 302 (2016), S. 88-99.
- 181) M. Schumacher, H. Weber, P. Jovari, Y. Tsuchiya, T.G.A. Youngs, I. Kaban, R. Mazzarello, *Structural, electronic and kinetic properties of the phase-change material $Ge_2Sb_2Te_5$ in the liquid state*, Scientific Reports 6 (2016), S. 27434/1-11.
- 182) R. Kubrin, R.M. Pasquarelli, M. Waleczek, H.S. Lee, R. Zierold, J.J. do Rosario, P.N. Dyachenko, J.M. Montero Moreno, A.Y. Petrov, R. Janssen, M. Eich, K. Nielsch, G.A. Schneider, *Bottom-up Fabrication of Multilayer Stacks of 3D Photonic Crystals from Titanium Dioxide*, ACS Applied Materials and Interfaces 8 (2016) Nr. 16, S. 10466-10476.
- 183) Y. Sun, C. Wang, Y. Xue, Q. Zhang, R.G. Mendes, L. Chen, T. Zhang, T. Gemming, M.H. Ruemmeli, X. Ai, L. Fu, *Coral-Inspired Nanoengineering Design for Long-Cycle and Flexible Lithium-Ion Battery Anode*, ACS Applied Materials and Interfaces 8 (2016) Nr. 14, S. 9185-9193.
- 184) B. Betz, P. Rauscher, R.P. Harti, R. Schaefer, H. Van Swygenhoven, A. Kaestner, J. Hovind, E. Lehmann, C. Gruenzweig, *In-situ visualization of stress-dependent bulk magnetic domain formation by neutron grating interferometry*, Applied Physics Letters 108 (2016) Nr. 1, S. 12405/1-4.
- 185) H. Himcinschi, E.-J. Guo, A. Talkenberger, K. Doerr, J. Kortus, *Influence of piezoelectric strain on the Raman spectra of $BiFeO_3$ films deposited on PMN-PT substrates*, Applied Physics Letters 108 (2016) Nr. 4, S. 42902/1-5.
- 186) X. Shi, P. Fischer, V. Neu, D. Elefant, J.C.T. Lee, D.A. Shapiro, M. Farmand, T. Tyliczszak, H.-W. Shiu, S. Marchesini, S. Roy, S.D. Kevan, *Soft x-ray ptychography studies of nanoscale magnetic and structural correlations in thin $SmCo_5$ films*, Applied Physics Letters 108 (2016) Nr. 9, S. 94103/1-5.
- 187) Y. Mao, L. Peng, Q. Deng, D. Nie, S. Wang, L. Xi, *Wetting behavior and interfacial interactions of molten $Cu_{50}Ti$ alloy with hexagonal BN and TiB_2 ceramics*, Ceramics International 42 (2016) Nr. 8, S. 9906-9912.
- 188) K. Junghans, M. Rosenkranz, A.A. Popov, *$Sc_3CH@C_{80}$: selective ^{13}C enrichment of the central carbon atom*, Chemical Communications 52 (2016) Nr. 39, S. 6561-6564.
- 189) K. Ruehlig, R. Mothes, A. Aliabadi, V. Kataev, B. Buechner, R. Buschbeck, T. Rueffer, H. Lang, *CuII bis(oxamato) end-grafted poly(amidoamine) dendrimers*, Dalton Transactions 45 (2016) Nr. 19, S. 7960-7979.
- 190) V. Vega, J.M. Montero-Moreno, J. Gracia, V.M. Prida, W. Rahimi, M. Waleczek, C. Bae, R. Zierold, K. Nielsch, *Long-Range Hexagonal Arrangement of TiO_2 Nanotubes by Soft Lithography-Guided Anodization*, Electrochimica Acta 203 (2016), S. 51-58.

- 191) M. Sturza, D.E. Bugaris, C.D. Malliakas, F. Han, D.Y. Chung, M.G. Kanatzidis, *Mixed-Valent NaCu₄Se₃: A Two-Dimensional Metal*, Inorganic Chemistry 55 (2016) Nr. 10, S. 4884–4890.
- 192) Zhang, L., S. Pauly, Z.W. Zhu, T. Gemming, H.M. Fu, J. Eckert, H.F. Zhang, *Ion milling-induced micrometer-sized heterogeneities and partial crystallization in a TiZrCuFeBe bulk metallic glass*, Intermetallics 73 (2016), S. 5–11.
- 193) Y. Xue, J. Deng, C. Wang, R.G. Mendes, L. Chen, Y. Xiao, Q. Zhang, T. Zhang, X. Hu, X. Li, M.H. Ruemmeli, L. Fu, *A pinecone-inspired nanostructure design for longcycle and high performance Si anodes*, Journal of Materials Chemistry A 4 (2016) Nr. 15, S. 5395–5401.
- 194) P.V. Leksin, A.A. Kamashev, J. Schumann, V.E. Kataev, J. Thomas, B. Buechner, I.A. Garifullin, *Boosting the superconducting spin valve effect in a metallic superconductor/ferromagnet heterostructure*, Nano Research 9 (2016) Nr. 4, S. 1005–1011.
- 195) K.E. Metlushka, D.N. Sadkova, L.N. Shaimardanova, K.A. Nikitina, K.A. Ivshin, D.R. Islamov, O.N. Kataeva, A.V. Alfonsov, V.E. Kataev, A.D. Voloshina, L.N. Punegova, V.A. Alfonsov, *First coordination polymers on the bases of chiral thiophosphorylated thioureas*, Inorganic Chemistry Communications 66 (2016), S. 11–14.
- 196) L.-C. Zhang, H. Attar, M. Calin, J. Eckert, *Review on manufacture by selective laser melting and properties of titanium based materials for biomedical applications*, Materials Technology 31 (2016) Nr. 2, S. 66–76.
- 197) A.J. Achkar, F. He, R. Sutarto, C. McMahon, M. Zwiebler, M. Huecker, G.D. Gu, R. Liang, D.A. Bonn, W.N. Hardy, J. Geck, D.G. Hawthorn, *Orbital symmetry of charge-density-wave order in La_{1.875}Ba_{0.125}CuO₄ and YBa₂Cu₃O_{6.67}*, Nature Materials 15 (2016), S. 616–620.
- 198) I.L. Vecchio, G. Giovannetti, M. Autore, P.D. Pietro, A. Perucchi, J. He, K. Yamaura, M. Capone, S. Lupi, *Electronic correlations in the ferroelectric metallic state of LiOsO₃*, Physical Review B 93 (2016) Nr. 16, S. 161113/1–5.
- 199) N. Martin, M. Deutsch, F. Bert, D. Andreica, A. Amato, P. Bonfa, R. De Renzi, U.K. Roessler, P. Bonville, L.N. Fomicheva, A.V. Tsvyashchenko, I. Mirebeau, *Magnetic ground state and spin fluctuations in MnGe chiral magnet as studied by muon spin rotation*, Physical Review B 93 (2016) Nr. 17, S. 174405/1–12.
- 200) S.-H. Baek, D.V. Efremov, J.M. Ok, J.S. Kim, J. van den Brink, B. Buechner, *Nematicity and in-plane anisotropy of superconductivity in beta-FeSe detected by ⁷⁷Se nuclear magnetic resonance*, Physical Review B 93 (2016) Nr. 18, S. 180502(R)/1–6.
- 201) S. Pandey, C. Ortix, *Topological end states due to inhomogeneous strains in wrinkled semiconducting ribbons*, Physical Review B 93 (2016) Nr. 19, S. 195420/1–5.
- 202) K. Koepernik, D. Kasinathan, D.V. Efremov, S. Khim, S. Borisenko, B. Buechner, J. van den Brink, *TaIrTe₄: A ternary type-II Weyl semimetal*, Physical Review B 93 (2016) Nr. 20, S. 201101/1–5.
- 203) M. Altmeyer, H.O. Jeschke, O. Hijano-Cubelos, C. Martins, F. Lechermann, K. Koepernik, A.F. Santander-Syro, M.J. Rozenberg, R. Valenti, M. Gabay, *Magnetism, Spin Texture, and In-Gap States: Atomic Specialization at the Surface of Oxygen-Deficient SrTiO₃*, Physical Review Letters 116 (2016) Nr. 15, S. 157203/1–6.
- 204) Q. Wang, J.T. Park, Y. Feng, Y. Shen, Y. Hao, B. Pan, J.W. Lynn, A. Ivanov, S. Chi, M. Matsuda, H. Cao, R.J. Birgeneau, D.V. Efremov, J. Zhao, *Transition from Sign-Reversed to Sign-Preserved Cooper-Pairing Symmetry in Sulfur-Doped Iron Selenide Superconductors*, Physical Review Letters 116 (2016) Nr. 19, S. 197004/1–5.
- 205) J. Suryawanshi, K.G. Prashanth, S. Scudino, J. Eckert, O. Prakash, U. Ramamurty, *Simultaneous enhancements of strength and toughness in an Al-12Si alloy synthesized using selective laser melting*, Acta Materialia 115 (2016), S. 285–294.
- 206) A. Gebert, M. Krautz, A. Waske, *Exploring corrosion protection of La-Fe-Si magnetocaloric alloys by passivation*, Intermetallics 75 (2016), S. 88–95.
- 207) A. Sanna, A.V. Fedorov, N.I. Verbitskiy, J. Fink, C. Krellner, L. Petaccia, A. Chikina, D.Y. Usachov, A. Grueneis, G. Profeta, *First-principles and angle-resolved photoemission study of lithium doped metallic black phosphorous*, 2D Materials 3 (2016), S. 25031/1–6.
- 208) S. Thirupathaiah, J. Fink, P.K. Maheshwari, V.V. Ravi Kishore, Z.-H. Liu, E.D.L. Rienks, B. Buechner, V.P.S. Awana, D.D. Sarma, *Effect of impurity substitution on band structure and mass renormalization of the correlated FeTe_{0.5}Se_{0.5} superconductor*, Physical Review B 93 (2016) Nr. 20, S. 205143/1–7.
- 209) V. Magdanz, M. Guix, F. Hebenstreit, O.G. Schmidt, *Dynamic Polymeric Microtubes for the Remote-Controlled Capture, Guidance, and Release of Sperm Cells*, Advanced Materials 28 (2016) Nr. 21, S. 4084–4089.
- 210) S. Boettner, M.R. Jorgensen, O.G. Schmidt, *Rolled-up nanotechnology: 3D photonic materials by design*, Scripta Materialia 122 (2016), S. 119–124.
- 211) P.K. Nag, R. Schlegel, D. Baumann, H.-J. Grafe, R. Beck, S. Wurmehl, B. Buechner, C. Hess, *Two distinct superconducting phases in LiFeAs*, Scientific Reports 6 (2016), S. 27926/1–7.

- 212) A. Krause, S. Doerfler, M. Piwko, F.M. Wissner, T. Jaumann, E. Ahrens, L. Giebeler, H. Althues, S. Schaedlich, J. Grothe, A. Jeffery, M. Grube, J. Brueckner, J. Martin, J. Eckert, S. Kaskel, T. Mikolajick, W.M. Weber, *High Area Capacity Lithium-Sulfur Full-cell Battery with Prelithiated Silicon Nanowire-Carbon Anodes for Long Cycling Stability*, Scientific Reports 6 (2016), S. 27982/1-12.
- 213) M. Klose, R. Reinhold, K. Pinkert, M. Uhlemann, F. Wolke, J. Balach, T. Jaumann, U. Stoeck, J. Eckert, L. Giebeler, *Hierarchically nanostructured hollow carbon nanospheres for ultrafast and long-life energy storage*, Carbon 106 (2016), S. 306-313.
- 214) J. Balach, H.K. Singh, S. Gomoll, T. Jaumann, M. Klose, S. Oswald, M. Richter, J. Eckert, L. Giebeler, *Synergistically Enhanced Polysulfide Chemisorption Using a Flexible Hybrid Separator with N and S Dual-Doped Mesoporous Carbon Coating for Advanced Lithium-Sulfur Batteries*, ACS Applied Materials and Interfaces 8 (2016) Nr. 23, S. 14586-14595.
- 215) J. Balach, T. Jaumann, S. Muehlenhoff, J. Eckert, L. Giebeler, *Enhanced polysulphide redox reaction using a RuO₂ nanoparticle-decorated mesoporous carbon as functional separator coating for advanced lithium-sulphur batteries*, Chemical Communications (2016) Nr. 52, S. 8134-8137.
- 216) G. Simutis, M. Thede, R. Saint-Martin, A. Mohan, C. Baines, Z. Guguchia, R. Khasanov, C. Hess, A. Revcolevschi, B. Buechner, A. Zheludev, *Magnetic ordering in the ultrapure site-diluted spin chain materials SrCu_{1-x}Ni_xO₂*, Physical Review B 93 (2016) Nr. 21, S. 214430/1-6.
- 217) I.G. Gonzalez-Martinez, A. Bachmatiuk, V. Bezugly, J. Kunstmann, T. Gemming, Z. Liu, G. Cuniberti, M.H. Ruemmel, *Electron-beam induced synthesis of nanostructures: A Review*, Nanoscale 8 (2016) Nr. 22, S. 11340-11362.
- 218) Y.S. Qin, Y. Shi, X.L. Han, K.K. Song, C.D. Cao, X.L. Li, S.H. Wang, J. He, L. Wang, I. Kaban, J. Eckert, *Formation and phase evolution of liquid phase-separated metallic glasses with double glass transition, crystallization and melting*, Materials Today Communications 8 (2016), S. 64-71.
- 219) Y. Yin, S. Li, S. Boettner, F. Yuan, S. Giudicatti, E.S. Ghareh Naz, L. Ma, O.G. Schmidt, *Localized Surface Plasmons Selectively Coupled to Resonant Light in Tubular Microcavities*, Physical Review Letters 116 (2016) Nr. 25, S. 253904/1-7.
- 220) A. Surrey, L. Schultz, B. Rellinghaus, *Electron beam induced dehydrogenation of MgH₂ studied by VEELS*, Advanced Structural and Chemical Imaging 2 (2016) Nr. 7, S. 1-9.
- 221) Yu.G. Naidyuk, G. Fuchs, D.A. Chareev, A.N. Vasiliev, *Doubling of the critical temperature of FeSe observed in point contacts*, Physical Review B 93 (2016) Nr. 14, S. 144515/1-6.
- 222) F. Karnbach, X. Yang, G. Mutschke, J. Froehlich, J. Eckert, A. Gebert, K. Tschulik, K. Eckert, M. Uhlemann, *Interplay of the Open Circuit Potential-Relaxation and the Dissolution Behavior of a Single H₂ Bubble Generated at a Pt Microelectrode*, The Journal of Physical Chemistry C 120 (2016) Nr. 28, S. 15137-15146.
- 223) X.H. Wang, A. Inoue, F.L. Kong, S.L. Zhu, M. Stoica, I. Kaban, C.T. Chang, E. Shalaan, F. Al-Marzouki, J. Eckert, *Influence of ejection temperature on structure and glass transition behavior for Zr-based rapidly quenched disordered alloys*, Acta Materialia 116 (2016), S. 370-381.
- 224) G. Prando, A. Alfonso, A. Pal, V.P.S. Awana, B. Buechner, V. Kataev, *Tuning the magnetocrystalline anisotropy in RCoPO by means of R substitution: A ferromagnetic resonance study*, Physical Review B 94 (2016) Nr. 2, S. 24412/1-12.
- 225) M. Nicoara, C. Locovei, V.A. Serban, R. Parthiban, M. Calin, M. Stoica, *New Cu-Free Ti-Based Composites with Residual Amorphous Matrix*, Materials 9 (2016) Nr. 5, S. 331/1-14.
- 226) J. Koerner, C.F. Reiche, T. Gemming, B. Buechner, G. Gerlach, T. Muehl, *Signal enhancement in cantilever magnetometry based on a co-resonantly coupled sensor*, Beilstein Journal of Nanotechnology 7 (2016), S. 1033-1043.
- 227) J. Koerner, C.F. Reiche, B. Buechner, T. Muehl, G. Gerlach, *Employing electro-mechanical analogies for co-resonantly coupled cantilever sensors*, Journal of Sensors and Sensor Systems 5 (2016) Nr. 2, S. 245-259.
- 228) M. Seifert, G.K. Rane, S.B. Menzel, T. Gemming, *The influence of barrier layers (SiO₂, Al₂O₃, W) on the phase formation and stability of RuAl thin films on LGS and CTGS substrates for surface acoustic wave technology*, Journal of Alloys and Compounds 688 Part A (2016), S. 228-240.
- 229) S.M. Avdoshenko, D.E. Makarov, *Reply to „Comment on ‘Reaction Coordinates and Pathways of Mechanochemical Transformation’“*, The Journal of Physical Chemistry B 120 (2016) Nr. 9, S. 2646-2647.
- 230) E.V. Bukovsky, B.W. Larson, T.T. Clikeman, Y.-S. Chen, A.A. Popov, O.V. Boltalina, S.H. Strauss, *Structures and structure-related electronic properties of new C₆₀(CF₃)₁₀ isomers*, Journal of Fluorine Chemistry 185 (2016), S. 103-117.
- 231) S. Calder, J.G. Vale, N.A. Bogdanov, X. Liu, C. Donnerer, M.H. Upton, D. Casa, A.H. Said, M.D. Lumsden, Z. Zhao, J.-Q. Yan, D. Mandrus, S. Nishimoto, J. van den Brink, J.P. Hill, D.F. McMorro, A.D. Christianson, *Spin-orbit-driven magnetic structure and excitation in the 5d pyrochlore Cd₂Os₂O₇*, Nature Communications 7 (2016), S. 11651/1-8.

- 232) M. Hoffmann, A. Marmodoro, A. Ernst, W. Hergert, J. Dahl, J. Lang, P. Laukkanen, M.P.J. Punkkinen, K. Kokko, *Quantitative description of short-range order and its influence on the electronic structure in Ag-Pd alloys*, Journal of Physics: Condensed Matter 28 (2016) Nr. 30, S. 305501/1-10.
- 233) T. Huebner, A. Boehnke, U. Martens, A. Thomas, J.-M. Schmalhorst, G. Reiss, M. Muenzenberg, T. Kuschel, *Comparison of laser-induced and intrinsic tunnel magneto-Seebeck effect in CoFeB/MgAl₂O₄ and CoFeB/MgO magnetic tunnel junctions*, Physical Review B 93 (2016) Nr. 22, S. 224433/1-6.
- 234) K. Iida, V. Grinenko, F. Kurth, A. Ichinose, I. Tsukada, E. Ahrens, A. Pukenas, P. Chekhonin, W. Skrotzki, A. Teresiak, R. Huehne, S. Aswartham, S. Wurmehl, I. Moench, M. Erbe, J. Haenisch, B. Holzapfel, S.-L. Drechsler, D.V. Efremov, *Hall-plot of the phase diagram for Ba(Fe_{1-x}Co_x)₂As₂*, Scientific Reports 6 (2016), S. 28390/1-9.
- 235) M. Khafaji, M. Vossoughi, M.R. Hormozi-Nezhad, R. Dinarvand, F. Boerrnert, A. Irajizad, *A new bifunctional hybrid nanostructure as an active platform for photothermal therapy and MR imaging*, Scientific Reports 6 (2016), S. 27847/1-12.
- 236) M. Khazaee, W. Xia, G. Lackner, R.G. Mendes, M. Ruemmeli, M. Muhler, D.C. Lupascu, *Dispersibility of vapor phase oxygen and nitrogen functionalized multi-walled carbon nanotubes in various organic solvents*, Scientific Reports 6 (2016), S. 26208/1-10.
- 237) R. Schuster, Y. Wan, M. Knupfer, B. Buechner, *Nongeneric dispersion of excitons in the bulk of WSe₂*, Physical Review B 94 (2016) Nr. 8, S. 85201/1-5.
- 238) K. Kuepper, O. Kuschel, N. Pathé, T. Schemme, J. Schmalhorst, A. Thomas, E. Arenholz, M. Gorgoi, R. Ovsyannikov, S. Bartkowski, G. Reiss, J. Wollschlaeger, *Electronic and magnetic structure of epitaxial Fe₃O₄(001)/NiO heterostructures grown on MgO(001) and Nb-doped SrTiO₃(001)*, Physical Review B 94 (2016) Nr. 2, S. 024401/1-10.
- 239) C. Li, Q. Hu, Y. Li, H. Zhou, Z. Lv, X. Yang, L. Liu, H. Guo, *Hierarchical hollow Fe₂O₃@MIL-101(Fe)/C derived from metal-organic frameworks for superior sodium storage*, Scientific Reports 6 (2016), S. 25556/1-8.
- 240) A. Maljuk, C.T. Lin, *Floating Zone Growth of Bi₂Sr₂Ca₂Cu₃O_y Superconductor*, Crystals 6 (2016) Nr. 5, S. 62/1-16.
- 241) N. Martin, M. Deutsch, J.-P. Itié, J.-P. Rueff, U.K. Roessler, K. Koepernik, L.N. Fomicheva, A.V. Tsyvashchenko, I. Mirebeau, *Magnetovolume effect, macroscopic hysteresis, and moment collapse in the paramagnetic state of cubic MnGe under pressure*, Physical review B 93 (2016) Nr. 21, S. 214404/1-5.
- 242) Sandeep, D.P. Rai, A. Shankar, M.P. Ghimire, A.P. Sakhya, T.P. Sinha, R. Khenata, S.B. Omran, R.K. Thapa, *Band-gap engineering of La_{1-x}Nd_xAlO₃ (x = 0, 0.25, 0.50, 0.75, 1) perovskite using density functional theory: A modified Becke Johnson potential study*, Chines Physics B 25 (2016) Nr. 6, S. 67101/1-7.
- 243) B. Sarac, L. Zhang, K. Kosiba, S. Pauly, M. Stoica, J. Eckert, *Towards the Better: Intrinsic Property Amelioration in Bulk Metallic Glasses*, Scientific Reports 6 (2016), S. 27271/1-8.
- 244) M.B. Schilling, A. Baumgartner, B. Gorshunov, E.S. Zhukova, V.A. Dravin, K.V. Mitsen, D.V. Efremov, O.V. Dolgov, K. Iida, M. Dressel, S. Zapf, *Tracing the σ_{\pm} symmetry in iron pnictides by controlled disorder*, Physical Review B 93 (2016), S. 174515/1-5.
- 245) L. Shi, K. Chen, R. Du, A. Bachmatiuk, M.H. Ruemmeli, K. Xie, Y. Huang, Y. Zhang, Z. Liu, *Scalable Seashell-Based Chemical Vapor Deposition Growth of Three-Dimensional Graphene Foams for Oil-Water Separation*, Journal of the American Chemical Society 138 (2016) Nr. 20, S. 6360-6363.
- 246) X. Sun, G.-P. Hao, X. Lu, L. Xi, B. Liu, W. Si, C. Ma, Q. Liu, Q. Zhang, S. Kaskel, O.G. Schmidt, *High-defect hydrophilic carbon cuboids anchored with Co/CoO nanoparticles as highly efficient and ultra-stable lithium-ion battery anodes*, Journal of Materials Chemistry A 4 (2016) Nr. 26, S. 10166-10173.
- 247) H.Q. Ta, A. Bachmatiuk, J.H. Warner, L. Zhao, Y. Sun, J. Zhao, T. Gemming, B. Trzebicka, Z. Liu, D. Pribat, M.H. Ruemmeli, *Electron-Driven Metal Oxide Effusion and Graphene Gasification at Room Temperature*, ACS Nano 10 (2016) Nr. 6, S. 6323-6330.
- 248) W. Xi, C.K. Schmidt, S. Sanchez, D.H. Gracias, R.E. Carazo-Salas, R. Butler, N. Lawrence, S.P. Jackson, O.G. Schmidt, *Molecular Insights into Division of Single Human Cancer Cells in On-Chip Transparent Microtubes*, ACS Nano 10 (2016) Nr. 6, S. 5835-5846.
- 249) F.S. Nogueira, Z. Nussinov, J. van den Brink, *Josephson Currents Induced by the Witten Effect*, Physical Review Letters 117 (2016) Nr. 16, S. 167002.
- 250) M. Medina-Sanchez, B. Ibarlucea, N. Perez, D.D. Karnaushenko, S.M. Weiz, L. Baraban, G. Cuniberti, O.G. Schmidt, *High-Performance Three-Dimensional Tubular Nanomembrane Sensor for DNA Detection*, Nano Letters 16 (2016) Nr. 7, S. 4288-4296.
- 251) D. Baczyszalski, F. Karnbach, X. Yang, G. Mutschke, M. Uhlemann, K. Eckert, C. Cierpka, *On the Electrolyte Convection around a Hydrogen Bubble Evolving at a Microelectrode under the Influence of a Magnetic Field*, Journal of The Electrochemical Society 163 (2016) Nr. 9, S. E248-E257.
- 252) E. Mueller, B. Buechner, C. Habenicht, A. Koenig, M. Knupfer, H. Berger, S. Huotari, *Doping dependent plasmon dispersion in 2H-transition metal dichalcogenides*, Physical Review B 94 (2016) Nr. 3, S. 35110/1-5.

- 253) C. Mueller, I. Neckel, M. Monecke, V. Dzaghan, G. Salvan, S. Schulze, S. Baunack, T. Gemming, S. Oswald, V. Engemaier, D.H. Mosca, *Transformation of epitaxial NiMnGa/InGaAs nanomembranes grown on GaAs substrates into freestanding microtubes*, RSC Advances 76 (2016) Nr. 6, S. 72568-72574.
- 254) P. Ma, Z.J. Wei, Y.D. Jia, C.M. Zou, S. Scudino, K.G. Prashanth, Z.S. Yu, S.L. Yang, C.G. Li, J. Eckert, *Effect of high pressure solidification on tensile properties and strengthening mechanisms of Al-20Si*, Journal of Alloys and Compounds 688 Part A (2016), S. 88-93.
- 255) D. Mikhailova, O.M. Karakulina, D. Batuk, J. Hadermann, A.M. Abakumov, M. Herklotz, A.A. Tsirlin, S. Oswald, L. Giebeler, M. Schmidt, J. Eckert, M. Knapp, H. Ehrenberg, *Layered-to-Tunnel Structure Transformation and Oxygen Redox Chemistry in LiRhO₂ upon Li Extraction and Insertion*, Inorganic Chemistry 55 (2016) Nr. 14, S. 7079-7089.
- 256) B. Terlan, A.A. Levin, F. Boerrnert, J. Zeisner, V. Kataev, M. Schmidt, A. Eychmueller, *A Size-Dependent Analysis of the Structural, Surface, Colloidal, and Thermal Properties of Ti_{1-x}B₂ (x = 0.03 - 0.08) Nanoparticles*, European Journal of Inorganic Chemistry 2016 (2016) Nr. 21, S. 3460-3468.
- 257) F. Boerrnert, A. Horst, M.A. Krzyzowski, B. Buechner, *A Variable-Temperature Continuous-Flow Liquid-Helium Cryostat Inside a (Scanning) Transmission Electron Microscope*, Microscopy and Microanalysis 22 (2016) Nr. Suppl. 3, S. 776-777.
- 258) J. Hufenbach, A. Helth, M.-H. Lee, H. Wendrock, L. Giebeler, C.-Y. Choe, K.-H. Kim, U. Kuehn, T.-S. Kim, J. Eckert, *Effect of cerium addition on microstructure and mechanical properties of high-strength Fe₈₅Cr₄Mo₈V₂C₁ cast steel*, Materials Science and Engineering A 674 (2016), S. 366-374.
- 259) N. Mattern, M. Zinkevich, J.H. Han, W. Loeser, *Experimental and thermodynamic assessment of the Co-Gd-Ti system*, CALPHAD: Computer Coupling of Phase Diagrams and Thermochemistry 54 (2016), S. 144-157.
- 260) F. Boerrnert, *Thoughts about next-generation (S)TEM instruments in science*, Micron 90 (2016), S. 1-5.
- 261) N. Muenzenrieder, D. Karnaushenko, L. Petti, G. Cantarella, C. Vogt, L. Buethe, D.D. Karnaushenko, O.G. Schmidt, D. Makarov, G. Troester, *Entirely Flexible On-Site Conditioned Magnetic Sensorics*, Advanced Electronic Materials 2 (2016) Nr. 8, S. 1600188/1-10.
- 262) Z.-J. Ying, P. Gentile, C. Ortix, M. Cuoco, *Designing electron spin textures and spin interferometers by shape deformations*, Physical Review B 94 (2016) Nr. 8, S. 81406/1-5.
- 263) F. Steckel, A. Matsumoto, T. Takayama, T. Takagi, B. Buechner, C. Hess, *Pseudospin transport in the Jeff = 1/2 antiferromagnet Sr₂IrO₄*, epl 114 (2016) Nr. 5, S. 57007/1-6.
- 264) S.J. Singh, U. Graefe, R. Beck, A.U.B. Wolter, H. Grafe, C. Hess, S. Wurmehl, B. Buechner, *Physical properties optimization of polycrystalline LiFeAs*, Physica C 529 (2016) Nr. 8, S. 8-20.
- 265) B. Escher, U. Kuehn, J. Eckert, C. Rentenberger, S. Pauly, *Influence of Ag and Co additions on glass-forming ability, thermal and mechanical properties of Cu-Zr-Al bulk metallic glasses*, Materials Science and Engineering A 673 (2016), S. 90-98.
- 266) S. Oswald, M. Hoffmann, M. Zier, *Peak position differences observed during XPS sputter depth profiling of the SEI on lithiated and delithiated carbon-based anode material for Li-ion batteries*, Applied Surface Science 401 (2016), S. 408-413.
- 267) M. Boenisch, T. Waitz, M. Calin, W. Skrotzki, J. Eckert, *Tailoring the Bain strain of martensitic transformations in Ti-Nb alloys by controlling the Nb content*, International Journal of Plasticity 85 (2016), S. 190-202.
- 268) Y. Yin, S. Li, V. Engemaier, S. Giudicatti, E. Saei Ghareh Naz, L. Ma, O.G. Schmidt, *Hybridization of photon-plasmon modes in metal-coated microtubular cavities*, Physical Review A 94 (2016) Nr. 1, S. 13832.
- 269) Z. Wang, R.T. Qu, K.G. Prashanth, J. Eckert, S. Scudino, *Compression behavior of inter-particle regions in high-strength Al₈₄Ni₇Gd₆Co₃ alloy*, Materials Letters 185 (2016), S. 25.
- 270) A. Winkler, P. Bergelt, L. Hillemann, S. Menzel, *Influence of viscosity in fluid atomization with surface acoustic waves*, Open Journal of Acoustics (2016), S. 1-10.
- 271) E.M. Paschalidou, F. Celegato, F. Scaglione, P. Rizzi, L. Battezzati, A. Gebert, S. Oswald, U. Wolff, L. Mihaylov, T. Spassov, *The mechanism of generating nanoporous Au by de-alloying amorphous alloys*, Acta Materialia 119 (2016), S. 177-183.
- 272) G.N. Churilov, A.A. Popov, N.G. Vnukova, A.I. Dudnik, G.A. Glushchenko, N.A. Samoylova, I.A. Dubinina, U.E. Gulyaeva, *A method and apparatus for high-throughput controlled synthesis of fullerenes and endohedral metal fullerenes*, Technical Physics Letters 42 (2016) Nr. 5, S. 475-477.
- 273) D. Ehlers, I. Stasinopoul, V. Tsurkan, H.-A. Krug von Nidda, T. Fehér, A. Leonov, I. Kézsmárki, D. Grundler, A. Loidl, *Skyrmion dynamics under uniaxial anisotropy*, Physical Review B 94 (2016) Nr. 1, S. 14406.
- 274) N. Forouzanmehr, M. Nili-Ahmadabadi, M. Boenisch, *The analysis of severely deformed pure Fe structure aided by X-ray diffraction profile*, The Physics of Metals and Metallography 117 (2016) Nr. 6, S. 624-633.

- 275) M. Hoffmann, S. Oswald, M. Zier, J. Eckert, *Auger and X-ray photoelectron spectroscopy on lithiated HOPG*, Surface and Interface Analysis 48 (2016) Nr. 7, S. 501-504.
- 276) M.F. Iakovleva, E.L. Vavilova, H.-J. Grafe, A. Maljuk, S. Wurmehl, B. Buechner, V. Kataev, *Spin Dynamics and Ground State of the Frustrated Diamond Lattice Magnet CoAl_2O_4 as seen by ^{27}Al NMR*, Applied Magnetic Resonance 47 (2016) Nr. 7, S. 727-735.
- 277) V.M. Katukuri, R. Yadav, L. Hozoi, S. Nishimoto, J. van den Brink, *The vicinity of hyper-honeycomb β - Li_2IrO_3 to a three-dimensional Kitaev spin liquid state*, Scientific Reports 6 (2016), S. 29585/1-8.
- 278) A.O. Leonov, T.L. Monchesky, N. Romming, A. Kubetzka, A.N. Bogdanov, R. Wiesendanger, *The properties of isolated chiral skyrmions in thin magnetic films*, New Journal of Physics 18 (2016), S. 65003/1-16.
- 279) S. Rex, F.S. Nogueira, A. Sudboe, *Topological magnetic dipolar interaction and nonlocal electric magnetization control in topological insulator heterostructures*, Physical Review B 94 (2016) Nr. 2, S. 020404/1-5.
- 280) H.S. Shin, B. Hamdou, H. Reith, H. Osterhage, J. Gooth, C. Damm, B. Rellinghaus, C. Pippel, K. Nielsch, *The surface-to-volume ratio: a key parameter in the thermoelectric transport of topological insulator Bi_2Se_3 nanowires*, Nanoscale 8 (2016) Nr. 28, S. 13552-13557.
- 281) D. Söpu, A. Foroughi, M. Stoica, J. Eckert, *Brittle-to-Ductile Transition in Metallic Glass Nanowires*, Nano Letters 16 (2016) Nr. 7, S. 4467-4471.
- 282) S.K. Srivastava, O.G. Schmidt, *Autonomously Propelled Motors for Value-Added Product Synthesis and Purification*, Chemistry - A European Journal 22 (2016) Nr. 27, S. 9072-9076.
- 283) D.Y. Usachov, A.V. Fedorov, O.Y. Vilkov, A.E. Petukhov, A.G. Rybkin, A. Ernst, M.M. Otrokov, E.V. Chulkov, I.I. Ogorodnikov, M.V. Kuznetsov, L.V. Yashina, E.Y. Kataev, A.V. Erofeevskaya, V.Y. Voroshnin, V.K. Adamchuk, C. Laubschat, D.V. Vyalikh, *Large-Scale Sublattice Asymmetry in Pure and Boron-Doped Graphene*, Nano Letters 16 (2016) Nr. 7, S. 4535-4543.
- 284) O. Vittorio, M. Cojoc, M. Curcio, U.G. Spizzirri, S. Hampel, F.P. Nicoletta, F. Iemma, A. Dubrovskaya, M. Kavallaris, G. Cirillo, *Polyphenol Conjugates by Immobilized Laccase: The Green Synthesis of Dextran-Catechin*, Macromolecular Chemistry and Physics 217 (2016) Nr. 13, S. 1488-1492.
- 285) U. Vogel, T. Gemming, J. Eckert, S. Oswald, *Analysis of the thermal and temporal stability of Ta and Ti thin films onto SAW-substrate materials (LiNbO_3 and LiTaO_3) using AR-XPS*, Surface and Interface Analysis 48 (2016) Nr. 7, S. 570-574.
- 286) D. Yadav, R. Bauri, A. Kauffmann, J. Freudenberger, *Al-Ti Particulate Composite: Processing and Studies on Particle Twinning, Microstructure, and Thermal Stability*, Metallurgical and Materials Transactions A 47 (2016) Nr. 8, S. 4226-4238.
- 287) L. Xi, I. Kaban, R. Nowak, G. Bruzda, N. Sobczak, M. Stoica, J. Eckert, *Investigation of Ni-B Alloys for Joining of TiB₂ Ultra-High-Temperature Ceramic*, Journal of Materials Engineering and Performance 25 (2016) Nr. 8, S. 3204-3210.
- 288) R. Nowak, N. Sobczak, G. Bruzda, J. Wojewoda-Budka, L. Litynska-Dobrzynska, M. Homa, I. Kaban, L. Xi, L. Jaworska, *Wettability and Reactivity of ZrB_2 Substrates with Liquid Al*, Journal of Materials Engineering and Performance 25 (2016) Nr. 8, S. 3310-3316.
- 289) A.T. Burkov, S.V. Novikov, V.V. Khovaylo, J. Schumann, *Energy filtering enhancement of thermoelectric performance nanocrystalline $\text{Cr}_{1-x}\text{Si}_x$ composites*, Journal of Alloys and Compounds 691 (2016), S. 89-94.
- 290) G. Lin, D.D. Karnaushenko, G.S. Canón Bermudez, O.G. Schmidt, D. Makarov, *Magnetic Suspension Array Technology: Controlled Synthesis and Screening in Microfluidic Networks*, Small 12 (2016) Nr. 33, S. 4553-4562.
- 291) L. Kuehn, A.-K. Herrmann, B. Rutkowski, M. Oezaslan, M. Nachttegaal, M. Klose, L. Giebel, N. Gaponik, J. Eckert, T.J. Schmidt, A. Czyrska-Filemonowicz, A. Eychmueller, *Alloying Behavior of Self-Assembled Noble Metal Nanoparticles*, Chemistry: A European Journal 22 (2016) Nr. 38, S. 13446-13450.
- 292) A. Winkler, R. Bruenig, C. Faust, R. Weser, H. Schmidt, *Towards efficient surface acoustic wave (SAW)-based microfluidic actuators*, Sensors and Actuators A 247 (2016), S. 259-268.
- 293) D. Gajda, A. Morawski, A.J. Zaleski, W. Haessler, K. Nenkov, M. Malecka, M.A. Rindfleisch, M.S.A. Hossain, M. Tomsic, *Experimental research of high field pinning centers in 2% C doped MgB_2 wires at 20 K and 25 K*, Journal of Applied Physics 120 (2016) Nr. 11, S. 113901/1-8.
- 294) M. Mietschke, P. Chekhonin, C. Molin, S. Gebhardt, S. Faehler, K. Nielsch, L. Schultz, R. Huehne, *Influence of the polarization anisotropy on the electrocaloric effect in epitaxial PMN-PT thin films*, Journal of Applied Physics 120 (2016), S. 114102/1-7.
- 295) Y. Zhang, Y. Chen, M. Mietschke, L. Zhang, F. Yuan, S. Abel, R. Huehne, K. Nielsch, J. Fompeyrine, F. Ding, O.G. Schmidt, *Monolithically Integrated Microelectromechanical Systems for On-Chip Strain Engineering of Quantum Dots*, Nano Letters 16 (2016) Nr. 9, S. 5785-5791.
- 296) F. Rueckerl, B. Mahns, E. Dodbiba, V. Nikolis, M. Herzig, B. Buechner, M. Knapfer, T. Hahn, J. Kortus, *Electronic properties of the charge transfer material $\text{MnPc}/\text{F4TCNQ}$* , The Journal of Chemical Physics 145 (2016), S. 114702/1-7.

- 297) S.A. Rounaghi, H. Eshghi, S. Scudino, A. Vyalikh, D.E.P. Vanpoucke, W. Gruner, S. Oswald, A.R. Kiani Rashid, M. Samadi Khoshkhoo, U. Scheler, J. Eckert, *Mechanochemical route to the synthesis of nanostructured Aluminium nitride*, Scientific Reports 6 (2016), S. 33375/1-11.
- 298) S. Zimmermann, F. Steckel, C. Hess, H.W. Ji, Y.S. Hor, R.J. Cava, B. Buechner, V. Kataev, *Spin dynamics and magnetic interactions of Mn dopants in the topological insulator Bi_2Te_3* , Physical Review B 94 (2016), S. 125205/1-8.
- 299) R. Shekurov, V. Miluykov, O. Kataeva, D. Krivolapov, O. Sinyashin, T. Gerasimova, S. Katsyuba, V. Kovalenko, Y. Krupskaya, V. Kataev, B. Buechner, I. Senkovska, S. Kaskel, *Reversible Water-Induced Structural and Magnetic Transformations and Selective Water Adsorption Properties of Poly(manganese 1,1'-ferrocenediyl-bis(H-phosphinate))*, Crystal Growth and Design 12 (2016), S. 5084-5090.
- 300) X. Tong, G. Wang, Z.H. Stachurski, J. Bednarcik, N. Mattern, Q.J. Zhai, J. Eckert, *Structural evolution and strength change of a metallic glass at different temperatures*, Scientific Reports 6 (2016), S. 30876/1-12.
- 301) J.E. Hamann-Borrero, S. Macke, W.S. Choi, R. Sutarto, F. He, A. Radi, I. Elfimov, R.J. Green, M.W. Haverkort, V.B. Zabolotnyy, H.N. Lee, G.A. Hinkov, V. Sawatzky, *Valence-state reflectometry of complex oxide heterointerfaces*, npj Quantum Materials 1 (2016), S. 16013/1-6.
- 302) S. Macke, J.E. Hamann-Borrero, R.J. Green, B. Keimer, G.A. Sawatzky, M.W. Haverkort, *Dynamical Effects in Resonant X-Ray Diffraction*, Physical Review Letters 117 (2016), S. 115501/1-6.
- 303) S. Partzsch, J.E. Hamann-Borrero, C. Mazzoli, J. Herrero-Martin, S. Valencia, R. Feyerherm, E. Dudzik, A. Vasiliev, L. Bezmaternykh, B. Buechner, J. Geckl, *Control of coexisting magnetic phases by electric fields in $\text{NdFe}_3(\text{BO}_3)_4$* , Physical Review B 94 (2016), S. 54421/1-7.
- 304) M. Zeng, L. Tan, L. Wang, R.G. Mendes, Z. Qin, Y. Huang, T. Zhang, L. Fang, Y. Zhang, S. Yue, M.H. Ruemmel, L. Peng, Z. Liu, S. Chen, L. Fu, *Isotropic Growth of Graphene toward Smoothing Stitching*, ACS Nano 10 (2016) Nr. 7, S. 7189-7196.
- 305) M. Taut, K. Koepf, *Electronic structure of interfaces between hexagonal and rhombohedral graphite*, Physical Review B 94 (2016) Nr. 3, S. 35446/1-6.
- 306) C. Struzzi, C.S. Praveen, M. Scardamaglia, N.I. Verbitskiy, A.V. Fedorov, M. Weinl, M. Schreck, A. Grueneis, S. Piccinin, S. Fabris, L. Petaccia, *Controlled thermodynamics for tunable electron doping of graphene on $\text{Ir}(111)$* , Physical Review B 94 (2016) Nr. 8, S. 85427/1-10.
- 307) M. Spindler, S. Herold, J. Acker, E. Brachmann, S. Oswald, S. Menzel, G. Rane, *Chemical etching of Tungsten thin films for high-temperature surface acoustic wave-based sensor devices*, Thin Solid Films 612 (2016), S. 322-326.
- 308) M. Moroni, S. Sanna, G. Lamura, T. Shiroka, R. De Renzi, R. Kappenberger, M.A. Afrassa, S. Wurmehl, A.U.B. Wolter, B. Buechner, P. Carretta, *Competing effects of Mn and Y doping on the low-energy excitations and phase diagram of $\text{La}_{1-y}\text{Y}_y\text{Fe}_{1-x}\text{Mn}_x\text{AsO}_{0.89}\text{F}_{0.11}$ iron-based superconductors*, Physical Review B 94 (2016), S. 54508/1-8.
- 309) A.O. Leonov, Y. Togawa, T.L. Monchesky, A.N. Bogdanov, J. Kishine, Y. Kousaka, M. Miyagawa, T. Koyama, J. Akimitsu, T. Koyama, K. Harada, S. Mori, D. McGrouther, R. Lamb, M. Krajnak, S. McVitie, R.L. Stamps, K. Inoue, *Chiral Surface Twists and Skyrmion Stability in Nanolayers of Cubic Helimagnets*, Physical Review Letters 117 (2016) Nr. 8, S. 87202/1-5.
- 310) A.O. Leonov, T.L. Monchesky, J.C. Loudon, A.N. Bogdanov, *Three-dimensional chiral skyrmions with attractive interparticle interactions*, Journal of Physics-Condensed Matter 28 (2016) Nr. 35, S. 1-4.
- 311) Y. Lei, H. Zeng, W. Luo, Y. Shuai, X. Wei, N. Du, D. Buerger, I. Skorupa, J. Liu, O.G. Schmidt, W. Zhang, H. Schmidt, *Ferroelectric and flexible barrier resistive switching of epitaxial BiFeO_3 films studied by temperature-dependent current and capacitance spectroscopy*, Journal of Materials Science-Materials in Electronics 27 (2016) Nr. 8, S. 7927-7932.
- 312) G. Lang, L. Veyrat, U. Graefe, F. Hammerath, D. Paar, G. Behr, S. Wurmehl, H.J. Grafe, *Spatial competition of the ground states in 1111 iron pnictides*, Physical Review B 94 (2016) Nr. 1, S. 14514/1-17.
- 313) S. Lamrani, A. Guitoum, R. Schaefer, S. Pofahl, V. Neu, M. Hemmou, N. Benbrahim, *Microstructure investigation and magnetic study of permalloy thin films grown by thermal evaporation*, European Physical Journal-Applied Physics 74 (2016) Nr. 3, S. 30302/1-6.
- 314) B.S. Kim, G. Choi, D.I. Shim, K.M. Kim, H.H. Cho, *Surface roughening for hemi-wicking and its impact on convective boiling heat transfer*, International Journal of Heat and Mass Transfer 102 (2016) Nr. 11, S. 1100-1107.
- 315) I. Ibrahim, T. Gemming, W.M. Weber, T. Mikolajick, Z. Liu, M.H. Ruemmel, *Current Progress in the Chemical Vapor Deposition of Type-Selected Horizontally Aligned Single-Walled Carbon Nanotubes*, ACS Nano 10 (2016) Nr. 8, S. 7248-7266.
- 316) D. Hollaender, D. Kulawinski, M. Thiele, C. Damm, S. Henkel, H. Biermann, U. Gampe, *Investigation of isothermal and thermo-mechanical fatigue behavior of the nickel-base superalloy IN738LC using standardized and advanced test methods*, Materials Science and Engineering A 670 (2016), S. 314-324.

- 317) J. Gooth, R. Zierold, P. Sergelius, B. Hamdou, J. Garcia, C. Damm, B. Rellinghaus, H.J. Pettersson, A. Pertsova, C. Canali, M. Borg, K. Nielsch, *Local Magnetic Suppression of Topological Surface States in Bi_2Te_3 Nanowires*, ACS Nano 10 (2016) Nr. 7, S. 7180–7188.
- 318) I. Avigo, S. Thirupathaiah, M. Ligges, T. Wolf, J. Fink, U. Bovensiepen, *Doping dependence and electron-boson coupling in the ultrafast relaxation of hot electron populations in $\text{Ba}(\text{Fe}_{1-x}\text{Co}_x)_2\text{As}_2$* , New Journal of Physics 18 (2016), S. 93028/1–9.
- 319) A. Waske, E. Lovell, A. Funk, K. Sellschopp, A. Rack, L. Giebeler, P.F. Gostin, S. Faehler, L.F. Cohen, *The impact of surface morphology on the magnetovolume transition in magnetocaloric $\text{LaFe}_{11.8}\text{Si}_{1.2}$* , APL Materials 4 (2016), S. 106101/1–6.
- 320) F. Hippauf, W. Nickel, G.-P. Hao, K. Schwedtmann, L. Giebeler, S. Oswald, L. Borchardt, S. Doerfler, J.J. Weigand, S. Kaskel, *The Importance of Pore Size and Surface Polarity for Polysulfide Adsorption in Lithium Sulfur Batteries*, Advanced Materials Interfaces 3 (2016) Nr. 18, S. 1600508/1–9.
- 321) M. Hossain, C. Telke, M. Sparing, A. Abdkader, A. Nocke, R. Unger, G. Fuchs, A. Berger, C. Cherif, M. Beitelschmidt, L. Schultz, *Mathematical modeling, simulation and validation of the dynamic yarn path in a superconducting magnet bearing (SMB) ring spinning system*, Textile Research Journal (2016), S. 1–12.
- 322) B.S. Kim, G. Choi, S. Shin, T. Gemming, H.H. Cho, *Nano-inspired fluidic interactivity for boiling heat transfer: impact and criteria*, Scientific Reports 6 (2016), S. 34348/1–11.
- 323) P. Ramasamy, M. Stoica, M. Calin, J. Eckert, *Effect of Cu and Gd on Structural and Magnetic Properties of Fe-Co-B-Si-Nb Metallic Glasses*, Solid State Phenomena 254 (2016), S. 60–64.
- 324) P. Ramasamy, A. Szabo, S. Borzel, J. Eckert, M. Stoica, A. Bardos, *High pressure die casting of Fe-based metallic glass*, Scientific Reports 6 (2016), S. 35258/1–11.
- 325) I. Pethes, I. Kaban, M. Stoica, B. Beuneu, P. Jovari, *Chemical ordering in $\text{Pd}_{81}\text{Ge}_{19}$ metallic glass studied by reverse Monte-Carlo modelling of XRD, ND and EXAFS experimental data*, Physica Scripta 91 (2016) Nr. 10, S. 104004/1–10.
- 326) H.Q. Ta, L. Zhao, D. Pohl, J. Pang, B. Trzebicka, B. Rellinghaus, D. Pribat, T. Gemming, Z. Liu, A. Bachmatiuk, M.H. Ruemmel, *Graphene-Line ZnO: A Mini Review*, Crystals 6 (2016) Nr. 8, S. 100/1–17.
- 327) S. Schneider, D. Pohl, S. Loeffler, J. Rusz, D. Kasinathan, P. Schattschneider, L. Schultz, B. Rellinghaus, *Magnetic properties of single nanomagnets: Electron energy-loss magnetic chiral dichroism on FePt nanoparticles*, Ultramicroscopy 171 (2016), S. 186–194.
- 328) D. Pelc, M. Vuckovic, H.-J. Grafe, S.-H. Baek, M. Pozek, *Unconventional charge order in a co-doped high- T_c superconductor*, Nature Communications 7 (2016), S. 12775/1–7.
- 329) Y. Sun, Y. Zhang, C. Felser, B. Yan, *Strong Intrinsic Spin Hall Effect in the TaAs Family of Weyl Semimetals*, Physical Review Letters 117 (2016) Nr. 14, S. 146403.
- 330) A.P. Storey, S.J. Ray, V. Hoffmann, M. Voronov, C. Engelhard, W. Buscher, G.M. Hieftje, *Emergence and consequences of lateral sample heterogeneity in glow discharge spectrometry*, Spectrochimica Acta Part B 126 (2016), S. 37–43.
- 331) K.G. Prashanth, K. Zhuravleva, I. Okulov, M. Calin, J. Eckert, A. Gebert, *Mechanical and Corrosion Behavior of New Generation Ti-45Nb Porous Alloys Implant Devices*, Technologies 4 (2016) Nr. 33, S. 1–12.
- 332) E. Haubold, K. Koepf, D. Efremov, S. Khim, A. Fedorov, Y. Kushnirenko, J. van den Brink, S. Wurmehl, B. Buechner, T.K. Kim, M. Hoesch, K. Sumida, K. Taguchi, T. Yoshikawa, A. Kimura, T. Okuda, S.V. Borisenko, *Experimental realization of type-II Weyl state in non-centrosymmetric TaIrTe_4* , Nature Materials (2016), S. 1–9.
- 333) A. Alfonso, E. Ohmichi, P. Leksins, A. Omar, H.L. Wang, S. Wurmehl, F.Y. Yang, H. Ohta, *Cantilever detected ferromagnetic resonance in thin $\text{Fe}_{50}\text{Ni}_{50}$, $\text{Co}_2\text{FeAl}_{0.5}\text{Si}_{0.5}$ and $\text{Sr}_2\text{FeMoO}_6$ films using a double modulation technique*, Journal of Magnetic Resonance 270 (2016), S. 183–186.
- 334) B. Betz, P. Rauscher, R.P. Harti, R. Schaefer, A. Irastorza-Landa, H. Van Swygenhoven, A. Kaestner, J. Hovind, E. Pomjakushina, E. Lehmann, C. Gruenzweig, *Magnetization Response of the Bulk and Supplementary Magnetic Domain Structure in High-Permeability Steel Laminations Visualized In Situ by Neutron Dark-Field Imaging*, Physical Review Applied 6 (2016) Nr. 2, S. 024024/1–7.
- 335) B. Betz, P. Rauscher, R.P. Harti, R. Schaefer, H. Van Swygenhoven, A. Kaestner, J. Hovind, E. Lehmann, C. Gruenzweig, *Frequency-Induced Bulk Magnetic Domain-Wall Freezing Visualized by Neutron Dark-Field Imaging*, Physical Review Applied 6 (2016) Nr. 2, S. 024023/1–5.
- 336) B.J. Eleazer, M.D. Smith, Popov, A.A., D.V. Peryshkov, *(BB)-Carbonyne Complex of Ruthenium: Synthesis by Double B-H Activation at a Single Metal Center*, Journal of the American Chemical Society 138 (2016) Nr. 33, S. 10531–10538.
- 337) A.A. El-Gendy, S. Hampel, B. Buechner, R. Klingeler, *Tuneable magnetic properties of carbon-shielded NiPt-nanoalloys*, Rsc Advances 6 (2016) Nr. 57, S. 52427–52433.
- 338) A.P. Espejo, R. Zierold, J. Gooth, J. Dendooven, C. Detavernier, J. Escrig, K. Nielsch, *Magnetic and electrical characterization of nickel-rich NiFe thin films synthesized by atomic layer deposition and subsequent thermal reduction*, Nanotechnology 27 (2016) Nr. 34, S. 345707/1–11.

- 339) N. Feng, X. Sun, H. Yue, D. He, *Rational design of hierarchical Ni embedded NiO hybrid nanospheres for high-performance lithium-ion batteries*, RSC Advances 6 (2016) Nr. 76, S. 72008-72014.
- 340) M. Gursul, B. Ozelcik, A. Ekicibil, M. Liu, A.I. Boltalin, I.V. Morozov, *Effect of Sodium Substitution on Structural and Magnetic Properties of $KFe_{2-y}Se_2$* , Journal of Superconductivity and Novel Magnetism 29 (2016) Nr. 9, S. 2401-2406.
- 341) S. Haindl, S. Molatta, H. Hiramatsu, H. Hosono, *Recent progress in pulsed laser deposition of iron based superconductors*, Journal of Physics D 49 (2016) Nr. 34, S. 345301/1-7.
- 342) G.B. Halasz, N.B. Perkins, J. van den Brink, *Resonant Inelastic X-Ray Scattering Response of the Kitaev Honeycomb Model*, Physical Review Letters 117 (2016) Nr. 12, S. 127203/1-6.
- 343) K. Junghans, K.B. Ghiassi, N.A. Samoylova, Q.M. Deng, M. Rosenkranz, M.M. Olmstead, A.L. Balch, A.A. Popov, *Synthesis and Isolation of the Titanium-Scandium Endohedral Fullerenes- $Sc_2TiC@I-h-C-80$, $Sc_2TiC@D-5h-C-80$ and $Sc_2TiC@I-h-C-80$: Metal Size Tuning of the Ti-IV/Ti-III Redox Potentials*, Chemistry-a European Journal 22 (2016) Nr. 37, S. 13098-13107.
- 344) A. Koitzsch, C. Habenicht, E. Mueller, M. Knapfer, B. Buechner, H.C. Kandpal, J. van den Brink, O. Nowak, A. Isaeva, T. Doert, *Jeff Description of the Honeycomb Mott Insulator $\alpha-RuCl_3$* , Physical Review Letters 117 (2016) Nr. 12, S. 126403/1-5.
- 345) D.V. Konarev, L.V. Zorina, S.S. Khasanov, A.A. Popov, A. Otsuka, H. Yamochi, G. Saito, R.N. Lyubovskaya, *A crystalline anionic complex of scandium nitride endometallofullerene: experimental observation of single-bonded $(Sc_3N@/(h)-C-80(-))_2$ dimers*, Chemical Communications 52 (2016) Nr. 71, S. 10763-10766.
- 346) V.P. Kravchuk, U.K. Roessler, O.M. Volkov, D.D. Sheka, J. van den Brink, D. Makarov, H. Fuchs, H. Fangohr, Y. Gaididei, *Topologically stable magnetization states on a spherical shell: Curvature-stabilized skyrmions*, Physical Review B 94 (2016) Nr. 14, S. 144402/1-11.
- 347) R. Morrow, A.E. Taylor, D.J. Singh, J. Xiong, S. Rodan, A.U.B. Wolter, S. Wurmehl, B. Buechner, M.B. Stone, A.I. Kolesnikov, A.A. Aczel, A.D. Christianson, P.M. Woodward, *Spin-orbit coupling control of anisotropy, ground state and frustration in $5d(2) Sr_2MgOsO_6$* , Scientific Reports 6 (2016), S. 32462/1-11.
- 348) F.S. Nogueira, Z. Nussinov, J. van den Brink, *Duality of a compact topological superconductor model and the Witten effect*, Physical Review D 94 (2016) Nr. 8, S. 85003.
- 349) M. Okada, H. Tanaka, N. Kurita, K. Johmoto, H. Uekusa, A. Miyake, M. Tokunaga, S. Nishimoto, M. Nakamura, M. Jaime, G. Radtke, A. Saul, *Quasi-two-dimensional Bose-Einstein condensation of spin triplets in the dimerized quantum magnet $Ba_2CuSi_2O_6Cl_2$* , Physical Review B 94 (2016) Nr. 9, S. 94421/1-8.
- 350) C.X. Peng, K.K. Song, L. Wang, D. Soppa, S. Pauly, J. Eckert, *Correlation between structural heterogeneity and plastic deformation for phase separating FeCu metallic glasses*, Scientific Reports 6 (2016), S. 34340/1-11.
- 351) M. Saloaro, M. Hoffmann, W.A. Adeagbo, S. Granroth, H. Deniz, H. Palonen, H. Huhtinen, S. Majumdar, P. Laukkanen, W. Hergert, A. Ernst, P. Paturi, *Toward Versatile Sr_2FeMoO_6 -Based Spintronics by Exploiting Nanoscale Defects*, ACS Applied Materials and Interfaces 8 (2016) Nr. 31, S. 20441-20448.
- 352) P. Sergelius, J. Gooth, S. Bassler, R. Zierold, C. Wiegand, A. Niemann, H. Reith, C. Shekhar, C. Felser, B.H. Yan, K. Nielsch, *Berry phase and band structure analysis of the Weyl semimetal NbP*, Scientific Reports 6 (2016), S. 33859/1-6.
- 353) R. Streubel, P. Fischer, F. Kronast, V.P. Kravchuk, D.D. Sheka, Y. Gaididei, O.G. Schmidt, D. Makarov, *Magnetism in curved geometries*, Journal of Physics D 49 (2016) Nr. 36, S. 363001/1-45.
- 354) B.A. Sun, K.K. Song, S. Pauly, P. Gargarella, J. Yi, G. Wang, C.T. Liu, J. Eckert, Y. Yang, *Transformation-mediated plasticity in CuZr based metallic glass composites: A quantitative mechanistic understanding*, International Journal of Plasticity 85 (2016), S. 34-51.
- 355) B.M.S. Teixeira, A.A. Timopheev, R. Schmidt, M.R. Soares, M. Seifert, V. Neu, N.A. Sobolev, *Transfer of spin reorientation in a NdCo₅/Fe bilayer*, Journal of Physics D 49 (2016) Nr. 31, S. 315002/1-10.
- 356) X.Y. Wang, F. Zhang, K.S. Schellharnmer, P. Machata, F. Ortmann, G. Cuniberti, Y.B. Fu, J. Hunger, R.Z. Tang, A.A. Popov, R. Berger, K. Muellen, X.L. Feng, *Synthesis of NBN-Type Zigzag-Edged Polycyclic Aromatic Hydrocarbons: 1,9-Diaza-9a-boraphenylene as a Structural Motif*, Journal of the American Chemical Society 138 (2016) Nr. 36, S. 11606-11615.
- 357) D.E. Williams, E.A. Dolgoplova, D.C. Godfrey, E.D. Ermolaeva, P.J. Pellechia, A.B. Greytak, M.D. Smith, S.M. Avdoshenko, A.A. Popov, N.B. Shustova, *Fulleretic Well-Defined Scaffolds: Donor-Fullerene Alignment Through Metal Coordination and Its Effect on Photophysics*, Angewandte Chemie-International Edition 55 (2016) Nr. 31, S. 9070-9074.
- 358) A.C. Niemann, T. Boehnert, A.-K. Michel, S. Baessler, B. Gotsmann, K. Neurohr, B. Toth, L. Peter, I. Bakonyi, V. Vega, V.M. Prida, J. Gooth, K. Nielsch, *Thermoelectric Power Factor Enhancement by Spin-Polarized Currents - A Nanowire Case Study*, Advanced Electronic Materials 2 (2016) Nr. 9, 1600058/1-8.
- 359) L. Zhang, H.F. Zhang, W.Q. Li, T. Gemming, Z.W. Zhu, H.M. Fu, J. Eckert, S. Pauly, *Negentropic stabilization of metastable beta-Ti in bulk metallic glass composites*, Scripta Materialia 125 (2016), S. 19-23.

- 360) Q. Zhang, W.J. Wang, X. Kong, R.G. Mendes, L.W. Fang, Y.H. Xue, Y. Xiao, M.H. Ruemmeli, S.L. Chen, L. Fu, *Edge-to-Edge Oriented Self-Assembly of ReS₂ Nanoflakes*, Journal of the American Chemical Society 138 (2016) Nr. 35, S. 11101-11104.
- 361) S. Mushtaq, E.B.M. Steers, V. Hoffmann, Z. Weiss, J.C. Pickering, *Evidence for charge transfer from hydrogen molecular ions to copper atoms in a neon-hydrogen analytical glow discharge*, Journal of Analytical Atomic Spectrometry 31 (2016) Nr. 11, S. 2175-2181.
- 362) M. Zwiebler, E. Schierle, E. Weschke, B. Buechner, A. Revcolevschi, P. Ribeiro, J. J. Geck, J. Fink, *Stripe order of La_{1.64}Eu_{0.2}Sr_{0.16}Cu_{0.4} in magnetic fields studied by resonant soft x-ray scattering*, Physical Review B 94 (2016), S. 165157/1-4.
- 363) S. Thirupathaiah, S. Ghosh, R. Jha, E.D.L. Rienks, K. Dolui, V.V. Ravi Kishore, B. Buechner, T. Das, V.P.S. Awana, D.D. Sarma, J. Fink, *Unusual Dirac Fermions on the Surface of a Noncentrosymmetric \bar{a} -BiPd Superconductor*, Physical Review Letters 117 (2016), S. 177001/1-5.
- 364) T. Ueltzhoffer, R. Streubel, I. Koch, D. Holzinger, D. Makarov, O.G. Schmidt, A. Ehresmann, *Magnetically Patterned Rolled-Up Exchange Bias Tubes: A Paternoster for Superparamagnetic Beads*, ACS Nano 10 (2016) Nr. 9, S. 8491-8498.
- 365) X. Lu, Y. Yin, L. Zhang, L. Xi, S. Oswald, J. Deng, O.G. Schmidt, *Hierarchically porous Pd/NiO nanomembranes as cathode catalysts in Li-O₂ batteries*, Nano Energy 30 (2016), S. 69-76.
- 366) A. Bogusz, D. Buerger, I. Skorupa, O.G. Schmidt, H. Schmidt, *Bipolar resistive switching in YMnO₃/Nb:SrTiO₃ pn-heterojunctions*, Nanotechnology 27 (2016), S. 455201/1-9.
- 367) K. Mathwig, H.R. Zafarani, J.M. Speck, S. Sarkar, H. Lang, S.G. Lemay, L. Rassaei, O.G. Schmidt, *Potential-Dependent Stochastic Amperometry of Multi-ferrocenylthiophenes in an Electrochemical Nanogap Transducer*, The Journal of Physical Chemistry C 120 (2016) Nr. 40, S. 23262-23267.
- 368) Y. Jia, F. Cao, P. Ma, S. Scudino, J. Eckert, J. Sun, G. Wang, *Microstructure and thermal conductivity of hypereutectic Al-high Si produced by casting and spray deposition*, Journal of Materials Research 31 (2016) Nr. 19, S. 2948-2956.
- 369) P. Cudazzo, E. Mueller, C. Habenicht, M. Gatti, H. Berger, M. Knupfer, A. Rubio, S. Huotari, *Negative plasmon dispersion in 2H-NbS₂ beyond the chargedensity-wave interpretation*, New Journal of Physics 18 (2016), S. 103050/1-6.
- 370) C. Schubert, V. Hoffmann, A. Kuemmel, J. Sinn, M. Haertel, A. Reuther, M. Thomalla, T. Gemming, J. Eckert, C. Leyense, *Compositional depth profiling of diamond-like carbon layers by glow discharge optical emission spectroscopy*, Journal of Analytical Atomic Spectrometry 31 (2016), S. 2207-2212.
- 371) M. Hetti, Q. Wei, R. Pohl, R. Casperson, M. Bartusch, V. Neu, D. Pospiech, V. Voit, *Magnetite Core-Shell Nanoparticles in Nondestructive Flaw Detection of Polymeric Materials*, ACS Applied Materials and Interfaces 8 (2016) Nr. 41, S. 28208-28215.
- 372) K. Manna, R. Sarkar, S. Fuchs, Y.A. Onyikienko, A.K. Bera, G. Aslan Cansever, S. Kamusella, A. Maljuk, C.G.F. Blum, L.T. Corredor, A.U.B. Wolter, S.M. Yusuf, M. Frontzek, L. Keller, M. Iakovleva, E. Vavilova, H.-J. Grafe, V. Kataev, H.-H. Klauss, D.S. Inosov, S. Wurmehl, B. Buechner, *Noncollinear antiferromagnetism of coupled spins and pseudospins in the double perovskite La₂CuIrO₆*, Physical Review B 94 (2016), S. 144437/1-16.
- 373) G.S. Thakur, G. Fuchs, K. Nenkov, Z. Haque, L.C. Gupta, A.K. Ganguli, *Coexistence of superconductivity and ferromagnetism in Sr_{0.5}Ce_{0.5}FBiS_{2-x}Se_x (x = 0.5 and 1.0), a non-U material with T_c < T_{FM}*, Scientific Reports 6 (2016), S. 375227/1-.
- 374) A. Queraltó, M. de la Mata, L. Martínez, C. Magén, M. Gibert, J. Arbiol, R. Huehne, X. Obradors, T. Puig, *Orientation symmetry breaking in self-assembled Ce_{1-x}Gd_xO_{2-y} nanowires derived from chemical solutions*, RSC Advances 6 (2016), S. 97226-97236.
- 375) S. Engelhardt, M. Mietschke, C. Molin, S. Gebhardt, S. Faehler, K. Nielsch, R. Huehne, *Structural and ferroelectric properties of epitaxial BaZr_xTi_{1-x}O₃ thin films*, Journal of Physics D 49 (2016), S. 495303/1-7.
- 376) F. Liu, C.-L. Gao, Q. Deng, X. Zhu, A. Kostanyan, R. Westerstroem, S. Wang, Y.-Z. Tan, J. Tao, S.-Y. Xie, A.A. Popov, T. Greber, S. Yang, *Triangular Monometallic Cyanide Cluster Entrapped in Carbon Cage with Geometry-Dependent Molecular Magnetism*, Journal of the American Chemical Society 138 (2016) Nr. 138, S. 14764-14771.
- 377) B.W. Larson, O.G. Reid, D.C. Coffey, S.M. Avdoshenko, A.A. Popov, O.V. Boltalina, S.H. Strauss, N. Kopidakis, G. Rumbles, *Inter-Fullerene Electronic Coupling Controls the Efficiency of Photoinduced Charge Generation in Organic Bulk Heterojunctions*, Advanced Energy Materials (2016), S. 1601427/1-11.
- 378) A.K. Chaubey, P.K. Gokuldoss, Z. Wang, S. Scudino, N.K. Mukhopadhyay, J. Eckert, *Effect of Particle Size on Microstructure and Mechanical Properties of Al-Based Composite Reinforced with 10 Vol.% Mechanically Alloyed Mg-7.4% Al Particles*, Technologies 4 (2016) Nr. 37, S. 1-8.
- 379) W. Liu, D. Haubold, B. Rutkowski, M. Oschatz, R. Huebner, M. Werheid, C. Ziegler, L. Sonntag, S. Liu, Z. Zheng, A.-K. Herrmann, D. Geiger, B. Terlan, T. Gemming, L. Borchardt, S. Kaskel, A. Czyrska-Filemonowicz, A. Eychmueller, *Self-Supporting Hierarchical Porous PtAg Alloy Nanotubular Aerogels as Highly Active and Durable Electrocatalysts*, Chemistry of Materials 28 (2016) Nr. 18, S. 6477-6483.

- 380) A.P. Storey, S.J. Ray, V. Hoffmann, M. Voronov, C. Engelhard, W. Buscher, G.M. Hieftje, *Wavelength Scanning with a Tilting Interference Filter for Glow-Discharge Elemental Imaging*, Applied Spectroscopy (2016), S. 1-9.
- 381) R. Locus, D. Verboekend, R. Zhong, K. Houthoofd, T. Jaumann, S. Oswald, L. Giebeler, G. Baron, B.F. Sels, *Enhanced Acidity and Accessibility in Al-MCM-41 through Aluminum Activation*, Chemistry of Materials 28 (2016) Nr. 21, S. 7731-7743.
- 382) K. Chen, C. Li, L. Shi, T. Gao, X. Song, A. Bachmatiuk, Z. Zou, B. Deng, Q. Ji, D. Ma, H. Peng, Z. Du, M.H. Ruemmeli, Y. Zhang, Z. Liu, *Growing three-dimensional biomorphic graphene powders using naturally abundant diatomite templates towards high solution processability*, Nature Communications 7 (2016), S. 13440/1-9.
- 383) A.N. Darinskii, M. Weihnacht, H. Schmidt, *Computation of the pressure field generated by surface acoustic waves in microchannels*, Lab on a Chip 16 (2016) Nr. 14, S. 2701-2709.
- 384) C. Heinemann, S. Heinemann, B. Kruppke, H. Worch, J. Thomas, H.P. Wiesmann, T. Hanke, *Electric field-assisted formation of organically modified hydroxyapatite (ormoHAP) spheres in carboxymethylated gelatin gels*, Acta Biomaterialia 44 (2016), S. 135-143.
- 385) S. Khim, K. Koepernik, D.V. Efremov, J. Klotz, T. Foerster, J. Wosnitza, M.I. Sturza, S. Wurmehl, C. Hess, J. van den Brink, B. Buechner, *Magnetotransport and de Haas-van Alphen measurements in the type-II Weyl semimetal TaIrTe₄*, Physical Review B 94 (2016) Nr. 16, S. 165145.
- 386) W. Lu, M. Zeng, X. Li, J. Wang, L. Tan, M. Shao, J. Han, S. Wang, S. Yue, T. Zhang, X. Hu, R.G. Mendes, M.H. Ruemmeli, L. Peng, Z. Liu, L. Fu, *Controllable Sliding Transfer of Wafer-Size Graphene*, Advanced Science 3 (2016) Nr. 9, S. 1600006/1-7.
- 387) C. Monney, V. Bisogni, K.-J. Zhou, R. Kraus, V.N. Strocov, G. Behr, S.-L. Drechsler, H. Rosner, S. Johnston, J. Geck, T. Schmitt, *Probing inter- and intrachain Zhang-Rice excitons in Li₂ CuO₂ and determining their binding energy* 94 (2016) Nr. 16, S. 165118/1-8.
- 388) O. Perevertov, R. Schaefer, *Magnetic properties and magnetic domain structure of grainoriented Fe-3%Si steel under compression*, Materials Research Express 3 (2016) Nr. 9, S. 96103/1-12.
- 389) W. Schottenhamel, M. Abdel-Hafiez, R. Fittipaldi, V. Granata, A. Vecchione, M. Huecker, A.U.B. Wolter, B. Buechner, *Dilatometric study of the metamagnetic and ferromagnetic phases in the triple-layered Sr₄ Ru₃ O₁₀ system*, Physical Review B 94 (2016) Nr. 15, S. 155154/1-4.
- 390) A. Sobolkina, V. Mechtcherine, S. T. Bergold, J. Neubauer, C. Bellmann, V. Khavrus, S. Oswald, A. Leonhardt, W. Reschetilowski, *Effect of Carbon-Based Materials on the Early Hydration of Tricalcium Silicate*, Journal of the American Ceramic Society 99 (2016) Nr. 6, S. 2181-2196.
- 391) H.Q. Ta, D.J. Perello, D.L. Duong, G.H. Han, S. Gorantla, V.L. Nguyen, A. Bachmatiuk, S.V. Rotkin, Y.H. Lee, M.H. Ruemmeli, *Stranski-Krastanov and Volmer-Weber CVD Growth Regimes To Control the Stacking Order in Bilayer Graphene*, Nano Letters 16 (2016) Nr. 10, S. 6403-6410.
- 392) C. Tarantini, K. Iida, J. Haenisch, F. Kurth, J. Jaroszynski, N. Sumiya, M. Chihara, T. Hatano, H. Ikuta, S. Schmidt, P. Seidel, B. Holzapfel, D.C. Larbalestier, *Intrinsic and extrinsic pinning in NdFeAs(O,F): vortex trapping and lock-in by the layered structure*, Scientific Reports 6 (2016), S. 36047/1-9.
- 393) N.I. Verbitskiy, A.V. Fedorov, C. Tresca, G. Profeta, L. Petaccia, B.V. Senkovskiy, .Y. Usachov, D.V. Vyalikh, L.V. Yashina, A.A. Eliseev, T. Pichler, A. Grueneis, *Environmental control of electron-phonon coupling in barium doped graphene*, 2D Materials 3 (2016) Nr. 4, S. 45003/1-8.
- 394) B. Weise, K. Sellschopp, M. Bierdel, A. Funk, M. Bobeth, M. Krautz, A. Waske, *Anisotropic thermal conductivity in epoxy-bonded magnetocaloric composites*, Journal of Applied Physics 120 (2016) Nr. 12, S. 125103/1-7.
- 395) H. Wilhelm, A.O. Leonov, U.K. Roessler, P. Burger, F. Hardy, C. Meingast, M.E. Gruner, W. Schnelle, M. Schmidt, M. Baenitz, *Scaling study and thermodynamic properties of the cubic helimagnet FeGe*, Physical Review B 94 (2016) Nr. 14, S. 144424.
- 396) K.G. Prashant, S. Scudino, J. Eckert, *Tensile Properties of Al-12Si Fabricated via Selective Laser Melting (SLM) at Different Temperatures*, Technologies 4 (2016) Nr. 38, S. 4040038/1-9.
- 397) I. Avigo, S. Thirupathiah, E.D.L. Rienks, L. Rettig, A. Charnukha, M. Ligges, R. Cortes, J. Nayak, H.S. Jeevan, T. Wolf, Y. Huang, S. Wurmehl, M.I. Sturza, P. Gegenwart, M.S. Golden, L.X. Yang, K. Rosnagel, M. Bauer, B. Buechner, M. Vojta, M. Wolf, C. Felser, J. Fink, U. Bovensiepen, *Electronic structure and ultrafast dynamics of FeAs-based superconductors by angle- and time-resolved photoemission spectroscopy*, Physica Status Solidi B (2016), S. 201600382/1-15.
- 398) S. Haindl, M. Kidszun, E. Kampert, *Iron pnictide thin films: Synthesis and Physics*, Physical Status Solidi B (2016), S. 201600341/1-12.
- 399) R. Yadav, N. Bogdanov, V. Katukuri, S. Nishimoto, J. van den Brink, L. Hozoi, *Kitaev exchange and field-induced quantum spin-liquid states in honeycomb alpha-RuCl₃*, Scientific Reports (2016), S. 37925/1-16.

- 400) M.N. Kiselev, D.V. Efremov, S.L. Drechsler, J. van den Brink, K. Kikoin, *Coupled multiple-mode theory for $s \pm$ pairing mechanism in iron based superconductors*, Scientific Reports (2016), S. 37508/1-17.
- 401) T. Gustmann, J.M. dos Santos, P. Gargarella, U. Kuehn, J. Van Humbeeck, S. Pauly, *Properties of Cu-Based Shape-Memory Alloys Prepared by Selective Laser Melting*, Shape Memory and Superelasticity (2016), S. 1-13.
- 402) K. Duschek, M. Uhlemann, H. Schloerb, K. Nielsch, K. Leistner, *Electrochemical and in situ magnetic study of iron/iron oxide films oxidized and reduced in KOH solution for magneto-ionic switching*, Electrochemistry Communications 72 (2016), S. 153-156.
- 403) F. Katmis, V. Lauter, F.S. Nogueira, B.A. Assaf, M.E. Jamer, P. Wei, B. Satpati, J.W. Freeland, I. Eremin, D. Heiman, P. Jarillo-Herrero, J.S. Moodera, *A high-temperature ferromagnetic topological insulating phase by proximity coupling*, Nature 533 (2016) Nr. 7604, S. 513-516.
- 404) N.B. Weingartner, C. Pueblo, F.S. Nogueira, K.F. Kelton, Z. Nussinov, *A Phase Space Approach to Supercooled Liquids and a Universal Collapse of Their Viscosity*, Frontiers in Materials 3 (2016), S. 50/1-12.
- 405) J. Liu, M. Zeng, L. Wang, Y. Chen, Z. Xing, T. Zhang, Z. Liu, J. Zuo, F. Nan, R.G. Mendes, S. Chen, F. Ren, Q. Wang, M.H. Ruemmeli, L. Fu, *Monolayer Crystals: Ultrafast Self-Limited, Growth of Strictly Monolayer WSe₂ Crystals*, Small 12 (2016) Nr. 41, S. 5741-5749
- 406) O. Dutko, D. Placha, M. Mikeska, G.S. Martynkova, P. Wrobel, A. Bachmatiuk, M.H. Ruemmeli, *Comparison of Selected Oxidative Methods for Carbon Nanotubes: Structure and Functionalization Study*, Journal of Nanoscience and Nanotechnology 16 (2016) Nr. 8, S. 7822-7825.
- 407) A.V. Chubukov, I. Eremin, D.V. Efremov, *Superconductivity versus bound-state formation in a two-band superconductor with small Fermi energy: Applications to Fe pnictides/chalcogenides and doped SrTiO₃*, Physical Review B 93 (2016), S. 174516/1-25.
- 408) J. Dufouleur, L. Veyrat, B. Dassonneville, C. Nowka, S. Hampel, P. Leksin, B. Eichler, O. G. Schmidt, B. Buechner, R. Giraud, *Enhanced Mobility of Spin-Helical Dirac Fermions in Disordered 3D Topological Insulators*, Nano Letters 16 (2016) Nr. 11, S. 6733-6737.
- 409) S. Khim, S. Aswartham, V. Grinenko, D. Efremov, C.G.F. Blum, F. Steckel, D. Gruner, A.U.B. Wolter, S.-L. Drechsler, C. Hess, S. Wurmehl, B. Buechner, *A calorimetric investigation of RbFe₂As₂ single crystals*, Physica Status Solidi B (2016), S. 1-7.
- 410) D. Placha, M.H. Ruemmeli, *Nanoparticles for Nanocomposites and Their Characterization-Selected Peer-Reviewed Articles from NanoOstrava 2015*, Journal of Nanoscience and Nanotechnology 16 (2016) Nr. 8, S. 7781-7782.
- 411) G. van Miert, C. Ortix, C.M. Smith, *Topological origin of edge states in two-dimensional inversion-symmetric insulators and semimetals*, 2D Materials 4 (2016) Nr. 1, S. 15023/1-9.
- 412) L. Xu, N.A. Bogdanov, A. Princep, P. Fulde, J. van den Brink, L. Hozoi, *Covalency and vibronic couplings make a nonmagnetic $j=3/2$ ion magnetic*, npj Quantum Materials 1 (2016), S. 16029/1-6.
- 413) H.M.G.A. Tholen, J.S. Wildmann, A. Rastelli, R. Trotta, C.E. Pryor, E. Zallo, O.G. Schmidt, P.M. Koenraad, A.Y. Silov, *Strain-induced g-factor tuning in single InGaAs/GaAs quantum dots*, Physical Review B 94 (2016) Nr. 24, S. 245301/1-6.
- 414) J. Deng, X. Lu, L. Liu, L. Zhang, O.G. Schmidt, *Introducing Rolled-Up Nanotechnology for Advanced Energy Storage Devices*, Advanced Energy Materials 6 (2016) Nr. 23, S. 1600797/1-20.
- 415) G. Churilov, A. Popov, N. Vnukova, A. Dudnik, N. Samoylova, G. Glushenko, *Controlled synthesis of fullerenes and endohedral metallofullerenes in high frequency arc discharge*, Fullerenes, Nanotubes and Carbon Nanostructures 24 (2016) Nr. 11, S. 675-678.
- 416) A. Fedorov, A. Yaresko, T.K. Kim, Y. Kushnirenko, E. Haubold, T. Wolf, M. Hoesch, A. Grueneis, B. Buechner, S.V. Borisenko, *Effect of nematic ordering on electronic structure of FeSe*, Scientific Reports 6 (2016), S. 36834/1-7.
- 417) Z.-Y. He, L. Zhang, W.-R. Shan, Y.-Q. Zhang, Y.-H. Jiang, R. Zhou, J. Tan, *Characterizations on Mechanical Properties and In Vitro Bioactivity of Biomedical Ti-Nb-Zr-CPP Composites Fabricated by Spark Plasma Sintering*, Acta Metallurgica Sinica (English Letters) 29 (2016) Nr. 11, S. 1073-1080.
- 418) N. Koukourakis, B. Fregin, J. Koenig, L. Buettner, J.W. Czarske, *Wavefront shaping for imaging-based flow velocity measurements through distortions using a Fresnel guide star*, Optics Express 24 (2016) Nr. 19, S. 22074-22087.
- 419) A.O. Leonov, J.C. Loudon, A.N. Bogdanov, *Spintronics via non-axisymmetric chiral skyrmions*, Applied Physics Letters 109 (2016) Nr. 17, S. 172404/1-4.
- 420) V. Linseis, F. Voelklein, H. Reith, P. Woias, K. Nielsch, *Platform for in-plane ZT measurement and Hall coefficient determination of thin films in a temperature range from 120 K up to 450 K*, Journal of Materials Research 31 (2016) Nr. 20, S. 3196-3204.
- 421) B. Nagy, Y. Khaydukov, D. Efremov, A.S. Vasenko, L. Mustafa, J.-H. Kim, T. Keller, K. Zhernenkov, A. Devishvili, R. Steitz, B. Keimer, L. Bottyan, *On the explanation of the paramagnetic Meissner effect in superconductor/ferromagnet heterostructures*, epl 116 (2016) Nr. 1, S. 17005/1-6.
- 422) S. Nayak, K. Dasari, D.C. Joshi, P. Pramanik, R. Palai, A. Waske, R.N. Chauhan, N. Tiwari, T. Sarkar, S. Thota, *Low-temperature anomalous magnetic behavior of Co₂TiO₄ and Co₂SnO₄*, Journal of Applied Physics 120 (2016) Nr. 16, S. 1639505/1-6.

- 423) V. Haehnel, X. Ma, C. Konczak, D. Pohl, M. Uhlemann, H. Schloerb, *Fe-based Magnetic Alloy Electrodeposition for Thin Films and Template Based Nanostructures*, ECS Transactions 75 (2016) Nr. 2, S. 3-17.
- 424) N. Koukourakis, B. Fregin, J. Koenig, L. Buettner, J. Czarske, *Wavefront shaping for imaging-based flow velocity measurements through distortions using a Fresnel guide star*, Optics Express 24 (2016) Nr. 19, S. 1-14.
- 425) C. Hess, H. Grafe, A. Kondrat, G. Lang, F. Hammerath, L. Wang, R. Klingeler, G. Behr, B. Buechner, *Nematicity in $\text{LaFeAsO}_{1-x}\text{F}_x$* , Physica Status Solidi B 254 (2016) Nr. 1, S. 1600214/1-8.
- 426) F. Steckel, F. Cagliaris, R. Beck, M. Roslova, D. Bombor, I. Morozov, S. Wurmehl, B. Buechner, C. Hess, *Combined resistivity and Hall effect study on $\text{NaFe}_{1-x}\text{Rh}_x\text{As}$ single crystals*, Physical Review B 94 (2016) Nr. 18, S. 184514/1-6.
- 427) H.-L. Feng, S. Calder, M.P. Ghimire, Y.-H. Yuan, Y. Shirako, Y. Tsujimoto, Y. Matsushita, Z. Hu, C.-Y. Kuo, L.H. Tjeng, T.-W. Pi, Y.-L. Soo, J. He, M. Tanaka, Y. Katsuya, M. Richter, K. Yamaura, *$\text{Ba}_2\text{NiOsO}_6$: A Dirac-Mott insulator with ferromagnetism near 100 K*, Physical Review B 94 (2016) Nr. 23, S. 235158/1-9.
- 428) G. Cirillo, M. Curcio, O. Vittorio, U.G. Spizzirri, F.P. Nicoletta, N. Picci, S. Hampel, F. Iemma, *Dual stimuli responsive Gelatin-CNT hybrid films as a versatile tool for the delivery of anionic drugs*, Macromolecular Materials and Engineering 301 (2016) Nr. 12, S. 1537-1547.
- 429) Y.G. Naidyuk, N.V. Gamayunova, O.E. Kvitnitskaya, G. Fuchs, D.A. Chareev, A.N. Vasiliev, *Analysis of nonlinear conductivity of point contacts on the base of FeSe in the normal and superconducting state*, Low Temperature Physics 42 (2016) Nr. 1, S. 31-35.

Contributions to conference proceedings and monographs

- 1) T. Gustmann, A. Neves, U. Kuehn, P. Gargarella, C.S. Kiminami, C. Bolfarini, J. Eckert, S. Pauly, *Fabrication of Cu-Al-Ni-Mn Shape-Memory Parts by Selective Laser Melting*, Fraunhofer Direct Digital Manufacturing Conference (DDMC) 2016, in: Proceedings of the Fraunhofer Direct Digital Manufacturing Conference 2016, ISBN 978-3-8396-1001-5 (2016).
- 2) J. Thielsch, F. Bittner, T.G. Woodcock, *Interplay of magnetic domains and microstructural features in Mn-Al based permanent magnets*, Workshop, Darmstadt/Germany, 28.8.-1.9.16, in: 24nd International Workshop on Rare Earth and Future Permanent Magnets and their Applications (2016).
- 3) F. Bittner, L. Schultz, T.G. Woodcock, *Microstructure-property relationships in bulk MnAl-C permanent magnetic materials processed in various ways*, Workshop, Darmstadt/Germany, 28.8.-1.9.16, in: 24nd International Workshop on Rare Earth and Future Permanent Magnets and their Applications (2016).
- 4) T. Mix, F. Bittner, K.-H. Mueller, L. Schultz, T.G. Woodcock, *Formation and Magnetic Properties of the L10 Phase in the Ternary Mn-Al-Ga System*, Workshop, Darmstadt/Germany, 28.8.-1.9.16, in: 24nd International Workshop on Rare Earth and Future Permanent Magnets and their Applications (2016).
- 5) A. Volegov, A.S. Bolyachkin, T.G. Woodcock, D.S. Neznaknin, N.V. Selezneva, N.V. Kudrevatykh, *Estimation of Intergrain Exchange Interaction from the Kelly Plot*, Workshop, Darmstadt/Germany, 28.8.-1.9.16, in: 24nd International Workshop on Rare Earth and Future Permanent Magnets and their Applications (2016).
- 6) K. Franke, L. Eng, M. Weihnacht, W. Haessler, J. Besold, *The creation of the piezoresponse microscopy twenty-three years ago*, ISAF/ECAPD/PFM Conference 21-25th August, 2016 in Darmstadt/Germany, 21.-25.8.16, in: 2016 Joint IEEE International Symposium on the Applications of Ferroelectrics, European Conference on Applications of Polar Dielectrics & Workshop on Piezoresponse Force Microscopy (ISAF/ECAPD/PFM) (2016).
- 7) D. Jehnichen, D. Pospiech, P. Friedel, A. Horechyy, A. Korwitz, A. Janke, F. Naether, C. Papadakis, J. Perlich, V. Neu, *Effects of nanoparticles on phase morphology in thin films of phase-separated diblock copolymers*, „The European Powder Diffraction Conference“ EPDIC15, Bari/ Italy, 12.-15.6.16, in: Powder Diffraction (2016).
- 8) M. Medina-Sanchez, M. Guix, S. Harazim, L. Schwarz, O.G. Schmidt, *Rapid 3D printing of complex polymeric tubular catalytic micromotors*, International Conference on Manipulation, Automation and Robotics at Small Scales (MARSS), Paris/ France, 8.-22.7.16, S. 1-6 (2016).
- 9) S.V. Biryukov, A. Sotnikov, H. Schmidt, *Surface acoustic wave momentum*, 2016 IEEE International Ultrasonics Symposium (IUS), Tours/ France, 18.-21.9.16, in: 2016 IEEE International Ultrasonics Symposium (IUS), Proceedings, ID 318, Tours/ France, 18.-21.9.16; 978-14673-9897-8, S. 1-4 (2016).
- 10) C. Faust, E. Angermann, A. Winkler, H. Schmidt, *Multi-purpose SAW-based device for comprehensive cell behavior studies*, Proceedings of the Acoustofluidics Conference, Copenhagen/ Denmark, 26.9.16 (2016).
- 11) L. Schwarz, M. Medina-Sanchez, O.G. Schmidt, *Easily scalable high speed magnetic micropropellers*, in: International Conference on Manipulation, Automation and Robotics at Small Scales (MARSS), Paris, S. 1-4 (2016).

- 12) A. Ascoli, V. Senger, R. Tetzlaff, N. Du, O.G. Schmidt, H. Schmidt, *BiFeO₃ memristor-based encryption of medical data*, in: Circuits and Systems (ISCAS), 2016 IEEE International Symposium on (2016).
- 13) J. Garcia, N. Perez, M. Mohn, T. Sieger, H. Schloerb, H. Reith, G. Schierning, K. Nielsch, *Fabrication of a Micro-Thermoelectric Cooler for Room Temperature Applications by Template Assisted Electrodeposition*, 22nd International Workshop on Thermal Investigations of ICs and Systems (THERMINIC), Budapest/ Hungary, 21.-23.9.16, in: 22nd International Workshop on Thermal Investigations of ICs and Systems (THERMINIC), S. 14-18 (2016).
- 14) P. Ramasamy, M. Stoica, S. Bera, M. Calin, J. Eckert, *Effect of replacing Nb with (Mo and Zr) on glass forming ability, magnetic and mechanical properties of FeCoBSiNb bulk metallic glass*, 23rd International Symposium on Metastable, Amorphous and Nanostructured Materials, ISMANAM 2016, Nara/ Japan, 3.-8.7.16, in: Journal of Alloys and Compounds (2016).
- 15) A.N. Darinskii, M. Weihnacht, H. Schmidt, *SAW transmission across wedge-like contacts in composite substrates*, 2016 IEEE International Ultrasonics Symposium, 18.-21.9.16, Tours/ France, in: Proceedings 2016 IEEE International Ultrasonics Symposium, September 18.-21.9.16, Tours/ France; Electronic ISBN: 978-1-4673-9897-8; Print on Demand (PoD) ISBN: 978-1-4673-9898-5, S. 1-4 (2016).

Invited Talks

- 1) V. Hoffmann, *Advances in glow discharge spectrochemistry*, Winter Conference on Plasma Spectrochemistry (EWCPS), Tucson/ USA, 8.-16.1.16 (2016).
- 2) S. Wurmehl, *Towards novel materials for magnonics - a crystal growth perspective*, 603. Wilhelm-Else-Hereaus Seminar on 'Magnonics - Spin Waves Connecting Charges, Spins and Photons', Bad Honnef/ Germany, 5.-8.1.16 (2016).
- 3) J. Fink, *Non-Fermi-liquid scattering rates, anomalous band dispersions, and Hund's metal behavior in ironpnictides and ironchalcogenides - an ARPES study*, Advances in Electron Spectroscopy - Experiment and Theory (AESET 2016), Mandi/ India, 18.-21.1.16 (2016).
- 4) G. Schierning, *Silicon-based nanocomposites from a scalable gas Phase Synthesis process for thermoelectric application*, Symposium, Duisburg/ Germany, 20.-21.1.16 (2016).
- 5) G. Schierning, *Nanocrystalline bulk Silicon for direct thermal energy conversion*, Vortrag, Daytona Beach/ USA, 27.1.16 (2016).
- 6) V.M. Fomin, *Vortex dynamics in self-organized superconductor micro- and nanostructures*, Seminar, Moscow Institute of Electronics and Mathematics HSE-NRU, Moscow/ Russia, 28.1.16 (2016).
- 7) V.M. Fomin, *Impact of topology and geometry on physical properties of solid-state micro- and nanostructures*, Seminar „Physical Materials Science“, Institute of Solid State Physics RAS, Chernogolovka/ Russia, 27.1.16 (2016).
- 8) J. Hufenbach, J. Zeisig, J. Sander, H. Wendrock, L. Giebeler, J. Eckert, U. Kuehn, *Entwicklung hochfester Stahlgusslegierungen*, Seminars des Instituts für Strukturphysik der TU Dresden, Dresden/ Germany, 26.1.16 (2016).
- 9) M. Stoica, *Fe-based soft magnetic bulk metallic glasses*, Seminar of the Laboratory of Metal Physics and Technology (LMPT), Department of Materials, ETH Zürich, Zurich/ Switzerland, 28.1.16 (2016).
- 10) G. Schierning, *Nanokristallines Silizium für thermoelektrische Generatoren*, Ministerium für Innovation, Wissenschaft und Forschung des Landes NRW, Duesseldorf/ Germany, 11.2.16 (2016).
- 11) R. Niemann, S. Hahn, A. Diestel, A. Backen, L. Schultz, K. Nielsch, M.F.-X. Wagner, S. Faehler, *Nucleation barrier of martensite in magnetic shape memory films*, Seminar of the Department of Functional Materials, ASCR Prague, Prague/ Czech Republic, 18.2.16 (2016).
- 12) K. Leistner, K. Duschek, A. Petr, H. Schloerb, S. Faehler, *Electrically tunable nanomagnets by electrolytic gating: Magneto-ionic effect and Interface Control*, Joint Conference MMM-Intermag, San Diego/ USA, 11.-15.1.16 (2016).
- 13) R. Niemann, A. Diestel, A. Backen, S. Hahn, M.F.-X. Wagner, L. Schultz, S. Faehler, *Nucleation barrier of martensite in magnetocaloric Heusler films*, 80. Jahrestagung der DPG und DPG-Frühjahrstagung, Regensburg/ Germany, 6.-11.3.16 (2016).
- 14) R. Huehne, *Fe-basierte Supraleiter - Herstellung, Eigenschaften und Anwendungsperspektiven*, Workshop „Neueste Entwicklungen auf dem Gebiet der LT/HT-Supraleiter“, Hanau/ Germany, 10.3.16 (2016).
- 15) S. Borisenko, *Time-reversal symmetry breaking type II Weyl state in YbMnBi₂*, APS March Meeting 2016, Baltimore/ USA, 12.-19.3.16 (2016).
- 16) S. Wurmehl, *Crystal growth at IFW*, Annual conference of the german society for crystal growth and crystallography (DGKK), Dresden/ Germany, 15.-18.3.16 (2016).
- 17) P.F. Siles, *Conductive AFM approaches towards functional nanoelectronics*, e-Seminar, online session for New AFM-enabled electrical measurement techniques, Keysight Technologies, Inc., Germany, 16.3.16 (2016).

- 18) T. Gustmann, J.M. dos Santos, A. Neves, U. Kuehn, P. Gargarella, C.S. Kiminami, C. Bolfarini, W.J. Botta, J. Eckert, S. Pauly, *Fabrication of Cu-based Shape-Memory Parts by Selective Laser Melting*, Fraunhofer Direct Digital Manufacturing Conference (DDMC) 2016, Berlin/ Germany, 16.-17.3.16 (2016).
- 19) V.M. Fomin, *Vortex dynamics in self-assembled superconductor micro- and nanostructures*, Seminar of the Department of Physics, Universita degli Studi di Napoli, Naples/ Italy, 21.3.16 (2016).
- 20) O.G. Schmidt, *3D Assembly of microtubular nanomembrane devices*, Seminar, University of Texas, Dallas/ USA, 22.3.16 (2016).
- 21) V.M. Fomin, *Theoretical modeling of electronic and optical properties of nanostructures: From the non-adiabaticity of semiconductor nanocrystals to the geometric and topological effects in quantum rings*, The Sixth Annual Meeting (March Meeting) of the Mediterranean Institute of Fundamental Physics (MIFP), Rome/ Italy, 25.3.16 (2016).
- 22) A. Sotnikov, H. Schmidt, *Precise microacoustic characterizaion of new piezoelectric crystals*, Sino-german workshop on Acoustics, Peking/ China, 14.-18.3.16 (2016).
- 23) O.G. Schmidt, *Nanophotonics with strainable and shapable nanomembranes*, Sino-German Symposium on Nano-Photonics and Nano-Optoelectronics, Herrenberg/ Germany, 4.-9.4.16 (2016).
- 24) C. Hess, *Unusual temperature evolution of superconductivity in LiFeAs*, COST Action MP1201 „Nanoscale Superconductivity“ Workshop „Probing Superconductivity at the Nanoscale : New advances“, Saas-Fee/ Switzerland, 12.-15.4.16 (2016).
- 25) C. Hess, *Introduction to scanning tunneling microscopy and spectroscopy on iron-based superconductors*, 2nd Summer School on Iron Pnictides of SPP1458, Storkow/ Germany, 4.-8.4.16 (2016).
- 26) S. Wurmehl, *Impact of concomitant Y and Mn substitution on magnetic and superconducting properties in $La_{1-z}Y_zFe_{1-y}Mn_yAsO_{0.9}F_{0.1}$* , 5th International Conference on Superconductivity and Magnetism (ICSM2016), 24.-30.4.16 (2016).
- 27) S. Borisenko, *ARPES Studies of Multiband Iron-Based Superconductors*, 5th International Conference on Superconductivity and Magnetism (ICSM2016), 24.-30.4.16 (2016).
- 28) R. Niemann, A. Diestel, A. Backen, S. Hahn, M.F.-X. Wagner, L. Schultz, S. Faehler, *Nucleation barrier and transformation path of martensite in epitaxial shape memory films*, Group Seminar of the Departament d'Estructura i Constituents de la Matèria, Universitat de Barcelona, Barcelona/ Spain, 7.4.16 (2016).
- 29) V.M. Fomin, *Vortex dynamics in self-assembled superconductor micro- and nanostructures*, COST Action MP1201 „Nanoscale Superconductivity“ Workshop „Probing Superconductivity at the Nanoscale : New advances“, Saas-Fee/ Switzerland, 12.-15.4.16 (2016).
- 30) A. Waske, B. Weise, M.-H. Lee, A. Gebert, *RE-containing vs. RE-free materials for magnetocaloric refrigeration*, MCAR2016, Clearwater/ USA, 18.4.-21.4.16 (2016).
- 31) B. Schleicher, S. Schwabe, A. Diestel, A. Waske, R. Huehne, P. Walter, L. Schultz, S. Faehler, *Towards Multicaloric Refrigeration in Ni-Mn-Ga-Co/PMN-PT Heterostructures*, MRS Spring Meeting and Exhibit, Phoenix/ USA, 28.3.-1.4.16 (2016).
- 32) K. Leistner, *Voltage-control of magnetism in metal/metal oxide thin films by electrochemical approaches and interface design*, Special Seminar, Department of Physics, Simon Fraser University, Burnaby/ Canada, 16.3.16 (2016).
- 33) C. Hess, *Spin and pseudo-spin heat transport of 2D quantum magnets*, International Conference on Superconductivity and Magnetism (ICSM) 2016, Fethiye/ Turkey, 24.-30.4.16 (2016).
- 34) S. Borisenko, *Spin-orbit Interaction in High-Tc Superconductors*, Energy, Materials and Nanotechnology (EMN) Croatia Meeting 2016, Dubrovnik/ Croatia, 4.-7.5.16 (2016).
- 35) I. Harnagea, S. Aswartham, A. Wolter-Giraud, U. Graefe, F. Hammerath, F. Steckel, A. Alfonsov, V. Kataev, S. Borisenko, C. Hess, S. Wurmehl, B. Buechner, *Single Crystal Growth and Characterization of Fe-Based Superconductors*, International Workshop on Fe-based superconductors, Dresden/ Germany, 23.-25.5.16 (2016).
- 36) S. Borisenko, *Nematicity and spin-orbit interaction in iron-based superconductors*, International Workshop & Seminar on Strong Correlations and the Normal State of the High Temperature Superconductors, Dresden/ Germany, 17.-20.5.16 (2016).
- 37) S. Borisenko, *Spin-orbit coupling in iron-based superconductors or Experimental realization of time-reversal symmetry breaking Weyl state*, International Conference on Low-Energy Electrodynamics in Solids (LEES) 2016, MoriYama (Shiga)/ Japan, 29.5.-3.6.16 (2016).
- 38) V.M. Fomin, *Phonon spectrum engineering in rolled-up micro- and nanoarchitectures*, Humboldt Kolleg „Nano-2016“, Chisinau/ Republic of Moldova, 11.5.16 (2016).
- 39) M. Stoica, P. Ramasamy, I. Kaban, S. Scudino, J. Wright, J. Eckert, *Influence of small Cu addition on the crystallization behavior of soft magnetic FeCoBSiNb bulk metallic glass*, THERMEC'2016, International Conference on Processing & Manufacturing of Advanced Materials: Processing, Fabrication, Properties, Applications, Graz/ Austria, 29.5.-3.6.16 (2016).

- 40) M. Stoica, S. Scudino, J. Bednarcik, I. Kaban, J. Eckert, *FeCoSiBNbCu Bulk Metallic Glass with Compressive Deformability*, TMS 2016, The 145th Annual meeting and exhibition, Nashville/ USA, 14.-18.2.16 (2016).
- 41) V.M. Fomin, *Phonon spectrum engineering in rolled-up micro- and nanoarchitectures*, XV. International Conference on Intergranular and Interphase Boundaries in Materials, Moscow/ Russia, 27.5.16 (2016).
- 42) F. Zhu, *Novel organic/hybrid nanoscale devices based on rolled-up nanomembrane*, The 1st Chemistry and Materials Day in Dresden, Dresden/ Germany, 28.5.16 (2016).
- 43) B. Buechner, *Polarons and orbitals in Fe based superconductors*, 3rd Internal Workshop GRK 1621, Meißen/ Germany, 27.5.16 (2016).
- 44) J. Fink, *ARPES studies of the electronic structure of Iron-based high-Tc superconductors*, Instituts-Kolloquium, Helmholtz-Zentrum Dresden-Rossendorf, Dresden/ Germany, 7.6.16 (2016).
- 45) J. Fink, *Influence of Lifshitz transitions and correlation effects on the scattering rates and the effective mass of the charge carriers in ferropnictides and ferrochalcogenides.*, International Conference Superstripes 2016, Ishia/ Italy, 26.-29.6.16 (2016).
- 46) V. Kataev, *Possible magnetic field induced hidden order in the low-dimensional quantum magnet LiCuSbO₄*, International Conference Superstripes 2016, Ishia/ Italy, 23.-28.6.16 (2016).
- 47) V. Kataev, *Multifrequency sub-THz ESR spectroscopy of correlated spin systems in strong magnetic fields*, Seminar zur Statistischen Physik, Bergische Universität Wuppertal, Wuppertal/ Germany, 2.6.16 (2016).
- 48) V. Kataev, *Exotic spin phases in the low-dimensional quantum magnet LiCuSbO₄*, International Conference on Superconductivity and Magnetism (ICSM) 2016, 24.-30.4.16 (2016).
- 49) J.E. Hamann-Borrero, *Depth and monolayer resolved spectroscopy of oxide heterostructures from resonant x-ray reflectivity*, Physics seminar, Max Planck Institute, Stuttgart/ Germany, 4.4.16 (2016).
- 50) J.E. Hamann-Borrero, *Depth and monolayer resolved spectroscopy of oxide heterostructures from resonant x-ray reflectivity*, FOKUS seminar on Physics of oxide materials and heterostructures, Julius Maximilian Universität Würzburg, Würzburg/ Germany, 11.4.16 (2016).
- 51) O.G. Schmidt, *Unconventional applications of flexible nanomembrane materials*, Nature Conference on Flexible Electronics, Nanjing/ China, 5.-9.6.16 (2016).
- 52) S. Borisenko, *ARPES of superconductors*, International Conference Superstripes 2016, Ishia/ Italy, 23.-28.6.16 (2016).
- 53) O.G. Schmidt, *3D Assembly of microtubular nanomembrane device architectures*, 3rd International Conference on the Challenges and Perspectives of Functional Nanostructures, Ilmenau/ Germany, 20.-22.6.16 (2016).
- 54) V. Haehnel, X. Ma, C. Konczak, D. Pohl, M. Uhlemann, H. Schloerb, *Fe- based Magnetic Alloy Electrodeposition For Thin Films and Template Based Nanostructures*, PRiME 2016 - 230th meeting of the Electrochemical Society, Honolulu/ USA, 2.-7.10.16 (2016).
- 55) D. Lindackers, *Entwicklung eines supraleitenden Präzisionslagers fuer eine Fluessig-Heliumpumpe*, 10. Tagung „Feinwerk-technische Konstruktion“, Dresden/ Germany, 22.-23.9.16 (2016).
- 56) J.K. Hufenbach, H. Wendrock, J. Sander, J. Zeisig, L. Giebler, J. Eckert, U. Kuehn, *Entwicklung hochfester Stahlgusslegierungen*, Spezialseminar an der Technischen Universität Bergakademie Freiberg, Freiberg/ Germany, 6.6.16 (2016).
- 57) J. Eckert, R.N. Shahid, P. Wang, K.G. Prashanth, M. Stoica, D. Zhang, *Bulk processing of nanostructured advanced materials*, TMS 2016, The 145th Annual meeting and exhibition, Nashville/ USA, 14.-18.2.16 (2016).
- 58) J.J. Krucic, B.S. Li, H. Shakur Shahabi, S. Scudino, J. Eckert, *Designed Heterogeneities Improve the Fracture Reliability of a Zr-based Bulk Metallic Glass*, TMS 2016, The 145th Annual meeting and exhibition, Nashville/ USA, 14.-18.2.16 (2016).
- 59) A. Waske, A. Funk, B. Weise, A. Rack, S. Faehler, *The Magnetovolume Transition of LaFe_{11.8}Si_{1.2} as a Model System to Understand the Influence of Volume Expansion on Hysteresis During First Order Phase Transitions*, CIMTECH 2016, Perugia/ Italy, 6.6.16 (2016).
- 60) A. Waske, A. Funk, B. Weise, M. Bierdel, A. Rack, *In-situ XRD and 3D imaging techniques for the study of magnetocaloric materials*, MRS Spring Meeting, Phoenix/ USA, 30.3.16 (2016).
- 61) A. Funk, B. Weise, M. Krautz, G. Potnis, M. Bierdel, M. Haack, K. Sellschopp, A. Waske, *Magnetocaloric La(Fe,Si)₁₃: In-situ experiments and fatigue behavior*, Colloquium of the Erich Schmid Institute of Materials Science, Leoben/ Austria, 11.3.16 (2016).
- 62) A. Waske, *Magnetocaloric Refrigeration: Research interests at IFW Dresden*, Seminar of the Physics and Astronomy Department of the Faculty of Sciences at Porto University, Porto/ Portugal, 15.10.16 (2016).
- 63) S. Borisenko, *ARPES of superconductors*, Multi-Component and Strongly-Correlated Superconductors, Nordita, Stockholm/ Sweden, 4.-29.7.16 (2016).
- 64) M. Stoica, S. Scudino, I. Kaban, P. Ramasamy, D. Söpu, B. Sarac, D. Ehinger, D. Geißler, J. Eckert, *Structural modifications of Fe-based BMGs induced by thermal cycling studied by mean of in-situ X-ray diffraction*, 23rd International Symposium on Metastable, Amorphous and Na, Nara/ Japan, 3.-8.7.16 (2016).

- 65) B. Buechner, *Polarons and orbitals in Fe based superconductors*, Superstripes 2016, Ischia/ Italy, 23.-28.6.16 (2016).
- 66) A. Gebert, *Corrosion Behaviour of Magnetic Materials*, Gordon Research Conference: Corrosion Aqueous, Colby-Sawyer College, New London, NH/ USA, 10.-15.7.16 (2016).
- 67) S. Oswald, *Challenges in binding energy referencing of XPS measurements for Li-based materials*, Seminarvortrag am KIT Karlsruhe, Institut für Angewandte Materialien IAM-ESS, Karlsruhe/ Germany, 7.7.16 (2016).
- 68) M. Calin, M. Boenisch, A. Helth, S. Pilz, L. Giebler, A. Gebert, W. Skrotzki, J. Eckert, *Thermal stability and structural characteristics of metastable beta-type Ti-Nb alloys for implant applications*, TMS 2016, Nashville/USA, 16.-18.2.16 (2016).
- 69) M. Calin, M. Boenisch, S. Pilz, S. Bera, A. Gebert, J. Eckert, *Property optimization of Ti-based biomaterials by structural design*, Conference „Diaspora si prietenii 2016“, Timisoara/ Romania, 24.-28.4.16 (2016).
- 70) M. Calin, M. Boenisch, A. Helth, S. Pilz, R. Schmidt, A. Gebert, T. Waitz, M. Zehetbauer, J. Eckert, *Nanostructured SPD-processed Ti-based materials for load-bearing orthopaedic applications*, THERMEC 2016, Graz/Austria, 29.5-3.6.16 (2016).
- 71) M. Calin, S. Bera, R. Parthiban, N. Zhang, M. Stoica, J. Eckert, *Effect of ‘soft’ atoms (Ga, In) on glass formation and mechanical behavior of Ni-free Ti-based bulk metallic glasses*, ISMANAM 2016, Nara/Japan, 3.-8.7.16 (2016).
- 72) O.G. Schmidt, *Microtubular NEMS for on- and off-chip applications*, International Conference on Manipulation, Automation and Robotics at Small Scales, Paris/ France, 18.-22.7.16 (2016).
- 73) O.G. Schmidt, *Shrinking the unshrinkable*, Scifoo 2016, Google Headquarters, Mountain View/ USA, 22.-24.7.16 (2016).
- 74) O.G. Schmidt, *Microtubular nanomembrane architectures: From 3D assembly to paradigm shifting technologies*, 9th Nano Conference for Next Generation, Manchester/ United Kingdom, 1.-2.8.16 (2016).
- 75) I. Kaban, L. Xi, R. Nowak, G. Bruzda, N. Sobczak, J. Eckert, *Wettability and interfacial interactions between TiB₂ ceramic and Ni-Al melts*, 9th International Conference on High Temperature Ceramic Mat, Toronto/ Canada, 26.6.-1.7.16 (2016).
- 76) R. Schmidt, S. Pilz, *Materials Characterization in M1 - selected techniques*, SFB/ TR 79 Young Scientist Workshop, Eisenach/ Germany, 26.-27.4.16 (2016).
- 77) A. Gebert, P.F. Gostin, D. Grell, E. Kerscher, *Electrochemical properties of metallic glasses and related composites*, LAM-16, Bad Godesberg/ Germany, 4.-6.9.16 (2016).
- 78) R. Niemann, A. Diestel, B. Schleicher, A. Backen, H. Seiner, O. Heczko, S. Hahn, M.F.-X. Wagner, L. Schultz, K. Nielsch, S. Faehler, *Nucleation of martensite in epitaxial Heusler films*, The Fifth International Conference on Ferromagnetic Shape Memory Alloys, Miyagi/ Japan, 5.-9.9.16 (2016).
- 79) S.B. Menzel, *Anwendung der FIB-Technik in der SAW-Technologie*, Workshop: „Von Nano bis Makro: Neue bildgebende Untersuchungsverfahren für Qualitätskontrolle und Materialforschung“, Dresden/ Germany, 8.-9.11.16 (2016).
- 80) M. Medina-Sanchez, *3D printed micromotors*, International Conference on Manipulation, Automation and Robotics at Small Scales, Paris/ France, 18.-22.7.16 (2016).
- 81) B. Rellinghaus, D. Pohl, A. Surrey, F. Schmidt, S. Wicht, S. Schneider, *On the phase stability of metallic nanoparticles - towards structure-property relations at the atomic scale*, 2016 Japan-German Joint Symposium on Advanced Characterization of Nanostructured Materials for Energy and Environment, Duesseldorf/ Germany, 27.-29.6.16 (2016).
- 82) B. Rellinghaus, *Structure-property relations at the very atomic level*, Workshop on Scientific Directions for Future Transmission Electron Microscopy, Forschungszentrum Juelich - Ernst Ruska-Center, Juelich/ Germany, 13.-15.7.16 (2016).
- 83) V. Hoffmann, *Analyse von Wasserstoff, Kohlenstoff und Sauerstoff mit der optischen Glimmentladungs-Spektrometrie*, 25. ICP-MS Anwendertreffen und 12. Symposium Massenspektrometrische Verfahren der Elementspurenanalyse, Siegen/ Germany, 12.-15.9.16 (2016).
- 84) B. Buechner, *Magnetic Moments and Hysteresis of an Endohedral Single-Molecule Magnet on a Metal*, The International Conference on Solid Films and Surfaces (ICSFS), Chemnitz/ Germany, 29.8.16 (2016).
- 85) V.M. Fomin, *Vortex matter in rolled-up superconductor micro- and nanotubes*, International Conference „Nano confined superconductors and their applications“, Garmisch-Partenkirchen/ Germany, 5.9.16 (2016).
- 86) M. Medina-Sanchez, *Sperm-Carrying micromotors for new assisted reproduction techniques*, Technical Video Conference on Micro and Nanotechnologies, IEEE Colombia and Javeriana University, Bogotá/ Colombia, 18.8.16 (2016).
- 87) M. Medina-Sanchez, *Miniaturized ultrasensitive biosensors*, Mini-Course, Science Week, EAN University, Bogotá/ Colombia, 25.8.16 (2016).
- 88) M. Medina-Sanchez, *Micromotors for biomedical and environmental applications*, Mini-Course, Science Week, EAN University, Bogotá/ Colombia, 26.8.16 (2016).
- 89) M. Medina-Sanchez, *On-chip and off-chip miniaturized platforms for biomedicine*, Science Week, EAN University, Bogotá/ Colombia, 27.8.16 (2016).

- 90) M. Medina-Sanchez, *Bio-hybrid micromotors: Assisted fertilization*, Seminar, Andes University, Bogotá/ Colombia, 29.8.16 (2016).
- 91) O.G. Schmidt, *The winding path of the spermbot*, Seminar, Colombian Fertility and Sterility Center, Bogotá/ Colombia, 2.9.16 (2016).
- 92) M. Medina-Sanchez, *Sperm-robots: Rethinking the assisted fertilization*, Seminar, Colombian Fertility and Sterility Center, Bogotá/ Colombia, 2.9.16 (2016).
- 93) J. Thomas, T. Gemming, K. Wetzig, *Analysis of Nanostructures by Analytical TEM*, EFDS Workshop „Von Nano bis Makro: Bildgebende Untersuchungsverfahren für Qualitätskontrolle und Materialforschung“, Dresden/ Germany, 8.-9.11.16 (2016).
- 94) R. Niemann, A. Diestel, S. Hahn, M.F.-X. Wagner, L. Schultz, S. Faehler, *Nucleation barrier and transformation path of martensite in epitaxial shape memory films*, Group Seminar, Materials Science and Engineering Department, College Station, Texas/ USA, 28.7.16 (2016).
- 95) O.G. Schmidt, *Engineering the smallest engines*, European Drive Technology Conference, Lucerne/ Switzerland, 7.-10.9.16 (2016).
- 96) R. Schaefer, I. Soldatov, *Progress in magneto-optical domain imaging*, Physikalisches Kolloquium der Universität Luxembourg, Luxembourg/ Luxembourg, 28.9.16 (2016).
- 97) R. Schaefer, I. Soldatov, *Progress in magneto-optical domain imaging*, Seminarvortrag an Far Eastern Federal University, Vladivostok/ Russia, 18.2.16 (2016).
- 98) R. Schaefer, I. Soldatov, *Progress in Magneto-Optical Kerr Microscopy*, Keynote talk at 2nd International Forum on Research and Technologies for Society and Industry (IEEE RTSI 2016), Bologna/ Italy, 7.-9.9.16 (2016).
- 99) R. Schaefer, *Magneto-Optical domain imaging*, Plenary talk at 16th Czech and Slovak Conference on Magnetism (CSMAG'16), Kosice/ Slovakia, 13.-17.6.16 (2016).
- 100) R. Schaefer, I. Soldatov, *Progress in magneto-optical domain imaging*, Seminar am Paul Scherrer Institut (PSI), Villigen/ Switzerland, 17.5.16 (2016).
- 101) R. Schaefer, I. Soldatov, *Progress in magneto-optical domain imaging*, International Conference on Superconductivity and Magnetism (ICSM2016), Fethiye/ Turkey, 24.-30.4.16 (2016).
- 102) A. Gebert, *Electrochemical properties of bulk glass-forming alloys*, VitriMetTech Workshop on Chemical Properties of Vitrified Metals, Universite Grenoble Alpes/ France, 12.-15.9.16 (2016).
- 103) O.G. Schmidt, *Microtubular NEMS: From 3D assembly to on- and off-chip applications*, E-MRS Spring Meeting, Warsaw/ Poland, 19.-22.9.16 (2016).
- 104) R. Rezaev, E. Levchenko, V. Fomin, *Simulation of rolled-up superconductor micro- and nanotubes*, 8th International Conference on Materials Science and Condensed Matter Physics, Chisinau/ Republic of Moldova, 14.9.16 (2016).
- 105) D. Karnaushenko, *Shapeable microelectronics*, Lecture, Novosibirsk State Technical University, Novosibirsk/ Russian Federation, 13.9.16 (2016).
- 106) J. Fink, *Non Fermi liquid behavior, Lifshitz transitions, and Hund's metal behavior in iron-based superconductors from ARPES*, Seminarvortrag, Institut für Festkörperphysik Wien/ Austria, 8.8.16 (2016).
- 107) J. Fink, *Introduction into current electron-energy-loss and angle-resolved photoelectron spectroscopy*, 17th International conference on the science and application of nanotubes and low-dimensional materials (NT16), Wien/ Austria, 7.-13.8.16 (2016).
- 108) V. Eckert, *Synthese und Charakterisierung von nadelförmigen Carbon Nanotubes (CNTs)*, Prozessverfahrenstechnisches Seminar (TU Dresden), Dresden/ Germany, 7.7.16 (2016).
- 109) J. Fink, *Non-Fermi-liquid behavior, Lifshitz transition and Hund's metal behavior in ferropnictides from ARPES*, International Workshop „Advances in preparation and investigation of emergent iron-based superconductors“, IFW Dresden, Dresden/ Germany, 23.-25.5.16 (2016).
- 110) C. Hess, *Unconventional superconductivity probed by scanning tunneling microscopy and spectroscopy*, Wiener Physikalisches Kolloquium, Universität Wien/ Austria, 18.4.16 (2016).
- 111) C. Hess, *Spin-Heat Transport in Low-Dimensional Quantum Magnets*, Physikalisches Kolloquium, Universität Bielefeld/ Germany, 30.5.16 (2016).
- 112) C. Hess, *Unconventional superconductivity in LiFeAs probed by scanning tunneling microscopy and spectroscopy*, International Workshop „Advances in preparation and investigation emergent iron-based superconductors“, IFW Dresden, Dresden/ Germany, 23.-25.5.16 (2016).
- 113) I. Kaban, *Structural and kinetic properties of Ge-Sb-Te phase-change alloys in liquid and supercooled liquid state*, Colloquium, Department of Applied Physics, School of Natural and Applied Sciences, Northwestern Polytechnical University, Xi'an/ P. R. China, 21.9.16 (2016).

- 114) I. Kaban, *Studies of structure-property relationship in liquid Ge-Sb-Te alloys*, Colloquium, The Key Laboratory for Liquid-Solid Structural Evolution and Processing of Materials Ministry of Education, Shandong University, Jinan/ P. R. China, 25.9.16 (2016).
- 115) P. Pahlke, M. Sieger, R. Ottolinger, J. Haenisch, B. Holzapfel, A. Usoskin, J. Stroemer, M. Lao, M. Eisterer, A. Meledin, G. van Tendeloo, A. Kursumovic, J.L. MacManus-Driscoll, B.H. Stafford, M. Bauer, K. Nielsch, L. Schultz, R. Huehne, *Implementing artificial BaHfO₃ and Ba₂Y(Nb/Ta)O₆ pinning centers in thick YBCO films on technical templates - a comparative study*, 2016 Applied Superconductivity Conference, Denver/ USA, 4.-9.9.16 (2016).
- 116) M. Calin, S. Bera, P. Ramasamy, M. Stoica, J. Eckert, *Improved mechanical behavior of Ni-free Ti-based bulk metallic glasses by minor In/Ga additions*, LAM 2016, Bonn - Bad Godesberg/ Germany, 4.-9.9.16 (2016).
- 117) H.-J. Grafe, F. Hammerath, *Impurity effects in $S = 1/2$ Heisenberg spin chains as probed by nuclear magnetic resonance*, 7th International Conference The New Generation in Strongly Correlated Electrons Systems 2016, 7th International Conference The New Generation in Strongly Correlated Electrons Systems 2016, International Centre for Theoretical Physics (ICTP) in Trieste/ Italy, 26.9.-30.9.16 (2016).
- 118) F. Ding, *Towards a semiconductor based quantum optics network*, International workshop on contacts in nanosystems: Interaction, control and quantum dynamics, Goslar/ Germany, 5.-7.10.16 (2016).
- 119) S. Pauly, T. Gustmann, J.M. dos Santos, P. Gargarella, U. Kuehn, *Cu-based shape memory alloys processed by selective laser melting*, Materials Science and Engineering Conference 2016, Darmstadt/ Germany, 27.-29.9.16 (2016).
- 120) T. Gustmann, U. Kuehn, P. Gargarella, J. Eckert, S. Pauly, *Influence of laser remelting on density, microstructure and material properties of selective laser melted Cu-Al-Ni-Mn shape-memory parts*, Materials Science and Engineering Conference 2016, Darmstadt/ Germany, 27.-29.9.16 (2016).
- 121) O.G. Schmidt, *Microtubular MEMS for microfluidic applications*, 3rd Molecular Biology Summit, London/ United Kingdom, 20.-21.10.16 (2016).
- 122) V. Haehnel, X. Ma, C. Konczak, M. Uhlemann, H. Schloerb, *Electrodeposition of Fe-based magnetic alloys for thin films and template based nanostructures*, Analytical Chemistry Seminar, University of Arkansas, Fayetteville/ USA, 14.10.16 (2016).
- 123) B. Buechner, *The Iron Age of High Temperature Superconductivity*, Physik-Kolloquium, Universität Regensburg/ Germany, 17.10.16 (2016).
- 124) B. Buechner, *Anisotropic magnetism and spin gap in α - RuCl₃*, International Workshop From Electronic Correlations to Functionality, Kloster Irsee/ Germany, 12.-15.9.16 (2016).
- 125) A. Wolter-Giraud, *Linarite - a quasi-1D model system to study exotic phases and peculiar high-field magnetism due to frustration*, 627. WE-Heraeus Seminar on „Low dimensional quantum systems: models and materials“, Physikzentrum Bad Honnef/ Germany, 31.10.-4.11.16 (2016).
- 126) J. Fink, *Influence of Lifshitz transitions and correlation effects on the scattering rates and the effective mass of the charge carriers in ferropnictides*, Workshop „What about U?“, Trieste/ Italy, 17.-21.10.16 (2016).
- 127) C. Hess, *Introduction to Scanning Tunnelling Spectroscopy of Correlated Materials*, Autumn School on Correlated Electrons, Forschungszentrum Juelich/ Germany, 13.-14.9.16 (2016).
- 128) W. Loeser, *Phase diagrams in solidification processing and crystal growth*, International Forum upon Liquid Physics and Solidification Science, Xi'an/ China, 26.-28.9.16 (2016).
- 129) C. Hess, *Emergent Quantum States on the Nanoscale*, Seminar, Technische Universitaet Chemnitz/ Germany, 11.1.16 (2016).
- 130) C. Hess, *Emergent quantum states and excitations in low dimensions and at interfaces*, Seminar, Universitaet Bielefeld/ Germany, 13.9.16 (2016).
- 131) C. Hess, *Spin-Heat Transport in Low-Dimensional Quantum Magnets*, International Workshop „Spin Caloritronics 7“, Utrecht/ Netherlands, 11.-15.7.16 (2016).
- 132) J.E. Hamann-Borrero, *Site selective spectroscopy with monolayer resolution from resonant x-ray reflectivity*, The Hamburg conference on resonant elastic x-ray scattering (REXS 2016), Hamburg/ Germany, 13.-17.6.16 (2016).
- 133) J.E. Hamann-Borrero, *Resonant X-ray reflectivity as a tool to study emergent phenomena at interfaces of complex matter*, Energy Material Nanotechnology Meeting, Dubrovnik/ Croatia, 4.-7.5.16 (2016).
- 134) B. Buechner, *Anisotropic Magnetism and field induced spin gap in hexagonal α - RuCl₃*, 2016 Hefei Conference on Novel Phenomena in High Magnetic Fields, Hefei/ China, 29.10.-1.11.16 (2016).
- 135) S.A. Rounaghi, S. Scudino, H. Eshghi, A. Vyalikh, D.E.P. Vanpoucke, W. Gruner, S. Oswald, A.R. Kiani Rashid, M. Samadi Khoshkhoo, U. Scheler, J. Eckert, *Mechanochemical Synthesis of Nanostructured Aluminum Nitride*, Materials Science & Technology 2016 Conference, Salt Lake City/ USA, 23.-27.10.16 (2016).

- 136) O.G. Schmidt, *Nanomembrane devices: From concepts to applications*, Hamburg Photon Science Colloquium, Hamburg/ Germany, 4.11.16 (2016).
- 137) A. Waske, A. Funk, A. Rack, R. Schaefer, *In-situ imaging techniques for the study of magnetocaloric materials*, MMM Conference, New Orleans/ USA, 31.10.-4.11.16 (2016).
- 138) M. Calin, S. Bera, J. Eckert, *Ti-based Metallic Glasses and Glassy-Matrix Composites: Phase Formation and Thermal Stability*, 2016 Sustainable Industrial Processing Summit & Exhibition, Dubois International Symposium, Hainan/ China, 6-10.11.2016 (2016).
- 139) O.G. Schmidt, *Shapeable electronics: Nanomembrane materials for novel applications*, BFO Innovationsforum, Dresden/ Germany, 21.-22.11.16 (2016).
- 140) M. Medina Sanchez, *SPERMBOTS: Micromotors for assisting sperm cells with motion deficiencies*, 2nd Congress on Robotics and Neuroscience (CRONE 2016), Valparaiso/ Chile, 29.10.16 (2016).
- 141) M. Uhlemann, *Magneto-electrochemistry*, Institutskolloquium, University Arkansas/ USA, 18.10.16 (2016).
- 142) B. Rellinghaus, D. Pohl, S. Schneider, S. Wicht, F. Schmidt, A. Surrey, K. Nielsch, *Local correlation of structure and magnetic properties down to the atomic scale*, Chinese-German Symposium on Advanced Electron Microscopy and Spectroscopy, Tsinghua University, Beijing, P.R./ China, 30.10.-5.11.16 (2016).
- 143) B. Rellinghaus, D. Pohl, A. Surrey, F. Schmidt, S. Wicht, S. Schneider, K. Nielsch, *The relevance of transmission electron microscopy for the understanding of novel nanostructured materials*, 6th International Conference on Materials Science and Technologies - RoMat 2016, Polytechnical University of Bucharest, Bucharest/ Romania, 9.-12.11.16 (2016).
- 144) V. Kataev, *Magnetic field induced 'hidden' spin phase in the low-dimensional quantum magnet LiCuSbO₄*, 627. WE-Heraeus-Seminar on Low dimensional quantum systems: models and materials, Bad Honnef/ Germany, 31.10.-4.11.16 (2016).
- 145) V. Kataev, *Sub-THz EPR spectroscopy of correlated spin systems in high magnetic fields*, XIX International Youth Scientific School „Actual Problems of Magnetic Resonance and Its Application“, Kazan/ Russia, 24.-28.10.16 (2016).
- 146) J. Fink, *Non-Fermi-liquid behavior, Lifshitz transitions, and Hund's metal behavior iron-based superconductors from ARPES*, Kolloquiumsvortrag, IFP, KIT, Karlsruhe/ Germany, 30.10.16 (2016).
- 147) R. Schaefer, I. Soldatov, *Progress in Magneto-Optical Domain Imaging*, Kolloquiumsvortrag im Department of Physics, National Taiwan, Taipei/ Taiwan, 12.10.16 (2016).
- 148) O.G. Schmidt, *Multifunctional nanomembrane microtube devices*, MRS Fall Meeting, Boston/ USA, 27.11.-2.12.16 (2016).
- 149) L. Ma, *Novel phenomena in microtubular nanomembrane cavities*, MRS Fall Meeting, Boston/ USA, 27.11.-2.12.16 (2016).
- 150) D. Makarov, *Active and passive electronics for smart implants*, MRS Fall Meeting, Boston/ USA, 27.11.-2.12.16 (2016).
- 151) O.G. Schmidt, *Nanophotonics with nanomembrane materials and architectures*, International Conference on Nanophotonics and Micro/Nano Optics, Paris/ France, 7.-9.12.16 (2016).
- 152) K. Leistner, *Voltage-tunable magnetism in hybrid nanostructures by electrochemical interface control*, Materials Science Institute Seminar, University of Oregon, Eugene/ USA, 22.4.16 (2016).
- 153) Y. Krupskaya, *Charge transport in organic semiconductor single crystals and interfaces*, Invited talk at the group seminar of „Computational Nanoelectronics“, TU Dresden, Dresden/ Germany, 8.11.16 (2016).
- 154) Y. Krupskaya, *Systematic comparative investigations on organic single crystals*, Invited talk at the 18th International Conference on Crystal Growth and Epitaxy (ICCGE18), Nagoya/ Japan, 7.-12.8.16 (2016).
- 155) B. Buechner, *Anisotropic magnetism and spin gap in α -RuCl₃*, SFB 1143 Internationale Konferenz (Correlated Magnetism: From Frustration to Topology), Kloster Nimbschen/ Germany, 20.-23.9.16 (2016).
- 156) S. Pauly, K. Kosiba, S. Scudino, U. Kuehn, A.L. Greer, *Designing microstructures of metallic glass matrix composites by flash-annealing*, Workshop at Shandong University, Weihai/ China (2016).
- 157) S. Pauly, U. Kuehn, S. Scudino, T. Gustmann, C. Schricker, J. Sander, H. Schwab, J. Hufenbach, F. Silze, *SLM für Spezialwerkstoffe, Werkstoffsymposium*, Dresden/ Germany, 8.-9.12.16 (2016).
- 158) J. Dufouleur, *Weakly-coupled quasi-1D helical modes in disordered 3D topological insulator quantum*, New trend in Topological Insulators, Wuerzburg/ Germany, 24.-29.7.16 (2016).
- 159) J. Dufouleur, *Weakly-coupled quasi-1D helical modes in disordered 3D topological insulator quantum*, EMN Summer 2016, Prag/ Czech Republic, 21.-24.6.16 (2016).
- 160) J. Dufouleur, *Quantum confinement and disorder in 3D topological insulator nanostructures*, Seminar at Regensburg University, Regensburg/ Germany (2016).
- 161) S. Johnston, *Enhancing superconductivity in FeSe thin films using oxide substrates phonons*, Photon Science Seminar, Paul Scherrer Institut, Villingen/ Switzerland, (2016).

- 162) S. Johnston, *Enhancing superconductivity in FeSe thin films using oxide substrates phonons*, University of Freiburg, Freiburg/ Switzerland (2016).
- 163) S. Johnston, *Enhancing superconductivity in FeSe thin films using oxide substrates phonons*, University of Zuerich, Zuerich/ Switzerland (2016).
- 164) A. Winkler, *Microscale acoustofluidics - acoustically-driven Fluidics*, 1st Summer School of the Research Training Group „Hydrogel-based Microsystems“, Radebeul/ Germany, 22.9.16 (2016).
- 165) A. Thomas, *Tunnel junctions based memristors as artificial synapses*, DPG spring Meeting 2016, Regensburg/ Germany, 11.3.16 (2016).
- 166) A. Thomas, *ALD deposited HfO₂-Based Magnetic Tunnel Junctions*, Novel High-k Application Workshop, Dresden/ Germany, 14.3.16 (2016).
- 167) A. Thomas, *Tunnel Magneto-Seebeck Effect*, Workshop on Thermoelectric Materials, Daejeon Republic of Korea/ Korea, 27.5.16 (2016).
- 168) A., Nielsch, K. Thomas, *Chalcogenide-type nanostructures: Interplay between Thermoelectric and Topological Insulators Properties*, HZB Future Workshop on Energy Materials Research, Berlin/ Germany, 11.10.16 (2016).
- 169) A. Thomas, *Atomic layer deposition for thin film devices*, Colloquium Walther-Meißner-Institute, Garching/ Germany, 11.11.16 (2016).
- 170) A. Thomas, K. Nielsch, *Chalcogenide-type nanostructures: Interplay between Thermoelectric and Topological Insulators Properties*, HZB Thermoelectrics Colloquium, Thermoelectrics Colloquium-Helmholtz-Zentrum Berlin, Berlin/ Germany, 24.11.16 (2016).
- 171) L. Hozoi, *Huge anisotropic exchange and exotic magnetism in honeycomb and pyrochlore iridates*, 20th Symposium on Topological Quantum Information, Athens/ Greece, 27.5.16 (2016).
- 172) L. Hozoi, *Orbital reconstruction through interlayer cation charge imbalance: insights from wave-function-based quantum chemistry calculations*, APS 2016 March Meeting (Focus Session ‘Orbital & Electronic Transitions in Oxide Heterostructures’), Baltimore/ USA, 14.-18.3.16 (2016).
- 173) H.-J. Grafe, *NMR and NQR on iron pnictide superconductors*, 2nd summer school on iron pnictides of the SPP1458, Storkow (Mark)/ Germany, 4.-8.4.16 (2016).
- 174) H.-J. Grafe, *Impurity effects in $S = 1/2$ Heisenberg spin chains as probed by nuclear magnetic resonance*, Seminar talk, Ecole Supérieure de Physique et de Chimie Industrielles, ESPCI, 10 Rue Vauquelin, 75005 Paris/ France, 8.12.16 (2016).
- 175) R. Schaefer, I. Soldatov, *Recent progress in magneto-optical domain imaging*, 6th International Conference on Materials Science and Technologies - ROMAT 2016 University Polytechnica of Bucharest/ Romania, 11.11.16 (2016).
- 176) R. Schaefer, *Micromagnetism and Magnetic Microstructure*, Forseight Session Magnetism of the XXIst Century: Physics, Materials, Technologies, Ekaterinburg/ Russia, 9.-10.12.16 (2016).
- 177) F. Zhu, *Fully integrated organic/hybrid nanoscale devices*, Seminar, Qingdao Institute of Bioenergy and Bioprocess Technology, Chinese Academy of Sciences, Qingdao/ China, 21.12.16 (2016).
- 178) H. Schmidt, *Magneto-optical properties of metals, half-metals, and garnets probed by vector-magneto-optical generalized ellipsometry*, Symposium talk, AVS 63rd International Symposium & Exhibition 2016, Nashville/ USA, 6.-11.11.16 (2016).
- 179) H. Schmidt, *Magneto-optical properties of metals, half-metals, and garnets probed by vector-magneto-optical generalized ellipsometry (VMOGE)*, Seminar, Otto-von-Guericke Universität Magdeburg/ Germany, 9.5.16 (2016).
- 180) H. Schmidt, *Advancing in-memory arithmetic based on CMOS-integrable memristive crossbar structures*, 10th International Conference on Circuits, Systems, Signal and Telecommunications (CSST ‘16), Barcelona/ Spain, 13.-15.2.16 (2016).
- 181) H. Schmidt, *Implementing associative, supervised, unsupervised, and deep learning in analog resistive switches for future information processing and data mining*, 15th International Conference on Artificial Intelligence, Knowledge Engineering and Data Bases (AIKED ‘16), Venice/ Italy, 29.-31.1.16 (2016).
- 182) H. Schmidt, *Magneto-optical properties of metals, half-metals, and garnets*, Institutsseminar, Friedrich-Schiller Universität Jena/ Germany, 8.1.16 (2016).
- 183) G. Schierning, *Nanocrystalline silicon with tungsten silicide inclusion phases: Morphology and thermoelectric properties*, E-MRS, SYMPOSIUM W, Materials and systems for micro-energy harvesting and storage, Lille/ France, 4.5.16 (2016).
- 184) G. Schierning, *Nanocrystalline silicon for thermoelectricity*, Thermoelectrics colloquium, HZB, Berlin/ Germany, 24.11.16 (2016).

Patents 2016

Issues of patents (issue decision date)

DE 10 2015 214 177 (11508 DE)	Drehbarer Batterieträger (01.02.2016) <i>Inventors:</i> Markus Herklotz, Jonas Weiß, Eike Ahrens, Lars Giebeler
DE 10 2011 007 898.3 (11102 DE)	Verfahren zur Herstellung von Halbzeugen auf Basis von intermetallischen Verbindungen (07.04.2016) <i>Inventors:</i> Jens Freudenberger, Tom Marr
DE 11 2011 101 243.8 (11002 DE)	Verfahren und Anordnung zur Manipulation von in einem magnetischen Medium gespeicherten Domäneninformationen (22.04.2016) <i>Inventor:</i> Rudolf Schäfer
CN 201180049051.8 (11013 CN)	Herstellungsverfahren für Seltenerd-magneten (04.05.2016) <i>Inventors:</i> Noritsungu Sakuma, Hidefumi Kishimoto, Akira Kato, Tetsuya Shoji, Dominique Givord, Nora Dempsey, Thomas George Woodcock, Oliver Gutfleisch, Gino Hrkac, Thomas Schrefl
JP 2013-516808 (11013 JP)	Herstellungsverfahren für Seltenerd-magneten (13.05.2016) <i>Inventors:</i> Noritsungu Sakuma, Hidefumi Kishimoto, Akira Kato, Tetsuya Shoji, Dominique Givord, Nora Dempsey, Thomas George Woodcock, Oliver Gutfleisch, Gino Hrkac, Thomas Schrefl
US 14/004,556 (11103 US)	Magnetoelektronisches Bauelement und Verfahren zu seiner Herstellung (26.05.2016) <i>Inventors:</i> Denys Makarov, Oliver G. Schmidt
EP 09797002.4 (10832 DE)	Beschichtetes magnetisches Legierungsmaterial und Verfahren zu seiner Herstellung (24.08.2016) <i>Inventors:</i> Julia Lyubina, Oliver Gutfleisch, Miheala Buschbeck
EP 09797002.4 (10832 FR)	Beschichtetes magnetisches Legierungsmaterial und Verfahren zu seiner Herstellung (24.08.2016) <i>Inventors:</i> Julia Lyubina, Oliver Gutfleisch, Miheala Buschbeck
EP 09797002.4 (10832 GB)	Beschichtetes magnetisches Legierungsmaterial und Verfahren zu seiner Herstellung (24.08.2016) <i>Inventors:</i> Julia Lyubina, Oliver Gutfleisch, Miheala Buschbeck
EP 09797002.4 (10832 AT)	Beschichtetes magnetisches Legierungsmaterial und Verfahren zu seiner Herstellung (24.08.2016) <i>Inventors:</i> Julia Lyubina, Oliver Gutfleisch, Miheala Buschbeck
EP 09797002.4 (10832 CH/LI)	Beschichtetes magnetisches Legierungsmaterial und Verfahren zu seiner Herstellung (24.08.2016) <i>Inventors:</i> Julia Lyubina, Oliver Gutfleisch, Miheala Buschbeck
EP 09797002.4 (10832 EP)	Beschichtetes magnetisches Legierungsmaterial und Verfahren zu seiner Herstellung (24.08.2016) <i>Inventors:</i> Julia Lyubina, Oliver Gutfleisch, Miheala Buschbeck
EP 1381531 (10217 EP)	Magnetanordnung für die Aufhängung und Führung schwebender Fahrzeuge und Transporteinrichtungen (07.10.2016) <i>Inventors:</i> Martina Falter, Peter Bartusch, Ludwig Schultz
DE 10 2016 216 283.7 (11602 DE)	Probenkarussell (27.10.2016) <i>Inventors:</i> Ulrich Stoeck, Jonas Weiß, Eike Ahrens, Lars Giebeler
DE 10 2013 210 383.2 (11314 DE)	Akustisches Oberflächenwellenbauelement mit vorwiegend in Ausbreitungsrichtung polarisierten Oberflächenwellen (07.11.2016) <i>Inventors:</i> Manfred Weihnacht, Hagen Schmidt, Alexander Darinskii
DE 10 2015 200 643.3 (11410 DE)	Verfahren zur Herstellung von neuronale Zellen enthaltenden strangförmigen Kapseln und strangförmige Kapseln (10.11.2016) <i>Inventors:</i> Andreas Winkler, Anne K. Meyer

EP 11788419.7 (11018 EP)	Oberflächenstrukturierte metallische Gläser und Verfahren zur Herstellung (07.12.2016) <i>Inventors:</i> Bujar Jerliu, Simon Pauly, Kumar Babu Sureddi, Sergio Scudino, Jürgen Eckert
13/824,572 (11013 US)	Herstellungsverfahren für Seltenerdsmagneten (13.12.2016) <i>Inventors:</i> Noritsungu Sakuma, Hidefumi Kishimoto, Akira Kato, Tetsuya Shoji, Dominique Givord, Nora Dempsey, Thomas George Woodcock, Oliver Gutfleisch, Gino Hrkac, Thomas Schrefl

Priority patent applications (priority date)

11529 DE	Asymmetric optical resonator and optical device comprising the asymmetric optical resonator (02.02.2016) <i>Inventors:</i> Libo Ma, Oliver G. Schmidt
11530 PCT	Kondensator und Verfahren zur Herstellung dieses Kondensators (04.02.2016) <i>Inventors:</i> Oliver G. Schmidt, Eric Pankenin, Shoichiro Suzuki
11601 DE	Akustoelektrischer Oszillator (24.03.2016) <i>Inventor:</i> Günter Martin
11512 DE	Bauelemente auf flexiblen Substraten und Verfahren zu ihrer Herstellung (01.06.2016) <i>Inventors:</i> Jens Ingolf Mönch, Denys Makarov, Oliver G. Schmidt
11618 DE	Vorrichtung für die Mikrofluidik (25.07.2016) <i>Inventors:</i> Andreas Winkler, Stefan Harazim
11619 DE	Akustisches Oberflächenwellenbauelement mit Drehung der Schwingungsebene (22.08.2016) <i>Inventors:</i> Hagen Schmidt, Manfred Weihnacht, Alexander Darinskii, Robert Weser
11602 DE	Probenkarussell (30.08.2016) <i>Inventors:</i> Ulrich Stoeck, Jonas Weiß, Eike Ahrens, Lars Giebler
11609 DE	Elektrolytssystem zur Herstellung Thermoelektrischer Schichten und Strukturen (13.09.2016) <i>Inventors:</i> Nicolás Pérez Rodríguez, Heike Schlörb, Melanie Mohn, Tom Sieger
11621 DE	Akustoelektrischer Oszillator basierend auf an Oberflächen geführten akustischen Wellen (06.10.2016) <i>Inventor:</i> Günter Martin
11612 DE	Verfahren zur Herstellung mindestens eines dreidimensionalen Bauelementes zur uni-, bi-, tri- oder multidirektionalen Messung und/oder Generierung von Vektorfelder (13.10.2016) <i>Inventors:</i> Daniil Karnaushenko, Dmitriy Karnaushenko, Oliver G. Schmidt
11624 DE	Thermomagnetischer Generator (18.11.2016) <i>Inventors:</i> Kai Sellschopp, Sebastian Fähler, Anja Waske
11622 DE	Dreidimensionaler Tomograf (22.11.2016) <i>Inventors:</i> Oliver G. Schmidt, Mariana Medina Sanchez, Sonja Maria Weiz

Trademarks

31656 DE	SAW Symposium SENSORS & ACTUATORS (06.12.2016) <i>Inventors:</i> Hagen Schmidt, Siegfried Menzel
----------	---

Graduation of young researchers 2016

PhD Theses

Azar Aliabadi	ESR and Magnetization Studies of Transition Metal Molecular Compounds, TU Dresden
Matthias Bönisch	Structural properties, deformation behavior and thermal stability of martensitic Ti-Nb alloys, TU Dresden
Nan Du	Novel applications of BiFeO ₃ (BFO)-based nonvolatile resistive switches, TU Chemnitz
Christian David Salazar Enriques	Scanning tunneling microscopy on low dimensional systems: dinickel molecular complexes and iron nanostructures, TU Dresden
Alexander Fedorov	Electronic structure of doped 2D materials, TU Dresden
Markus Gellesch	Statistical study of the effect of annealing treatments on assemblies of intermetallic magnetic nanoparticles related to the Heusler compound Co ₂ FeGa, TU Dresden
Nadine Heming	Untersuchung der Volumen- und Oberflächeneigenschaften von Hexaboriden, TU Dresden
Tony Jaumann	Zur Degradation und Optimierung von nanostrukturierten Siliciumanoden in Lithium-Ionen- und Lithium-Schwefel-Batterien, TU Dresden
Fatemeh Asgharazadeh Javid	Phase formation, martensitic transformation and mechanical Properties of Cu-Zr-based alloys, TU Dresden
Daniil Karnaushenko	Shapeable microelectronics, TU Chemnitz
Frederik Klein	Graphitisierung von tetraedischem amorphem Kohlenstoff mittels Elektronen im Rastertunnel und Rasterelektronenmikroskop, TU Dresden
Britta Koch	Scaffold dimensionality and confinement determine single cell morphology and migration, TU Dresden
Julia Körner	Gekoppelte Oszillatoren als neuartige Sensoren für Cantilever-Magnetometrien, TU Dresden
Tobias Kosub	Ferromagnet-free magnetoelectric thin film elements, TU Chemnitz
Gungun Lin	Multifunctional droplet-based micro-magnetofluidic devices, TU Chemnitz
Veronika Magdanz	Rolled up microtubes for the capture, guidance and release of single spermatozoa, TU Dresden
Ignacio G. Gonzalez Martinez	Novel thermal and electron-beam approaches for the fabrication of boron-rich nanowires, TU Dresden
Christian Nowka	Untersuchungen zu Gasphasentransporten in quasibinären Systemen von Bi ₂ Se ₃ mit Bi ₂ Te ₃ , Sb ₂ Se ₃ , MnSe und FeSe zur Erzeugung von Nanokristallen, TU Dresden
Christopher Reiche	Novel sensors for scanning force microscopy based on carbon nanotube mechanical resonators, TU Dresden
Ludwig Reichel	Gedehnte epitaktische Fe-Co-X Schichten (X = B, C, N) mit erhöhter magnetischer Anisotropie, TU Dresden
Ahmad Omar	Disentangling the Intrinsic Attributes and the Physical Properties in Cobalt-based Quaternary Heusler Compounds, TU Dresden
Steven Rodan	Nuclear magnetic resonance and specific heat studies of half-metallic ferromagnetic Heusler compounds, TU Dresden
Wolf Schottenhamel	Aufbau eines hochauflösenden Dilatometers und einer hydrostatischen SQUID-Druckzelle sowie Untersuchungen an korrelierten Übergangsmetalloxiden, TU Dresden
Ivan Soldatov	Thermoelectric effects and anisotropy in magnetic films, TU Dresden
Alexander Surrey	Preparation and Characterization of Nanoscopic Solid State Hydrogen Storage Materials, TU Dresden
Louis Veyrat	Quantum Transport Study of Spin-Helical Dirac Fermions in 3D Topological Insulator Nanostructures, TU Dresden
Uwe Vogel	Grenzflächenbildung zwischen LiNbO ₃ (LiTaO ₃) und Barriereschichten für den Einsatz bei Metallisierungssystemen für SAW-Strukturen, TU Dresden
Sebastian Wicht	Atomar aufgelöste Strukturuntersuchungen für das Verständnis der magnetischen Eigenschaften von FePt-HAMR-Prototypmedien, TU Dresden
Stephan Zimmermann	Elektronenspinresonanz an niederdimensionalen und frustrierten magnetischen Systemen, TU Dresden

Diploma and Master Theses

Sascha Balakin	Thermische Stabilität und thermoplastisches Verformungsverhalten von Ni-freien Ti-basierten und Zr-basierten massiven metallischen Gläsern für biomedizinische Anwendungen, TU Dresden
Nooshin Bandari	Fabrication of SU-8 shadow mask for multi-layers of metal/oxide deposition, TU Chemnitz
Paul Bergelt	Abscheidung und Charakterisierung metallischer Dünnschichten durch Kondensation mikroakustisch erzeugter Aerosole, TU Dresden
Hagen Bryja	Herstellung und Charakterisierung verspannter epitaktischer BaTiO ₃ Schichten für elektrokalendarische Untersuchungen, TU Dresden
Kenny Duschek	Untersuchung magneto-ionischer Effekte an elektrodeponierten Fe-Schichten in basischen Elektrolyten, HTW Dresden
Stefan Engelhardt	Strukturelle und ferroelektrische Eigenschaften von epitaktischen BaZr _x Ti _{1-x} O ₃ -Schichten, TU Dresden
Clemens Gütter	Magnetkraftmikroskopie: Methodenweiterentwicklung und Messungen an gerollten Nanomembranen, TU Dresden
Florian Heinsch	Studium der Hochtemperatur-Ladungsdichtewellen in reinem und interkaliertem Tantaldisulfid mittels Röntgendiffraktion, TU Dresden
Zongqi Hou	NMR – Untersuchungen von Al und Si dotiertem LiMgPO ₄ , TU Dresden
Fabia Kochta	Mikrostrukturelle und elektrochemische Analyse von biodegradierbaren FeMnC(B,S)-Legierungen für medizinische Anwendungen, HTW Dresden
Martin Leinert	Einfluss von Heterogenitäten auf das Verformungsverhalten von Cu _{47,5} Zr _{47,5} Al ₅ basierten metallischen Gläsern, TU Dresden
Xiao Ma	Elektrochemische Präparation und Charakterisierung von CoFe-Mikromagneten für Mikrofluidikanwendungen, TU Dresden
Karthikeyan Manga	Thermal Conductivity Characterization of Organic Thin Films by Three-Omega Technique, TU Chemnitz
Jörg Pribbenow	Evaluierung der Möglichkeit zur Ummantelung von Nanopartikeln aus der Gasphase im Flug, TU Dresden
Wenjing Ren	Mikrostrukturelle Untersuchung von nanostrukturierten W/Mo mehrschichtigen Dünnschichten, TU Dresden
Juliane Ruda	Synthese 1,4-Dicyanobenzen basierter poröser leitfähiger Polymere und deren Anwendung als Matrixmaterial in Lithium-Schwefel Akkumulatoren, TU Dresden
Sebastian Schimmel	Konstruktion und Inbetriebnahme eines Molekularverdampfers für Tunnelmikroskopiemessungen endohedraler Fullerene im Ultrahochvakuum, TU Dresden
Tobias Schorr	NMR-Messungen am Eisenpniktid BaFe ₂ As ₂ unter uniaxialem Druck, TU Dresden
Christian Schricker	Fertigung eines massiven Zr-Basis-Glases mittels selektivem Laserschmelzens, TU Dresden
Stefan Schwabe	In-situ Charakterisierung des strukturellen Phasenübergangs variabel dehnbarer, epitaktischer Ni-Mn-Ga-Co-Schichten, TU Dresden
Richard Ulm	Elektrolytische Wasserstoffherzeugung in überlagerten Magnetfeldern, HTW Dresden
Yu Wan	Elektronenenergieverlustspektroskopie an WSe ₂ , TU Dresden
Bruno Weise	Herstellung und Charakterisierung der Magnetokalorischen Legierung NiCoMnAl, TU Dresden
Jonas Zehner	Kerr mikroskopische Untersuchungen der magnetischen Mikrostruktur epitaktischer Fe- und FePt-Dünnschichten sowie Fe(Pt)/Polymer-Elektrolyt-Heterostrukturen für magneto-ionische Effekte, TU Dresden
Julian Zeisner	ESR-Spektroskopie an magnetisch frustrierten und quasieindimensionalen Übergangsmetallverbindungen, TU Dresden

Calls and Awards 2016

Professorships

Qingming Deng	Assistant Professorship, Huaiyin Normal Univ., China
Fei Ding	Full Professorship, Univ. Hannover
Laura Corredor-Bohórquez	Full Professorship, Univ. Federal do Rio Grande do Norte, Brazil
Bernd Rellinghaus	Guest Professorship, Bergakademie TU Freiberg

Awards

Gungun Lin	Chinese Government Award for Outstanding Chinese Student Abroad
Qingming Deng	Chinese Government Award for Outstanding Chinese Student Abroad
Vladimir Fomin	Admission as a member in the Mediterranean Institute of Fundamental Physics
Alexey N. Bogdanov	EPS CMD Europhysics Prize 2016, together with P. Böni, C. Pfleiderer, A. Rosch und A. Vishwanath
Max Sieger	IEEE Council on Superconductivity Graduate Study Fellowship in Applied Superconductivity

Best poster/best contribution awards

F. Karnbach	Hydromag Best Poster Prize at the 10th PAMIR International Conference on Fundamental and Applied MHD, 20-24 June 2016 in Cagliari
M. Medina-Sanchez, M. Guix, S. Harazim, L. Schwarz, O. G. Schmidt:	Best Conference Paper Award of the International Conference on Manipulation, Automation and Robotics at Small Scales (MARSS), 18-22 July 2016 in Paris
M. Medina-Sanchez, B. Ibarlucea, N. Perez, D. D. Karnaushenko, S. M. Weiz, L. Baraban, G. Cuniberti, O. G. Schmidt:	Best Paper Award of the 9 th International Workshop on Impedance Spectroscopy, 26-28. Sept. 2016 in Chemnitz
M. Calin, A. Gebert, A.C. Ghinea, P. F. Gostin, S. Abdi, C. Mickel, J. Eckert:	2016 MSC Impact Editor's Choice Award of Materials Science Engineering C

IFW Awards

Ulrich Rößler & Alexey Bogdanov	IFW Research Prize 2016
Daniil Karnaushenko	IFW Junior Research Award 2016
Libo Ma	IIN Research Prize 2016
Ivan Kaban	IKM Research Prize 2016
Carmine Ortix	ITF Research Prize 2016
Daniil Karnaushenko	Tschirnhaus-Medal of the IFW for excellent PhD theses
Julia Körner	Tschirnhaus-Medal of the IFW for excellent PhD theses
Tobias Kosub	Tschirnhaus-Medal of the IFW for excellent PhD theses
Gungun Lin	Tschirnhaus-Medal of the IFW for excellent PhD theses
Veronika Magdanz	Tschirnhaus-Medal of the IFW for excellent PhD theses
Christopher Reiche	Tschirnhaus-Medal of the IFW for excellent PhD theses
Ludwig Reichel	Tschirnhaus-Medal of the IFW for excellent PhD theses
Alexander Surrey	Tschirnhaus-Medal of the IFW for excellent PhD theses
Sebastian Wicht	Tschirnhaus-Medal of the IFW for excellent PhD theses

Scientific conferences 2016

March 6 – 10	2nd SELECTA Workshop (Smart ELECTrodeposited Alloys for environmentally sustainable applications) Training on research methodologies, characterization techniques and reporting scientific results
April 3 – 6	612. WE-Heraeus Seminar „Electron and phonons: Interfaces and interactions“, Physikzentrum Bad Honnef
April 4 – 6	2nd Workshop „Floating Zone Technique“, IFW Dresden
April 4 – 8	2nd Summer School of SPP 1458 on Iron Pnictides in Storkow near Berlin
May 3 – 4	Seminar zum IFW-Forschungsthema 2.4 „Nanoscale Magnets“, Evangelische Akademie Meißen
June 20 – 22	final seminar of the DFG Priority Program 1386, Jüfa Jülich
June 30 – July 1	Workshop on Resonant Inelastic and Elastic X-Ray Scattering 2016, IFW Dresden
Aug. 30	Workshop „Thermoelectric materials“, IFW Dresden
Oct. 20 – 21	SAW Sensor and Actuator Symposium 2016 (SAW Symposium 2016) Dresden
Oct 31 – Nov 4	627th WE-Heraeus Seminar „Low dimensional quantum systems: models and materials“ in Bad Honnef, Germany
Nov. 25	Nanomagnetism Workshop, IFW Dresden
27 Nov – 2 Dec	Symposium “Nanomembrane Materials” at MRS Fall Meeting, Boston, USA, Chairs: Y.F. Mei, J.-H. Ahn, J. Rogers, O.G. Schmidt

Guests and Scholarships 2016

Guest scientists (stay of 4 weeks and more)

Name	Home Institute	Home country
Dr. Aswartham, Saicharan	University of Kentucky, USA	India
Dr. Bachmatiuk, Alicja	Wroclaw Research Centre ILT	Poland
Dr. Bashlakov, Dmytro	B.Verkin Institute Kharkiv	Ukraine
Dr. Burkov, Aleksandr	A.F. Ioffe Institut, St.Petersburg	Russia
Dr. Cagliaris, Federico	Univ.Genua	Italy
Cherniavskii, Ivan O.	Lomonosov Moscow State Univ.	Russia
Denisova, Kseniia	Lomonosov Moscow State Univ.	Russia
Egunov, Aleksandr	Institute of Materials Science of Mulhouse	France
Dr. Fernandez S. Pablo Roberto	TU Dresden	Costa Rica
Prof. Fu Lei	Wuhan Univ.	China
Gamaiunova, Nina	B.Verkin Institute Kharkiv	Ukraine
Dr. Hong Xiaochen	Fudan Univ.	China
Dr. Hu Han	Nanyang Technological Univ. Singapore	China
Dr. Huang, Shao-Zhuan	Wuhan Univ. of Technology	China
Dr. Johnston, Steven Sinclair	Univ. of Tennessee, Knoxville	Canada
Dr. Jung, Hyoyun	Yonsei Univ.	Korea
Kamashev, Andrey	Zavoisky Phys.-Techn. Institute Kazan	Russia
Dr. Kandpal, Hemchandra	Indian Institute of Technology Roorkee	India
Kondo, Massaya	Osaka Univ.	Japan
Dr. Kvitnytska, Oksana	B.Verkin Institute Kharkiv	Ukraine
Dr. Lee, Jae-Ki	Korea Electrotechnology Research Institute	Korea
Li Yuan	Institute of Semiconductors Beijing	China
Dr. Liu, Fupin	Univ. of Science and Technology Hefei	China
Dr. Machata, Peter	Slovak Univ. of Technology Bratislava	Slovakia
Dr. Makhazra, Sami A M	Palestinian Territories	
Dr. Mikhailova, Daria	MPI CPFS Dresden	Russia
Dr. Morozov, Igor	Lomonosov Moscow State Univ.	Russia
Dr. Morrow, Ryan Christopher	Ohio State Univ.	USA
Prof. Dr. Naidiuk, Iurii	B.Verkin Institute Kharkiv	Ukraine
Dr. Neild, Adrian	Monash Univ. Australia	UK
Dr. Novikov, Sergei	A.F. Ioffe Institut, Sankt Petersburg	Russia
Dr. Parzych, Grzegorz	TU Dresden	Poland
Dr. Prando, Giacomo	TU Dresden	Italy
Dr. Ray, Rajyavardhan	TU Dresden	India
Dr. Rienks, Emile	TU Dresden	Netherlands
Dr. Roslova, Mariia	TU Dresden	Russia
Dr. Seiro, Silvia	Univ.Salzburg	Italy
Dr. Valldor, Björn Martin	MPI CPFS Dresden	Sweden
Dr. Valligatla, Sreeramulu		India
Dr. Velez, Patricio	Consejo Nacional Argentina	Argentina
Wang, Jiawei	Hong Kong Univ.	China
Dr. Yakhvarov, Dmitry	Institute of Organic & Phys. Chem. Kazan	Russia
Yakymovych, Andriy		Ukraine

Scholarships

Name	Home country	Donor
Dr. Dassonneville, Bastien	France	Alexander von Humboldt Foundation
Dr. Ghimire, Madhav Prasad	Nepal	Alexander von Humboldt Foundation
Dr. Kim Beom, Seok	Korea	Alexander von Humboldt Foundation
Dr. Kravchuk, Volodymyr	Ukraine	Alexander von Humboldt Foundation
Dr. Morrow, Ryan Christopher	USA	Alexander von Humboldt Foundation
Prof. Dr. Pickett, Warren	USA	Alexander von Humboldt Foundation
Dr. Shrestha, Nabeen Kumar	Nepal	Alexander von Humboldt Foundation
Prof. Dr. Singh, Avinash	USA	Alexander von Humboldt Foundation
Dr. Zhang, Yang	China	Alexander von Humboldt Foundation
Prof. Dr. Zotos, Xenophon	Greece	Alexander von Humboldt Foundation
Dr. Du, Yun	China	China Scholarship Council
Dr. Wang, Jing	China	China Scholarship Council
Deng, Liang	China	China Scholarship Council
Liu, Lixiang	China	China Scholarship Council
Lu, Xueyi	China	China Scholarship Council
Sui, Yan Fei	China	China Scholarship Council
Sun, Xiaolei	China	China Scholarship Council
Wang, Ju	China	China Scholarship Council
Wang, Pei	China	China Scholarship Council
Xi, Lixia	China	China Scholarship Council
Xu, Haifeng	China	China Scholarship Council
Yin, Yin	China	China Scholarship Council
Zhang, Long	China	China Scholarship Council
Prof. Czeppe, Tomasz Henryk	Poland	DAAD
Dr. Fedorov, Fedor	Russia	DAAD
Prof. Lishchynskyy, Igor	Ukraine	DAAD
Saha, Snehajyoti	India	DAAD
Ghunaim, Rasha	Palästinian territories	DAAD
Shahid, Rub Nawaz	Pakistan	DAAD
Dr. Ahmad, Mushtaq	Pakistan	DAAD Leibniz-Programm
Dr. Moravkova, Zuzana	Czech Rep.	DAAD Leibniz-Programm
Linnemann, Julia	Germany	Deutsche Bundesstiftung Umwelt
Dr. Vavilova, Evgeniia	Russia	TU Chemnitz
Dr. Gorshenkov, Mikhail Vladimirovich	Russia	TU Dresden; EU MULTIC-Programm
Madian, Mahmoud	Egypt	Graduate Academy TU Dresden
Surrey, Alexander	Germany	Graduate Academy TU Dresden
Perea, Cabarcas Darling	Columbia	COLCIENCIAS Columbia
Dr. Zilic, Dijana	Croatia	Croatian Science Foundation (CSF)
Dr. Wuppulluri, Madhuri	India	Eleonore Trefftz Guest Professorship
Vieira, Rafael	Portugal	EU - ERASMUS MUNDUS
Dr. Tynell, Tommi Paavo	Finnlandia	Finnish Cultural Foundation
Salimian, Maryam	Iran, Islam. Rep.	FCT Portugal
Dr. Alshwawreh, Nidal K. Hamed	Canada	German Jordanian University
Miyajima, Tomohiro	Japan	Graduate School of Engineering Kyushu Univ.
Li, Haichao	China	Harbin Institute of Technology
Bönisch, Matthias	Austria	International Graduate School
Chirkova, Alisa	Russia	International Graduate School

Name	Home country	Donor
Liu, Bo	China	International Graduate School
Salman, Omar Oday	Iraq	Iraq Gov.
Sasaki, Sho	Japan	Japan Student Services Organisation (JASSO)
Wang, Vivian	USA	Krupp-Praktikantenprogramm für Stanford-Studenten
Foroughi Alireza	Iran, Islam. Rep.	Iran Gov.
Lara Ramos, David Alberto	Mexico	Mexico Gov.
Dr. Gan, Li-Hua	China	Natural Science Foundation of China
Günes, Taylan	Turkey	Research Council of Turkey
Karatas, Özgül	Turkey	Research Council of Turkey
Dr. Wang, Shenghai	China	Shandong University

Guest stays of IFW members at other institutes 2016

Jeroen van den Brink	25.01.2016 – 04.03.2016 / 14.03.2016 – 22.04.2016, Research stay at Harvard University, Cambridge (MA), USA, Common project in the area of theoretical photon science, which focusses on the modelling of resonant inelastic x-ray scattering responses
Bastien Dassonneville	06.02.2016 – 21.02.2016, Laboratoire de Physique des Solides, Orsay, Paris, France
Romain Giraud	01.11.2016 – 18.11.2016, Spintec, Grenoble, France
Veronika Hähnel	07.10.2016 – 22.10.2016, Research stay at University of Arkansas (Department of Chemistry & Biochemistry), Fayetteville, USA
Junhee Han	07.06.2016 – 01.07.2016, Research stay at Institute of Industrial Technology, Incheon, Korea
Florian Kiebert	24.11.2016 – 24.12.2016, Monash University Melbourne, Australia
Karin Leistner	17.01.2016 – 17.07.2016, Research stay at SFU Vancouver, Canada
Ignacio G. Gonzales Martinez	31.03.2016 – 19.04.2016, Research stay at Oxford University, Oxford, England
Robert Niemann	14.02. – 21.02.2016, Research stay at ASCR Prague, Czech Rep. 03.04. – 24.04.2016, Measurements at Univ. de Barcelona, Spain 18.07. – 07.08.2016, Research stay at Texas A&M University, College Station, TX, USA
Rafael Gregorio Mendes	28.06.2016 – 15.07.2016, Research stay at Suzhou Univ., China
Jinbo Pang	05.01.2016 – 03.02.2016, Research stay at CMPW PAN (Polish Academy of Sciences), Zabrze, Poland
Parthiban Ramasamy,	02.02.2016 – 24.02.2016, Synchrotron measurement at Institute of Technology (INPG), Grenoble, France
Christin Schlesier	27.04.2016 – 30.05.2016, Paul-Scherrer-Institut, Villigen & Physik-Institut, Uni Zürich, Schweiz
Sebastian Schneider	25.04. – 23.05.2016, Research stay and measurements at Pacific Northwest National Laboratory, Richland, WA, USA 24.07.–08.08.2016, Microscopy & Microanalysis Meeting, Columbus, OH, USA
Ivan Soldatov	14.02. – 20.02.2016, Research stay at Far Eastern Federal University, Wladiwostok, Russia 18.03. – 26.04.2016, Research stay and measurements at University of California, San Diego, USA
Mihai Stoica	17.01.2016 – 31.01.2016, Research stay at ETH, Zürich, Switzerland
Andreas Winkler	12.05.2016 – 28.05.2016, Research stay at Monash University, Melbourne, Australia and invited visit at University of Technology and Design in Singapore
Ulrike Wolff	30.09. – 31.12.2016, Research stay and measurements at Jozef Stefan Institut Ljubljana, Slovenia

Board of trustees

Jörg Geiger, Saxonian Ministry of Science and Art - Head -

Dr. Herbert Zeisel, Federal Ministry of Education and Research (up to 31.12.2016)

Dr. Peter Schroth, Federal Ministry of Education and Research (from 01.01.2017 on)

Prof. Dr. Gerhard Rödel, TU Dresden

Prof. Dr. Sibylle Günter, MPI for Plasma Physics

Scientific Advisory Board

Prof. Dr. Maria-Roser Valenti, Univ. Frankfurt, Germany - Head -

Prof. Dr. Robert H. Blick, Univ. Hamburg (from 01.10.2016 on)

Prof. Dr. Sang-Wook Cheong, Rutgers (from 01.10.2016 on)

Prof. Dr. Silke Christiansen, HZB Berlin, Germany

Prof. Dr. Andrey Chubukov, Univ. of Minnesota, USA

Prof. Dr. Ralph Claessen, Univ. Würzburg (from 01.10.2016 on)

Prof. Dr. Philippe M. Fauchet, Vanderbilt Univ., USA (up to 30.09.2016)

Prof. Dr. Matthias Göken, Univ. Erlangen-Nürnberg, Germany

Prof. Dr. Alan Lindsay Greer, Univ. of Cambridge, U.K. (up to 30.09.2016)

Prof. Dr. Rolf Hellinger, Siemens AG Erlangen, Germany (up to 30.09.2016)

Prof. Dr. Xavier Obradors Berenguer, Univ. Autònoma de Barcelona, Spain (up to 30.09.2016)

Prof. Dr. Nini Pryds, TU Denmark (from 01.10.2016 on)

Prof. Dr. Roberta Sessoli, Univ. di Firenze, Italy

Prof. Dr. Eberhardt Umbach, Karlsruhe Institute of Technology, Germany (up to 30.09.2016)

Publisher:

Leibniz Institute for Solid State and Materials Research Dresden

Executive Board Prof. Dr. Burkard Hillebrands, Scientific Director
Dr. Doreen Kirmse, Administrative Director

Address Helmholtzstrasse 20
D-01069 Dresden

Phone +49 (0)351 4659 0

Fax +49 (0)351 4659 540

Internet <http://www.ifw-dresden.de>

e-mail info@ifw-dresden.de

Research organization of IFW Dresden

Institute for Solid State Research (IFF)	Institute for Metallic Materials (IMW)	Institute for Complex Materials (IKM)	Institute for Integrative Nanosciences (IIN)	Institute for Theoretical Solid State Physics (ITF)
Prof. Dr. Bernd Büchner – 808	Prof. Dr. Kornelius Nielsch – 104	Dr. Thomas Gemming – 298 (temp.)	Prof. Dr. Prof. h. c. Oliver G. Schmidt – 800	Prof. Dr. Jeroen van den Brink – 400
Secr.: Kerstin Höllner – 300 Katja Schmiedel – 805	Secr.: Svea Fleischer – 102 Linda Petersohn – 324	Secr.: Brit Präßler-Wüstling – 217 Janett Schuster – 198	Secr.: Kristina Krummer – 810	Secr.: Grit Rötzer – 380
Surface dynamics	Chemical synthesis of materials	Solidification processes and complex structures	Rolled-up photonics	Quantum Chemistry
Dr. Hagen Schmidt – 278	Dr. Heike Schlörb – 230	Dr. Ivan Kaban – 644	Dr. Libo Ma – 1153	Dr. Liviu Hozoi – 1829
Transport and scanning probe microscopy	Functional oxide layers and superconductors	Magnetic composites and applications	Integrated nanophotonics	Quantum theory of complex nanoarchitectures
Dr. Christian Heß – 533	Dr. Ruben Hühne – 716	Dr. Anja Waske – 846	Dr. Fei Ding – 752	Dr. Carmine Ortix – 352
Chemistry of nanomaterials	Magnetic materials	Micro- and nanostructures	Micro- and nanobiomedical engineering	Numerical solid state physics
Dr. Alexey Popov – 871	Dr. Thomas G. Woodcock – 221	Dr. Thomas Gemming – 298	Dr. Mariana Medina Sanchez – 489	Dr. Manuel Richter – 360
Magnetic properties	Functional magnetic films	Chemistry of functional materials		
Dr. Vladislav Kataev – 328	Dr. Sebastian Fähler – 328	Dr. Annett Gebert – 275		
Electronic and optical properties	Quantum materials and devices	Electrochemical energy storage		
Prof. Dr. Martin Knupfer – 544	PD Dr. Andy Thomas – 746	Dr. Lars Giebeler – 652		
Synchrotron methods	Thermoelectric materials and devices	Alloy design and processing		
Dr. Sergey Borisenko – 566	Dr. Gabi Schierner – 1875	Dr. Uta Kühn – 402		
Crystal growth and synthesis of inorganic materials	Metal physics	Metallic glasses and composites		
Dr. Sabine Wurmehl – 519	Prof. Dr. Jens Freudenberger – 550	Dr. Simon Pauly – 451		
	Magnetic microstructures			
	Prof. Dr. Rudolf Schäfer – 223			
	Metastable and nanostructured materials			
	Dr. Bernd Rellinghaus – 754			

Date: January 2017

Scientific Advisory Board

Head: Prof. Dr. Maria-Roser Valenti
J.-W. Goethe-Univ. Frankfurt

Board of Trustees

Head: MDgt Jörg Geiger

Executive Board

Scientific Director

Prof. Dr. Burkard Hillebrands

Ass.: Dr. Carola Langer - 234

Secr.: Ines Firlle - 100

Administrative Director

Dr. Doreen Kirmse

Secr.: Anja Hänig - 200

Public Relation, Media

Safety Officer

Project Funding,
EU-Office

Internal Auditor

Knowledge and
Technology Transfer

Controlling

Member of the



Institute for Solid State Research (IFF)

Prof. Dr.
Bernd Büchner - 808

Secr.: Kerstin Höllner - 300
Katja Schmiedel - 805

Surface dynamics

Transport and
scanning probe microscopy

Chemistry of nanomaterials

Magnetic properties

Electronic and
optical properties

Synchrotron methods

Crystal growth and synthesis
of inorganic materials

Institute for Metallic Materials (IMW)

Prof. Dr.
Kornelius Nielsch - 104

Secr.: Svea Fleischer - 102
Linda Petersohn - 324

Chemical synthesis
of materials

Functional oxide layers
and superconductors

Magnetic materials

Functional magnetic films

Quantum materials
and devices

Thermoelectric materials
and devices

Metal physics

Magnetic microstructures

Metastable and
nanostructured materials

Institute for Complex Materials (IKM)

Dr.
Thomas Gemming (temp.) - 298

Secr.: Brit Präßler-Wüstling - 217
Janett Schuster - 198

Solidification processes
and complex structures

Magnetic composites
and applications

Micro- and nanostructures

Chemistry of
functional materials

Electrochemical energy storage

Alloy design and processing

Metallic glasses and composites

Institute for Integrative Nanosciences (ITF)

Prof. Dr. Prof. h. c.
Oliver G. Schmidt - 800

Secr.: Kristina Krummer - 810

Rolled-up photonics

Integrated nanophotonics

Micro- and nanobiomedical
engineering

Institute for Theoretical Solid State Physics (ITF)

Prof. Dr.
Jeroen van den Brink - 400

Secr.: Grit Rötzer - 380

Quantum Chemistry

Quantum theory of complex
nanoarchitectures

Numerical solid state physics

Research Technology Division (BFT)

Prof. Dr.
Dirk Lindackers - 580

Secr.: Nicole Büttner - 505

Electrical Engineering
and Electronics

Mechanical Engineering

Information Technologies

Administrative Division (BVW)

Dipl.-Kffr. - 620
Friederike Jaeger

Secr.: n.n. - 621

Finance Department

Human Resources

Purchase and Disposal

Library

Facility Management

Labour Council

Equal Opportunity
Commissioner

Representative Body for
Disabled Employees

Confidential Representative
(Ombudsperson)

Data Security Officer

Scientific-Technical
Council (WTR)

Standort Chemnitz
Smart Systems Campus
Technologie-Campus 1
D-09126 Chemnitz

Standort Niedersedlitz
InfoCenter SupraTrans
Straße des 17. Juni 25
D-01257 Dresden

Address

Helmholtzstrasse 20
D-01069 Dresden

Phone

Tel.: +49 351 46 59-0
Fax: +49 351 46 59-540

Internet

www.ifw-dresden.de
info@ifw-dresden.de

Date: January 2017